DISSERTATION

Classical and quantum phase transitions in strongly correlated electron systems

ausgeführt zum Zwecke der Erlangung des akademischen Grades eines Doktors der Naturwissenschaften unter der Leitung von

University Prof. Dr. Karsten Held
Associate Prof. Dr. Alessandro Toschi

E 138 - Institut für Festkörperphysik
eingereicht an der Technischen Universität Wien
Fakultät für Physik

von

Dipl.Ing. Thomas Schäfer

Matrikelnummer: e0725587
Missongasse 9, A-3550 Langenlois

Wien, am 28. Oktober 2016

This thesis has been refereed by Prof. Karsten Held (TU Wien) and Prof. Walter Metzner (Max-Planck Institute Stuttgart) and graded with the highest possible grade.

This thesis has been defended at the TU Wien on the 28th of September 2016 in front of the commission of Prof. Karsten Held (TU Wien), Prof. Walter Metzner (Max-Planck Institute Stuttgart) and Prof. Helmut Leeb (TU Wien) “with distinction”.

The author of this thesis is entitled to request a “Promotio sub auspiciis Praesidentis rei publicae”, the promotion by the federal president of Austria, which is the highest honor for university and school studies achievable in Austria.

For my parents
Elfriede and Gerhard

Contents

Abstract

Strongly correlated electron systems exhibit some of the most fascinating phenomena of condensed matter physics. Beyond the famous example of the Mott-Hubbard metal-to-insulator transition and the occurrence of classical phase transitions like magnetic and charge ordering as well as superconductivity, quantum phase transitions in strongly correlated systems are currently under intense research. These transitions are quite intriguing, because they occur at zero temperature, where quantum fluctuations dominate the physics in contrast to their classical, thermal counterparts, but they affect broad sectors of the phase diagram of both real materials and model systems. Their theoretical description, however, faces big challenges, both analytical and numerical, so that a comprehensive theory could not be established hitherto.

This dissertation aims at a theoretical understanding of classical and quantum phase transitions by exploiting cutting-edge field theoretical many-body methods: the dynamical mean field theory (DMFT), which treats local correlations, but neglects spatial correlations and the dynamical vertex approximation (DΓA), a diagrammatic extension of DMFT, which additionally incorporates spatial correlations on every length scale. These state-of-the-art methods are applied to one of the most important and fundamental model systems in condensed matter physics, the Hubbard model. First, precursor features of phase transitions are analyzed. They can, in fact, be of very different kind: In the case of the Mott-Hubbard transition they appear as divergent irreducible vertices, in the case of second order phase transitions as (charge-, spin- and pairing-) fluctuations. Then, the influence of the vicinity of second order phase transitions on one-particle spectra is investigated for various dimensionality. Interesting features of self-energies in specific dimensions are highlighted. In the next step, the fate of the Mott-Hubbard metal-insulator transition is determined for two dimensions, where the DMFT is known to become an inadequate approximation because it neglects spatial correlations. Eventually, the magnetic phase diagram of the doped Hubbard model in three dimensions (especially the region around its magnetic quantum critical point) is analyzed. The simultaneous treatment of strong local and non-local fluctuations makes DΓA particularly well suited to study the competing processes which control the physics of a strong-coupling quantum critical point. The DΓA critical exponents of the magnetic susceptibility and correlation length for the Hubbard model are determined, providing evidence for a significant violation of the prediction of the conventional Hertz-Millis-Moriya theory.

Deutsche Kurzfassung (German abstract)

In stark korrelierte Elektronensystemen lassen sich eindrucksvolle Phänomene der Physik der kondensierten Materie beobachten: Hier treten neben dem berühmten Mott-Hubbard Übergang von einem Metall zu einem Isolator auch klassische Phasenübergänge wie Magnetismus, Ladungsordnung und Supraleitung auf. Darüber hinaus zeigen diese Systeme Quantenphasenübergänge, die Gegenstand intensiver modernster Forschung sind. Was diese Übergänge so bemerkenswert macht, ist die Tatsache, dass sie im Gegensatz zu klassischen Übergängen am absoluten Temperaturnullpunkt stattfinden. Dies macht Quantenphasenübergänge zum Einen sehr faszinierend, zum Anderen theoretisch sehr schwer zu beschreiben: Bis dato existiert keine umfassende Theorie der Quantenkritikalität.

Das Ziel dieser Dissertation ist die theoretische Beschreibung von klassischen und Quantenphasenübergängen durch die Anwendung von hochaktuellen quantenfeldtheoretischen Methoden auf das fundamentalste Modell für elektronische Korrelationen, das Hubbard-Modell. Die hierfür verwendeten Methoden sind die dynamische Molekularfeldtheorie (DMFT), welche in der Lage ist, lokale Korrelationen zu beschreiben, aber räumliche Korrelationen vernachlässigt, und die dynamische Vertexapproximation (DΓA), welche zusätzlich räumliche Fluktuationen auf beliebigen Längenskalen berücksichtigt. Zuerst werden Vorboten von Phasenübergängen näher untersucht. Beim Mott-Hubbard Übergang werden diese durch divergierende irreduzible Vertexfunktionen und bei klassischen Phasenübergängen durch starke Ladungs-, Spin- oder Paarfluktuationen repräsentiert. Danach wird der Einfluss von Dimensionalität und Nähe zu Phasenübergängen auf das Spektrum des Systems untersucht. Spezifische Relationen für die Selbstenergie in verschiedenen Dimensionen werden herausgearbeitet. Im nächsten Schritt wird das Schicksal des Mott-Hubbard Metall-Isolator-Übergangs in zwei Dimensionen bestimmt, wo die DMFT zu dessen Beschreibung nicht ausreicht, weil hier räumliche Korrelationen sehr stark werden. Schließlich wird das magnetische Phasendiagramm für das lochdotierte Hubbard-Modell in drei Dimensionen berechnet und analysiert. Die DΓA ist hierfür prädestiniert, weil sie die simultane Behandlung von zeitlichen und räumlichen Korrelationen erlaubt, was insbesondere wichtig für die Beschreibung eines quantenkritischen Punktes bei starker Wechselwirkung ist. Die (quanten)kritischen Exponenten der magnetischen Suszeptibilität und Korrelationslänge werden mittels der DΓA bestimmt. Diese stehen im Widerspruch zur konventionellen Hertz-Millis-Moriya Theorie.

List of Publications

Peer-reviewed journal publications

- O. Gunnarsson, T. Schäfer, J. P. F. LeBlanc, J. Merino, G. Sangiovanni, G. Rohringer, and A. Toschi, *Parquet decomposition calculations of the electronic self-energy*, Phys. Rev. B **93**, 245102 (2016), featured as Editor's Suggestion.

- P. Pudleiner, T. Schäfer, D. Rost, G. Li, K. Held, and N. Blümer, *Momentum structure of the self-energy and its parametrization for the two-dimensional Hubbard model*, Phys. Rev. B **93**, 195134 (2016).

- O. Gunnarsson, T. Schäfer, J. P. F. LeBlanc, E. Gull, J. Merino, G. Sangiovanni, G. Rohringer, and A. Toschi, *Fluctuation Diagnostics of the Electron Self-Energy: Origin of the Pseudogap Physics*, Phys. Rev. Lett. **114**, 236402 (2015).
  See also popular article of the TU press office (German): *Das Rauschen fester Körper*, https://www.tuwien.ac.at/aktuelles/news_detail/article/9527/.

- T. Schäfer, A. Toschi and J. M. Tomczak, *Separability of dynamical and nonlocal correlations in three dimensions*, Phys. Rev. B **12**, 121107(R) (2015).

- A. Valli, T. Schäfer, P. Thunström, G. Rohringer, S. Andergassen, G. Sangiovanni, K. Held, and A. Toschi, *Dynamical vertex approximation in its parquet implementation: Application to Hubbard nanorings*, Phys. Rev. B **11**, 115115 (2015).

- T. Schäfer, F. Geles, D. Rost, G. Rohringer, E. Arrigoni, K. Held, N. Blümer, M. Aichhorn, and A. Toschi, *Fate of the false Mott-Hubbard transition in two dimensions*, Phys. Rev. B **12**, 125109 (2015).

- T. Schäfer, G. Rohringer, O. Gunnarsson, S. Ciuchi, G. Sangiovanni, and A. Toschi, *Divergent Precursors of the Mott-Hubbard Transition at the Two-Particle Level*, Phys. Rev. Lett. **110**, 246405 (2013).
  See also popular article of the TU press office (German): *Wo die Drachen wohnen*, https://www.tuwien.ac.at/aktuelles/news_detail/article/8264/.

Conference proceedings

- O. Gunnarsson, T. Schäfer, J. P. F. LeBlanc, E. Gull, J. Merino, G. Sangiovanni, G. Rohringer, and A. Toschi, *Fluctuation Diagnostics of Electronic Spectra*, Proceedings of the Vienna Young Scientists Symposium 2016, ISBN 978-3-9504017-2-1.
- T. Schäfer, A. Toschi, and K. Held, *Dynamical vertex approximation for the two-dimensional Hubbard model*, J. Magn. Magn. Mater. **400**, 107-111 (2015).
- H. Ostad-Ahmad-Ghorabi, T. Schäfer, A. Spielauer, G. Aschinger, and D. Collda-Ruiz, *Development of the digital storage Fuon*, Proceedings of the 19th International Conference on Engineering Design (ICED13), Design for Harmonies, Vol. 2: Design Theory and Research Methodology, Seoul, Korea, 19-22.08.2013, ISBN 978-1-904670-45-2.

Preprints

- O. Gunnarsson, J. Merino, T. Schäfer, G. Sangiovanni, G. Rohringer, and A. Toschi, *Electron spectra, fluctuations and real space correlations*, in preparation (2016).
- T. Schäfer, S. Ciuchi, M. Wallerberger, P. Thunström, O. Gunnarsson, G. Sangiovanni, G. Rohringer, and A. Toschi, *Non-perturbative landscape of the Mott-Hubbard transition: Multiple divergence lines around the critical endpoint*, preprint arXiv:1606.03393 (2016).
- T. Schäfer, A. A. Katanin, K. Held, and A. Toschi, *Quantum criticality with a twist - interplay of correlations and Kohn anomalies in three dimensions*, preprint arXiv:1605.06355 (2016).

Acknowledgements

Writing a thesis is a truly gigantic project - and simply not possible to achieve on one's own. In this Chapter, I want to thank all the people which made this project possible (and apologize to the ones I may have forgotten).

First of all, I want to thank **Karsten Held**, in whose group I had the honor to work as a PhD candidate. Speaking to Karsten about physics, one can immediately acknowledge his great physical intuition and fascination for this subject. Also, I have to admire his great leading skills, as he has to coordinate roughly fifteen people in the group simultaneously and manages to keep a productive environment and cooperative atmosphere for every member. Furthermore, he achieved to persuade me to play soccer, which is not a big talent of mine, in particular...

I am honestly indebted to **Alessandro Toschi**, who not only was the supervisor of my master thesis, but also agreed to co-supervise my PhD thesis. And without him - I do not have a doubt about this - this thesis would not have gone in this great way it did. Throughout the years, Alessandro not only became one of the most admired physicists of mine, but also a true friend. He taught me incredibly much about physics, indeed, but also how to make Italian pasta appropriately ("al dente", the noodle has to fit the sauce), where to find the best pizza in Rome ("L'Antico Moro" in Trastevere) and the basics of Italian politics (I will not comment on this particular issue). I hope we will have many more "typical TU days". Grazie mille!

Speaking of Italians, big thanks go to **Giorgio Sangiovanni**, also member of my thesis advisory committee. Actually, he was the first physicists with whom I collaborated. I really enjoyed it and the scientific discussions (sometimes stimulated by a glass of good wine) and my stay in Würzburg. Also thanks for showing me Vincanta and Campello. Some good physical ideas stem from there and this special location is further acknowledged in one or the other paper. Grazie, professore!

Also I have to thank **Georg Rohringer**, the co-supervisor of my master thesis, another great physicist and great support. I learned incredibly many things from Georg and he became sort of a “role model” with his very keen mind and strategies to attack problems. I hope this collaboration and camaraderie will be prolonged, despite his dislike of Paris (“the streets are really narrow compared to Moscow, I don’t like them”) and pasta cooking habits (“20 minutes - for all sorts of pasta”).

Throughout the years of my studies, I met a lot of inspiring people, be it in international collaborations or in the groups of Karsten, Alessandro, Giorgio and **Sabine Andergassen**. Especially, I want to thank **Olle Gunnarsson** for many great collaborations and for inviting my for a stay at the Max-Planck Institute in Stuttgart and **Sergio Ciuchi** and **Markus Wallerberger** for their great inputs for the precursor projects. Big thanks go to my former colleague **Angelo Valli** for giving me insight into the nano-world. Also the projects together with **Jan Tomczak** I enjoyed really much (last but not least because of his great sense of humor). Furthermore, many (physical and non-physical) advices of **Philipp Hansmann** were really, really useful (although Alessandro sometimes complains about some of them). Big thanks also to **Anna Galler**, with whom I actually began my physics studies and I can speak freely in my Austrian dialect without any problems. Thank you, **Patrik Thunström** for lots of discussions which really went into depth. For the co-organization of the condensed matter theory journal club, I want to thank **Patrik Gunacker**. A fun time it was staying with my current and former office mates, **Nils Wentzell** (thanks for showing me the beauty of fRG), **Petra Pudleiner** (my self-energy collapses!), **Ciro Taranto** (another Italian, carbo-hydrate antagonist and great physicist) and **Agnese Tagliavini** (the smell of cooked rice reminded me to go for Asian food nearly every day). Speaking of food, very useful tips came from **Sumanta Bhandary** (Indian restaurant in Floridsdorf), but I resisted the ones of **Oleg Janson** and **Marco Battiato** (TU Mensa, but thanks for sharing the unbelievable experience of “Katy’s Garage” in Dresden and the sad animal stories told there). Also, I want to thank my colleagues of the doctoral school **Fabian Lackner** and **Liang Si** (great dumplings!), **Gang Li** (I hope, the fortune cookies will pay off) and **Tin Ribic** (Falicov-Kimball rules). Thank you, **Andreas Hausoel**, for showing me beautiful Würzburg. Great insights, I also got from my teaching and supervision experiences: the discussions with and questions of **Marie-Therese Philipp**, **Benjamin Klebel** and **Clemens Watzenböck** really inspired me to rethink and concertize ideas - don’t stop doing so! Truly inspiring were also the discussions with **Daniel Springer**, the most recent member of our group (I think, finally, I understood ED). Furthermore, I want to thank **Motoharu Kitatani** - I am sure, we will find superconductivity at some point. And big thanks also go to **Lukas Sölkner**, who studied physics with me and became a real friend (and, in fact, is as a big oenophile as I am).

Great support I also got from **Joachim Burgdörfer** as a member of my thesis advisory committee, **Ulrich Schubert** and **Andrey Pimenov** as speakers of the doctoral school Solids4Fun and many

other Professors at the TU Wien, like my first physics professor, **Gerfried Hilscher**, who, sadly, passed away recently. Big thanks also to my first analysis professor, **Gabriela Schranz-Kirlinger**, who brightened the tough days of the first semester at university, **Herwig Michor** for supervising my bachelor thesis and **Martin Müller** for his great explanations of the rules of thermodynamics ("Je blauer, desto heißer."). Also I have to mention and honor the devotional administrative efforts of **André Vogel** (don't let the bat bite another time!) and **Angelika Bosak** (perhaps we may go for a Salsa dance once).

I also want to acknowledge the financial support of the **Austrian Science Fund (FWF)** throughout my master and PhD studies via the doctoral college "Building Solids for Functions (Solids4Fun)" (W 1243) and the international project "Quantum criticality in strongly correlated magnets (QCM)" (I 610-N16) and the support via the great computational environment of the Vienna Scientific Cluster (VSC) (especially, I want to mention **Jan Zabloudil** here).

Es gibt offensichtlich viele Menschen, ohne die eine derartige Dissertation nicht zustande kommen könnte. Aber wenige sind so fundamental daran beteiligt wie die folgenden. Den Gedanken, überhaupt Physik zu studieren, habe ich meinem Vater, **Gerhard Schäfer**, seines Zeichens Elektriker im Technischen Service der Österreichischen Bundesbahnen zu verdanken, als er mir als Kind einen Elektronikbaukasten schenkte. Meine erste Begegnung mit Phasenübergängen hatte ich dank meiner Mutter, **Elfriede Schäfer**, gelernte Köchin, als sie mir die Kunst des Kochens beibrachte. Ich war davon sofort fasziniert (nicht nur von den zugrunde liegenden physikalischen Prozessen, aber durchaus auch vom Geschmack). Diese Faszination wurde in der Schule (besonders im Physikunterricht) verstärkt - vielen Dank an meine Klassenvorstände **Mag. Franz Mauß** und **Dr. Doris Steiner** sowie eine meine Physiklehrerin **Mag. Gertrude Rind**.

Mein innerster, höchster Dank gilt meiner Familie, die mich vor und während des Studiums (und eigentlich bei allem was ich in meinem Leben tat), immer zu hundert Prozent unterstützt hat. Zu dieser zähle ich auch **Katharina Kölbl**, die mich liebevoll durch mein Studium und die Dissertation begleitet hat und hoffentlich noch lange begleiten wird (kleines Detail am Rande: Physiker brauchen manchmal auch Unterstützung bei der korrekten Farbwahl).

And now: let's start with physics...

1 Introduction

"If you want to become a great chef, you have to work with great chefs. And that's exactly what I did."

- Gordon Ramsay (British chef and restaurateur, *1966)

When I was ten years or so, my mother, who is truly a great chef, started to teach me how to cook Of course, cooking is an art[1], but we started out very simply: by boiling an egg. And this is how I first became interested in phase transitions...

Classical phase transitions are a true every-day phenomenon as one knows from the example of boiling water. Specifically, starting in the system's liquid state and progressively increasing its temperature while keeping its pressure constant, one can notice that at a certain temperature the liquid starts to exhibit bubbles of steam, i.e. water in its gaseous phase. In the transition process, both, this gaseous phase and the water's liquid phase can be stabilized, which is a hallmark of a so-called first-order transition. Here, a certain amount of (latent) heat is necessary to transform the liquid into the gaseous phase. Fig. 1.1 shows the schematic phase-diagram of water (H_2O) as a function of pressure p and temperature T.

Additionally to the phase transition lines solid-gas (sublimation), solid-liquid (melting) and liquid-gas (boiling), where first order transitions take place, one can identify a point, where an exact discrimination of the liquid and gaseous phase is no longer possible anymore. This is the so-called **critical point** of the transition line. The coexistence region vanishes and the transition therefore becomes **continuous**, i.e. a **second-order** phase transition, at the point. In the vicinity of such a continuous phase transition, the system is very susceptible for external perturbations associated with its particular type. This implies, via the fluctuation-dissipation theorem (see, e.g. [1]), that at

[1] as one can easily see, e.g., by trying to remember all the draconic Italian rules for *appropriately* cooking pasta, which I should also learn during my doctoral studies...

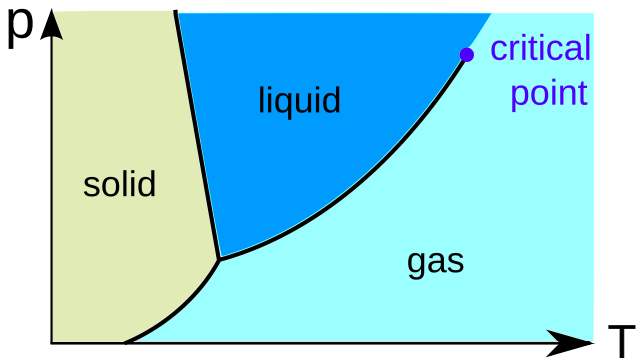

Figure 1.1: Schematic phase diagram temperature against pressure of H_2O.

this point the system exhibits fluctuations on every length scale. For the case of a liquid-gas transition this fact is impressively demonstrated by the effect of critical opalescence (see Fig. 1.2). This phenomenon is nothing else but the scattering of light by the (density) fluctuations of the system at the critical point of a second-order phase transition, which can make a transparent gas opaque in the proximity of a critical point.

The transition from a liquid to a gas is by far not the only one possible and there exist systems, especially in the context of strong electronic correlations, that show a whole plethora of them. Examples range from magnetism in heavy-fermion compounds [3], over superconductivity in iron-pnictides [4] to the famous Mott-Hubbard transition in, e.g., V_2O_3 [5]. A class of systems where this is especially true is the one of copper-oxide (CuO) compounds, which are commonly referred to as **cuprates** [6] (see Fig. 1.3). In the basic (stoichiometric) configuration, where the Cu site hosts one electron on average (half-filling) and at low temperatures, these compounds are **Mott insulators**, i.e. in an insulating state which is driven by the Coulomb interaction of the electrons. Furthermore, the system is magnetically ordered, specifically in an antiferromagnetic (AF) pattern, where up- and down-spins are alternating.

Figure 1.2: (taken from [2]) The phenomenon of critical opalescence which can be found in, e.g., SF_6: scattering of light on density fluctuations at every length scale, that are exhibited at the critical point of the first-order liquid-gas phase transition.

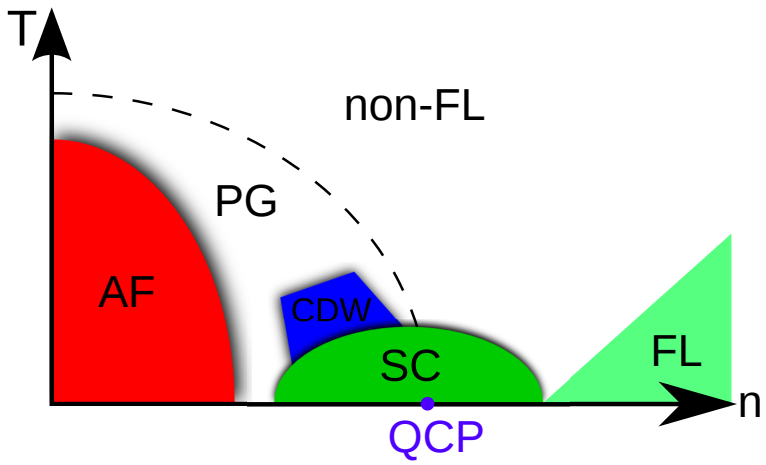

Figure 1.3: Schematic phase diagram of the high-temperature superconductors of the cuprate class upon doping. Classically ordered phases with antiferromagnetism (AF), charge density wave (CDW) and (unconventional) superconducting (SC) order coexist along with their fluctuations reaching well into the unordered phase (shadows). The pseudogap phase and regions of (non-)Fermi liquid behavior are shown and a potential quantum critical point (QCP) are indicated.

Introducing more holes into the system by doping, one enters the so-called **pseudogap** regime, where parts of the Fermi-surface are gapped out, depending on their crystal momenta. However, this phase is not immediately associated with an ordering phenomenon and the entrance into the pseudogap phase, thus does not represent an actual phase transition. At higher temperatures the gradual Fermi surface gapping is dissolved. However, the system does still not behave like a Fermi-liquid as can be inferred by investigating, e.g., the temperature dependence of the electrical resistivity, which is linear in an extremely broad temperature range. In fact, this part of the phase diagram exhibits **non-Fermi liquid** behavior. Lowering the temperature at this doping level, the famous **unconventional superconductivity** dome (SC) appears. The highest transition temperature defines the optimal doping level and can be significantly higher than the condensation temperature of liquid nitrogen (77 K). This is especially interesting for technological applications, since one of the defining properties of superconductors, their ability to conduct electrical current without dissipation, in principle becomes available without requiring the system to be cooled with liquid helium. Almost attached to the superconducting dome, recently [7], a charge-ordered phase has been found, which is coined charge density wave (CDW). Increasing the doping level further, one arrives at a metallic Fermi-liquid phase, that exhibits similar properties as a non-interacting electron gas.

One of the commonalities among the onsets of ordered phases (AF, CDW, SC) is that the existence of a phase transition is signaled already in the unordered phase by the emergence of fluctuations associated with the specific kind of order. This is indeed very similar to the phenomenon of criti-

cal opalescence discussed before: also for other second-order phase transitions than the critical point of the liquid-gas one, the systems exhibit fluctuations on every length scale in the immediate vicinity of the transition. Specifically, one will observe strong spin, charge or particle-particle (pairing) fluctuations in the example of Fig. 1.3 (indicated by shadows of the actual ordered phases), depending on the ordering considered.

All the phase transitions introduced so far are classical phase transitions, which means that they are triggered by temperature and take place at finite temperatures. An even more intriguing phenomenon is that of **quantum phase transitions** (QPTs) [8–10]. Here, the ground state of the system is changed by varying a non-thermal control parameter (like doping or pressure). The point of change defines a **quantum critical point (QCP)** at zero temperature. Despite their occurrence at $T = 0$ only, quantum phase transitions are by no means a purely academic phenomenon: the sheer existence of a QCP in a phase diagram can lead to an unconventional excitation spectrum at finite temperatures giving rise to, e.g. non-Fermi liquid behavior like the linear resistivity previously discussed for the optimally doped cuprates. This is the reason, why some theoretical approaches for describing the high-temperature superconductors suggest that a QCP is “hidden” below the superconducting dome, giving rise to the non-Fermi liquid region above it, the pseudogap phase and the superconductivity itself.

All these fascinating phenomena naturally raise the question, in which way they can be described theoretically. For both classes, classical and quantum phase transitions, there exist basic theories, which lead to somewhat related descriptions. These are the famous **Landau-Ginzburg-Wilson** and **Hertz-Millis-Moriya theories**, respectively, whose general spirit will be outlined in the following (for a general introduction see [11] and [9, 12–14]).

Usually, the transition from one phase to another is accompanied by a reduction of the symmetry of the system (spontaneous symmetry breaking)[2]. Generally, this term describes the lifting of a degeneracy in the ground state by breaking one of the symmetries, which are present in the original Hamiltonian, but not respected by one particular choice for the system’s ground state. For instance, the paramagnetic phase above the AF phase in Fig. 1.3 is SU(2)-symmetric as the microscopic Hamiltonian of the system, whereas the ordered phase at lower temperatures is not. In order to discriminate the two phases, it is then useful to introduce the notion of an order parameter, i.e. a physical quantity that is zero in the unordered and finite in the ordered (symmetry-broken) phase. As an example, for a paramagnetic to antiferromagnetic transition, the (staggered) magnetization can serve as an order parameter. In the Landau-Ginzburg-Wilson approach, the free energy of the system is being expanded into a power series with respect to this order parameter near the critical point, where the order parameter is small. This expansion can be used, e.g., to

[2] With some notable exceptions, e.g. the liquid-gas transition.

calculate critical exponents of the model, for instance exponents for the temperature dependence of the respective susceptibilities. For systems that (due to their dimensionality, range of the interaction and symmetry of the order parameter) fall into the same class, these exponents are the same, i.e. “universal”.

The Landau-Ginzburg-Wilson approach is a very successful general framework for the description of classical phase transitions. However, as it is a classical theory, it completely neglects quantum fluctuations, which are a necessary ingredient for the description of quantum phase transitions. The Hertz-Millis-Moriya theory amends the Landau-Ginzburg approach by the introduction of quantum fluctuations. In his seminal work, Hertz studied itinerant electron systems by applying a renormalization group (RG) treatment to model systems and concluded that at zero temperature, static and dynamic properties are interwoven. Later, Millis analyzed how the existence of a quantum phase transition affects properties of these systems at finite temperatures.

Despite all the theoretical efforts for describing classical and quantum phase transitions, these transitions are far from being understood in strongly correlated electron systems in general and in the cuprates in particular. The reason for this is twofold: first, the electrons in the cuprates are strongly correlated and, second, the cuprates are (due to their strongly anisotropic layered structure) effectively **low-dimensional** (quasi-two-dimensional, to be specific). Due to the strong electronic correlations, common perturbative techniques as well as density functional theory, fail in reproducing their properties and phase diagrams. This implies that (many-body) techniques must be exploited, among which one of the most prominent is the **dynamical mean field theory** (DMFT) [15–19]. The DMFT is a very powerful technique that is able to exactly take into account all **local correlations** of the system. However, in cases of low dimensions or in the proximity to second-order phase transitions, also **spatial correlations** have to be included, which means that one even has to go beyond DMFT in order to describe the physics there accurately.

While this discussion highlighted some of the most challenging subjects of contemporary condensed matter physics, the aim of the thesis is to make a significant progress in the fundamental understanding by applying a cutting-edge diagrammatic many-body technique beyond DMFT, the **dynamical vertex approximation (DΓA)** [20], to the most famous model system for electron correlated systems, the **Hubbard model** [21] in three, two and one dimensions. By doing so, the nature of classical and quantum phase transitions in strongly correlated electron systems will be investigated and their properties be analyzed also in correlated regimes not accessible to the theory hitherto.

The thesis is structured as follows:

- In **Chapter 2** the basic strategies for treating strong electronic correlations are outlined. The basic models which are used throughout the thesis, the Hubbard model and the Anderson impurity model, and the many-body techniques exploited to analyze their properties, the dynamical mean-field theory and the dynamical vertex approximation, are introduced and described in detail.

- **Chapter 3** investigates precursors of phase transitions. In particular, precursor features of the Mott-Hubbard transition are identified by divergent irreducible two-particle vertex quantities and the highly non-perturbative landscape of the Mott-Hubbard transition is investigated. Furthermore, the implication of these precursors on the physical analysis of the one-particle spectrum via its so-called parquet decomposition is analyzed. To overcome the interpretational difficulties encountered there, eventually, the fluctuation diagnostics method is introduced.

- In the course of **Chapter 4** the impact of the proximity of phase transitions on the one-particle spectrum is analyzed for strongly correlated systems in various dimensions. Starting at infinite dimensions, where the DMFT is the exact solution, the dimensionality of the system is progressively reduced. In three dimensions, the space-time separability of the self-energy is discussed. Going to two dimensions, it is shown that, under certain circumstances, the self-energy collapses onto a single curve under the reparametrization with the non-interacting electron dispersion. Finally, spatial correlations and the applicability of the dynamical vertex approximation are discussed for (finite-sized) one-dimensional Hubbard nano-rings.

- The fate of the famous Mott-Hubbard metal-insulator transition in two dimensions is determined in **Chapter 5**. There it is shown that if, in the (unfrustrated) two-dimensional Hubbard model on a square lattice, spatial correlations on all length scales are included on top of DMFT, the paramagnetic phase is always insulating at low enough temperatures. In particular it is demonstrated, that the critical interaction value is progressively reduced to zero by antiferromagnetic Slater-paramagnons.

- In **Chapter 6**, magnetic phase transitions in the three-dimensional Hubbard model are analyzed. Its phase diagram for half-filling is recalled and extended to the more interesting hole-doped case by means of DMFT as well as DΓA. If the hole doping becomes large enough, the system exhibits a quantum critical point. The critical exponents for the magnetic susceptibility and the correlation length are analyzed for the classical as well as the quantum phase transitions in this model and the influence of the Fermi surface structure (Kohn anomalies) is pointed out.

- Finally, conclusions from the results of the thesis are drawn in **Chapter 7** and an outlook for future investigations based on the progress triggered by this work will be given.

2

Many-body theory: models and methods

"In theory, the big news is the DMFT which gives us a systematic way to deal with the major effects of strong correlations. After nearly 50 years, we are finally able to understand the Mott transition, for instance, at last."

- Philip Warren Anderson (American physicist, *1923)

The description of the fascinating phenomena taking place in strongly correlated electron systems is very challenging, not only because of the huge number of involved particles, but also due to their strong mutual interactions. Therefore, strategies beyond perturbation theory, mean-field theories and density functional theory have to be formulated. In this Chapter, first the basic strategies to tackle these challenges are outlined: (i) the simplification of the essence of the problem by setting up model Hamiltonians and (ii) the replacement of wave-function based methods by other, more "condensed" (one- and two-particle Green function) quantities, which still allow to access the observables of interest. Specifically, starting from the full solid state Hamiltonian, the simplest model for treating electronic correlations, the Hubbard model, is deduced alongside the, methodologically very useful, Anderson impurity model. In the second part of this Chapter, the dynamical mean-field theory (DMFT) is introduced, which maps the Hubbard model onto a self-consistently determined Anderson impurity model. DMFT is able to include all temporal fluctuations, but neglects spatial correlations. Subsequently, strategies for extending the DMFT to also include spatial correlations are discussed and one of its diagrammatic extensions, the dynamical vertex approximation, is presented. Both of these methods will be extensively used throughout this thesis. Therefore, the current implementation of the dynamical vertex approximation as used in this thesis is discussed in details at the end of this chapter.

Unlike in many other areas of physics, in condensed matter theory the governing Hamiltonian can be written down straightforwardly:

$$H = H_0 + V_{ee} \tag{2.1}$$

with

$$H_0 = \sum_{\sigma=(\uparrow,\downarrow)} \int d^3r \Psi^\dagger_\sigma(\vec{r}) \left[-\frac{\hbar^2}{2m}\partial^2 - \sum_l \frac{e^2}{4\pi\epsilon_0} \frac{Z_l}{\left|\vec{r} - \vec{R}_l\right|} \right] \Psi_\sigma(\vec{r})$$

$$V_{ee} = \frac{1}{2} \sum_{\sigma,\sigma'} \int d^3r d^3r' \Psi^\dagger_\sigma(\vec{r}) \Psi^\dagger_{\sigma'}(\vec{r}') \frac{e^2}{4\pi\epsilon_0} \frac{1}{|\vec{r} - \vec{r}'|} \Psi_{\sigma'}(\vec{r}') \Psi_\sigma(\vec{r})$$

where $\Psi^\dagger_\sigma(\vec{r})$ and $\Psi_\sigma(\vec{r})$ are field operators which create or respectively destroy an electron of charge $-e$ and spin σ at position $\vec{r}$ and l are the lattice ions with charge Z_l at the positions $\vec{R}_l$. The electron's mass is denoted by m, $\hbar$ is the Planck constant and ϵ_0 is the dielectric constant in vacuum.

Despite its small number of fundamental ingredients (electrons, protons and the Coulomb interaction), Eq. (2.1) cannot be rigorously solved to obtain the quantum mechanical wave function, due to a two-fold reason: First, condensed matter systems generally consist of $\sim 10^{23}$ particles, and, second, they are heavily interacting mutually, giving rise to a high degree of correlations.

In order to tackle this problem, two complementary strategies can be applied:

- The general many-body Hamiltonian is transformed to a simpler model, which, however, still contains the essential physics of the original problem.
- The (exact) diagonalization procedure for Eq. (2.1) for obtaining the system's wave-function is replaced by other approximate methods which still provide access to the system's properties of interest.

In the following sections examples from both routes will be explained that also found the basis of the methods used in this thesis. First, two basic models for electronic correlations are introduced: the Hubbard model and the (periodic) Anderson impurity model. Second, two non wave-function-based methods for the treatment of electronic correlations are discussed in detail: the dynamical mean-field theory and the dynamical vertex approximation. The dynamical mean field theory and its cluster extensions in the context of the Hubbard model have already been used in the master thesis of the author [22], so that in the following, for the sake of self-containment, the relevant parts are recapitulated from there.

2.1 Modellization of electronic correlations

In many situations, for interpreting (or predicting) experimental results, it is not necessary to calculate the general solution to the definite problem of interest (i.e. the wave function for the $\sim 10^{23}$ particle problem). One way for retrieving valuable informations about the system and, at the same time, at least approximately, explaining and predicting experimental results is paved by simplifying Eq. (2.1) in order to build model Hamiltonians. In this section two prototypical model Hamiltonians will be discussed: the Hubbard model, often considered as the simplest model for electronic correlations, and the periodic Anderson model as a basic (realistic) model for heavy fermion compounds.

2.1.1 The Hubbard model

If one considers a lattice of ions which are separated by a distance larger than the Bohr radius, one can approximate the original lattice problem in the **tight-binding approximation** (see e.g. [23]). In a first step the Hamiltonian is represented by a superposition of atomic orbital states or **Wannier states**. These Wannier states constitute an orthonormal basis of the one-particle Hilbert space, meaning that there exists a (unitary) transformation from real to Wannier space. This implies that the field operators in real space in Eq. (2.1) can be written in terms of field operators at each lattice site i:

$$\Psi_\sigma^\dagger(\vec{r}) = \sum_{i=1}^{N} \psi_{\vec{R}_i}^*(\vec{r}) c_{i\sigma}^\dagger \tag{2.2}$$

Furthermore one can Fourier transform the Wannier state operators $c_{i\sigma}^\dagger$ to momentum space

$$c_{k\sigma}^\dagger = \frac{1}{\sqrt{N}} \sum_{i=1}^{N} e^{i\vec{k}\vec{R}_i} c_{i\sigma}^\dagger \tag{2.3}$$

so that the single particle part of the Hamiltonian in Eq. (2.1) becomes (see [23])

$$H_0 = \sum_{\vec{k}} \epsilon_k c_{k\sigma}^\dagger c_{k\sigma} = \sum_{ii'} t_{ii'} c_{i\sigma}^\dagger c_{i'\sigma} \tag{2.4}$$

where

$$t_{ii'} = \frac{1}{N} \sum_{\vec{k}} e^{i\vec{k}(\vec{R}_i - \vec{R}_{i'})} \epsilon_k = \int d^d r \; \psi_{\vec{R}_i}^* \frac{\hbar^2 \partial^2}{2m} \psi_{\vec{R}_j}^*$$

denotes the **hopping amplitude** for a particle to transit from site i to site i'. Similarly one can apply this procedure to the electron-electron interaction term in Eq. (2.1) and finally obtains for the fully

transformed Hamiltonian:

$$H = \sum_{ii'} t_{ii'} c^\dagger_{i\sigma} c_{i'\sigma} + \sum_{ii'jj'} U_{ii'jj'} c^\dagger_{i\sigma} c^\dagger_{i'\sigma} c_{j\sigma} c_{j'\sigma}. \tag{2.5}$$

If the overlap of neighboring orbitals becomes weak, the dominant electronic interaction is the on-site Coulomb interaction, or **Hubbard interaction**. In this limit one finally arrives at the simplest model for the description of electronic correlation in solid state physics, the **Hubbard model** (see. Fig. 2.1, [21]). For the single band case (and only considering nearest neighbor hopping), the Hamiltonian of the Hubbard model reads

$$H = -t \sum_{\langle i,j\rangle\sigma} c^\dagger_{i,\sigma} c_{j,\sigma} + U \sum_i n_{i\uparrow} n_{i\downarrow} \tag{2.6}$$

where $-t$ is the hopping amplitude of the electron to hop from lattice site i to j, $c^\dagger_{i,\sigma}$ and $c_{j,\sigma}$ are the creation and annihilation operators for creating or destroying an electron with spin σ on site i or j respectively, and $\langle i,j\rangle$ denote nearest neighbor sites which are counted once in the sum. The **Coulomb energy** (or Hubbard interaction) U has to be paid whenever a single site is occupied by two electrons. The interpretation of the two ingredients of this model is quite transparent as they correspond to the two competing energy scales of a correlated electron system, i.e. the **kinetic and the potential energy**.

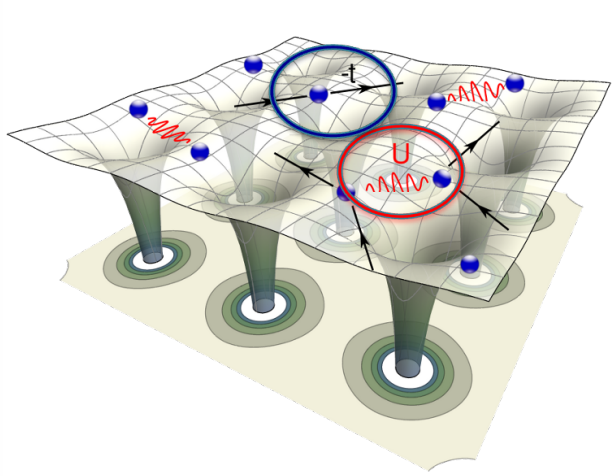

Figure 2.1: Illustration of the Hubbard model as a description of correlated electrons in solids (from [24]). The electron can hop from one site to another with the hopping amplitude $-t$. An energy U has to be paid whenever a double occupation occurs.

It is worth noting at this point that, although this model represents already a great simplification compared to real material systems described by Eq. (2.1), it is still not solvable except for trivial or quite specific (e.g. one-dimensional) cases. However, the challenging task of working with the Hubbard model is highly rewarding, since most of the interesting physics in highly correlated electron systems indeed originates from the (direct or indirect) result of the **competition of kinetic and potential energy**, which is well captured by this model Hamiltonian.

In the next sections, the Anderson impurity and the periodic Anderson models are introduced. They are doubly related to the Hubbard model: the Anderson impurity model is the key algorithmic ingredient for a powerful tool to analyze the Hubbard model (within the dynamical mean-field theory) and the periodic Anderson model is the minimal extension to the Hubbard model aiming to cover the basic physics of heavy fermion compounds.

2.1.2 The Anderson impurity model

Originally introduced for describing the properties of an magnetic atom embedded in a metallic environment [25], the applicability of the Anderson impurity model (AIM) is much broader today, as it provides the key to the treatment of local correlations, also in the Hubbard model. The Hamiltonian of the AIM can be interpreted as an interacting impurity hybridizing with non-interacting (conduction band) electrons. In its second quantized form it reads

$$H = \sum_{k\sigma} \epsilon_k a^\dagger_{k\sigma} a_{k\sigma} + \sum_{k\sigma} V_k (c^\dagger_\sigma a_{k\sigma} + a^\dagger_{k\sigma} c_\sigma) + U n_\uparrow n_\downarrow - \mu(n_\uparrow + n_\downarrow). \tag{2.7}$$

Here, $a^\dagger_{k\sigma}$ ($a_{k\sigma}$) creates (annihilates) an electron with spin σ at a bath of energy ϵ_k, $c^\dagger_{k\sigma}$ ($c_{k\sigma}$) creates (annihilates) an electron with spin σ at the impurity site. V_k quantifies the hybridization strength between impurity and bath and U is the purely local repulsion between two electrons at the impurity site. $n_\sigma = c^\dagger_\sigma c_\sigma$ counts the number of electrons with spin σ on the impurity site.

If the hybridization of the conduction band electrons and the impurity is maintained and, simultaneously, the single impurity of the AIM is extended to a periodic lattice of interacting impurities, one arrives at the periodic Anderson model.

2.1.3 The periodic Anderson model

The periodic Anderson model (PAM) is the minimal model for the description of f-electron systems, especially heavy-fermion compounds [26]. In this model, the (realistic) conduction bands are represented by a single band with dispersion ϵ_{kd} and one degenerate atomic level ϵ_f representing the

f-electrons. The Hamiltonian of the PAM reads as

$$H = \sum_{k\sigma} \epsilon_k d^\dagger_{kd\sigma} d_{k\sigma} + \epsilon_f \sum_{i\sigma} f^\dagger_{i\sigma} f_{i\sigma} + \sum_{k\sigma} V_k (d^\dagger_{k\sigma} f_{k\sigma} + f^\dagger_{k\sigma} d_{k\sigma}) + U_f \sum_i n_{fi\uparrow} n_{fi\downarrow} - \mu \sum_{i\sigma} n_{fi\sigma} + n_{di\sigma}, \tag{2.8}$$

where $d^\dagger_{k\sigma}$ ($d_{k\sigma}$) creates (annihilates) a conduction electron with momentum k and spin σ and $f^\dagger_{k\sigma}$ ($f_{k\sigma}$) creates (annihilates) an impurity electron with momentum k and spin σ. $n_{di\sigma}$ ($n_{fi\sigma}$) is the number operator of the conduction (impurity) electrons.

The Hubbard model, as well as the PAM, cannot be solved exactly in arbitrary dimensions. However, there exists a powerful tool for retrieving physical observables from these model, the dynamical mean field theory, which is introduced in the following section.

2.2 Dynamical mean-field theory and its extensions

The essence of dynamical mean field theory (DMFT) is to map the whole many body problem of Eq. (2.1) onto a single site Anderson impurity model (AIM) to be determined self-consistently [15]. For retrieving physical quantities (e.g. via the calculation of the self-energy) one has to solve a self-consistency cycle based on the single-site (AIM) quantity and the local component of the same quantity of the original lattice. This corresponds to treating the spatial degrees of freedom of a given system at a mean-field theory level (like in a classical mean or Weiss field theory), whereas fully retaining local temporal fluctuations (or "quantum fluctuations"). The mapping becomes exact in the limit of infinite coordination number and DMFT, therefore, is an exact theory in this asymptotic regime [16, 17]. More formally, for a fixed lattice geometry the limit of infinite coordination corresponds to the limit of high spatial dimensions or high temperatures.

2.2.1 The diagrammatic content of DMFT

If one considers the expectation value for the kinetic energy part of the Hubbard Hamiltonian including next neighbor (NN) hopping only

$$\langle H_{\text{kin}} \rangle = -t \sum_{(i,j),\sigma} \left\langle c^\dagger_{i,\sigma} c_{j,\sigma} \right\rangle \tag{2.9}$$

and the coordination number (i.e. the number of next neighbors for each lattice site) of the lattice is z, the probability (i.e. the absolute square of the hopping amplitude) that an electron hops from a site j to a next neighbor site of j is $P \propto \frac{1}{z}$. From this consideration one can deduct that in the limit of infinite coordination $z \to \infty$ the proper scaling of the kinetic energy in the Hubbard

model (Eq. (2.6)) is $t \propto \frac{1}{\sqrt{z}}$. Indeed, as it was shown by W. Metzner and D. Vollhardt, the only scaling, for which the Hubbard model physics remains non-trivial in the limit of infinite coordination is $t \propto \frac{1}{\sqrt{z}}$, whereas the proper scaling of the potential energy is trivial because it is purely local [16]. The crucial point, however, is, that with this scaling also all self-energy skeleton diagrams become purely local in the limit $z \to \infty$ (see Fig. 2.2) [16, 18], and, hence:

$$\Sigma(\nu, \vec{k}) \to \Sigma(\nu). \tag{2.10}$$

Therefore, from the diagrammatic point of view, **DMFT** corresponds to regarding all completely **local one-particle irreducible diagrams** as the electronic self-energy (see also Fig. 2.2), which physically corresponds to consider only the **local part** of the electronic correlation, but **without any perturbative restriction**.

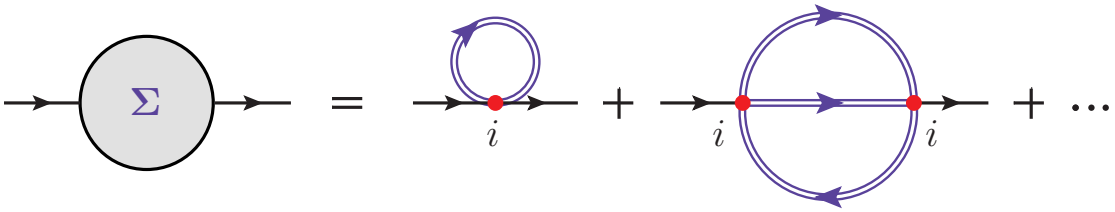

Figure 2.2: Diagrammatic content of the DMFT (taken from [27]). The thick red dot denotes the local interaction U, the single lines the non-interacting and the double lines the dressed Green functions. All local one-particle irreducible diagrams are regarded as the electronic self-energy.

2.2.2 Self-consistency cycle and impurity solvers

From the practical point of view, one of the keys for explaining the success of DMFT is the above mentioned mapping of the original lattice problem onto an Anderson impurity problem. Such a mapping is possible because the same diagrams which constitute the (purely local) DMFT self-energy can also be obtained from the Anderson impurity model in Eq. (2.7) [28] provided the on-site interaction U coincides with the one of the original Hubbard model in Eq. (2.6) and the interacting Green functions are the same. In the definition of the Anderson impurity model, $a^{\dagger}_{\vec{k}l\sigma}$ and $a_{\vec{k}l\sigma}$ are the creation and annihilation operators of conduction band electrons with dispersion $\epsilon_l(\vec{k})$, $c^{\dagger}_{im\sigma'}c_{in\sigma'}$ are the creation and annihilation operators of the impurity site and $V_{lm}(\vec{k})$ defines the hybridization between conduction band and impurity site electrons.

2.2.2.1 The DMFT self-consistency cycle

As pointed out by Georges and Kotliar [17], due to the equivalence of the (purely local) diagrams which constitute the self-energy of both DMFT and Anderson impurity model, one is able set up a

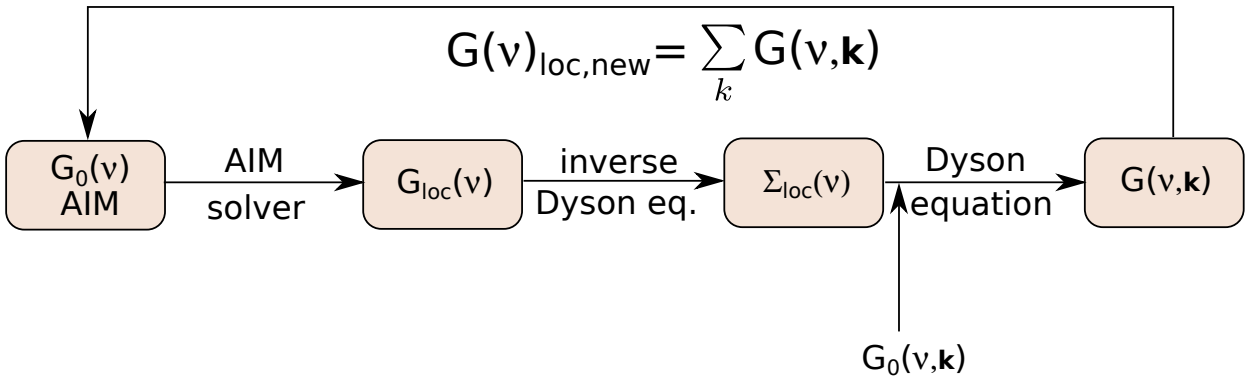

Figure 2.3: Self-consistency cycle of the DMFT. The bottleneck of the algorithm is given by the solution of the impurity problem.

self-consistency cycle for the Green function of the Anderson impurity model $G_{\text{AIM}}(\nu)$ and the local DMFT Green function

$$G_{\text{loc}}(\nu) = \frac{1}{V_{\text{BZ}}} \int\limits_{1^{\text{st}}\,\text{BZ}} d^d k \; G_{\text{DMFT}}(\nu, \vec{k}) = \frac{1}{V_{\text{BZ}}} \int\limits_{1^{\text{st}}\,\text{BZ}} d^d k \; \frac{1}{i\nu - \epsilon_k + \mu - \Sigma(\nu)} \tag{2.11}$$

where V_{BZ} is the volume of the first Brillouin zone. The local self-energy $\Sigma(\nu)$, which defines the **local Green function** via the **Dyson equation**

$$\Sigma(\nu) = G_0^{-1}(\nu) - G^{-1}(\nu), \tag{2.12}$$

can be obtained from the AIM via

$$\Sigma(\nu) = \mathcal{G}_0^{-1}(\nu) - G_{\text{AIM}}^{-1}(\nu) \tag{2.13}$$

where the **electronic bath function** of the AIM

$$\mathcal{G}_0^{-1}(\nu) = i\nu - t - \sum_{\vec{k}n} \frac{V_{nl}^{\dagger}(\vec{k}) V_{nm}(\vec{k})}{i\nu - \epsilon_n(\vec{k})} \tag{2.14}$$

can be considered as the quantum (dynamical) counterpart of a classical Weiss mean-field. Fig. 2.3 schematically shows all the steps for performing a self-consistency loop of DMFT. Among these steps one can note that the computational bottleneck of the algorithm is given by the solution of the impurity problem.

Common impurity solvers are based on exact diagonalization (ED) or Lanczos algorithms [15], numerical renormalization group (NRG, [29]), quantum Monte Carlo (QMC) or semi analytical methods like iterated perturbation theory (IPT, see e.g. [30]). In this work mainly ED and QMC will be used, those impurity solvers will be briefly discussed in the following sections.

2.2.2.2 Exact diagonalization (ED)

In exact diagonalization (ED) one solves the AIM by approximating the Hamiltonian of the AIM with an Hamiltonian built up by a finite number of orbitals n_S (**discretization of the bath**) [15]. The matrix-represented Hamiltonian is then diagonalized by standard algorithms.

Specifically, for solving the AIM in ED, one has to perform essentially three steps:

1. The Weiss function
$$\mathcal{G}_0(\nu)^{-1} = i\nu - \int_{-\infty}^{\infty} d\omega' \, \frac{\Delta(\omega')}{i\nu - \omega'} \tag{2.15}$$
is approximated by a discretized bath:
$$\mathcal{G}_0^{n_S}(\nu)^{-1} = i\nu - \sum_{p=2}^{n_S} \frac{V_p^2}{i\nu - \tilde{\epsilon}_p} \tag{2.16}$$

2. The obtained Hamiltonian of Eq. (2.16) is **diagonalized exactly**. The corresponding Green function is calculated via its Lehmann (spectral) representation [57].

3. The DMFT self-consistency condition provides a new Weiss function $\mathcal{G}_0$ which is again approximated by a function $\mathcal{G}_0^{n_S}$ with a new set of V_p and $\tilde{\epsilon}_p$.

ED provides very accurate and stable numerical results on the Matsubara axis (see again [15]). However, the scaling of the ED algorithm with n_S is very costly, which makes the calculation of two-particle vertex quantities (see Sec. 2.3.1) already quite challenging even for the single-band Hubbard model. A detailed discussion of possible accuracy issues and checks of ED algorithms can be found in Appendix A.

2.2.2.3 Hirsch-Fye Quantum Monte Carlo (QMC)

An efficient and well-established approach of an impurity model solver is the Hirsch-Fye Quantum Monte Carlo method [31]. Hirsch and Fye mapped the interacting Anderson impurity model of Eq. (2.7) onto a sum of non-interacting problems with a single particle under the influence of a time-dependent field, whereupon this sum is evaluated by Monte Carlo sampling. The most

important steps of Hirsch-Fye QMC (HF-QMC) are summarized in the following, for more details see [18, 32, 33].

The Hamiltonian H for the (single or cluster) impurity is assumed to be expressed in two parts

$$H = \underbrace{H_0}_{\text{non-interacting}} + \underbrace{H_1}_{\text{interacting}} \tag{2.17}$$

and the interaction on the impurity cluster to be local. In a first step, the imaginary time interval $[0, \beta]$ is divided (**Trotter discretization**) into L steps of size

$$\Delta\tau = \frac{\beta}{L} \tag{2.18}$$

Now the thermodynamic partition function can be expressed in terms of these time slices

$$Z = \mathsf{Tr}(e^{-\beta H}) = \mathsf{Tr}(\prod_{i=1}^{L} e^{-\Delta\tau H}) \tag{2.19}$$

and one can apply the **Trotter-Suzuki decomposition** [34]

$$e^{-\Delta\tau H} = e^{-\frac{\Delta\tau H_0}{2}} e^{-\Delta\tau H_1} e^{-\frac{\Delta\tau H_0}{2}} + \mathcal{O}(\Delta\tau^3) \tag{2.20}$$

Using the cyclic property of the trace one arrives at

$$Z \approx \mathsf{Tr}(\prod_{i=1}^{L} e^{-\Delta\tau H_0} e^{-\Delta\tau H_1}) \tag{2.21}$$

with an error of the order $\Delta\tau^2$. With the use of Hirsch's identity for a purely locally interacting Hamiltonian,

$$e^{-\Delta\tau U(n_{i\uparrow}n_{i\downarrow} - \frac{1}{2}(n_{i\uparrow}+n_{i\downarrow}))} = \frac{1}{2}\sum_{s_i=\pm 1} e^{a s_i (n_{i\uparrow} - n_{i\downarrow})} \tag{2.22}$$

where

$$\cosh(a) = e^{\frac{\Delta\tau U}{2}} \tag{2.23}$$

one introduces an auxiliary Ising field (so called **Hubbard-Stratonovich field**) so that the interacting problem has been mapped onto the sum over all possible configurations of the auxiliary field of non-interacting Ising-spins. The partition function becomes [15]

$$Z = \sum_{\{s_1,...,s_L\}} \det\left[G_\uparrow^{-1}(s_1,...,s_L)\right] \det\left[G_\downarrow^{-1}(s_1,...,s_L)\right], \tag{2.24}$$

which requires the summation over 2^L configurations. Therefore, in HF-QMC, the interacting Green function is calculated by stochastic Monte Carlo sampling, where

$$\det\left[G_{\uparrow}^{-1}(s_1,...,s_L)\right]\det\left[G_{\downarrow}^{-1}(s_1,...,s_L)\right]$$

is the stochastic weight and the configurations $\{s_1,...,s_L\}$ are the outcome of a Markov process which visits configurations of Ising variables with a single spin-flip dynamic. For a more rigorous derivation of the Hirsch-Fye QMC algorithm see Sec. VI. A1b in [15].

From the description and practical applications of the HF-QMC method three immediate drawbacks emerge [35]:

1. It requires an equally spaced time discretization.
2. At large interactions and low temperatures difficulties in managing the discretization and equilibration arise and particular care should be taken to treat the systematic errors introduced by the Trotter discretization (see [33]).
3. In the multi-orbital case, treating the SU(2)-invariant local interactions becomes very challenging.

At least parts of those drawbacks can be overcome by another QMC technique called **continuous time QMC** (CT-QMC), whose fundamental concept is avoiding the time discretization by sampling in a diagrammatic expansion, instead of sampling the configurations in a complete set of states (see [35–38]).

2.2.3 Successes and limitations of the DMFT

DMFT nowadays is a well-established, successful and applicable technique in the field of strongly correlated electron systems. In fact, the non-perturbative nature of DMFT has allowed, for the first time, for a coherent and general description of the Mott-Hubbard transition. However, the success of this theory should not lead to forget that there exist some important limitations of DMFT:

1. While local quantum fluctuations are fully taken into account by DMFT, due to its mean field nature in space, **spatial correlations are totally neglected**. This has the immediate consequence that DMFT will perform poorly in all situations in which these correlations become crucial, e.g. in the vicinity of (second-order) phase transitions where the correlation length is diverging. Also for the description of low dimensional systems, such as layered, surface- and nano-systems non-local spatial correlations play an important role and have to be considered.

2. If DMFT is applied to not infinitely coordinated systems, its self-consistency is guaranteed at the one-particle level only. This means that for $d \neq \infty$ the momentum-integrated density-density correlation function of the lattice computed in DMFT is not equal to the corresponding quantity of the associated AIM:

$$\sum_{\vec{q}} \chi(\vec{q}) \neq \chi_{\text{loc}}^{\text{AIM}} \tag{2.25}$$

leading to an intrinsic ambiguity in the calculations at least of the local response functions.

To overcome these limitations, one has to take a step beyond DMFT, as it is discussed in the following section.

2.2.4 Going beyond DMFT

Among all existing extensions of DMFT, one can essentially individuate two classes: **cluster extensions** and **diagrammatic extensions**. In a nutshell the former are based on a simple generalization of the DMFT algorithm from a single site to a cluster of sites (either in real or in momentum space), whereas the later aim at including the most relevant non-local diagrams to the DMFT.

2.2.4.1 Cluster extensions of DMFT

Several methods of cluster extensions of DMFT have been proposed, for instance

- cellular dynamical mean field theory (CDMFT), based on clusters in real space and
- dynamical cluster approximation (DCA), based on clusters in momentum space.

This section will focus on the DCA, more details on CDMFT (as well as on DCA) can be found in [39]. This introduction essentially follows [40].

Quantum cluster approaches systematically include non-local correlations to DMFT by mapping the infinite periodic lattice onto a finite sized cluster problem. This implies that spatial correlations are fully included up to the size of such a cluster, while spatial correlations on larger scales are treated still at a mean-field level.

In DMFT the Green function G_{loc} is **coarse grained** over the whole Brillouin zone

$$G_{\text{loc}}(\nu) = \sum_{\vec{k} \in 1^{\text{st}}\,\text{BZ}} G(\nu, \vec{k}), \tag{2.26}$$

which results in a momentum-independent self-energy. In DCA instead, the reciprocal lattice is divided into N_c cells of size Δk (see Fig. 2.4). Different common patching schemes can be obtained

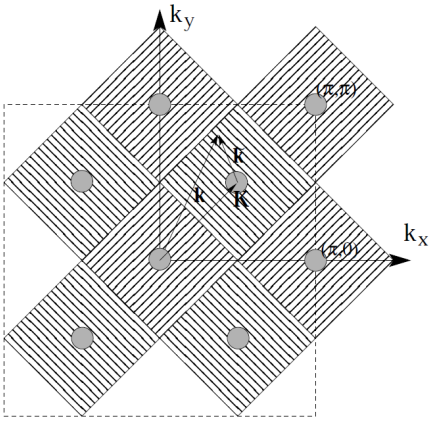

Figure 2.4: Coarse graining cells in DCA for $N_c = 8$ that partition the first Brillouin zone. The cells are centered at a cluster momentum $\vec{K}$. To construct the DCA cluster $\vec{k}$ is mapped to the nearest cluster center $\vec{k}$ so that $\tilde{\vec{k}} = \vec{k} - \vec{K}$ remains in the cell around $\vec{K}$ (taken from [40]).

from Fig. 2.5. Note that the coarse graining is only performed within each cell so that non-local spatial correlations up to a length of $\xi \approx \frac{\pi}{\Delta k}$ are taken into account. This new cluster problem can be solved again by techniques as HF-QMC [31] or CT-QMC (especially in its weak-coupling version, [35]), until the (in this case DCA) self-consistency is reached.

DCA, as well as other cluster extensions of DMFT, have been successfully applied in many cases (see [39]). However, if the inclusion of spatial correlations on all length scales is needed, one has to abandon the cluster extension schemes and adopt the complementary treatment of the diagrammatic methods described in the next section.

2.2.4.2 Diagrammatic extensions of DMFT - an overview

To overcome the limitations of cluster extensions of DMFT, several so-called diagrammatic extension have been proposed, which are in principle able to include spatial correlations on every length scale. The **dynamical vertex approximation** (DΓA), which will be introduced and discussed in

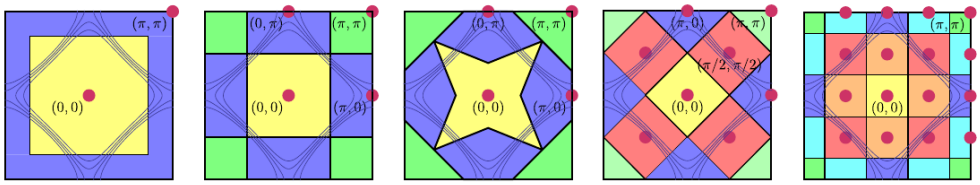

Figure 2.5: Different DCA patching schemes (taken from [41]).

detail in Sec. 2.3.2, is based on the assumption of the locality of the fully irreducible vertex Λ.

A different approach for including long-range spatial correlations beyond DMFT is the **dual fermion approach** (DF). In DF these correlations are treated systematically by introducing additional auxiliary degrees of freedom via a Hubbard-Stratonovich transformation for the non-local degrees of freedom, which are called **dual fermions**. A subsequent integration of the local degrees of freedom yields a new problem in terms of the dual fermions which interact via the reducible local 4-point full vertex F (see Sec. 2.3.1) of the AIM[1]. For a detailed description of the DF approach and its application to the two-dimensional Hubbard model see [43] and also [44].

An approach which aims at the unification of DΓA and DF is the recently proposed **one-particle irreducible functional approach** (1PI, [45]). Similarly to DF, the 1PI is also based on functional integral methods. The difference lies in the type of vertices utilized: in DF, the basic object is the reducible vertex, whereas it is the full vertex in case of the 1PI.

Recently, also a completely different path to the access to spatial electronic correlations has been proposed by the unification of DMFT with the functional renormalization group (fRG), coined **DMF^{2}RG** [46]. In this method, local correlations are fully taken into account by DMFT. On top of these, non-local correlations are systematically included by means of the functional renormalization group flow equations.

Most recently, an extension of DMFT was proposed, that interpolates between the spin-fluctuation or GW approximations at weak coupling and the atomic limit at strong coupling by approximating the dynamical three-leg interaction vertex γ (see next section) by its purely local counterpart. This approach has been coined TRILEX [47]. A different method exploits the local expansion of the functional construction of the fully irreducible four-point vertex Λ, hence its name QUADRILEX [48].

Common to all of these methods is, that they heavily rely on the ability to access two-particle (i.e. vertex) quantities. This is why, in the next section, an introduction to two-particle quantities precedes the detailed discussion of the diagrammatic extension of DMFT which is used throughout the rest of this thesis, the dynamical vertex approximation.

[1] Note, that in principle the exact integration of the local degrees of freedom would yield also higher vertex function (6-point, 8-point etc.) for the dual fermion interaction. These contributions are, however, usually neglected. In this context, see also the discussion in [42].

2.3 The dynamical vertex approximation - a step beyond DMFT

2.3.1 A two-particle quantity crash course

The sum of all connected (one-particle irreducible, 1PI) two-particle (2P) diagrams, i.e. all connected diagrams which two fermionic particles enter and leave, defines the physical scattering amplitude between two electrons (or holes) and is formally denoted as **full vertex** F. It is important to note that the knowledge of the full vertex fully determines the one-particle spectrum (self-energy) of the many-body problem via an exact relation: the **Dyson-Schwinger equation of motion** [49]. For the Hubbard model, this relation reads

$$\Sigma(k) = \frac{Un}{2} - \frac{U}{\beta^2} \sum_{k'q} F_{\uparrow\downarrow}^{kk'q} G(k') G(k'+q) G(k+q) \tag{2.27}$$

and is depicted in Fig. 2.6. Here, U is the (purely local) Hubbard interaction, n is the filling ($n = 1$ corresponds to the half-filled case) and β is the inverse temperature. The indices k, k' and q are four-indices, i.e. $k = (\nu, \vec{k})$ and $q = (\omega, \vec{q})$, where $\nu = (2j+1)\frac{\pi}{\beta}$ is a fermionic Matsubara frequency, whereas $\omega = 2j\frac{\pi}{\beta}$ is a bosonic one ($j \in \mathbb{Z}$).

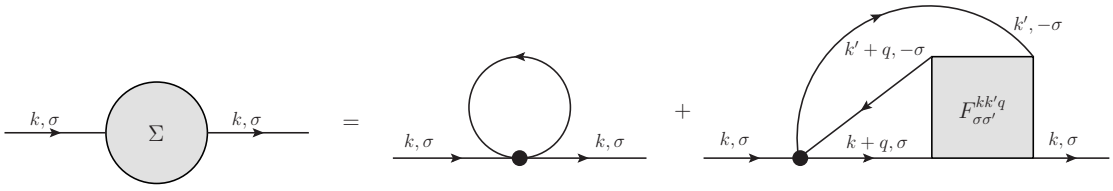

Figure 2.6: Dyson-Schwinger equation of motion as an exact relation between the two-particle full connected vertex F and the one-particle self-energy Σ.

As explained in Ref. [50] and adopting the notation of Ref. [51], the sum for the full vertex F can be subdivided in terms of the 2P reducibility of the diagrams contained. **Reducibility at the two-particle level** (2PR) means that a diagram with two ingoing and two outgoing legs will fall apart in two by cutting two fermionic propagator lines, i.e. separating two legs from two other ones. It is possible to decompose the full vertex F into reducible contributions Φ_ℓ in specific particle-hole or particle-particle channels ($\ell = \mathrm{pp}, \mathrm{ph}, \overline{\mathrm{ph}}$) and in fully 2P irreducible (2PI, i.e. irreducible in every channel) contributions Λ in the following way:

$$F^{kk'q} = \Lambda^{kk'q} + \Phi_{\mathrm{pp}}^{kk'q} + \Phi_{\mathrm{ph}}^{kk'q} + \Phi_{\overline{\mathrm{ph}}}^{kk'q} \tag{2.28}$$

which is called **parquet equation [50,52–55]**. Exemplary diagrams of such a classification can be found in Fig. 2.7.

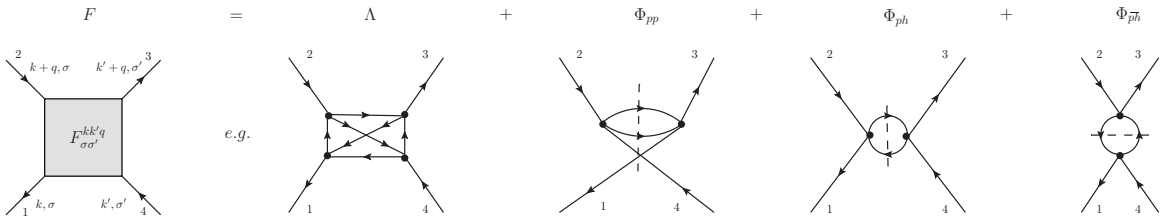

Figure 2.7: Parquet equation and two-particle reducibility.

An alternative decomposition of F can be performed in terms of **irreducible vertices in a specific channel** Γ_ℓ:

$$F^{kk'q} = \Phi_\ell^{kk'q} + \Gamma_\ell^{kk'q} \tag{2.29}$$

which corresponds to the **Bethe-Salpeter equation** [50]. Its graphical representation for one specific channel is displayed in Fig. 2.8.

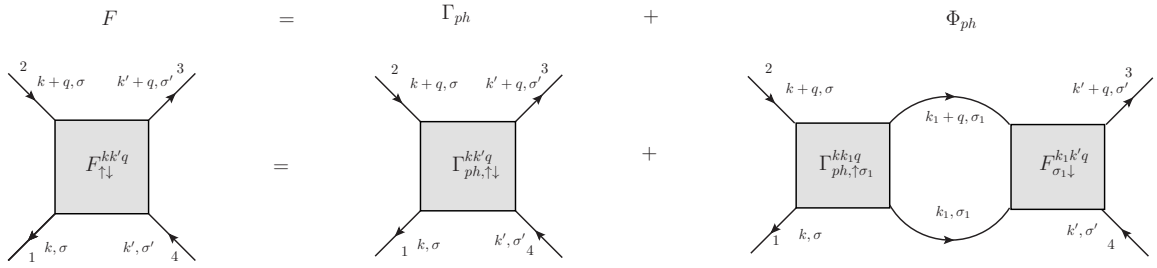

Figure 2.8: Bethe-Salpeter equation in the ph-channel.

Extraction of two-particle vertex functions in DMFT

All the vertex functions introduced above can be calculated from the local generalized susceptibilities of an auxiliary Anderson impurity model, associated with a DMFT self-consistent solution, by using the above relations Eq. (2.28) and (2.29). Following the notation of Ref. [51] we define the local generalized susceptibility in particle-hole notation as

$$\begin{aligned}\chi^{\nu\nu'\omega}_{\mathrm{ph},\sigma\sigma'} = &\int_0^\beta d\tau_1 d\tau_2 d\tau_3 e^{-i\nu\tau_1} e^{i(\nu+\omega)\tau_2} e^{-i(\nu'+\omega)\tau_3} \\ &\times \left[\left\langle T_\tau c^\dagger_\sigma(\tau_1) c_\sigma(\tau_2) c^\dagger_{\sigma'}(\tau_3) c_{\sigma'}(0)\right\rangle \right. \\ &\left. - \left\langle T_\tau c^\dagger_\sigma(\tau_1) c_\sigma(\tau_2)\right\rangle \left\langle T_\tau c^\dagger_{\sigma'}(\tau_3) c_{\sigma'}(0)\right\rangle\right]\end{aligned} \tag{2.30}$$

where $\beta = 1/T$ is the inverse temperature, T_τ is the imaginary time-ordering operator and ν, ν' and ω denote the two fermionic and the bosonic Matsubara frequencies, respectively. Note that this expression contains both one-particle (1P) and two-particle (2P) Green functions and that the connection to the full vertex F can be established via

$$\chi^{\nu\nu'\omega}_{\sigma\sigma'} = \chi^{\nu\nu'\omega}_0 \delta_{\sigma\sigma'} - \frac{1}{\beta^2} \sum_{\nu_1\nu_2} \chi^{\nu\nu_1\omega}_0 F^{\nu_1\nu_2\omega}_{\sigma\sigma'} \chi^{\nu_2\nu'\omega}_0 \tag{2.31}$$

where

$$\chi^{\nu\nu'\omega}_0 = -\beta G(\nu) G(\nu+\omega) \delta_{\nu\nu'} \tag{2.32}$$

is the product of two one-particle Green functions ("bubble term"). For an easier physical interpretation one usually builds linear combinations of the above expression to obtain

$$\chi^{\nu\nu'\omega}_{\mathsf{c(s)}} = \chi^{\nu\nu'\omega}_{\mathsf{ph},\uparrow\uparrow} \pm \chi^{\nu\nu'\omega}_{\mathsf{ph},\uparrow\downarrow}, \tag{2.33}$$

i.e. the generalized susceptibilities in the charge and spin channel, respectively. Similarly, one can equally well define local generalized susceptibilities in the particle-particle notation, see e.g. [50, 51, 56]:

$$\begin{aligned} \chi^{\nu\nu'\omega}_{\mathsf{pp},\sigma\sigma'} = \int_0^\beta & d\tau_1 d\tau_2 d\tau_3 e^{-i\nu\tau_1} e^{i(\omega-\nu')\tau_2} e^{-i(\omega-\nu)\tau_3} \\ & \times \left[\left\langle T_\tau c^\dagger_\sigma(\tau_1) c_\sigma(\tau_2) c^\dagger_{\sigma'}(\tau_3) c_{\sigma'}(0) \right\rangle \right. \\ & \left. - \left\langle T_\tau c^\dagger_\sigma(\tau_1) c_\sigma(\tau_2) \right\rangle \left\langle T_\tau c^\dagger_{\sigma'}(\tau_3) c_{\sigma'}(0) \right\rangle \right] \end{aligned} \tag{2.34}$$

Out of the generalized susceptibilities the physical (i.e. measurable in conventional spectroscopy experiments) susceptibilities in the (spin-diagonalized) channels r = c, s, pp $\uparrow\downarrow$ can be calculated by summing over the fermionic Matsubara frequencies

$$\chi_{\mathsf{r}}(\omega) = \frac{1}{\beta^2} \sum_{\nu\nu'} \chi^{\nu\nu'\omega}_{\mathsf{r}}. \tag{2.35}$$

At the same time, from the generalized susceptibilities, the 2P irreducible vertices in a given channel can be extracted by inverting the corresponding local Bethe-Salpeter equations:

$$\chi^{\nu\nu'\omega}_{\mathsf{c(s)}} = \chi^{\nu\nu'\omega}_0 - \frac{1}{\beta^2} \sum_{\nu_1\nu_2} \chi^{\nu\nu_1\omega}_0 \Gamma^{\nu_1\nu_2\omega}_{\mathsf{c(s)}} \chi^{\nu_2\nu'\omega}_{\mathsf{c(s)}} \tag{2.36}$$

where $\Gamma^{\nu\nu'\omega}_{\mathsf{c(s)}}$ denotes the vertex function irreducible in the selected (c(harge)- or s(pin)-) channel. Making the inversion explicit, the irreducible vertex reads

$$\left[\Gamma^{\nu\nu'}_{\mathsf{c(s)}}\right]^\omega = \beta^2 \Big(\left[\chi^{\nu\nu'}_{\mathsf{c(s)}}\right]^{-1} - \left[\chi^{\nu\nu'}_0\right]^{-1} \Big)^\omega \tag{2.37}$$

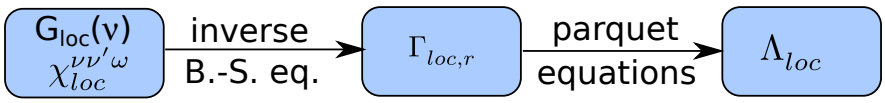

Figure 2.9: Flow-chart inverse parquet.

and, similarly, for the particle-particle channel one has [56]

$$\left[\tilde{\Gamma}^{\nu\nu'}_{\text{pp},\uparrow\downarrow}\right]^{\omega} = \beta^2\Big(\left[\tilde{\chi}^{\nu\nu'}_{\text{pp},\uparrow\downarrow} - \chi^{\nu\nu'}_{0,\text{pp}}\right]^{-1} + \left[\chi^{\nu\nu'}_{0,\text{pp}}\right]^{-1}\Big)^{\omega} \tag{2.38}$$

where $\tilde{\chi}^{\nu\nu'\omega}_{\text{pp},\uparrow\downarrow} = \chi^{\nu(\omega-\nu')\omega}_{\text{pp},\uparrow\downarrow}$, $\tilde{\Gamma}^{\nu\nu'\omega}_{\text{pp},\uparrow\downarrow} = \Gamma^{\nu(\omega-\nu')\omega}_{\text{pp},\uparrow\downarrow}$ and

$$\chi^{\nu\nu'\omega}_{0,\text{pp}} = -\beta G(\nu)G(\omega-\nu)\delta_{\nu\nu'} \tag{2.39}$$

This derivation shows that, once one obtained the 1P and 2P Green functions from a DMFT calculation, the irreducible vertex in a specific channel can be calculated by a simple inversion of the generalized susceptibility χ represented as a matrix of the fermionic Matsubara frequencies, keeping the bosonic one fixed.

Please note that the calculation of the fully irreducible vertex $\Lambda^{\nu\nu'\omega}$ requires the inversion of the parquet equation (Eq. 2.28) and, therefore, cannot be represented as a simple inversion of the generalized susceptibility χ. The extraction of the fully irreducible vertex is a procedure coined **inverse parquet**. It can be schematically seen in Fig. 2.9. Specifically, for a DMFT vertex-calculation, it consists of the following steps:

1. A DMFT calculation is performed until self-consistent convergence. The (local) Green function $G_{\text{loc}}(\nu)$ as well as the (local) generalized susceptibility $\chi^{\nu\nu'\omega}_{\text{loc}}$ are extracted from the self-consistently determined Anderson impurity model.

2. The (local) irreducible vertices in each channel $\Gamma^{\nu\nu'\omega}_{\text{loc},r}$ are calculated via the Bethe-Salpeter equations (2.29). These can be written also directly for the generalized susceptibilities instead of the full vertex $F^{\nu\nu'\omega}_{\text{loc}}$ (see [56]).

3. The reducible vertices $\Phi^{\nu\nu'\omega}_{\text{loc},r}$ are determined again by usage of the Bethe-Salpeter equations (2.29). Eventually, the (again local) fully irreducible vertex $\Lambda^{\nu\nu'\omega}_{\text{loc}}$ can be obtained via the local parquet equation, i.e. Eq. (2.28) for local quantities without momentum index.

Many-body approximation schemes on different diagrammatic levels

It turns out to be quite illustrative for the purpose of classifying the different types of vertices introduced in the previous section, to connect well-known many-body approximation schemes with the corresponding approximations of vertices on different levels of the diagrammatics $\mathcal{V}^{kk'q} = (F, \Gamma_r, \Lambda)^{kk'q}$ (see also [51]). These can be roughly separated in schemes which approximate these vertices by a constant $\mathcal{V}^{kk'q} \approx U$ or by their purely local counterparts $\mathcal{V}^{kk'q} \approx \mathcal{V}^{\nu\nu'\omega}_{\text{loc}}$.

Starting at the shallowest level of the diagrammatics, if one substitutes the full vertex $F^{kk'q} = U$, after inserting into the Dyson-Schwinger equation of motion (2.27), one arrives at **second order perturbation theory** for the electronic self-energy. For the full vertex F there does not exist an obvious approximation scheme which uses only its local counterpart, although, one may be tempted to classify the dual fermion approach into this category. However, one has to keep in mind, that the dual fermion approach relies on a transformation to dual space, which makes its classification rather delicate here.

Diving into a deeper level of the diagrammatics, one can approximate the irreducible vertex in a specific channel by a constant $\Gamma_r^{kk'q} = U$. Here, in order to obtain the self-energy, one has to calculate F using the Bethe-Salpeter equations (2.29), followed by the Dyson-Schwinger equation of motion (2.27). The ladders that are built with the bare interaction U in one specific channel lead to the **random phase approximation** (RPA) in this channel (see e.g. [57]). In other schemes, like the **fluctuation exchange approximation** (FLEX) [58] or the **pseudopotential parquet approximation** [50], the ladders are built with the same or different values for the static interaction, respectively. A different path is chosen for the **ladder-version of the dynamical vertex approximation**, where $\Gamma^{kk'q} = \Gamma^{\nu\nu'\omega}_{\text{loc}}$. This method will be described in detail in Sec. 2.3.2.2.

Finally arriving on the deepest diagrammatic level, one can aim to approximate the fully irreducible vertex. In order to define the vertices on all levels of the diagrammatics (and, eventually, the self-energy) consistently with the choice of Λ, one has to iterate the so-called **parquet scheme** until self-consistency [59, 60]. This scheme is depicted in Fig. 2.10. As one can see, it consists of two nested loops, whose steps are the following:

1. The lattice system's 1P and 2P quantities (G, F and Γ_r) are initialized.
2. Inner Loop
   (a) F is updated from Γ_r and G via the Bethe-Salpeter equations (2.29).
   (b) The updated reducible vertices Φ_r are calculated from F and Γ_r, again via the Bethe-Salpeter equations.

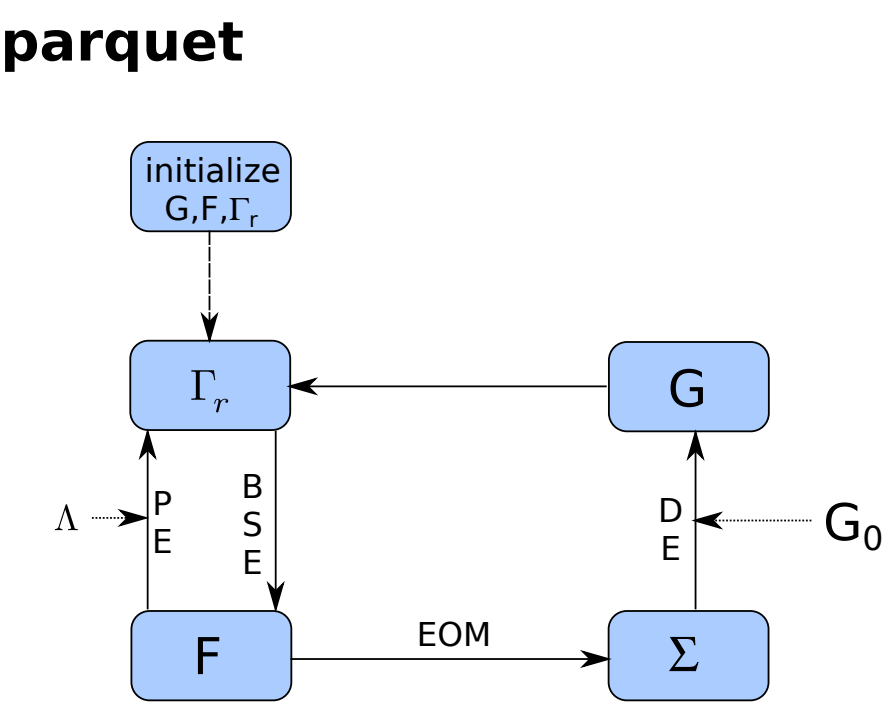

Figure 2.10: Flow-chart parquet.

(c) From the parquet equation (2.28), with the input of a certain choice of the fully irreducible vertex Λ, the irreducible vertices Γ_r are updated.

(d) The inner loop is iterated for a fixed G, until self-consistency for F and Γ_r is reached.

3. The self-energy Σ is calculated for the self-consistently determined full vertex F by means of the Dyson-Schwinger equation of motion (2.27).

4. The Green function is updated via the Dyson equation (2.12). Now the inner loop (2.) is entered again with the updated Green function G. The procedure is iterated until self-consistency for G is reached (outer loop).

Depending on the choice of the fully irreducible vertex, two approximation schemes can be defined: (i) the so-called **parquet-approximation** (PA), where $\Lambda^{kk'q} = U$ [50,53,61], and (ii) the **dynamical vertex approximation** (DΓA), where $\Lambda^{kk'q} = \Lambda^{\nu\nu'\omega}_{\text{loc}}$, which is at the very heart of this thesis and will be introduced and discussed in detail in Sec. 2.3.2 [20].

2.3.2 The dynamical vertex approximation

The approach for diagrammatically including non-local correlations to cluster extensions of DMFT, that serves as the basis of this thesis, is the dynamical vertex approximation (DΓA). A proposal advanced by A. Toschi, K. Held and A. Katanin in 2007 was to push the requirement of **locality** one

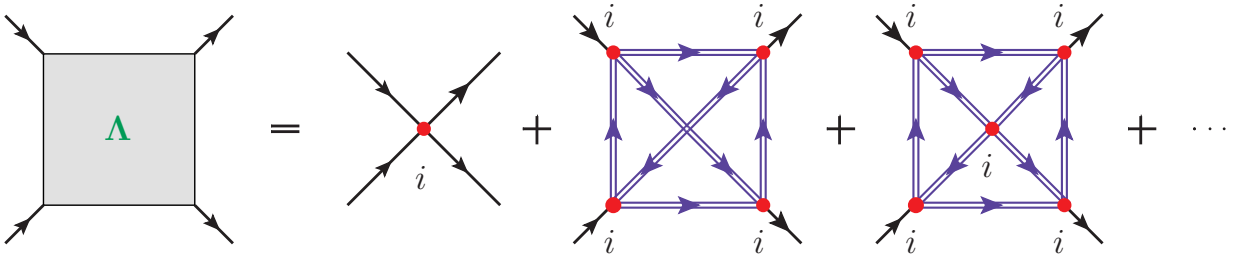

Figure 2.11: Diagrammatic content of the dynamical vertex approximation (DΓA). The DΓA assumes the locality of the two-particle fully irreducible vertex Λ, whose lowest order diagrammatic contributions are shown. They can be calculated directly from the single-site AIM. The (local) vertex Λ represents the crucial input for the DΓA calculations, which can, in this way, include spatial correlations at all length scales beyond DMFT (taken from [27]).

level higher in the hierarchy of diagrams, namely at the two-particle level [20]. More specifically, the two-particle quantity corresponding to the self-energy for which the assumption of locality is made, is the **two-particle fully irreducible vertex** Λ (Fig. 2.11), often also indicated by $\Lambda = \Gamma_{\text{irr}}$, from which the name **dynamical vertex approximation (DΓA)** originally stems from. Note that the locality at the two-particle level does not imply the locality at the one-particle level at all (see Sec. 2.3.1), so that spatial correlations at all length scales can now be included systematically and in a fully non-perturbative way.

Diagrammatic variants of the dynamical vertex approximation

As already discussed in Sec. 2.3.1 about the relationship of many-body approximation schemes with diagrammatic levels, there are currently two schemes of the DΓA conceivable: the (parquet-based) DΓA, where the assumption of locality is done at the level of the fully irreducible vertex Λ as well as the ladder-DΓA where the irreducible vertex in a specific channel (usually the ph-channels, Γ_{ph}) is assumed to be purely local. In the next two subsections both calculational algorithms are described and advantages and drawbacks are discussed.

2.3.2.1 The parquet formulation of the DΓA

As previously stated, the DΓA takes the DMFT-assumption of locality of the fully irreducible one-particle quantity (i.e. the self-energy) to a higher level of the diagrammatics (i.e. to the fully irreducible vertex Λ). The fully irreducible vertex Λ serves as a basic building brick for the construction of the non-local full (connected) two-particle vertex F and the non-local Green function. Fig. 2.12 shows the schematic flow of a (fully self-consistent, parquet-based) DΓA-calculation, which consists of the following steps:

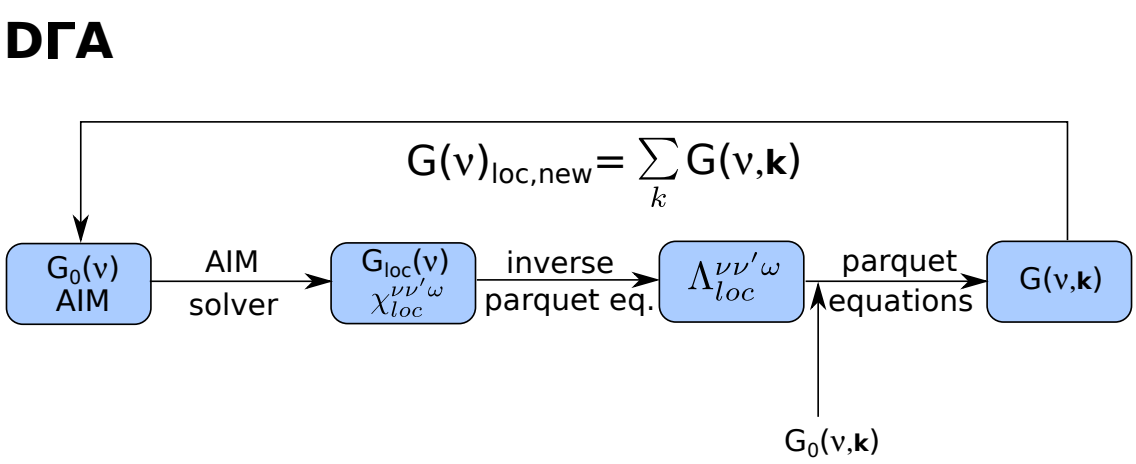

Figure 2.12: Flow-chart DΓA.

1. An Anderson impurity model is solved and its local Green function $G_{\text{loc}}(\nu)$ as well as its local generalized susceptibilities $\chi_{\text{loc}}^{\nu\nu'\omega}$ are extracted.

2. From $G_{\text{loc}}(\nu)$ and $\chi_{\text{loc}}^{\nu\nu'\omega}$ the (local) fully irreducible vertex $\Lambda_{\text{loc}}^{\nu\nu'\omega}$ is calculated by means of an inverse parquet scheme (see Sec. 2.3.1 and Fig. 2.9).

3. In this step, the actual DΓA assumption is implemented: together with the non-interacting lattice Green function $G_0(\nu,\vec{k})$, $\Lambda_{\text{loc}}^{\nu\nu'\omega}$ is used as an input for the (self-consistent) parquet scheme, depicted in Fig. 2.10 in Sec. 2.3.1. The final result of the parquet scheme is a (non-local) self-energy $\Sigma(\nu,\vec{k})$ from which one obtains the non-local Green function $G(\nu,\vec{k})$.

4. Eventually, the new local Green function $G_{\text{new,loc}}(\nu) = \sum_{\vec{k}} G(\nu,\vec{k})$ is calculated and serves as the local Green function of a new auxiliary Anderson impurity model. The iteration scheme is closed with 1. and iterated until convergence.

In comparison with the ladder-implementation, which will be discussed in detail in the following subsection, the parquet-based version of DΓA certainly has some advantages:

- The starting AIM does not need to be a fully converged DMFT solution, as all local and non-local correlations are generated by the DΓA algorithm itself.

- All channels (the (ph,pp)-channels or density/magnetic/singlet/triplet channels) are treated on equal footing. This might be a crucial advantage in cases were the leading instability is unknown or in cases of competing instabilities.

The drawbacks in comparison with the ladder-version of DΓA are:

- The parquet algorithm is computationally very demanding in comparison with the task of the solution of an AIM as well as constructing simply Bethe-Salpeter ladders in a certain channel.

- Parquet solvers are also numerically very demanding and asymptotic behavior of vertex functions has to be exploited in order to be able to set up a proper numerical environment to perform the calculations [59, 60].

If, however, a physical channel is dominant in a certain parameter regime, a computationally and numerically much simpler implementation of the DΓA can be exploited to treat non-local correlations: the ladder-version of the DΓA. This version is utilized predominantly in this thesis, which is the reason why it is discussed in more detail in the subsequent subsection.

2.3.2.2 The ladder-DΓA

As discussed in the previous subsection, the computational costs of the full parquet-implementation of DΓA are quite heavy. If one of the physical channels can be singled out a-priori to be the dominating one, however, a simpler scheme than the full-parquet one can be proposed: the ladder-version of the DΓA, which will be introduced in the present subsection.

Starting at recalling the full momentum- and frequency-dependent parquet-equation

$$F^{kk'q}_{\uparrow\downarrow} = \Lambda^{kk'q}_{\uparrow\downarrow} + \Phi^{kk'q}_{\mathsf{pp},\uparrow\downarrow} + \Phi^{kk'q}_{\mathsf{ph},\uparrow\downarrow} + \Phi^{kk'q}_{\overline{\mathsf{ph}},\uparrow\downarrow} \tag{2.40}$$

one can stress that the assumption of DΓA is the locality of the fully irreducible vertex, which leads to

$$F^{kk'q}_{\mathsf{D\Gamma A},\uparrow\downarrow} = \Lambda^{\nu\nu'\omega}_{\mathsf{loc},\uparrow\downarrow} + \Phi^{kk'q}_{\mathsf{pp},\uparrow\downarrow} + \Phi^{kk'q}_{\mathsf{ph},\uparrow\downarrow} + \Phi^{kk'q}_{\overline{\mathsf{ph}},\uparrow\downarrow}. \tag{2.41}$$

Please note that it is absolutely necessary to keep the reducible vertices fully momentum- and frequency dependent in those channels r where they are supposed to exhibit a second order phase transition. The (local and non-local) fluctuations, which are generated by such a transition are crucially connected to the transition itself and, hence, have to be incorporated properly in the theory.

If the dominant instability is known a priori, also the respective reducible vertex should be the dominant one with respect to its momentum-dependence. Hence, one strategy to further simplify Eq. (2.41) is to restrict all but the dominant reducible vertex to local approximations. As in most of the systems analyzed in this thesis, the dominant fluctuation is a magnetic one, the short derivation for the ladder-DΓA equations presented here will focus on this channel. Similar derivations can be found in [20, 56].

As the magnetic channel is singled out to be the dominant channel, in addition to the fully irre-

ducible vertex, the pp-channel is approximated by its purely local counterpart:

$$F^{kk'q}_{\text{ladder-D}\Gamma\text{A},\uparrow\downarrow} = \Lambda^{\nu\nu'\omega}_{\text{loc},\uparrow\downarrow} + \Phi^{\nu\nu'\omega}_{\text{loc,pp},\uparrow\downarrow} + \Phi^{kk'q}_{\text{ph},\uparrow\downarrow} + \Phi^{kk'q}_{\overline{\text{ph}},\uparrow\downarrow}. \tag{2.42}$$

Please note that on the ladder-DΓA the corresponding Bethe-Salpeter equations are built up with the local irreducible vertices $\Gamma_{\text{loc,c/s}}$, so that the full vertex just depends on the transferred momentum $\vec{q}$ as well as on three frequencies:

$$F^{\nu\nu'\omega}_{\text{r},\vec{q}} = \Gamma^{\nu\nu'\omega}_{\text{loc,r}} + \frac{1}{\beta}\sum_{\nu_1,\vec{k}_1} \Gamma^{\nu\nu_1\omega}_{\text{loc,r}} G_{\text{DMFT}}(\nu_1,\vec{k}_1) G_{\text{DMFT}}(\nu_1+\omega,\vec{k}_1+\vec{q}_1) F^{\nu_1\nu'\omega}_{\text{r},\vec{q}}. \tag{2.43}$$

For the actual implementation, the generalized susceptibilities rather than the full vertices are used. They are equivalent up to contributions stemming from $\vec{k}$-summed bare DMFT-bubbles

$$\chi^{\nu\omega}_{0,\vec{q}} = -\sum_{\vec{k}} G_{\text{DMFT}}(\nu,\vec{k}) G_{\text{DMFT}}(\nu+\omega,\vec{k}+\vec{q}) \tag{2.44}$$

leading to the relation

$$\chi^{\nu\nu'\omega}_{\text{r},\vec{q}} = -\beta\delta_{\nu\nu'}\chi^{\nu\omega}_{0,\vec{q}} + \chi^{\nu\omega}_{0,\vec{q}} F^{\nu\nu'\omega}_{\text{r},\vec{q}} \chi^{\nu'\omega}_{0,\vec{q}}. \tag{2.45}$$

For reasons, which will become clear in the following, one rewrites this Bethe-Salpeter equation for the generalized susceptibilities in term of physical susceptibilities

$$\chi^{\omega}_{\text{r},\vec{q}} = \frac{1}{\beta^2}\sum_{\nu\nu'} \chi^{\nu\nu'\omega}_{\text{r},\vec{q}}. \tag{2.46}$$

In order to do so, following [20, 62, 63], one can separate the Bethe-Salpeter ladder in the ph-channels r=c(harge)/s(pin) by the bare interaction U_r instead of the local irreducible vertex $\Gamma^{\nu\nu'\omega}_{\text{loc,r}}$ via an auxiliary susceptibility

$$\chi^{*,\nu\nu'\omega}_{\text{r},\vec{q}} = \left[\left(\chi^{\nu\omega}_{0,\vec{q}}\right)^{-1}\delta_{\nu\nu'} + \frac{1}{\beta^2}\left(\Gamma^{\nu\nu'\omega}_{\text{loc,r}} - U_\text{r}\right)\right]^{-1} \tag{2.47}$$

where the inversion is done in (ν,ν') (ω is kept fixed) and $U^{\nu\nu'}_\text{r}$ =const., depending on the channel ($U_\text{c} = +U$ and $U_\text{s} = -U$, where U is the bare Hubbard interaction). This separation leads to the following Bethe-Salpeter equation:

$$\chi^{\nu\nu'\omega}_{\text{r},\vec{q}} = \chi^{*,\nu\nu'\omega}_{\text{r},\vec{q}} - \frac{1}{\beta}\sum_{\nu_1\nu_2} \chi^{*,\nu\nu_1\omega}_{\text{r},\vec{q}} U^{\nu_1\nu_2}_\text{r} \chi^{\nu_2\nu'\omega}_{\text{r},\vec{q}} \tag{2.48}$$

Iterating the last equation reveals

$$\begin{aligned}
\chi^{\nu\nu'\omega}_{\mathsf{r},\vec{q}} &= \chi^{*,\nu\nu'\omega}_{\mathsf{r},\vec{q}} - \frac{1}{\beta}\sum_{\nu_1\nu_2}\left[\chi^{*,\nu\nu_1\omega}_{\mathsf{r},\vec{q}} U_{\mathsf{r}} \chi^{*,\nu_2\nu'\omega}_{\mathsf{r},\vec{q}} - \frac{1}{\beta^2}\sum_{\nu_3\nu_4}\chi^{*,\nu\nu_1\omega}_{\mathsf{r},\vec{q}} U_{\mathsf{r}} \chi^{\nu_2\nu_3\omega}_{\mathsf{r},\vec{q}} U_{\mathsf{r}} \chi^{*,\nu_4\nu'\omega}_{\mathsf{r},\vec{q}}\right] = \\
&= \chi^{*,\nu\nu'\omega}_{\mathsf{r},\vec{q}} - \frac{U_{\mathsf{r}}}{\beta^2}\sum_{\nu_1\nu_2}\chi^{*,\nu\nu_1\omega}_{\mathsf{r},\vec{q}}\chi^{*,\nu_2\nu'\omega}_{\mathsf{r},\vec{q}} + \frac{U_{\mathsf{r}}^2}{\beta^2}\sum_{\nu_1\nu_4}\chi^{*,\nu\nu_1\omega}_{\mathsf{r},\vec{q}}\left(\frac{1}{\beta^2}\sum_{\nu_2\nu_3}\chi^{\nu_2\nu_3\omega}_{\mathsf{r},\vec{q}}\right)\chi^{*,\nu_4\nu'\omega}_{\mathsf{r},\vec{q}} = \\
&= \chi^{*,\nu\nu'\omega}_{\mathsf{r},\vec{q}} - U_{\mathsf{r}}(1-U_{\mathsf{r}}\chi^{*,\omega}_{\mathsf{r},\vec{q}})\frac{1}{\beta^2}\sum_{\nu_1\nu_2}\chi^{*,\nu\nu_1\omega}_{\mathsf{r},\vec{q}}\chi^{*,\nu_2\nu'\omega}_{\mathsf{r},\vec{q}} \qquad (2.49)
\end{aligned}$$

which, in turn, with the definition of the triangular vertex

$$\gamma^{\nu\omega}_{\mathsf{r},\vec{q}} = \left(\chi^{\nu\omega}_{0,\vec{q}}\right)^{-1}\frac{1}{\beta}\sum_{\nu'}\chi^{*,\nu\nu'\omega}_{\mathsf{r},\vec{q}}, \qquad (2.50)$$

yields

$$F^{\nu\nu'\omega}_{\mathsf{r},\vec{q}} = \left(\chi^{\nu\omega}_{0,\vec{q}}\right)^{-1}\left[\beta\delta_{\nu\nu'} - \chi^{*,\nu\nu'\omega}_{\mathsf{r},\vec{q}}\left(\chi^{\nu\omega}_{0,\vec{q}}\right)^{-1}\right] + U_{\mathsf{r}}(1-U_{\mathsf{r}}\chi^{\omega}_{\mathsf{r},\vec{q}})\gamma^{\nu\omega}_{\mathsf{r},\vec{q}}\gamma^{\nu'\omega}_{\mathsf{r},\vec{q}} \qquad (2.51)$$

for the full (lattice) vertex. Inserting the full lattice vertex into the Dyson-Schwinger equation of motion (2.27), eventually, reveals the self-energy of the ladder-DΓA:

$$\begin{aligned}
\Sigma^{\mathsf{ladder}}_{\mathsf{D\Gamma A}}(\nu,\vec{k}) = \frac{Un}{2} + \frac{U}{2\beta^2}\sum_{\omega,\vec{q}}\Big[&\gamma^{\nu\omega}_{\mathsf{c},\vec{q}} - 3\gamma^{\nu\omega}_{\mathsf{s},\vec{q}} + U\gamma^{\nu\omega}_{\mathsf{c},\vec{q}}\chi^{\omega}_{\mathsf{c},\vec{q}} + 3U\gamma^{\nu\omega}_{\mathsf{s},\vec{q}}\chi^{\omega}_{\mathsf{s},\vec{q}} + 2 + \qquad (2.52)\\
&- \sum_{\nu',\vec{k}'}\left(F^{\nu\nu'\omega}_{\mathsf{loc,c}} - F^{\nu\nu'\omega}_{\mathsf{loc,s}}\right)G_{\mathsf{DMFT}}(\nu',\vec{k}')G_{\mathsf{DMFT}}(\nu'+\omega,\vec{k}'+\vec{q})\Big]G_{\mathsf{DMFT}}(\nu+\omega,\vec{k}+\vec{q})
\end{aligned}$$

Please note the following:

- In this rewritten form, the physical susceptibilities enter the equation of motion for the self-energy.
- The full lattice vertex $F^{\nu\nu'\omega}_{\mathsf{r},\vec{q}}$ differs from the lattice vertex obtained by the parquet equations in view of the fact that (i) it is built up with ladders only in the particle-hole channels and (ii) it is not determined self-consistently like in a parquet-approach.
- The full lattice vertex serves merely as an auxiliary quantity to calculate reducible vertices via Bethe-Salpeter equations.
- Expressed in terms of full vertices, the full lattice vertex in ladder-DΓA reads as the one obtained in [20, 56]:

$$F^{\nu\nu'\omega}_{\mathsf{ladder},\vec{k}\vec{k}'\vec{q},\uparrow\downarrow} = \frac{1}{2}\left(F^{\nu\nu'\omega}_{\mathsf{c},\vec{q}} - F^{\nu\nu'\omega}_{\mathsf{s},\vec{q}}\right) - F^{\nu(\nu+\omega)(\nu'-\nu)}_{\mathsf{s},\vec{k}-\vec{k}'} - \frac{1}{2}\left(F^{\nu\nu'\omega}_{\mathsf{loc,c}} - F^{\nu\nu'\omega}_{\mathsf{loc,s}}\right) \qquad (2.53)$$

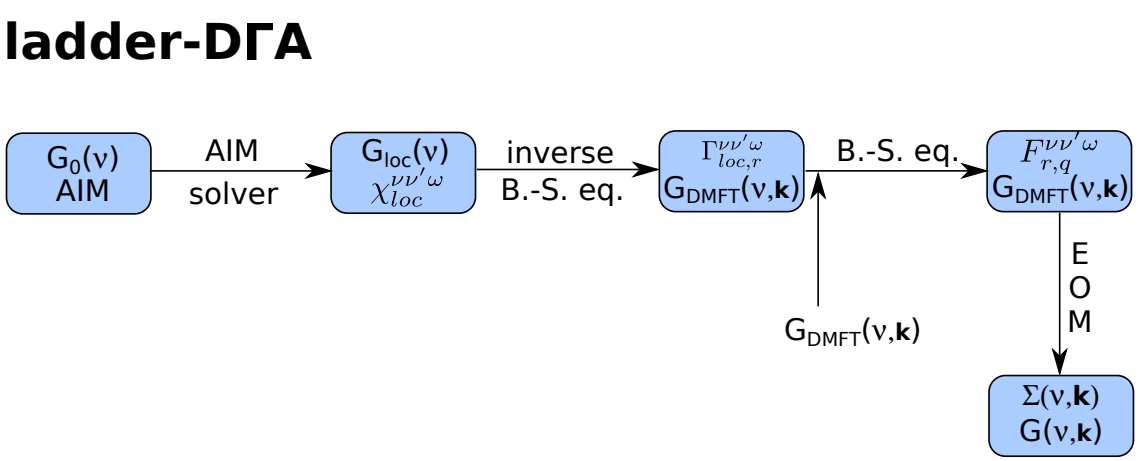

Figure 2.13: Flow-chart ladder-DΓA.

yielding an alternative form of the ladder-DΓA self-energy:

$$\Sigma^{\text{ladder}}_{\text{D}\Gamma\text{A}}(\nu,\vec{k}) = \frac{Un}{2} - \frac{U}{2\beta^2}\sum_{\nu'\omega}\sum_{\vec{k}'\vec{q}}\left(F^{\nu\nu'\omega}_{\text{c},\vec{q}} - 3F^{\nu\nu'\omega}_{\text{s},\vec{q}} - F^{\nu\nu'\omega}_{\text{loc,c}} + F^{\nu\nu'\omega}_{\text{loc,s}}\right)\times$$
$$G_{\text{DMFT}}(\nu',\vec{k}')G_{\text{DMFT}}(\nu'+\omega,\vec{k}'+\vec{q})G_{\text{DMFT}}(\nu+\omega,\vec{k}+\vec{q}) \quad (2.54)$$

Algorithmic flow of the ladder-DΓA

In order to perform an actual ladder-DΓA calculation, the following steps have to be processed (see also Fig. 2.13):

1. As a first step, a full self-consistent DMFT-cycle has to be performed, out of which the local Green function $G_{\text{loc}}(\nu)$ as well as the local generalized susceptibilities $\chi^{\nu\nu'\omega}_{\text{loc}}$ have to be extracted.

2. For the target channel (usually the physically dominant one), the local irreducible vertices $\Gamma^{\nu\nu'\omega}_{\text{loc,r}}$ are calculated by means of the inverse Bethe-Salpeter equations (2.29).

3. The lattice Bethe-Salpeter ladders are built, using the local irreducible vertex $\Gamma^{\nu\nu'\omega}_{\text{loc,r}}$ and the Green function from DMFT, $G_{\text{DMFT}}(\nu,\vec{k})$ as building bricks. This yields the full vertex function $F^{\nu\nu'\omega}_{\text{ladder},\vec{k}\vec{k}'\vec{q}}$ (or the corresponding generalized susceptibility) of Eq. 2.53.

4. The full lattice vertex $F^{\nu\nu'\omega}_{\text{r},\vec{q}}$ (or, alternatively, the corresponding generalized susceptibility) and the DMFT Green function are inserted into the Dyson-Schwinger-equation of motion in order to obtain the ladder-DΓA self-energy $\Sigma^{\text{ladder}}_{\text{D}\Gamma\text{A}}(\nu,\vec{k})$ of Eq. 2.54.

Please note the following points:

- Quite different from DMFT as well as parquet-based DΓA, the ladder-DΓA is a one-shot calculation, performed on top of a full DMFT self-consistency cycle.
- The previous point indicates, that the fixing of the average occupancy per lattice site can lead to problems, keeping in mind that the chemical potential is fixed to the DMFT one.
- In turn, this means that the high-frequency asymptotics of the self-energy will probably not exhibit the correct $\frac{1}{i\nu}$-dependence (as, e.g. DMFT would yield), as will be shown in the next subsection. The deeper reason lies in the construction of the ladder diagrams for $\chi_{\mathrm{r},\vec{q}}^{\nu\nu'\omega}$, since for this, a local irreducible vertex Γ is combined with a momentum-dependent Green function G, which violates the Baym-Kadanoff relation (Ward identity) [64, 65]:

  $$\Gamma = \frac{\delta\Sigma}{\delta G}. \tag{2.55}$$

  This, in turn, means, that the self-consistency cannot be restored by a pure one-particle level approach.

The above points are considered by the so-called Moriyaesque λ-correction, which will be discussed in detail in the subsequent subsection.

Moriyaesque λ-corrections

In the previous subsection that lack of both one- and two-particle self-consistency has been mentioned. Here, its consequences are discussed further and a possible solution to this problem (the so-called Moriyaesque λ-correction) is introduced.

In a first step, an analysis of the asymptotic properties ($i\nu \to \infty$) of the self-energy calculated via the Dyson-Schwinger equation is called for. Recalling this equation in four-index notation

$$\Sigma(k) = \frac{Un}{2} - \frac{U}{\beta^2}\sum_{k',q} F_{\uparrow\downarrow}^{kk'q} G(k')G(k'+q)G(k+q) \tag{2.56}$$

one may discriminate the separate contributions in powers of ν (see also [56]), yielding in first order

$$\Sigma(k) = \frac{Un}{2} + \frac{1}{i\nu}\frac{U^2}{\beta^3}\sum_{k_1,k',q} \chi_{\uparrow\uparrow}^{k_1k'q} + \mathcal{O}\left(\frac{1}{(i\nu)^2}\right). \tag{2.57}$$

For the exact $\chi_{\uparrow\uparrow}^{kk'q}$ and for the SU(2)-symmetric case, the sum in the equation above can be calculated analytically:

$$\frac{1}{\beta^3}\sum_{k_1,k',q} \chi_{\uparrow\uparrow}^{k_1k'q} = \langle n_\uparrow n_\downarrow\rangle - \langle n_\uparrow\rangle\langle n_\downarrow\rangle = \frac{n}{2}\left(1-\frac{n}{2}\right) \tag{2.58}$$

For the self-energy one obtains (for the Hubbard and AIM respectively):

$$\Sigma(k) = \frac{Un}{2} + \frac{1}{i\nu}U^2\frac{n}{2}\left(1-\frac{n}{2}\right) + \mathcal{O}\left(\frac{1}{(i\nu)^2}\right) \tag{2.59}$$

Now one can immediately see, that the disagreement between the momentum-dependent DMFT susceptibility and the susceptibility constructed by means of the ladder-approximation in DΓA implies a difference in the asymptotics of the respective self-energies. Also, this observation shows a direct route how to restore, on the one hand, the asymptotics of the self-energy and, on the other hand, the self-consistency on the two-particle level: the susceptibility has to be corrected in a way which has still to be determined. These effective corrections should, of course, push the system into a "more physical" direction. Bearing in mind that DMFT neglects all spatial correlations, which lead e.g. to a general overestimation of the transition temperatures for second-order phase transitions, one could think of adapting the physical susceptibility by introducing the effect of spatial fluctuations. Essentially, this idea follows Moriya's spin fluctuation theory in itinerant magnetic systems [66], hence the name **Moriyaesque λ-corrections**.

In the vicinity of a second-order phase transition, the physical susceptibility, which describes the ordering phenomenon (i.e. for frequency $\omega = 0$ and characteristic ordering vector/momentum $\vec{Q}$), can be expanded, leading essentially to an Ornstein-Zernicke form of the correlation function [67], which reads

$$\chi^{\omega=0}_{\mathrm{r},\vec{q}} = \frac{A}{\left(\vec{q}-\vec{Q}\right)^2 + \xi^{-2}} \tag{2.60}$$

A denotes a proportionality constant and ξ the correlation length in channel r. The effect of spatial correlations is, like in the case of purely local temperature fluctuations, to destroy the order, which in turn means, that the transition temperature has to be lowered with respect to an approximation, which neglects these fluctuations. Straightforwardly, the effect of these fluctuations can be encapsulated as an effective **descrease in the correlation length** quantified by a (positive and real) constant λ. This **λ-corrected physical susceptibility** reads:

$$\chi^{\lambda,\omega}_{\mathrm{r},\vec{q}} = \left[\left(\chi^{\omega}_{\mathrm{r},\vec{q}}\right)^{-1} + \lambda_{\mathrm{r}}\right]^{-1} \overset{\omega=0}{=} \frac{A}{\left(\vec{q}-\vec{Q}\right)^2 + \xi^{-2} + \lambda_{\mathrm{r}}} \tag{2.61}$$

The physical susceptibilities in Eq. (2.52) can now be substituted by the λ-corrected ones in order to obtain the ladder-DΓA self-energy. It then reads

$$\begin{aligned}\Sigma^{\text{ladder}}_{\text{D}\Gamma\text{A}}(\nu,\vec{k}) &= \frac{Un}{2}+\frac{U}{2\beta^2}\sum_{\omega,\vec{q}}\Big[\gamma^{\nu\omega}_{\text{c},\vec{q}}-3\gamma^{\nu\omega}_{\text{s},\vec{q}}+U\gamma^{\nu\omega}_{\text{c},\vec{q}}\chi^{\lambda_\text{c},\omega}_{\text{c},\vec{q}}+3U\gamma^{\nu\omega}_{\text{s},\vec{q}}\chi^{\lambda_\text{s},\omega}_{\text{s},\vec{q}}+2+\\ &- \sum_{\nu',\vec{k}'}\left(F^{\nu\nu'\omega}_{\text{loc,c}}-F^{\nu\nu'\omega}_{\text{loc,s}}\right)G_{\text{DMFT}}(\nu',\vec{k}')G_{\text{DMFT}}(\nu'+\omega,\vec{k}'+\vec{q})\Big]G_{\text{DMFT}}(\nu+\omega,\vec{k}+\vec{q}).\end{aligned} \tag{2.62}$$

Algorithmically, assuming that the dominant channel is the spin channel, the value of λ can be determined in several ways:

1. **Optical inspection**
   The first implementation of the λ-correction utilized the fact discussed above, that the correct adaptation of the susceptibility implies the correct high-frequency asymptotics of the ladder-DΓA self-energy. Practically, the (imaginary part of the) ladder-DΓA self-energy (multiplied by the Matsubara frequency leading to constant asymptotics of the plot), was plotted as a function of the Matsubara frequency on top of the DMFT one (which exhibits the correct $\frac{1}{i\nu}$ asymptotics). Then, the λ-parameter was updated in such a way that the lines were expected to lie close on/to each other. Of course, this approach bears serious drawbacks in terms of accuracy as well as practical applicability and automation.

2. Exploiting **sum rules**
   A much more convenient approach is to exploit the relation (2.58). Rewriting this equation and performing partial summations yields

$$\frac{1}{\beta^3}\sum_{\nu\nu'\omega}\sum_{\vec{k}\vec{k}'\vec{q}}\chi^{\nu\nu'\omega}_{\vec{k}\vec{k}'\vec{q},\uparrow\uparrow}=\frac{1}{\beta}\sum_{\omega\vec{q}}\chi^{\omega}_{\vec{q},\uparrow\uparrow}=\frac{1}{2\beta}\sum_{\omega\vec{q}}\left(\chi^{\omega}_{\text{c},\vec{q}}+\chi^{\omega}_{\text{s},\vec{q}}\right)=\frac{n}{2}\left(1-\frac{n}{2}\right) \tag{2.63}$$

   Since the DMFT self-energy exhibits the correct high-frequency asymptotics for its self-energy, its local generalized susceptibility obeys this sum-rule:

$$\frac{1}{\beta^3}\sum_{\nu\nu'\omega}\chi^{\nu\nu'\omega}_{\uparrow\uparrow}=\frac{n}{2}\left(1-\frac{n}{2}\right) \tag{2.64}$$

   This relation provides a condition for the λ-corrections:

$$\sum_{\vec{q},\omega}\chi^{\lambda,\omega}_{\uparrow\uparrow,\vec{q}}\stackrel{!}{=}\sum_{\omega}\chi^{\omega}_{\text{loc},\uparrow\uparrow} \tag{2.65}$$

   However, for the susceptibility $\chi^{\omega}_{\uparrow\uparrow,\vec{q}}$, unlike for the charge and spin susceptibilities, no obvious, physically motivated form near a phase transition exists. Therefore, it has to be composed

by the physical charge and spin susceptibilities, and the λ-corrections are assumed to be carried over to either one (the dominant, e.g. spin) channel

$$\sum_{\vec{q},\omega} \chi^{\lambda,\omega}_{\uparrow\uparrow,\vec{q}} = \frac{1}{2}\sum_{\vec{q},\omega}\left(\chi^{\omega}_{\mathrm{c},\vec{q}} + \chi^{\lambda_\mathrm{s},\omega}_{\mathrm{s},\vec{q}}\right) \overset{!}{=} \frac{1}{2}\sum_{\omega}\left(\chi^{\omega}_{\mathrm{loc,c}} + \chi^{\omega}_{\mathrm{loc,s}}\right) \tag{2.66}$$

or to both channels in an equal manner

$$\sum_{\vec{q},\omega} \chi^{\lambda,\omega}_{\uparrow\uparrow,\vec{q}} = \frac{1}{2}\sum_{\vec{q},\omega}\left(\chi^{\lambda_\mathrm{c},\omega}_{\mathrm{c},\vec{q}} + \chi^{\lambda_\mathrm{s},\omega}_{\mathrm{s},\vec{q}}\right) \overset{!}{=} \frac{1}{2}\sum_{\omega}\left(\chi^{\omega}_{\mathrm{loc,c}} + \chi^{\omega}_{\mathrm{loc,s}}\right) \tag{2.67}$$

that is usually split into two separate equations

$$\sum_{\vec{q},\omega} \chi^{\lambda_\mathrm{c},\omega}_{\mathrm{c},\vec{q}} \overset{!}{=} \sum_{\omega} \chi^{\omega}_{\mathrm{loc,c}} \tag{2.68}$$

$$\sum_{\vec{q},\omega} \chi^{\lambda_\mathrm{s},\omega}_{\mathrm{s},\vec{q}} \overset{!}{=} \sum_{\omega} \chi^{\omega}_{\mathrm{loc,s}}. \tag{2.69}$$

In most of the following calculations, the latter implementation of the λ-correction has been used. Otherwise, it will be explicitly stated. A further, empirically found, remark can be made with respect to a possible frequency-dependent λ-correction: although in principle possible, a λ-correction constant in frequency-space turns out to be sufficient for the assurance of the correct asymptotics of the ladder-DΓA self-energy. For a recent discussion of methods for λ-corrections see [68].

For a detailed introduction to the current implementation of the ladder-DΓA including technical details, see Sec. 2.4. Please also note that, at least for some set of parameters, the application of the λ-correction can lead to unphysical results far away from the Fermi surface (see Sec. 4.3.4 for the case of nanoscopic structures).

2.4 Current implementation of the ladder-DΓA algorithm

After the synopsis of the necessary theory in Sec. 2.3.2.2, in this final part of the chapter, the current implementation of the ladder-DΓA is discussed. This discussion should serve as a reference to the actual user of the program and, therefore, will explain the necessary set-up, its structure and the typical parameters for which the program can/may be used reliably. Common checks for the application of the program and the obtained results can be found in Appendix B.

The aim of the program is to calculate the non-local DΓA self-energy in ladder-approximation (the

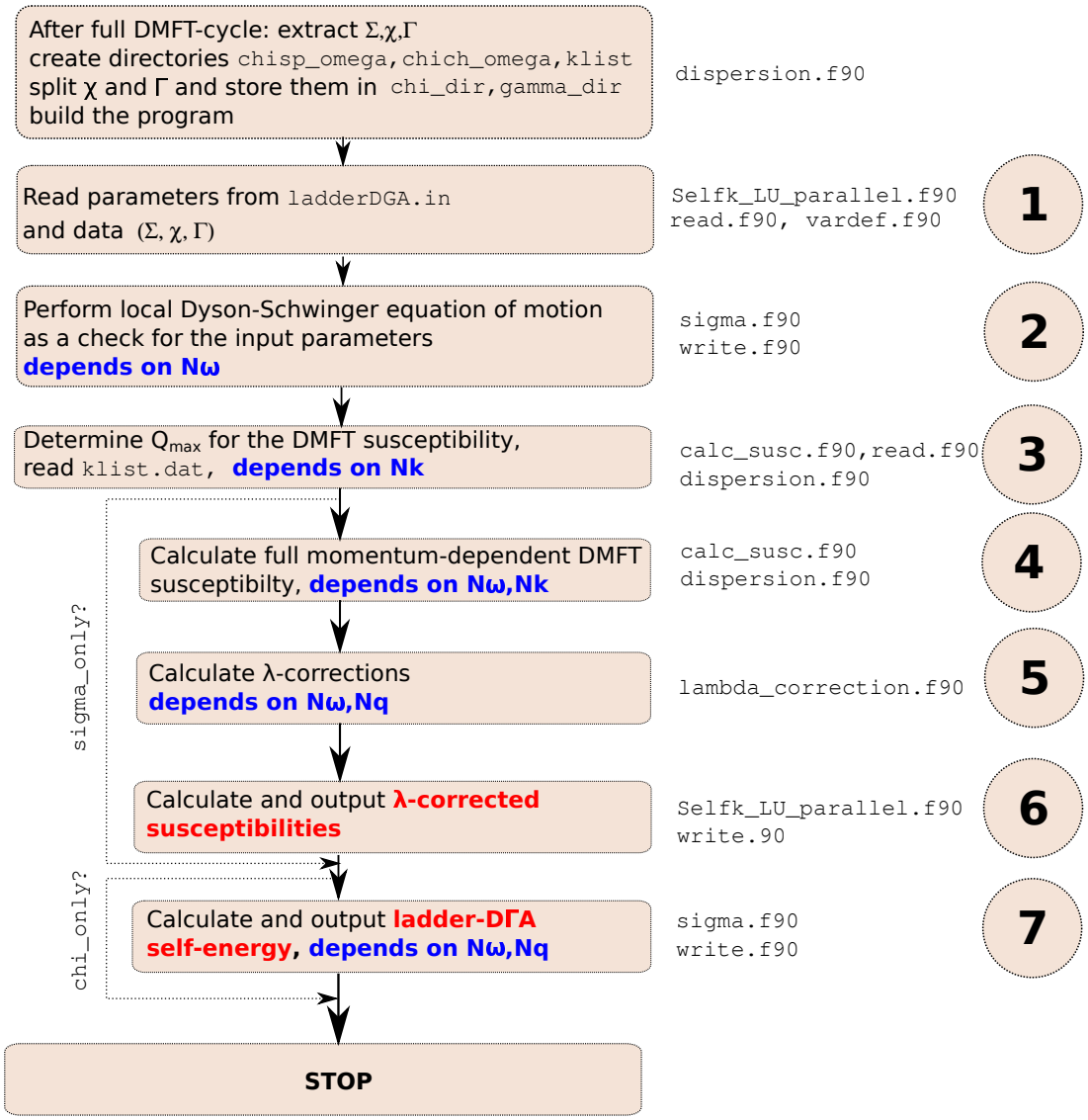

Figure 2.14: Flow-chart algorithm ladder-DΓA. The necessary steps 1. - 7. are describe in detail in the main text of this section. The modules which are utilized to achieve the separate tasks are written in typewriter font.

magnetic channel is singled out as the dominant one in this implementation) for the two- or three-dimensional Hubbard model on a square or cubic lattice[2] and, either as byproducts or quantities of main interest, the λ-corrected susceptibilities. The program is written in the FORTRAN90 standard and is subdivided into several modules of which `Selfk_LU_parallel.f90` is the main module. As

[2]There exist versions for every dimensionality (one-, two- and three-dimensional Hubbard model). The latest version which is described here, however, is written for two and three dimensions.

its name indicates, the program is MPI-parallelized in the bosonic Matsubara frequencies using one core per frequency (e.g., in the Dyson-Schwinger equation of motion). Fig. 2.14 summarizes the algorithmic flow of the program, indicating the necessary inputs and modules for every step, which are now discussed in detail:

Setting up the program
Before one can start an actual ladder-DΓA-calculation, a full DMFT calculation has to be performed, where the (local) DMFT self-energy $\Sigma_{\text{DMFT}}(\nu)$, the local generalized susceptibilities $\chi^{\nu\nu'\omega}_{\text{loc,r}}$ and the local irreducible vertices $\Gamma^{\nu\nu'\omega}_{\text{loc,r}}$ in channel r=c(harge)/s(pin) have to be extracted. The self-energy is actually provided by two files: the local DMFT self-energy in `gm_wim` and the (inverse) Weiss field of the self-consistently determined AIM in `g0mand`. The vertices have to be given in subdirectories (`chi_dir` and `gamma_dir`, respectively), split into files with constant bosonic Matsubara frequencies, the total number of which is denoted by $2N_\omega - 1$ (so that, e.g., the file `chiXXX` in `chi_dir` contains the data for the zeroth bosonic Matsubara frequency for `XXX`$= N_\omega - 1$).

The following directories serve as output directories and have to be explicitly created: `klist`, `chisp_omega` and `chich_omega`.

In `dispersion.f90`, the dispersion relation of the lattice has to be given. For reasons, which will become clear in the following steps, the form the dispersion relation has to be written in terms of $\sin(k_i)$- and $\cos(k_i)$-terms for the reciprocal spatial directions i of the Brillouin zone.

For building the program, the included `make`-file can be used. The command for linking the production version of the program is `make run`.

1. **Reading parameters and data**
   When the program is started, as a first step, parameters and input data are read. The main input file for parameters is `ladderDGA.in`, which, therefore, are described in Tab. 2.1. After initializing the program with the values from `ladderDGA.in`, $\Sigma_{\text{DMFT}}(\nu)$ ($= \mathcal{G}_0^{-1}(\nu) - G^{-1}_{\text{loc,DMFT}}(\nu)$, including the Hartree term), $\chi^{\nu\nu'\omega}_{\text{loc,r}}$ and $\Gamma^{\nu\nu'\omega}_{\text{loc,r}}$ are read.

2. **Perform local Dyson-Schwinger equation of motion**
   Mainly as a test for the correct definition of the input parameters, the local Dyson-Schwinger equation of motion is used to check, how well it reproduces the original DMFT self-energy.

parameter(s)	description
`U, mu, beta, nden`	Hubbard parameters of the (self-consistently determined) AIM: U, μ, $\beta = 1/T$, n
`Iwbox`	number of positive fermionic/bosonic Matsubara frequencies N_ω
`shift`	manual shift of bosonic frequencies (usually 0)
`LQ`	number of momentum points for the transferred momentum N_q
`nint`	number of momentum points for internal momentum N_k
`k_number`	number of $\vec{k}$-points for which $\Sigma(\nu, \vec{k})$ shall be calculated and that are specified in `klist.dat`
`sigma_only`	`.TRUE.`: λ_r have to be given, $\chi^{\lambda_\mathrm{r}=0,\nu\nu'\omega}_{\mathrm{r},\vec{q}}$ are read, only $\Sigma(\nu, \vec{k})$ is calculated
`chi_only`	`.TRUE.`: only $\chi^{\lambda_\mathrm{r},\nu\nu'\omega}_{\mathrm{r},\vec{q}}$ and λ_r are calculated, the calculation of $\Sigma(\nu, \vec{k})$ is omitted

Table 2.1: Description of the input parameters in `ladderDGA.in`.

The local version of the Dyson-Schwinger equation of motion is given by

$$\begin{aligned}\Sigma^{\text{ladder}}_{\text{loc}}(\nu) = \quad & \frac{Un}{2} + \frac{U}{2\beta^2}\sum_{\omega}\Big[\gamma_{\text{c}}^{\nu\omega} - 3\gamma_{\text{s}}^{\nu\omega} + U\gamma_{\text{c}}^{\nu\omega}\chi^{\omega}_{\text{loc,c}} + 3U\gamma_{\text{s}}^{\nu\omega}\chi^{\omega}_{\text{loc,s}} + 2 \\ - \quad & \sum_{\nu'} F^{\nu\nu'\omega}_{\text{loc},\uparrow\downarrow} G_{\text{DMFT}}(\nu')G_{\text{DMFT}}(\nu'+\omega)\Big] G_{\text{DMFT}}(\nu+\omega).\end{aligned} \tag{2.70}$$

The outcome of this calculation is written to `klist/SELF_LOC_parallel`, where the format of the file is

$$\nu \quad \text{Re}\Sigma_{\text{DMFT}}(\nu) \quad \text{Im}\Sigma_{\text{DMFT}}(\nu) \quad \text{Re}\Sigma^{\text{ladder}}_{\text{loc}}(\nu) \quad \text{Im}\Sigma^{\text{ladder}}_{\text{loc}}(\nu).$$

Please note that the agreement between the self-energies **crucially depends on** N_ω, i.e. the number of Matsubara frequencies used, and, that usually the asymptotics of the DMFT self-energy is not well reproduced.

3. **Determine $\vec{Q}_{\text{max}}$ for the DMFT susceptibility**
   As the vector, where the (momentum-dependent DMFT) susceptibility $\chi^{\lambda_\mathrm{r}=0,\omega=0}_{\mathrm{r},\vec{q}}$ exhibits its maximum, is of particular interest, it turns out to be convenient, to substitute one data point of the (otherwise uniform) $\vec{q}$-momentum-grid by this vector $\vec{Q}_{\text{max}}$. As it turned out in the special case of the (magnetic) quantum critical point of the three dimensional doped Hubbard model on a cubic lattice, there, the maxima are given by $\vec{Q}_{\text{max}} = (\pi, \pi, q_{\text{max}})$. This means, for this determination it is sufficient to consider one-dimensional momentum slices of the DMFT bubble, whereas the fully momentum-dependent DMFT-bubble (see next step) is calculated with the updated $\vec{q}$-grid including $\vec{Q}_{\text{max}}$. The actual determination of q_{max} is achieved by a simple bracketing algorithm with a termination precision given by `qmaxprec`.

In this step, also the $\vec{k}$-points for which the ladder-DΓA self-energy shall be calculated, are read from `klist.dat`, which has to contain exactly `k_number` lines. Furthermore, the momentum-array for the internal ($\vec{k}$') and external ($\vec{q}$) momentum-grids are initialized and their $\sin$- and $\cos$-values are calculated and stored in arrays in order to save time for their evaluation during the bubble-calculation.

Please note that this step **depends on** N_k, i.e. the number of internal $\vec{k}'$-points used.

4. **Calculate momentum-dependent DMFT susceptibility**
In this step, the $(\vec{k},\vec{k}')$ integrated DMFT susceptibility ($\lambda_\mathrm{r}=0$) is calculated using the relation

$$\chi_{\mathrm{r},\vec{q}}^{\lambda_\mathrm{r}=0,\nu\nu'\omega} = \left[\Gamma_{\mathrm{loc,r}}^{\nu\nu'\omega} - \chi_{0,\vec{q}}^{\nu\omega}\delta_{\nu\nu'}\right]^{-1}, \tag{2.71}$$

where

$$\chi_{0,\vec{q}}^{\nu\omega} = -\sum_{\vec{k},\vec{k}'} G_{\mathrm{DMFT}}(\nu,\vec{k})G_{\mathrm{DMFT}}(\nu+\omega,\vec{k}+\vec{q})\delta_{\vec{k}\vec{k}'}$$

is Eq. (2.44) for the momentum-dependent DMFT-bubble and the inversion is carried out in (ν,ν')-space. The following technical aspects are noteworthy:

- In principle, the integration over $(\vec{k},\vec{k}')$ is carried out using a Gauss-Legendre integration with an order specified by `ng` in `dispersion.f90` and a number of integration points of `nint` (see Tab. 2.1). If one sets `ng`$=1$ and adapts `tsteps=(/1.0/)` and `weights=(/2.0/)`, a rectangular integration is recovered.
- The integration is carried out for external $\vec{q}$-points of the **fully irreducible Brillouin zone**. For other dispersion relations than the simple cubic one, this may have to be adapted.
- This steps is implemented in exactly the same way as for the determination of $\vec{Q}_\mathrm{max}$ in the previous one (step 3.).

Please note that this step **crucially depends on** N_ω **and** N_k, i.e. the number of Matsubara frequencies and internal $\vec{k}$-points, and that the step is only carried out, if the flag `sigma_only=.FALSE.`. This, in turn, means, that the λ-correction parameters already have been calculated and have to be given in `ladderDGA.in` (see Tab. 2.1).

5. **Calculate λ-corrections**
In this algorithmic step, the Moriyaesque λ-corrections for the physical susceptibilities are

determined. The condition introduced in Sec. 2.3.2.2,

$$\frac{1}{2}\sum_{\vec{q},\omega}\left(\chi^{\lambda_\mathsf{c},\omega}_{\mathsf{c},\vec{q}}+\chi^{\lambda_\mathsf{s},\omega}_{\mathsf{s},\vec{q}}\right)\overset{!}{=}\frac{1}{2}\sum_{\omega}\left(\chi^{\omega}_{\mathsf{loc,c}}+\chi^{\omega}_{\mathsf{loc,s}}\right). \tag{2.72}$$

is implemented for **charge- and spin-channel separately**, i.e.

$$\sum_{\vec{q},\omega}\chi^{\lambda_\mathsf{c},\omega}_{\mathsf{c},\vec{q}} \overset{!}{=} \sum_{\omega}\chi^{\omega}_{\mathsf{loc,c}} \tag{2.73}$$

$$\sum_{\vec{q},\omega}\chi^{\lambda_\mathsf{s},\omega}_{\mathsf{s},\vec{q}} \overset{!}{=} \sum_{\omega}\chi^{\omega}_{\mathsf{loc,s}}. \tag{2.74}$$

These conditions can be reformulated in terms of the root-finding of the following functional expression:

$$f(\lambda)=\sum_{\vec{q},\omega}\left[\chi(\omega,\vec{q})^{-1}+\lambda\right]^{-1}-\sum_{\omega}\chi_{\mathsf{loc}}(\omega),$$

which can be done (due to this analytic expression) by applying Newton's root finding algorithm. The function $f(\lambda)$ has several roots, however, in order to avoid the divergence of the physical susceptibility (and, therefore, render the susceptibility for $\omega=0$ purely positive), one usually wants to track the root with the largest $\lambda=\lambda^*$. Analyzing the function $f(\lambda)$ (see also Fig. 2.15) gives several hints and restrictions for how to find the correct root (if possible):

- $f(\lambda)$ posses poles at $-\chi^{-1}(\omega=0,\vec{q})$, which means, in turn, that the largest λ-value at pole is given by

$$\lambda^{\text{max-pole}}=\mathsf{max}_{\vec{q}}\left[-\chi^{-1}(\omega=0,\vec{q})\right]=\mathsf{min}_{\vec{q}}\left[\chi^{-1}(\omega=0,\vec{q})\right].$$

- $f(\lambda)$ is strictly monotonically decreasing (excepting the divergence points), as one can easily see by calculating the first derivative $f'(\lambda)$, which is also needed as input for Newton's algorithm:

$$f'(\lambda)=-\sum_{\vec{q},\omega}\left[\chi^{-1}(\omega,\vec{q})+\lambda\right]^{-2}<0.$$

- $f(\lambda)$ is a convex function for $\lambda>\lambda^{\text{max-pole}}$:

$$f''(\lambda)=2\sum_{\vec{q},\omega}\left[\chi^{-1}(\omega,\vec{q})+\lambda\right]^{-3}>0,\quad\forall\lambda>\lambda^{\text{max-pole}}.$$

- For $\lambda>\lambda^{\text{max-pole}}$, $f(\lambda)$ only has one root, i.e. λ^*.

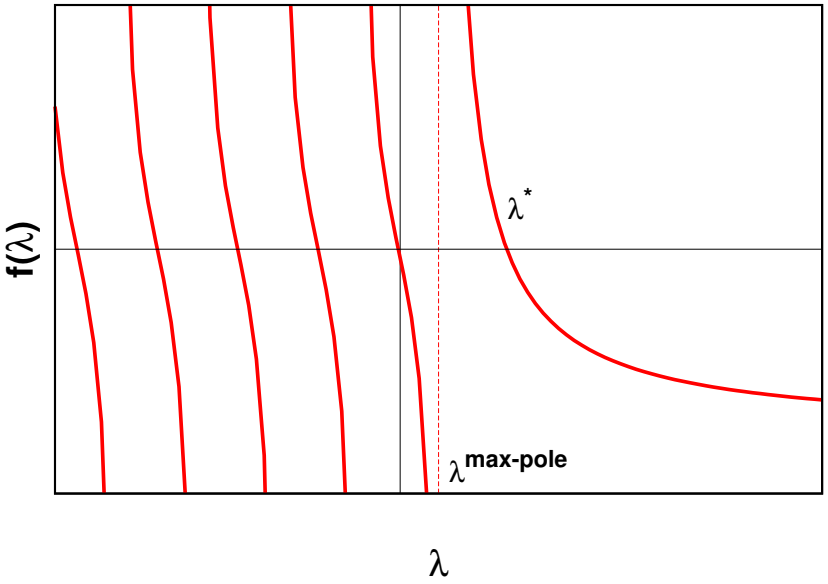

Figure 2.15: Determining the Moriyaesque λ-corrections with Newton's algorithm.

For a Newton-algorithm with starting value

$$\lambda_0 = \lambda^{\text{max-pole}} + \delta, \quad \delta > 0$$

and iteration condition

$$\lambda_{n+1} = \lambda_n - \frac{f(\lambda_n)}{f'(\lambda_n)}$$

these considerations lead to three different scenarios:

(a) $\lambda_0 \in \left[\lambda^{\text{max-pole}}\right]$
λ will remain in $\left[\lambda^{\text{max-pole}}\right]$ and quadratically converges against λ^*.

(b) $\lambda_0 > \lambda^* \wedge \lambda_1 = \lambda_0 - \frac{f(\lambda_0)}{f'(\lambda_0)} < \lambda^{\text{max-pole}}$
The algorithm has to start over with a smaller δ (bisection).

(c) $\lambda_0 > \lambda^* \wedge \lambda_1 = \lambda_0 - \frac{f(\lambda_0)}{f'(\lambda_0)} > \lambda^{\text{max-pole}}$
After the next iteration, one will end up in $\left[\lambda^{\text{max-pole}}, \lambda^*\right]$ due to the convexity of $f(\lambda)$ and can continue with (a).

The $\vec{q}$-integrals are carried out over the **fully irreducible Brillouin-zone** as the analogue sums for the self-energy (see the detailed discussion there in step 7.). The separate iteration steps are logged in `lambda_correction_ch.dat` and `lambda_correction_sp.dat`, respec-

tively, which are formatted in the following way:

$$\text{step} \quad \lambda \quad \sum_{\vec{q},\omega} \chi_{\vec{q}}^{\lambda,\omega} \quad \sum_{\omega} \chi_{\text{loc}}^{\omega} \quad \sum_{\vec{q},\omega} \chi_{\vec{q}}^{\prime\lambda,\omega} \quad \sum_{\vec{q},\omega} \chi_{\vec{q}}^{\prime\prime\lambda,\omega}$$

Here, the following points are noteworthy:

- The sums in the format above are complex sums, i.e. two floats per sum will be written.
- The sums for the AIM (local susceptibilities) are restricted to the positive summands via the (automatically set) variable `sum_ind` (correct behavior of $\chi_{\text{AIM}}(\tau)$, which can be spoilt in numerical calculations).

Please note further that this step **depends on** N_q, i.e. the number of external momentum points, and is only carried out, if the flag `sigma_only=.FALSE.`.

6. **Calculate λ-corrected susceptibilities**
   In this step, relying on the input of the full momentum-dependent DMFT susceptibilities, the λ-corrected susceptibilities are obtained by

$$\chi_{\text{r},\vec{q}}^{\lambda_{\text{r}},\omega} = \left[\chi_{\text{r},\vec{q}}^{\lambda_{\text{r}}=0,\omega} + \lambda_{\text{r}}\right]^{-1}. \tag{2.75}$$

   Depending on the channel they are written in files `chiXXX` with constant bosonic Matsubara frequency into the subdirectories `chisp_omega` and `chich_omega` respectively. The format of these output files in two dimensions is (analogously in three dimensions):

$$q_x \quad q_y \quad \text{Re}\chi_{\text{r},\vec{q}}^{\lambda_{\text{r}},\omega} \quad \text{Im}\chi_{\text{r},\vec{q}}^{\lambda_{\text{r}},\omega} \quad \text{Re}\chi_{\text{r},\vec{q}}^{\lambda_{\text{r}}=0,\omega} \quad \text{Im}\chi_{\text{r},\vec{q}}^{\lambda_{\text{r}}=0,\omega}$$

   with $q_x \geq q_y$. The $\vec{q}$-grid is represented by an equal-spaced grid[3], whose number (linear dimension) of intervals is given by `LQ`.

   Please note that this step is only carried out, if the flag `sigma_only=.FALSE.`.

7. **Calculate ladder-DΓA self-energies**
   In this very last step of the algorithm, the ladder-DΓA self-energy is calculated via the (non-

[3] except for the substituted $\vec{Q}_{\text{max}}$, see step 3.

local) Dyson-Schwinger equation of motion, Eq. (2.62), which is recalled here:

$$\begin{aligned}\Sigma^{\text{ladder}}_{\text{D}\Gamma\text{A}}(\nu,\vec{k}) &= \frac{U}{2\beta^2}\sum_{\omega,\vec{q}}\Big[\gamma^{\nu\omega}_{\text{c},\vec{q}} - 3\gamma^{\nu\omega}_{\text{s},\vec{q}} + U\gamma^{\nu\omega}_{\text{c},\vec{q}}\chi^{\lambda_\text{c},\omega}_{\text{c},\vec{q}} + 3U\gamma^{\nu\omega}_{\text{s},\vec{q}}\chi^{\lambda_\text{s},\omega}_{\text{s},\vec{q}} + 2 + \\ &- \sum_{\nu',\vec{k}'}\left(F^{\nu\nu'\omega}_{\text{loc,c}} - F^{\nu\nu'\omega}_{\text{loc,s}}\right)G_{\text{DMFT}}(\nu',\vec{k}')G_{\text{DMFT}}(\nu'+\omega,\vec{k}'+\vec{q})\Big]G_{\text{DMFT}}(\nu+\omega,\vec{k}+\vec{q}).\end{aligned} \tag{2.76}$$

Please note that the constant Hartree part of the self-energy is not included here. In the program, the three-leg vertices for charge- and spin-channel, respectively, are denoted `vrgch` and `vrgsp`. It is noteworthy that the λ-corrected physical susceptibilities enter in the formula and that in the current implementation both ph-channels are treated on equal footing (see step 5.). The $\vec{q}$-integration is carried out over the fully irreducible Brillouin-zone, which means that, e.g. for two dimensions, $q_x \geq q_y$ and a factor has to be introduced in order to account for the $\vec{q}$-point multiplicity. This factor consists of two parts: one takes into account the points at the borders of the Brillouin-zone, the other one the multiplicity of the point itself. The first condition is rather straightforwardly implemented by a factor of $\frac{1}{2}$ whenever, e.g., $q_x = \pi$. The latter is implemented as an integer division of the momentum-*indices* of the $\vec{q}$-points. For two dimensions this integer-division reads (`ix` is the index for q_x, `iy` for q_y and `iz` for q_z, respectively):

$$2/((1+iy)/(1+ix)+1)$$

and, analogously, for three dimensions:

$$6/((1+iy)/(1+ix)+(1+iz)/(1+iy)+3((1+iz)/(1+ix))+1)).$$

Particularly, special attention has to be paid for the calculation of the dispersion relations (`eklist`) used in the (non-local) DMFT Green function, which depends on symmetries of the lattice (mirror-/inversion-symmetries), and one would need to be adapt in case that these symmetries are broken in the specific problem considered. The calculated self-energies are written to the subdirectory `klist`, named `SELF_Q_XXX` where `XXX` indicates the corresponding line in `klist.dat` specifying the $\vec{k}$-point for which the self-energy has been calculated. The output format of the files is

$$\nu \quad \text{Re}\Sigma^{\text{ladder}}_{\text{D}\Gamma\text{A}}(\nu,\vec{k}) \quad \text{Im}\Sigma^{\text{ladder}}_{\text{D}\Gamma\text{A}}(\nu,\vec{k}).$$

Depending on the version of the program, there can be additional columns that contain *partial sums* of only specific terms of the full sum in Eq. (2.62) (**"parquet decomposition"**).

Please note that the external Matsubara sum over ω is implicitly carried out via the parallelization and an MPI-summation command. Please note furthermore that this step **depends on N_ω and N_q**, i.e. the number of Matsubara frequencies and external $\vec{q}$-points, and that the step is only carried out, if the flag `chi_only=.FALSE.`.

Typical settings for the program's parameters in two and three dimensions

In order to obtain reliable and convergent results from the ladder-DΓA program, as indicated in the previous section, the three parameters N_ω, N_k and N_q have to be adjusted correctly. Of course, the values given in Tab. 2.2 can only be regarded as a rough guideline and calculations should be checked individually for convergence (especially for working points in the vicinity of (quantum) phase transitions). All the interaction and temperatures in this section are measured in units of $4t$ (t is the hopping parameter of the Hubbard Hamiltonian in Eq. (2.6)).

- Number of (positive) fermionic and bosonic Matsubara frequencies N_ω

  In principle, like in every calculations involving Matsubara frequencies, N_ω has to be adjusted according to the temperature. Tab. 2.2 shows this number used for typical calculations, with which one usually converges in the number of Matsubara frequencies. For temperatures below these points, extrapolations have to be performed.

β-range	N_ω	N_k (2D/3D)	N_q (2D/3D)
$[10, 20]$	40	60/4	40/40
$[30, 40]$	60	60/4	60/40
$[50, 60]$	100	60/4	120/60
$[70, 80]$	120	60/6	160/80
$[100, 120]$	160	60/6	200/120

Table 2.2: Summary of typical values of N_ω, N_k and N_q.

- Number of internal $\vec{k}'$-summation points N_k

  The actual number of the points in the Brillouin-zone depends on the integration algorithm used. Tab. 2.2 assumes a fifth-order Gauss-Legendre method, which means the actual number of $\vec{k}$-points per dimension is $5N_k$.

- Number of external $\vec{q}$-summation points N_q

  Here, it should be noted that in practice, although N_ω my be influenced by the values of λ and the corresponding $\chi_{\vec{q}}^{\lambda,\omega}$, while the self-energy $\Sigma_{\mathrm{D\Gamma A}}^{\mathrm{ladder}}(\nu, \vec{k})$ and the correlations length ξ seem to be rather robust against the alteration of N_ω.

3

Precursors of phase transitions - from divergent vertices to fluctuation diagnostics

"Similarly, another famous little quantum fluctuation that programs you is the exact configuration of your DNA."

- Seth Lloyd (American physicist, *1960)

The vicinity of phase transitions from unordered to ordered phases is characterized by a huge variety of phenomena and physical processes. The extension and the nature of these effects, however, change significantly if one considers those transitions occuring in strongly correlated electron systems, such as the case of the Mott-Hubbard metal-insulator transition. In particular, in this Chapter it will be shown, how precursor effects of the Mott transition can indeed occur even far from the transition itself, marking a breakdown of perturbation theory. In fact, by gradually increasing the Coulomb interaction in the half-filled Hubbard model (solved by means of DMFT), and approaching the corresponding Mott metal-insulator transition, two-particle vertex functions exhibit low-frequency divergencies already well inside the metallic phase. These divergencies are, then, shown to be responsible also for the breakdown of the unambiguous interpretations of the so-called parquet-decomposition of the self-energy, that aims at identifying which physical scattering processes are responsible for yielding a certain physical one-particle spectrum (e.g. pseudogap features). In the last part of this Chapter, the difficulties stemming from this breakdown are circumvented by introducing an analysis method for the electronic self-energy based on partial summations of the Dyson-Schwinger equation of motion, coined "fluctuation diagonstics" approach.

3.1 Vertex divergencies as precursors of the Mott-Hubbard transition

Parts of this section (marked by a vertical sidebar) have already been published in the APS journal Phys. Rev. Lett. **110**, 246405 (2013).

Among all fascinating phenomena characterizing the physics of correlated electronic systems, one of the most important is undoubtedly the Mott-Hubbard metal-to-insulator transition (MIT) [69]. Here, the onset of an insulating state is a direct consequence of the strong Coulomb repulsion, rather than of the underlying electronic band-structure. Mott MITs have been indeed identified in several correlated materials [5], especially in the class of transition metal oxides and heavy fermions. The interest in the Mott MIT is not limited however to the transition "per se", but it is also for the correlated (bad) metallic regime in its proximity. In fact, this region of the phase-diagram often displays a rich variety of intriguing or exotic phases, that is often related to the physics of the high-temperature superconducting cuprates.

An exact theoretical description of the Mott MIT represents a considerable challenge due to its intrinsically non-perturbative nature in terms of the electronic interaction. However, a significant progress was achieved with the invention of the dynamical mean field theory (DMFT) (see Sec. 2.2). By an accurate treatment of *local* quantum correlations, DMFT has allowed for the first non-perturbative analysis of the Mott-Hubbard MIT in the Hubbard model [21], and, in combination with ab-initio methods [18, 70], also for the interpretation and the prediction of experimental spectroscopic results for strongly correlated materials, such as, e.g., the paramagnetic phases of V_2O_3 (see also Fig. 3.1, [71] and Chapter 5). Theoretically, several "hallmarks" of the onset of the Mott insulating phase can be unambiguously identified in DMFT: At the one-particle level, a divergence of the local electronic self-energy in the zero-frequency limit is observed, reflecting the opening of the Mott spectral gap, while, at the two-particle level, the local spin susceptibility $\chi_{\mathrm{s}}^{\omega=0}$ diverges at $T=0$, due to the onset of long-living local magnetic moments in the Mott phase.

While the characterization of the MIT itself is quite clear, at least on a DMFT level, the physics of the correlated metal regime in the vicinity of the MIT is far from being trivial and presents several anomalies. One can recall here: the occurrence of kinks of purely electronic origin [72] in the angular resolved one-particle spectral functions or in the electronic specific heat, the formation of large instantaneous magnetic moments, screened by the metallic dynamics [73], the abrupt change of the out-of-equilibrium behavior after a quench of the electronic interaction [74], and the changes in the energy-balance between the paramagnetic and the low-temperature (antiferromagnetically) ordered phase, which also affect the restricted optical sum-rules [75]. Also motivated by these observations, many DMFT calculations aimed at a general characterization of this regime, e.g., by

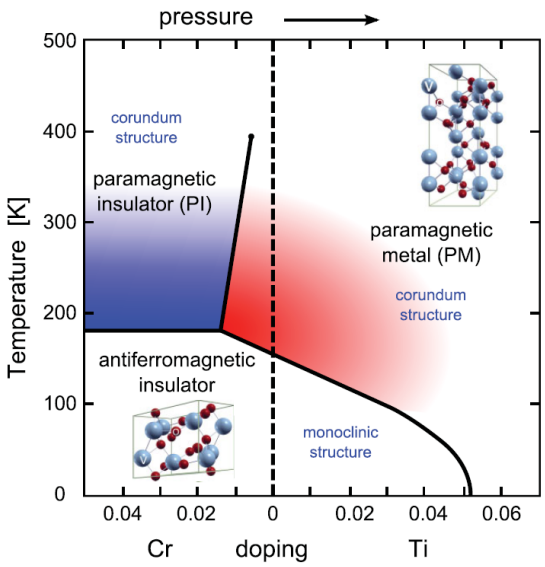

Figure 3.1: Phase diagram of V_2O_3, a prototypical material which exhibits a Mott metal-insulator transition, upon the application of pressure or doping (taken from [71]).

studying the phase-diagram of the half-filled Hubbard model. However, no trace of other phase transitions has been found beyond the MIT itself and the (essentially) mean-field antiferromagnetically ordered phase, which is not of interest here. Hence, one of the main outcomes of the previous DMFT analyses, mostly focusing on the evolution of one-particle spectral properties (and, to less extent, on susceptibilities [77]), has been the definition of the "borders" of the so-called crossover regions at higher T than those where the MIT can be observed. The shape of these crossover regions has been analyzed in many different ways [15, 33, 76, 78, 79]. One should note here, that the (different) criteria used for defining crossover regimes imply a certain degree of arbitrariness. Furthermore, the crossover region is located at much higher Ts than those, where some of the abovementioned anomalies are observed.

In this section, going beyond the standard, typically one-particle, DMFT analyses, a completely unambiguous criterion to distinguish the "weakly" and the "strongly"-correlated regions in the phase-diagram is presented. By studying the frequency structure of the two-particle local vertex functions of DMFT, one can observe the **divergence of the local Bethe-Salpeter equation in the charge channel.** This divergence defines a regime remarkably different, also in shape, from the crossover region, where non-perturbative precursor effects of the MIT become active, even well inside the low-temperature metallic phase. The precise definition of such a regime allows for a general interpretation of the anomalous physics emerging as a precursor of the MIT. Furthermore, the analysis presented here, showing the occurrence of peculiar divergent features in some of the two-particle local vertex functions of DMFT is also expected to have a significant impact on future calculations

for strongly correlated electron systems, because the two-particle local vertex functions represent a crucial ingredient for both (i) the calculation of dynamical momentum-dependent susceptibilities in DMFT [15,44,80], as well as (ii) the diagrammatic extensions [20,43,45,46] of the DMFT, aiming at the inclusion of non-local spatial correlations.

3.1.1 DMFT results at the two particle-level

For this analysis, the Hubbard model on a square lattice in the paramagnetic phase at half-filling, that is one of the most basic realizations of the MIT in DMFT, is considered (see Eq. (2.6)). Hereafter, all energy scales will be given in units of $D = 4t = 1$, i.e., of the half of the standard deviation of the non-interacting DOS[1].
Differently from previous studies, the focus here is on the analysis of the two-particle local vertex functions computed with DMFT. By using a HF-QMC impurity solver (see Sec. 2.2.2.3), whose accuracy has been also tested in selected cases with exact-diagonalization DMFT calculations (see Sec. 2.2.2.2), first the generalized local susceptibility $\chi_{\mathsf{c}}^{\nu\nu'\omega}$ is computed and the corresponding local irreducible vertex $\Gamma_{\mathsf{c}}^{\nu\nu'}$ obtained via the inverse Bethe-Salpeter equations (2.29). The vertex $\Gamma_{\mathsf{c}}^{\nu\nu'\omega}$ can be viewed as the two-particle counter-part of the electronic self-energy and, for a half-filled system, it is a purely real function. The numerical results for $\Gamma_{\mathsf{c}}^{\nu\nu',\omega=0} =: \Gamma_{\mathsf{c}}^{\nu\nu'}$ are reported in Fig. 3.2 for four different values of the electronic interaction U at a fixed temperature of $T = 0.1$.

Starting to examine the first panel, corresponding to the smallest value of $U = 1.2$, one observes two main diagonal structures in the Matsubara frequency space: These structures are easily interpretable as originated by reducible ladder-processes in the (transverse) particle-hole ($\nu = \nu'$) and in the particle-particle ($\nu = -\nu'$) channels respectively [51]. Following the behavior of the local spin susceptibility in the Mott phase, the main diagonal structure will diverge exactly at the MIT ($U_{\mathsf{MIT}} \sim 3$) in the $T = 0$ limit [51, 82]. In contrast to these standard properties of $\Gamma_c^{\nu\nu'}$, visible in the first panel, the analysis of the other three panels of Fig. 3.2 shows the **emergence of a low-frequency singular behavior** of the vertex functions for a **value of U much smaller than that of the MIT**: Already at $U = 1.27$ (second panel), one observes a strong enhancement of the vertex function at the lowest Matsubara frequencies (note the change in the intensity-scale). This is visible as an emergent "butterfly"-shaped structure, where the intense red-blue color coding indicates alternating signs in the (ν,ν') space. Remarkably, such a low-energy structure becomes predominant over the other ones along the diagonals. That a true divergence takes place is suggested by the third panel ($U = 1.28$), where the intensity of the"butterfly" structure is equally strong but the signs are now inverted as indicated by the colors. This is also shown more quantitatively by the values of $\Gamma_c^{\nu\nu'}$ along a selected path of $\Gamma_c^{\nu\nu'}$ in frequency space (lower panels in Fig. 3.2).

[1] As in DMFT the kinetic energy scale is controlled by D, DMFT results for different DOSes essentially coincides, provided the value of D is the same.

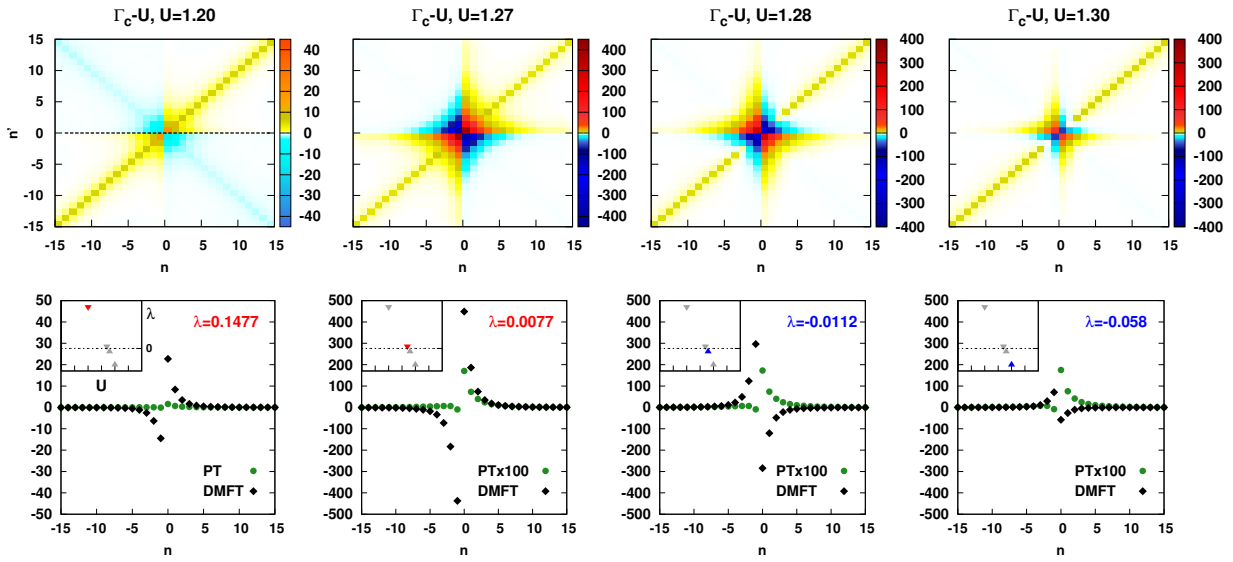

Figure 3.2: *Upper row*: Evolution of the frequency dependent two-particle vertex function, irreducible in the charge channel, ($\Gamma_c^{\nu\nu'}$) for increasing U. The data have been obtained by DMFT at zero external frequency ($\omega = 0$) and fixed temperature ($T = 0.1$); *lower row*: linear snapshot of the same Γ_c along the path marked by the dashed line in the first panel of the upper row, i.e., as a function of $\nu = \frac{\pi}{\beta}(2n+1)$ for $n' = 0$ ($\nu' = \frac{\pi}{\beta}$), compared to perturbation theory (PT) results. In the legends/insets the closest-to-zero eigenvalue (λ) of $\chi_c^{\nu\nu'}/\chi_0^{\nu\nu'}$ is reported for each U.

Note that the inversion of the signs **cannot be captured by perturbation theory** calculations (green circles), marking the non-perturbative nature of the result. The rigorous proof of the divergence is provided by the evolution of the matrix $\chi_c^{\nu\nu'}$, which is positive definite at weak-coupling, while one of its eigenvalues (see legends and insets in the bottom row of Fig. 3.2) becomes negative crossing 0. Finally, by further increasing U, the low-energy structure weakens, indicating that at fixed $T = 0.1$ this vertex divergence is taking place only for a specific value of the Hubbard interaction, i.e., for $\widetilde{U} \simeq 1.275$.

This finding naturally leads to the crucial question of the temperature dependence of the results: Does such a divergence occur for all temperatures, and if yes, is the temperature dependence of $\widetilde{U}$ significant? As one can immediately understand from Fig. 3.3, the answer to both questions is positive[2]: By repeating the analysis of Fig. 3.2 for different temperatures, one can the loci ($\widetilde{T}, \widetilde{U}$, red dots in Fig. 3.3) in the phase-diagram, where the low-frequency divergence of $\Gamma_c^{\nu\nu'}$ occurs. This

[2]In the (unpublished) appendix of arXiv:1104.3854v1, a two-particle vertex divergence was also reported for one temperature, whose position would have been controlled by U rather than by T. This expectation is, however, not verified by the data of Fig. 3.3.

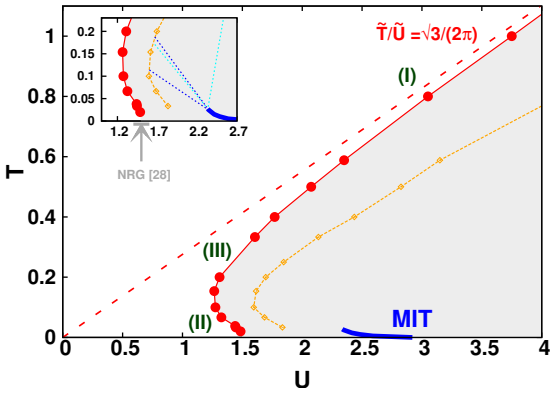

Figure 3.3: Instability lines of the local irreducible vertices in the charge (Γ_c red circles) and in the particle-particle channels (Γ_{pp} orange diamonds) reported in the DMFT phase diagram of the half-filled Hubbard model (the data of the MIT, blue solid line, are taken from Ref. [33, 76]). The red dashed line indicates the corresponding instability condition ($\widetilde{T} = \frac{\sqrt{3}}{2\pi}\widetilde{U}$) estimated from the atomic limit. Inset: zoom on the low-T region, where also different estimations (dashed blue lines [33, 76]) of the crossover region are indicated.

defines a curve $\widetilde{T}(U)$ with a quite peculiar shape, where three regions can be distinguished:

(I) At very high T, the behavior is almost perfectly linear $\widetilde{T} \propto \widetilde{U}$.

(II) In the low T limit the curve strongly bends, extrapolating for $T \to 0$ at $\widetilde{U}(0) \sim 1.5 \ll U_{\text{MIT}} \sim 3$.

(III) At intermediate T the curve interpolates between these two regimes, with a "re-entrance" clearly affected by the presence of the MIT at larger U (blue line in Fig. 3.3).

Please note that by increasing U much further than the $\widetilde{T}(U)$ curve, one eventually observes a divergence also of the local Bethe-Salpeter in the particle-particle channel (orange points in Fig. 3.3), while for all values of T, U considered, no similar divergence is found in the spin channel.

3.1.2 Interpretation of the results

In contrast to the case of the main diagonal structures of the vertex functions, the interpretation of the low-frequency divergences of $\Gamma_c^{\nu\nu'}$ is not directly related to the MIT. However, even if at low T the divergences take place in the metallic region of the phase-diagram, the re-entrance shape of the $\widetilde{T}(U)$ curve is indeed remarkably affected by the position of the MIT: The most natural interpretation is, hence, that the shaded area in the phase diagram defines the region where the precursor effects of the MIT physics preclude the perturbative description and become a crucial ingredient in determining the properties of the system. This interpretation is evidently supported by the fact that the signs of the two-particle vertex functions are correctly predicted in perturbation theory only up to the left-hand side of the $\widetilde{T}(U)$ curve.

More generally, the $\widetilde{T}(U)$ curve can be identified as the limit of the region of applicability of schemes based on the Baym-Kadanoff [81] functional $\Phi[G]$, since $\frac{\delta^2\Phi}{\delta G^2} = \Gamma_c$ can no longer be defined on that line. At the same time, the low-frequency singularities of the vertex may render problematic the numerical evaluation of the Bethe-Salpeter equation to compute momentum-dependent DMFT response functions in specific regions of the phase-diagrams, suggesting the use of alternative procedures [83].

As the singularity of Γ_{c} (and later on of Γ_{pp}) is not associated to simultaneous divergences in the other channels, the application of the local parquet equations [51, 64] allows to identify the ultimate root of these divergences in the *fully* two-particle irreducible diagrams (see Sec. 3.2.1). Hence, this is an "intrinsic" divergence, deeply rooted in the diagrammatics and not generated by ladder scattering processes in *any* channel. From a more physical point of view, the fact that the only irreducible vertex Γ not displaying no singularities at low-frequencies is the spin one might also indicate the emergent role played by preformed local magnetic moments as MIT precursors, even in regions where the metallic screening is rather effective.

Beyond these general considerations, however, one may analyze the three regimes of the $\widetilde{T}(U)$ curve in detail, also discussing the relation with the emergence of some of the anomalous properties of the physics in the vicinity of the MIT. The analysis of the high-T linear regime [(I) in Fig. 3.3] of $\widetilde{T}(U)$ is probably the easiest: Here $U, T \gg D$, and hence a connection with the **atomic limit (**$D = 0$**)** can be established: Using analytic expressions [51, 84] for the reducible two-particle vertex functions as an input for the local Bethe-Salpeter equations (2.29), one can find that the low-frequency divergence of $\Gamma_c^{\nu\nu'}$ occurs at $\widetilde{T}/\widetilde{U} = \frac{\sqrt{3}}{2\pi}$ and that the eigenvector associated to the vanishing eigenvalue of $\chi_{\mathrm{c}}^{\nu\nu'}$ has the particularly simple form: $\frac{1}{\sqrt{2}}(\delta_{\nu(\pi T)} - \delta_{\nu(-\pi T)})$ (see also Sec. 3.2.2). As it is clear from the comparison with the red dashed line in Fig. 3.3 this proportionality exactly matches the high-T linear behavior of our $\widetilde{T}(U)$ curve. Crossing this curve in its high-T linear regime, which extends indeed over a large portion of the phase-diagram, corresponds to entering a region where the thermal occupation of the high-energy doubly-occupied/empty states becomes negligible, letting the physics be dominated by the local moments.

The connection with the local moment physics also holds for the low-T region (II), though via a different mechanism: For $T \to 0$, the relevant energy scales are the kinetic ($\sim D$) and the potential (U) energy, whose competition is regulated by quantum fluctuations. In this case, obviously, only numerical results are available: We observe that the extrapolated value of $\widetilde{U}(0) \sim 1.5$ falls in the same region (gray arrow in inset of Fig. 3.3), where DMFT(NRG) [85] see a first clear separation of the Hubbard sub-bands from the central quasi-particle peak in the spectral function $A(\omega)$. It should be recalled here that the formation of well-defined minima in $A(\omega)$ between the central

quasi-particle peak and the Hubbard sub-bands, is directly connected with the anomalous phenomenon of the appearance of kinks in the electronic self-energy and specific heat [72]. At the same time, more recent DMFT(DMRG) [86] data rather indicate that for $U \geq \widetilde{U}(0) \sim 1.5$ two sharp peak-features emerge at the inner edges of the Hubbard sub-bands, which, however, would be already visible at $U \geq 1$.

Looking for a more analytical description of this scenario, one may consider the DMFT solution of the much simpler Falicov-Kimball (FK) model [87, 88]: Here one can exactly show that $\Gamma_c^{\nu\nu'}$ indeed diverges before the MIT is reached (precisely at: $\widetilde{U}^{\mathsf{FK}} = \frac{1}{\sqrt{2}} U_{\mathsf{MIT}}^{\mathsf{FK}}$). However, for the FK results, a direct relation with the formation of the two minima in $A(\omega)$ cannot be completely identified, as the renormalization of the central peak is not captured in this scheme[3]. Finally, an interesting observation can be made about the most complicate intermediate T regime (III), where all energy scales (D, U, T) are competing: Recent out-of-equilibrium calculations for the Hubbard model have shown [74], that after a quench of the interaction (i.e., from $U = 0$ to $U > 0$), the system's relaxation occurs in two different (non-thermal) ways. The changeover between these two regimes, however, appears for a given set of parameters $\bar{U} \sim 1.65$ and $T_{\mathsf{eff}} \sim 0.4$, in close proximity of the vertex instability-line in the phase diagram.

3.2 The non-perturbative landscape surrounding the MIT

Parts of this section are available as a preprint arXiv:1606.03393 (2016).

As already discussed in Sec. 3.1.1 for the Hubbard model, in certain regions of the (T, U)-plane, the local irreducible vertex in the charge channel $\Gamma_{\mathsf{c}}^{\nu\nu'\omega=0}$ as well as the particle-particle up-down channel $\Gamma_{\mathsf{pp},\uparrow\downarrow}^{\nu\nu'\omega=0}$ diverge and change sign at low fermionic frequencies. Starting at low temperature, the lines first start to bend away from the critical endpoint of the MIT like they tried to "avoid" it. These divergence lines, for strong couplings, can be traced up to the atomic limit, where their slopes follow the (semi-)analytic results obtained. Please note again that a divergent irreducible vertex in a specific channel Γ_{r} is caused by an eigenvalue of the corresponding generalized susceptibility χ_{r} passing zero. Also, one should recall that these divergences are different from those which occur at physical phase transitions, e.g. the Mott-Hubbard transition at $T=0$ where the divergences (i) appear at the level of the full vertex F and (ii) take place at both low and high frequencies.

In Fig. 3.4 additional data of the positions of the divergences are reported, making richer the DMFT "map" of the region surrounding the Mott-Hubbard MIT. Specifically, the blue line marks the

[3] Note that the DMFT solution of the FK model, which is of the coherent potential approximation (CPA) form, can only capture the MIT via a rigid separation of the Hubbard band: Here the formation of a central minimum occurs already at $U = \frac{1}{2} U_{\mathsf{MIT}}^{FK}$.

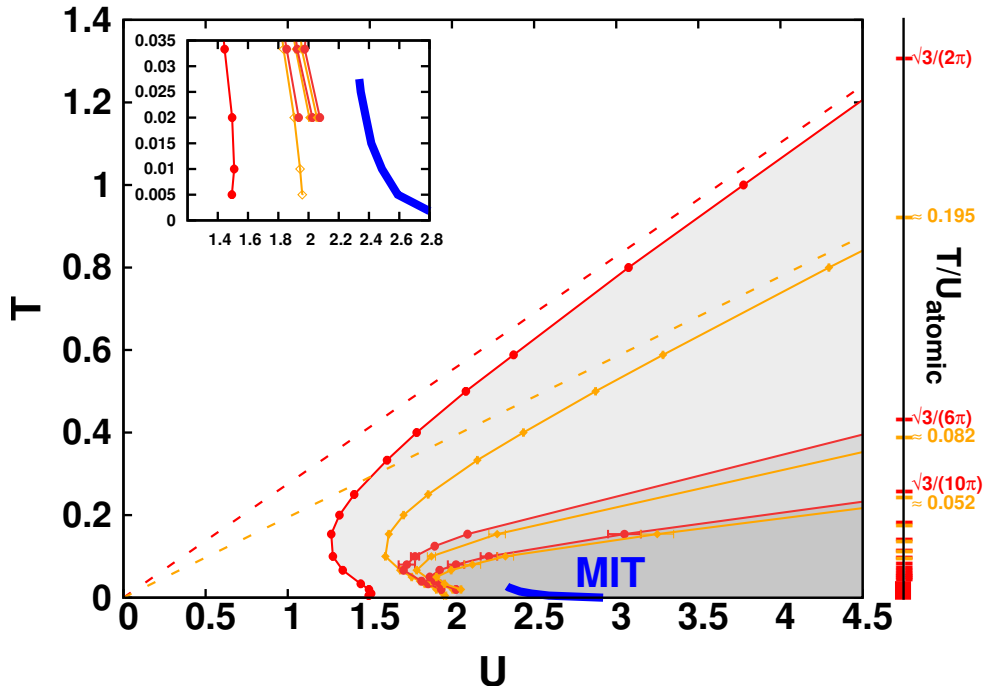

Figure 3.4: DMFT phase diagram showing the landscape surrounding the Mott-Hubbard MIT in the half-filled unfrustrated Hubbard model. The blue line indicates the MIT [33]. The red lines show the points where $\Gamma_{\mathrm{c}}^{\nu\nu'\omega=0}$ diverges at low frequencies, whereas an additional divergence of $\Gamma_{\mathrm{pp},\uparrow\downarrow}^{\nu\nu'\omega=0}$ takes place simultaneously to the one of $\Gamma_{\mathrm{c}}^{\nu\nu'\omega=0}$ at the orange lines. The inset zooms into the low-temperature regime. On the right-hand side, the (exact) values of the ratio T/U for the atomic limit ($t = 0$) are listed.

MIT. The red lines indicate the points in the phase diagram where $\Gamma_{\mathrm{c}}^{\nu\nu'\omega=0}$ diverges, whereas at the orange lines *both* $\Gamma_{\mathrm{c}}^{\nu\nu'\omega=0}$ and $\Gamma_{\mathrm{pp},\uparrow\downarrow}^{\nu\nu'\omega=0}$ diverge simultaneously.

Remarkably, this analysis extends the results of the previous section in a significant and non-trivial way. In fact, the two lines already reported there are not the only ones where a vertex divergence takes place: by approaching the MIT from the metallic phase, one observes several eigenvalues of the generalized charge and particle-particle susceptibilities passing through zero at certain values of $(\tilde{T}, \tilde{U})$, which determine the corresponding divergencies of the irreducible vertices to diverge at those points as well as a sign change of their low-frequency structure on the two sides of the divergence line. Even more astonishing, the lines seem to **accumulate at the critical endpoint of the MIT**, where the maximum number of the eigenvalues of the charge susceptibility has passed zero. In this respect it is also remarkable that the irreducible vertex in the spin channel $\Gamma_{\mathrm{s}}^{\nu\nu'\omega}$ does not exhibit low-frequency divergences in the whole phase diagram considered. These findings evidently provide a strong support to the heuristic interpretation proposed in the preceding section of the low-frequency singularities as precursors of the Mott-Hubbard transition and their possible relation

to the formation of local and instantaneous magnetic moments well inside the metallic regime.

3.2.1 Behavior of the full vertex F and divergence of the fully irreducible vertex Λ

In order to gain further insight into the nature of the divergences of the irreducible vertices, an investigation of the properties of the full vertex F and the fully irreducible vertex Λ is called for at the same points $(\tilde{T}, \tilde{U})$ where the divergences of $\Gamma^{\nu\nu'\omega=0}_{\mathrm{c(pp\uparrow\downarrow)}}$ take place. The upper panel of Fig. 3.5 shows a density plot of the full vertex $F_{\mathrm{c}}^{\nu\nu'\omega=0}$ for the specific temperature $T = 0.1$ at varying values of the interaction U. The first divergence of the irreducible vertex in the charge channel $\Gamma_{\mathrm{c}}^{\nu\nu'\omega}$ at this temperature is located between $U = 1.27$ and $U = 1.28$. One can deduce from the density plot and the frequency cut at $\nu' = \frac{\pi}{\beta}$ (lower panel of Fig. 3.5) that the full vertex F does not exhibit any qualitative change crossing the first red line in the phase diagram in Fig. 3.4. Hence, we can conclude that there is no phase transition associated with the divergence line of Fig. 3.4, because a divergence of F is necessary for making the physical χ divergent (see Eq. (2.31)). Given this result for the full vertex F and the divergence in the irreducible charge vertex Γ_{c}, the parquet Eq. (2.28) dictates the behavior of the fully irreducible vertex $\Lambda_{\mathrm{c}}^{\nu\nu'\omega=0}$: as F does not show any qualitative change crossing the divergence line, Λ also has to diverge in order to equalize the divergence in Γ_{c} to leave F qualitatively unchanged. Fig. 3.6 shows that this is indeed the case: One can see that the low-frequency divergences of $\Gamma_{\mathrm{c}}^{\nu\nu'\omega}$ also persist at this most fundamental level of the 2P diagrammatics, i.e., the fully irreducible vertex Λ. Increasing the coupling strength from $U = 1.27$

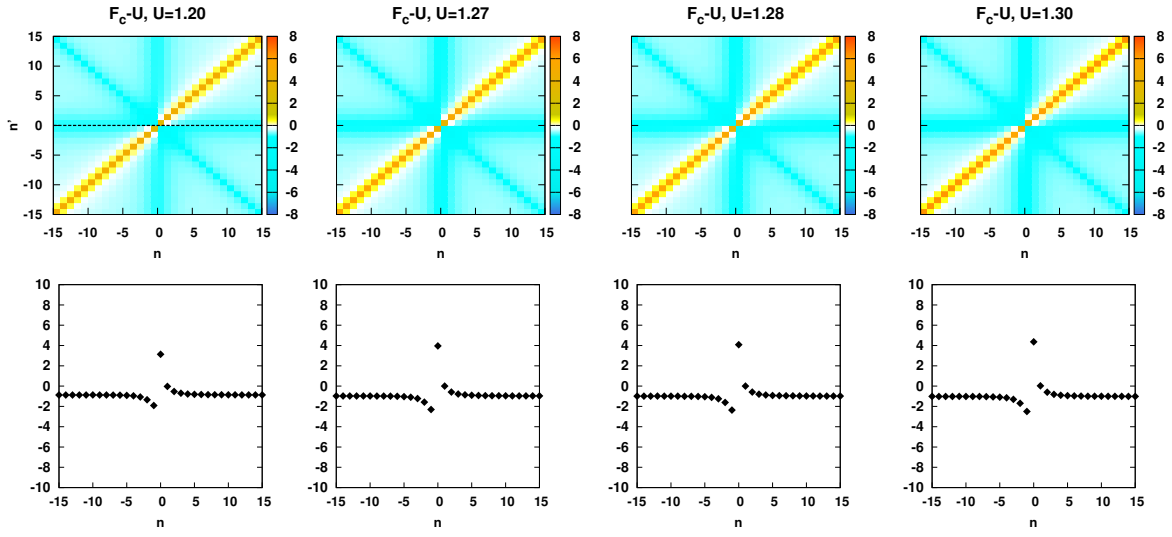

Figure 3.5: Upper panel: density plot of the full vertex $F_{\mathrm{c}}^{\nu\nu'\omega=0} - U$ in the vicinity of the first divergence line (red line) of Fig. 3.4 at $T = 0.1$. Lower panel: frequency cut of the density plot shown in the upper panel at frequency $\nu' = \frac{\pi}{\beta}$. One cannot observe any qualitative change crossing the line.

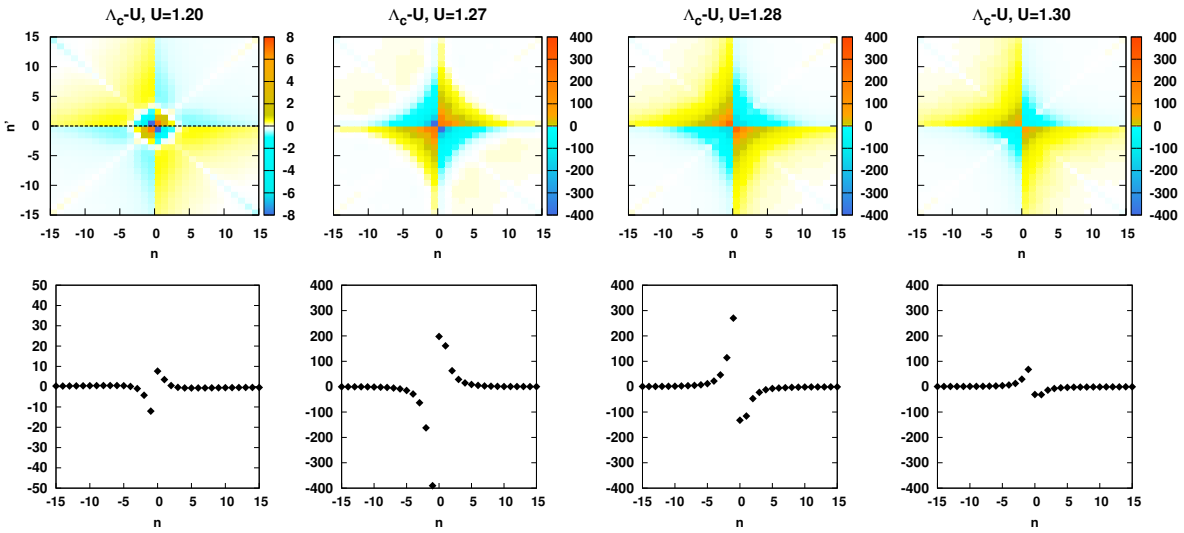

Figure 3.6: Upper panel: density plot of the fully irreducible vertex $\Lambda_{\mathrm{c}}^{\nu\nu'\omega=0} - U$ in the vicinity of the first divergence line (red line) of Fig. 3.4 and $T = 0.1$. Lower panel: frequency cut of the density plot shown in the upper panel at frequency $\nu' = \frac{\pi}{\beta}$. The low-frequency divergences of $\Gamma_{\mathrm{c}}^{\nu\nu'\omega=0}$ persist at this level of the diagrammatics.

to $U = 1.28$ in this case results in a divergence and change of sign of the low-frequency structure of the fully irreducible vertex in complete analogy to the ones obtained for the irreducible vertex. Considering the fully irreducible vertex as the most fundamental vertex function, one could even argue that these divergences have their origin in the divergence of $\Lambda_{\mathrm{c}}^{\nu\nu'\omega}$. This relation will be further analyzed in the case of the atomic limit in Sec. 3.2.2.2.

3.2.2 Divergences in the atomic limit of the Hubbard model

As one can see in the upper right part of the phase diagram in Fig. 3.4 the divergence lines of Γ_{r} can be followed up to high values of $(\tilde{T}, \tilde{U})$, even to the limit of negligibly small bandwidth ($D \to 0$, atomic limit), where the only remaining energy scale of the system can be expressed by the ratio U/T. The atomic limit is extremely useful for gaining further insight into the structure of the divergences presented in the previous section, because in this limit analytic formulas for the full vertex F are known, so that all two-particle quantities can be calculated exactly [51, 56, 84, 89]. Exploiting the analytic form of the full vertex F_{c}, in Se.c 3.2.2.1 the structure of the eigenvalues and eigenvectors of the generalized susceptibilities χ_{r} is analyzed, obtaining a first classification of the different lines. In Sec. 3.2.2.2 the fully irreducible vertex Λ is decomposed via the parquet equation (2.28) and Bethe-Salpeter equations (2.29) (parquet decomposition) at the first and second divergence point of Γ_{c} in the atomic limit in order to identify the specific contribution of its constituents.

3.2.2.1 Structure of the eigenvectors of the generalized susceptibilities χ_{r}

In the limit $D = 0$ the (completely local) one and two-particle Green functions F and G can be calculated analytically [51,56,84,89] and obviously coincide for the Hubbard and Anderson impurity model. Therefore all the two-particle quantities introduced in Sec. 2.3.1 can be calculated exactly in this limit. Starting the analysis of the generalized susceptibility in the charge channel $\chi_{\mathrm{c}}^{\nu\nu'(\omega=0)}$ in the atomic limit [56], one can notice that most of the terms depend on ν^2 and ν'^2 rather than on ν and ν', leading to the symmetry transformation $\nu \to -\nu$ and $\nu' \to -\nu'$. This suggests the possible ansatz for the eigenvector connected with vanishing eigenvalues $\lambda_{\mathrm{c},\bar{\nu}} = 0$ of $\chi_{\mathrm{c}}^{\nu\nu'(\omega=0)}$ [56]:

$$e_{\mathrm{c},\bar{\nu}} = \frac{1}{\sqrt{2}} \left[\delta_{\nu\bar{\nu}} - \delta_{\nu(-\bar{\nu})}\right], \tag{3.1}$$

where $\bar{\nu}$ is an arbitrary fixed fermionic Matsubara frequency. One should recall that a divergence of the irreducible vertex Γ_{r} is caused by an eigenvalue of the corresponding generalized susceptibility χ_{r} passing zero, because these two quantities are connected via a simple matrix inversion. By inserting this ansatz (3.1) into the eigenvalue equation, one can see that all parts of $\chi_{\mathrm{c}}^{\nu\nu'\omega=0}$ which are invariant under $\nu \to -\nu$ and $\nu' \to -\nu'$ vanish when acting on the eigenvector, so that only contributions proportional to $\delta_{\nu\nu'}$ and $\delta_{\nu(-\nu')}$ survive. These give

$$\sum_{\nu'} \chi_{\mathrm{c}}^{\nu\nu'\omega=0} e_{\mathrm{c},\bar{\nu}}(\nu') = \underbrace{\beta \frac{\bar{\nu}^2 - \frac{3U^2}{4}}{(\bar{\nu}^2 + \frac{U^2}{4})^2}}_{\lambda_{\mathrm{c},\bar{\nu}}} e_{\mathrm{c},\bar{\nu}}(\nu), \tag{3.2}$$

so that the condition for a vanishing eigenvalue $\lambda_{\mathrm{c},\bar{\nu}} \stackrel{!}{=} 0$ can be expressed as

$$\bar{\nu} = \frac{\pi}{\tilde{\beta}}(2\bar{n}+1) = \frac{\sqrt{3}\tilde{U}}{2} \quad \Leftrightarrow \quad \frac{\tilde{T}}{\tilde{U}} = \frac{\sqrt{3}}{2\pi} \frac{1}{2\bar{n}+1}. \tag{3.3}$$

The values of these ratios are listed in red on the right-hand side of Fig. 3.4, where one can also see that the slope of the extrapolated first divergence line of $\Gamma_{\mathrm{c}}^{\nu\nu'\omega=0}$ of DMFT coincides with the ratio Eq. (3.3) with $\bar{n} = 0$. One should note, however, that the ansatz of Eq. (3.1) is not the only one causing $\lambda_{\mathrm{c},\bar{\nu}}$ to pass zero.

Performing a similar analysis for the particle-particle up-down channel one arrives at the follow-

ing form of the eigenvector of $\chi_{\text{pp},\uparrow\downarrow}^{\nu\nu'\omega=0}$ in the atomic limit:

$$e_{\text{pp},\uparrow\downarrow}(\nu) = 2B\cos\left(\frac{\beta B}{2}\right)\sqrt{\frac{2B}{\beta[\beta B - \sin(\beta B)]}}\frac{1}{\nu^2 - B^2}, \tag{3.4}$$

with a real positive constant B, which leads to a vanishing eigenvalue $\lambda_{\text{pp},\uparrow\downarrow}$ in this channel. Inserting this ansatz into the eigenvalue equation of the generalized susceptibility in the particle-particle up-down channel leads to an infinite set of transcendental equations (from which only two are independent) for the two real positive variables $\tilde{U}/\tilde{T}$ and B. After further simplification these equations read

$$\frac{\tilde{T}}{\tilde{U}} = -\frac{\tan(B/2)}{2B}, \qquad B = \frac{\sqrt{-1+3e^{U/2}}U}{2\sqrt{1+e^{U/2}}} \tag{3.5}$$

They can be solved numerically and give the orange ratio values on the right-hand side of Fig. 3.4 and confirming the high-temperature behavior of the orange lines therein, where both Γ_{r} and $\Gamma_{\text{pp},\uparrow\downarrow}$ diverge.

To locate the region of the phase diagram where the divergences become essentially captured by the atomic limit description one can calculate the DMFT-result of the eigenvector $e_{\text{c},\bar{\nu}}$ associated with the first zero eigenvalue at finite temperature. Specifically, Fig. 3.7 shows the evolution of the corresponding eigenvector of[4] $\chi_{\text{c}}^{\nu\nu'\omega=0}$ from the atomic limit to finite U and low temperatures following the first divergence line of $\Gamma_{\text{c}}^{\nu\nu'\omega=0}$. One can notice that within the region where the divergence curve in the phase diagram can be approximated well by a straight line and the eigenvector of $\chi_{\text{c}}^{\nu\nu'\omega=0}$ can be quite well estimated by the ansatz in Eq. (3.1). On the other hand, for lower temperatures and smaller interactions, its frequency structure deviates significantly from the delta-peaked one of Eq. (3.1).

3.2.2.2 Parquet decomposition of the fully irreducible vertex Λ_{c}

As already mentioned in Sec. 3.2.1 the divergences of the irreducible vertices Γ_{r} root at a "deeper" level of the diagrammatics, i.e. they are associated with the divergence of the fully irreducible vertex Λ. In order to demonstrate this, one can start from the Bethe-Salpeter Eq. (2.29) and the parquet Eq. (2.28). By combining them one arrives at the following explicit decomposition of the fully irreducible vertex into different channels:

$$\begin{aligned}\Lambda_{\text{c}}^{\nu\nu'\omega} = \Gamma_{\text{c}}^{\nu\nu'\omega} + \Phi_{\text{c}}^{\nu(\nu+\omega)(\nu'-\nu)} + \frac{3}{2}\Phi_{\text{s}}^{\nu(\nu+\omega)(\nu'-\nu)} \\ -\frac{1}{2}\Phi_{\text{singlet}}^{\nu\nu'(\nu+\nu'+\omega)} - \frac{3}{2}\Phi_{\text{triplet}}^{\nu\nu'(\nu+\nu'+\omega)}\end{aligned} \tag{3.6}$$

[4] Actually, in order to increase the numerical stability of the calculations, the eigenvector of $(\chi_{\text{c}}/\chi_0)^{\nu\nu'\omega=0}$ is plotted, which coincides with the one of $\chi_{\text{c}}^{\nu\nu'\omega=0}$.

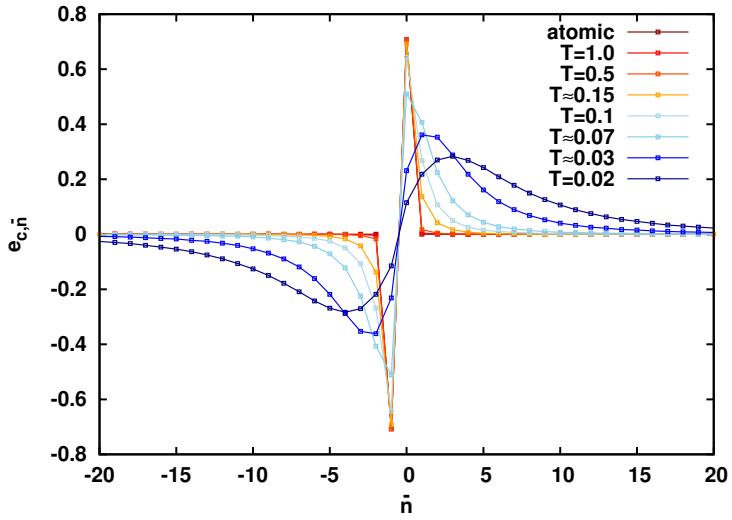

Figure 3.7: Evolution of the frequency structure of the eigenvector of $\chi_{\mathrm{c}}^{\nu\nu'\omega=0}$ associated with the first zero eigenvalue as a function of temperature and interaction along the first divergence line of Fig. 3.4, plotted as a function of the Matsubara index $\bar{n}$.

where

$$\Phi_{\mathrm{singlet}}^{\nu\nu'\omega} = \Phi_{\mathrm{pp},\uparrow\downarrow}^{\nu\nu'\omega} + \Phi_{\mathrm{pp},\uparrow\downarrow}^{\nu(\omega-\nu')\omega} \tag{3.7}$$

$$\Phi_{\mathrm{triplet}}^{\nu\nu'\omega} = \Phi_{\mathrm{pp},\uparrow\downarrow}^{\nu\nu'\omega} - \Phi_{\mathrm{pp},\uparrow\downarrow}^{\nu(\omega-\nu')\omega} \tag{3.8}$$

are the reducible particle-particle vertices in singlet and triplet channel respectively [51]. For convenience one can introduce the following notation for the single terms in Eq. (3.6) when fixing the bosonic and one fermionic frequency in order to obtain a frequency cut:

$$\Lambda_{\mathrm{c}}^{\nu(\nu'=\pi/\beta)(\omega=0)} =: \Gamma_{\mathrm{c}}^{\nu} + \Phi_{\mathrm{c}}^{\nu} + \frac{3}{2}\Phi_{\mathrm{s}}^{\nu} - \frac{1}{2}\Phi_{\mathrm{singlet}}^{\nu} - \frac{3}{2}\Phi_{\mathrm{triplet}}^{\nu} \tag{3.9}$$

Based on the results of the previous sections one expects that crossing (i) the **first divergence** line, the low frequency structure of Γ_{c} and Λ_{c} both change sign and crossing (ii) the **second divergence** line, additionally (at least one of) the pp-channels should show a qualitative change. In both cases the spin channels should at most display quantitative changes increasing the interaction value.

In the atomic limit the frequency-cut of the decomposition of the fully irreducible vertex indeed displays this behavior as can be seen in Fig. 3.8 and 3.9 at an interaction value before and after the first and second divergence line of the phase diagram respectively. Starting at an interaction value of $U/T = 3.62$, by inspecting Fig. 3.8 (red lines and crosses), one observes that at low frequen-

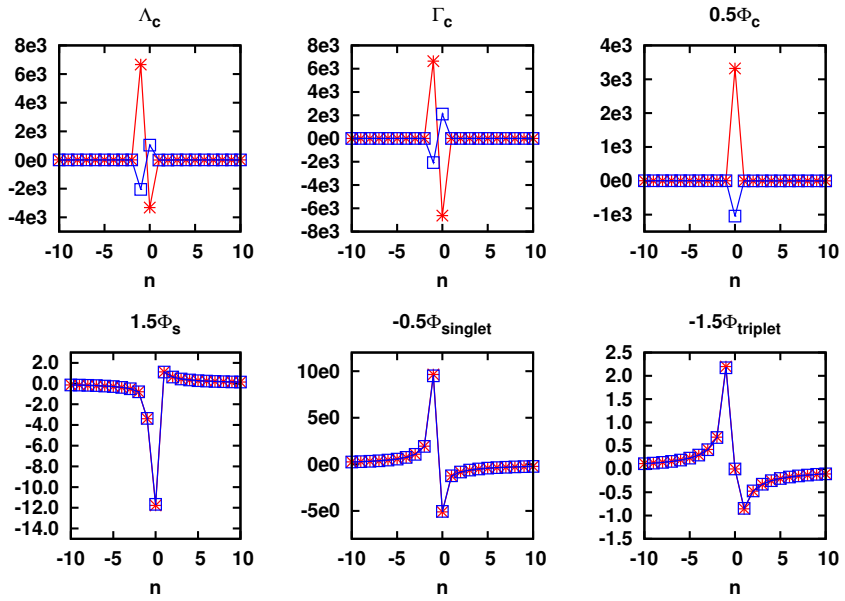

Figure 3.8: Parquet decomposition of the fully irreducible vertex Λ_c in the atomic limit before ($U/T = 3.62$, red lines and crosses) and after ($U/T = 3.63$, blue lines and boxes) the point of the first divergence of $\Gamma_c^{\nu\nu'\omega=0}$ at $\tilde{U}/\tilde{T} = 2\pi/\sqrt{3} \approx 3.628$.

cies the irreducible charge vertex Γ_c is strongly enhanced and that this enhancement is positive for negative Matsubara frequencies and vice versa. Crossing the divergence line to $U/T = 3.63$, this low-frequency structure changes sign as discussed previously (blue lines and boxes). The same behavior can be observed for the fully irreducible vertex Λ_c in this case. A similar enhanced feature also appears in the reducible charge vertex Φ_c, whereas for the particle-particle as well as the magnetic reducible vertices (not explicitly shown), instead, crossing the divergence line does not have a qualitative impact.

Turning to the second divergence line shown in Fig. 3.9, not only the irreducible and reducible charge vertices exhibit an enhancement and change of sign when increasing the interaction value from $U/T = 5.13$ (red lines and crosses) to $U/T = 5.14$ (blue lines and boxes). Also, simultaneously, the ones in the particle-particle up-down channel (which is incorporated in the singlet channel) show a strong enhancement and change of sign in the low-frequency structure. On the other hand both spin and triplet channel do not show any qualitative change passing the second divergence line.

In the following section, the influence of these vertex divergencies on a method, which (in a quite straightforward) manner, aims at the unambiguous identification of scattering processes affecting physical one-particle spectra, the so-called parquet decomposition of the self-energy, will be

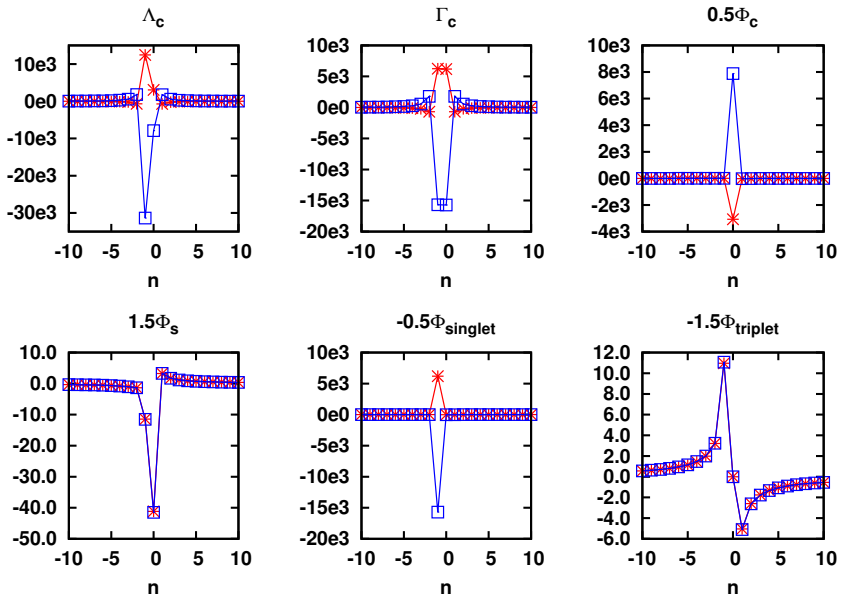

Figure 3.9: Parquet decomposition of the fully irreducible vertex Λ_c in the atomic limit before ($U/T = 5.13$, red lines and crosses) and after ($U/T = 5.14$, blue lines and boxes) the point of the second divergence of $\Gamma_c^{\nu\nu'\omega=0}$ and the first divergence of $\Gamma_{pp\uparrow\downarrow}^{\nu\nu'\omega=0}$ at $\tilde{U}/\tilde{T} \approx 5.135$.

shown.

3.3 Parquet decomposition of the electronic self-energy

Parts of this section (marked by a vertical sidebar) have already been published in the *APS journal* Phys. Rev. B **93**, 245102 (2016).

The purpose of this section is (i) to develop methods that improve the physical interpretation of the self-energy results in strongly correlated systems, and (ii) to understand how the correlated physics is actually captured by diagrammatic approaches beyond the perturbative regime. Here, this is achieved by applying a parquet-based diagrammatic decomposition to the self-energy. Specifically, DMFT and DCA results are used for this parquet decomposition, thus avoiding any perturbative approximation for the vertex. The method is applied to the Hubbard model on cubic (three dimensional, $3d$) and square (two-dimensional, $2d$) lattices. In these cases, quite a bit is already known about the physics, which, to some extent, allows for a check of the methodology.

It is recalled briefly here, that in the parquet schemes two-particle diagrams are classified according to whether they are **two-particle reducible (2PR)** in a certain channel, i.e., whether a diagram can be split in two parts by only cutting two Green's functions, or are fully irreducible at the two-particle level (2PI). Diagrams reducible in a particular channel can then be related to spe-

cific physical processes. Specifically, one obtains three classes of reducible diagrams, longitudinal (ph) and transverse ($\bar{\text{ph}}$) particle-hole diagrams and particle-particle (pp) diagrams. Because of the electronic spin, the particle-hole diagrams can be rearranged, more physically, in terms of spin (magnetic) and charge (density) contributions, while for pp the $\uparrow\downarrow$ term (essential for the singlet pairing) will be explicitly kept.

In this section, the parquet equations, Bethe-Salpeter equations and the equation of motion (EOM) which relate the vertices in the different channels to each other and to the self-energy are explicitly calculated by using the 2PR and 2PI vertices of the DMFT and DCA calculations. Hence, apart from statistical errors, an "exact" diagrammatic expansion of the self-energy of DMFT ($N_c = 1$) or DCA ($N_c > 1$) clusters is obtained. Since, within the parquet formalism, the physical processes are automatically associated to the different scattering channels, these calculations can be exploited to extract an unbiased physical interpretation of DMFT and DCA self-energies and to investigate the structure of the Feynman diagrammatics beyond the perturbative regime.

One should note here that, from the merely conceptual point of view, the **parquet decomposition** is the most "natural" route to disentangle the physical information encoded in self-energies and correlated spectral functions. The parquet procedure can be compared, e.g., to the recently introduced fluctuation diagnostics approach (see [90] and Sec. 3.4), which also aims at extracting the underlying physics of a given self-energy: In the fluctuation diagnostics the quantitative information about the role played by the different physical processes is extracted by studying the different representations (e.g., charge, spin, or particle-particle), in which the EOM for the self-energy, and specifically the full two-particle scattering amplitude, can be written. Hence, in this respect, the parquet decomposition provides a more direct procedure, because it does not require any further change of representation for the momentum, frequency, spin variables, and can be readily analyzed at once, provided that the vertex functions have been calculated in an channel-unbiased way. However, as will be discussed in this section, the parquet decomposition presents also **disadvantages** with respect to the fluctuation diagnostics, because (i) it requires working with 2PI vertices, which makes the procedure somewhat harder from a numerical point of view, and (ii) it faces intrinsic instabilities for increasing interaction values.

By applying this procedure to the 2d Hubbard model at intermediate values of U (of the order of half the bandwidth), large contributions from spin-fluctuations are found. This is consistent with a common belief that $\vec{q} = (\pi, \pi)$ spin fluctuations are very important for the physics, as well as with the fluctuation diagnostics results [90]. For the 3d Hubbard model similar physics was first proposed by Berk-Schrieffer [91]. Later spin fluctuations have been proposed to be important for the 2d Hubbard model and similar models by many groups [92–95]. It should be noted, however, that the contributions of the other channels to the parquet decomposition are not small by themselves.

Rather, the other (non-spin) channel contributions to $\Sigma(\vec{k}, i\nu)$ appear to play the role of "screening" the electronic scattering originated by the purely spin-processes. The latter would lead, otherwise, to a significant overestimation of the electronic scattering rate. At larger values of U the parquet decomposition starts displaying strong oscillation at low-frequencies in all its term, *but* the spin contribution. Physically, this might be an indication that the spin fluctuations also predominate in the non-perturbative regime, where, however, the parquet distinction among the remaining (secondary) channels loses its physical meaning. The reason for this can be traced back to the occurrence of **singularities in the generalized susceptibilities of these (secondary) channels**. Such singularities are reflected in the corresponding divergencies of the two-particle irreducible vertex functions (see Sec. 3.1.1), in the DMFT solution of the Hubbard and Falicov-Kimball models [96–102]. Here the study of their origin is extended and the results of Sec. 3.1.1 are extended to DCA.

The results of the following section are relevant also beyond the specific problem of the physical interpretation of the self-energy. In fact, the parquet decomposition can be also used to develop new quantum many-body schemes. Wherein some simple approximation might be introduced for the irreducible diagrams that are considered to be particularly fundamental. The parquet equations are then used to calculate the reducible diagrams. In the results presented in this section, however, for strongly correlated systems the contribution to the self-energy from the irreducible diagrams diverges for certain values of U both in DMFT and DCA. This makes the derivation of good approximations for these diagrams for strongly correlated systems rather challenging. It remains, however, an interesting question if the parquet decomposition can be modified in such a way that these problems are avoided.

3.3.1 The parquet decomposition method

By using the Dyson-Schwinger equation of motion (2.27), the electronic self-energy Σ can be expressed in terms of the two-particle vertex function. The equation of motion for Σ is a well-known, general relation of many-body theory with a two-particle interaction. However, valuable information may be obtained by inserting the parquet decomposition of Eq. (2.28) into the equation of motion (2.27) and, in particular, its specific expression for $F_{\uparrow\downarrow}^{kk'q}$:

$$F_{\uparrow\downarrow}^{kk'q} = \Lambda_{\uparrow\downarrow}^{kk'q} + \Phi_{pp,\uparrow\downarrow}^{kk',k+k'+q} + \frac{1}{2}\Phi_{\mathrm{c}}^{kk'q} - \frac{1}{2}\Phi_{\mathrm{s}}^{kk'q} - \Phi_{\mathrm{s}}^{k,k+q,k'-k}. \tag{3.10}$$

This way, *after* all internal summations are performed, the expression for Σ is naturally split in four terms:

$$\Sigma = \tilde{\Sigma}_{\Lambda} + \tilde{\Sigma}_{\mathrm{pp}} + \tilde{\Sigma}_{\mathrm{c}} + \tilde{\Sigma}_{\mathrm{s}} \tag{3.11}$$

evidently matching the corresponding 2PI and 2PR terms of Eq. (3.10): This represents the **parquet decomposition of the self-energy**. In fact, the four terms in Eq. (3.11) describe the contribution of the different channels (pp, charge, spin), as well as of the 2PI scattering processes, to the self-energy. Since each scattering channel is associated with definite physical processes, Eq. (3.11) can be exploited, in principle, for gaining a better understanding of the physics underlying a given self-energy calculation.

In the following section, this idea will be applied to specific cases of interest. In particular, the performance of a parquet decomposition of the self-energy is tested in the cases of the three and two-dimensional Hubbard model on a simple cubic/square lattice (see Eq. (2.6)). For the sake of definiteness, $t = 0.25$ eV for the $2d$ case, and $t = \frac{1}{2\sqrt{6}} \simeq 0.204$ eV for the 3d case. This choice ensures that the standard deviation (D) of the non-interacting DOS of the square and the cubic lattices considered is exactly the same ($D = 1$eV), and thus allows for a direct comparison of the U values used in the two cases, provided they are expressed in units of D. This Hamiltonian constitutes an important testbed case for applying the idea of a parquet decomposition, since Eq. (2.6) provides a quintessential representation of a strongly correlated system. Moreover, in the 2d case Eq. (2.6) is frequently adopted, e.g., to study the still controversial physics of cuprate superconductors [103, 104]. In this framework, please note that typical values for U are about $U = 8|t| = 2$eV, i.e., U is equal to the non-interacting bandwidth $W = 8|t|$. This choice corresponds to a rather strong correlation regime, as it is clearly seen even in a purely DMFT context [105]. In this section, however, also smaller values of U, of the order of half bandwidth, are considered, corresponding to a regime of more moderate correlations.

3.3.2 Parquet decomposition calculations

In this section the parquet decomposition of an electron self-energy computed by DMFT and DCA is studied (see Sec. 2.2 and 2.2.4.1). In these non-perturbative methods a cluster with N_c sites is embedded in a self-consistent electronic bath. The calculation of a generalized susceptibility is rather time-consuming when compared against computing only single-particle quantities. For this reason the calculations are restricted to the tractable values of $N_c = 1$ (DMFT), 4 and 8 (DCA). The results are therefore not fully converged with respect to N_c, but, nevertheless, will illustrate well the specific points made in the following sections. The cluster problem has been solved using both Hirsch-Fye and continuous time (CT) methods (see Sec. 2.2.2.3).

3.3.2.1 DMFT results

Consistent with the discussion of the previous section, the Dyson-Schwinger equation of motion (2.27) will be used together with Eq. (3.11) to express the self-energy in terms of contributions from

the different parquet channels. Starting to apply the parquet decomposition to the easier case of the DMFT self-energy, in particular, the focus will be on one of the most studied cases in DMFT, the half-filled Hubbard model in $3d$, where DMFT describes a Mott-Hubbard metal-insulator transition at a finite $U = U_{\mathsf{MIT}}$. The specific parameters in Eq. (2.6) have been chosen in this case as follows: $n = 1$ (half-filling) and $\beta = 26$ eV^{-1}. The results of the parquet decomposition of the DMFT self-energy are shown in Fig. 3.10 in the weak-to-intermediate coupling regime $U \ll U_{\mathsf{MIT}} \sim 3$ eV. The plots show the imaginary part of the DMFT self-energy (solid black line) as a function of the Matsubara frequencies iν and for two different values of U (one should recall that Σ does not depend on momentum in DMFT, and that in a particle-hole symmetric case, as the one we consider here, it does not have any real part beyond the constant Hartree term).

By computing the DMFT generalized local ($N_c = 1$) susceptibility of the associated impurity problem, and proceeding as described in the previous section, Im $\Sigma(i\nu)$ is actually decomposed into the four contributions from terms in Eq. (3.11), depicted by different colors/symbols in the plots. Before analyzing their specific behaviors, please note that their sum (gray dashed line) does reproduce precisely the value of Im Σ directly computed in the DMFT algorithm. Since all the four terms of Eq. 3.11 are calculated independently from the parquet-decomposed equation of motion, this result represents indeed a stringent test of the numerical stability and the algorithmic correctness of our parquet decomposition procedure. Given the number of steps involved in the algorithm, illustrated in the previous section, the fulfillment of such a self-consistency test is particularly significant, and, indeed, it has been verified for all the parquet decomposition calculations presented in this section.

By considering the most weak-coupling data first ($U = 0.5$eV, left panel of Fig. 3.10), one can notice that the 2PI contribution (Σ_Λ in Eq. (3.11), plum-colored open squares in the Figure) lies almost on top of the "exact" DMFT self-energy. At weak-coupling this is not particularly surprising, because $\Lambda_{\uparrow\downarrow} \simeq U + O(U^4)$, while all the 2PR contributions are at least $O(U^2)$. Hence, when the 2PI vertex is inserted into the equation of motion, $\tilde{\Sigma}_\Lambda$ simply reduces to the usual second-order perturbative diagram. In this situation (i.e., Im $\Sigma(i\nu) \simeq \tilde{\Sigma}_\Lambda$), it is interesting to observe that the other **sub-leading contributions** (spin, particle-particle scattering and charge channel) are not fully negligible. Rather, they **almost exactly compensate each other**: the extra increase of the scattering rate [i.e.: -Im $\Sigma(i\nu \to 0)$] due to the spin-channel is compensated (or "screened") almost perfectly by the charge- and the particle-particle channel.

Not surprisingly, the **validity of this cancellation is gradually lost by increasing U.** At $U = 1.0$ (right panel of Fig. 3.10), which is still much lower than U_{MIT}, one observes that the 2PI contribution no longer provides so accurate values for Im $\Sigma(\nu)$. At the same time, the contributions of all scattering channels increase: the low-frequency behavior of the spin channel now would provide -taken on its own- a scattering rate even larger than the true one of DMFT. Consistently, a correspondingly

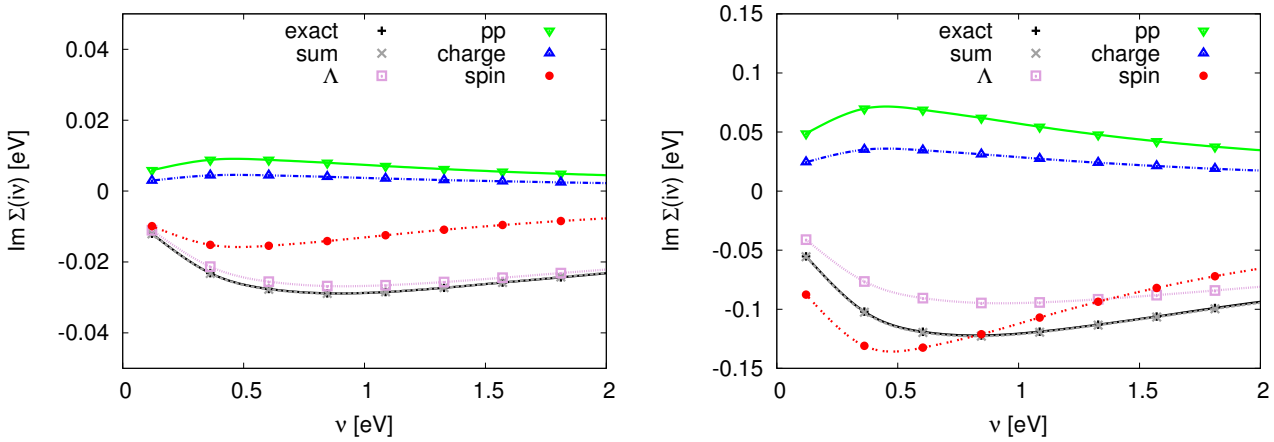

Figure 3.10: Parquet decomposition of the DMFT self-energy $\Sigma(\nu)$ of the $3d$ Hubbard model at half-filling ($n = 1$). The full (black, "exact") and dashed (gray, "sum") lines show Σ as computed in DMFT, and as the sum of the parquet contributions, respectively. The colored symbols display the different contributions to $\Sigma(\nu)$ according to Eq. (3.11). The parameters of the calculation are: $N_c = 1$ (DMFT), $t = \frac{1}{2\sqrt{6}} \simeq 0.204$ eV, $\beta = 26$ eV^{-1} with two different values of the Hubbard interaction: $U = 0.5$ eV (left panel), $U = 1$ eV (right panel).

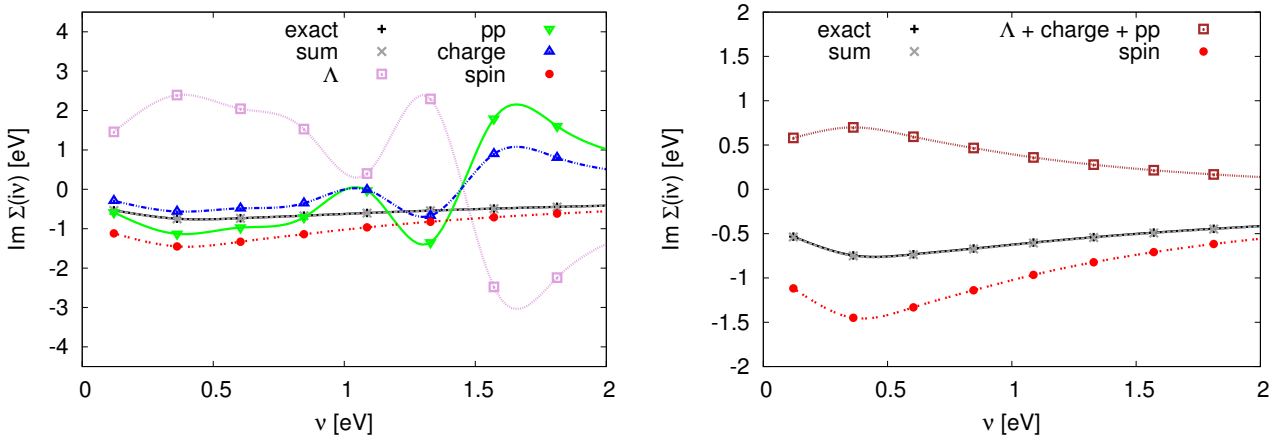

Figure 3.11: left panel: Parquet decomposition of the DMFT self-energy $\Sigma(\nu)$ as in Fig. 3.10, but with $U = 2$ eV. Right panel: Bethe-Salpeter decomposition in the spin channel of the same DMFT self-energy.

larger compensation of the charge and the particle-scattering channels contribution is observed. At higher frequency, these changes with respect to the previous case are mitigated, matching the intrinsic perturbative nature of the high-frequency/high-T expansions [56, 80, 106].

The situation described above, which suggests an important role of spin fluctuations, partially screened by charge and particle-particle scattering processes, displays important changes at

intermediate-to-strong coupling U. This is well exemplified by the data reported in Fig. 3.11 (left panel). Despite the DMFT self-energy still displays a low-frequency metallic bending ($U = 2.0$ is on the metallic side of the DMFT MIT), in the low-frequency region one observes the appearance of a huge oscillatory behavior in the parquet decomposition of Σ: All contributions to Im Σ, *but* the spin term, are way larger than the self-energy itself and fluctuate so strongly in frequency, that several changes of sign are observed. This makes it obviously very hard to define any kind of hierarchy for the impact of the corresponding scattering channels on the final self-energy result.

Hence, at these intermediate-to-strong values of U the parquet decomposition procedure appears to be no longer able to fully disentangle the physics underlying a given (here: DMFT) self-energy. At the same time, one should stress that the strong oscillations visible in the parquet decomposition of Fig. 3.11 can *not* be ascribed to numerical accuracy issues. In fact, one observes, that, also in this problematic case, the self-consistency test works as well as for the other data sets: the total sum of such oscillating contributions, still reproduces the Im $\Sigma(\nu)$ from DMFT in the whole frequency range considered. The reason of such a behavior has to be traced back, instead, to the divergencies of the 2PI vertices reported in DMFT in Sec. 3.1.1. It is worth stressing here, that there is only one contribution to $\Sigma(\nu)$, which never displays wild oscillation, even for intermediate-to-strong U: the spin channel. This means that even when the parquet decomposition displays a strong oscillatory behavior, a Bethe-Salpeter decomposition in this specific (spin) channel will always remain well-behaved and meaningful. This is explicitly shown in Fig. 3.11 (right panel), where all the contributions to $\Sigma(\nu)$, but $\tilde{\Sigma}_{\mathrm{s}}$, (i.e., formally: all the contributions 2PI in the spin channel) are summed together: Here no oscillation is visible. The results of such Bethe-Salpeter decomposition of $\Sigma(\nu)$ in the spin channel suggests then again an interpretation of a physics dominated by this scattering channel, though -this time- in the non-perturbative regime: Strong (local) spin fluctuations, originated by the progressive formation of localized magnetic moments, are responsible for the major part of the electronic self-energy and scattering rate. Their effect is, as before, partly reduced, or screened, by the scattering processes in the other channels (opposite sign contribution to Im Σ). Differently as before, however, the specific role of the "secondary" channels can no longer be disentangled via the parquet decomposition.

3.3.2.2 DCA results

In this subsection, the numerical results for the parquet decomposition of self-energy data computed in DCA are discussed. Different from DMFT, the DCA self-energy provides a more accurate description of finite dimensional systems, as it is also explicitly dependent on the momenta of the discretized Brillouin zone (i.e., a cluster of N_c patches in momentum space) of the DCA (see Sec. 2.2.4.1). Parquet decomposition results for the self-energy of the two-dimensional Hubbard model with hopping parameter $t = -0.25$ for different values of the density n and of the interaction U

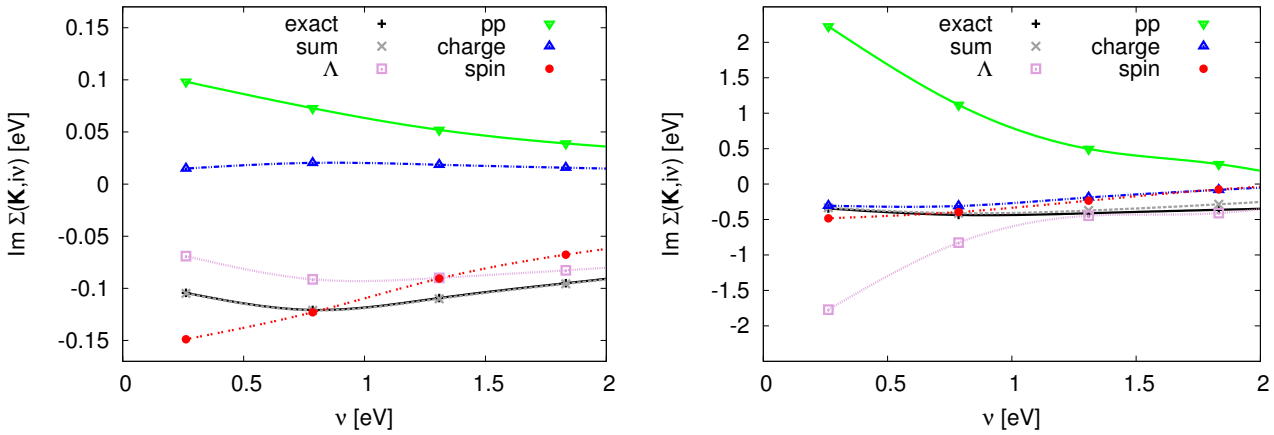

Figure 3.12: Parquet decomposition of the DCA self-energy $\Sigma[\vec{k} = (\pi, 0), \nu]$. The same convention of Fig. 3.10 is adopted. The parameters of the calculations are $N_c = 8$, $t = 0.25$ eV, $\beta = 12$ eV^{-1} and the filling is $n = 0.85$ with two different values of the Hubbard interaction: $U = 1.0$ eV (left panel), $U = 2.0$ eV (right panel)

are presented here. In particular, the focus is on the self-energy at the so called anti-nodal point, $\vec{k} = (\pi, 0)$, because it usually displays the strongest correlation effects for this model and also because the vector $\vec{k} = (\pi, 0)$ is always present in both clusters we used ($N_c = 4, 8$) in our DCA calculation. Please note, however, that the results of the parquet decomposition for the other relevant momenta of this system, i.e. the nodal one $\vec{k} = (\pi/2, \pi/2)$, (for $N_c = 8$ where it is available), are qualitatively similar.

As for the DMFT case, starting by considering a couple of significant cases at fixed density (here $n = 0.85$, corresponding to the typical 15% of hole doping of the optimally doped high-T$_c$ cuprates), and performing the parquet decomposition for different U, the left panel of Fig. 3.12 shows the calculations performed at a moderate $U = 4|t| = 1$eV (interaction equal to the semibandwidth). As one can see the results are qualitatively similar to the DMFT ones at intermediate coupling (right panel of Fig. 3.10), which one could indeed interpret in terms of predominant spin-scattering processes, partially screened by the other channels. However, also in DCA, extracting such information from the parquet decomposition becomes rather problematic for larger values of U. At $U = 8|t| = 2$ eV (interaction equal to the bandwidth: Fig. 3.12 right panel), the parquet decomposition appears dominated by contributions from the 2PI and the pp channel: These become an order of magnitude larger than the spin-channel contribution and of the total DCA self-energy. This finding, in turn, indicates the occurrence of large cancellation effects in the parquet-decomposed basis, making quite hard any further physical interpretation.

It is also instructive to look at the effect of a change in the level of hole-doping on the parquet

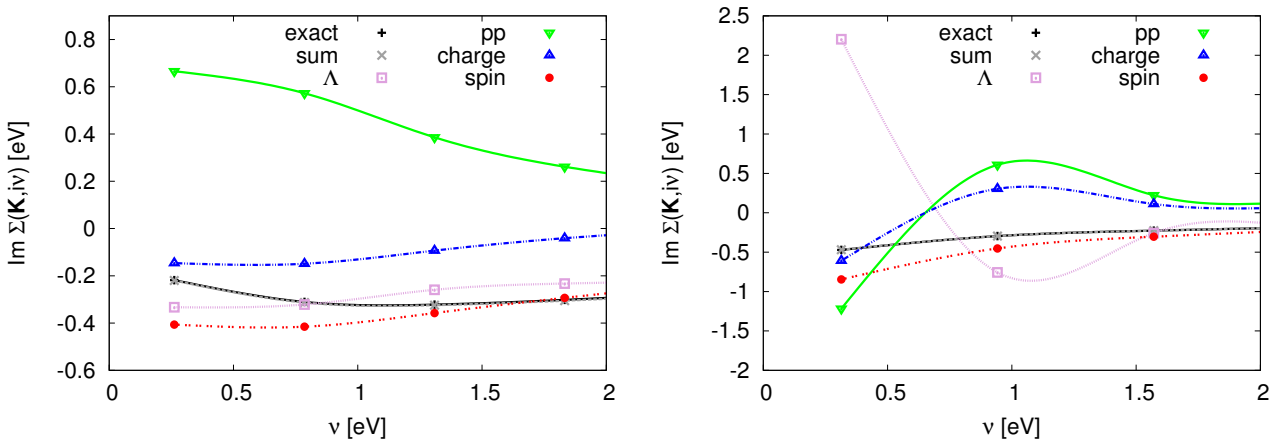

Figure 3.13: Parquet decomposition of the DCA self-energy $\Sigma[\vec{k} = (\pi, 0), i\nu]$ ($N_c = 8$) at different dopings. Left panel: high hole doped case ($n = 0.75$) for the same interaction/temperature values as in right panel of Fig. 3.12 ($U = 2$ eV and $\beta = 12$ eV^{-1}). Right panel: undoped case ($n = 1$), at intermediate-to-strong coupling ($U = 1.4$ eV and $\beta = 10$ eV^{-1}, calculated for a $N_c = 4$ DCA cluster.

decomposition calculations. This is done in Fig. 3.13: In the left panel of the figure results for the highly doped case $n = 0.75$ (25% hole doping) are shown. Despite the large value of the interaction $U = 2$ eV, this parquet decomposition looks qualitatively similar to the one at moderate coupling of the less doped case Fig. 3.12 (left panel). Conversely, at half-filling ($n = 1$, right panel of Fig. 3.13), although choosing a lower value of $U = 1.4$ eV, the parquet decomposition displays the very same large oscillations among different channel contributions observed in the DMFT data (Fig. 3.11, left panel). Hence, the parquet decomposition procedure applied to the DCA results allows for extending the considerations drawn from the DMFT analysis of the previous section: For a large enough value of U and moderate or no doping, the parquet decomposition of the self-energy becomes rather problematic, as some channel contributions (supposed to be secondary) become abruptly quite large, or even strongly oscillating, with large cancellation between different terms. The inclusion of non-local correlations within the DCA allows for the demonstration of that this is not a special aspect of the peculiar, purely local, DMFT physics, but it survives also in presence of non-local correlations. In this perspective it is interesting to investigate, whether the **singularities in the parquet decomposition,** with their intrinsically non-perturbative nature, already occur in a parameter region where the DCA self-energy displays a strong momentum differentiation, with pseudogap features. As discussed in Sec. 3.4, such a case is achieved in a $N_c = 8$ DCA calculation for e.g. $n = 0.94$ (6% hole doping), $U = 1.75$ eV, $\beta = 60$ eV$^{-}1$ (with the additional inclusion of a realistic next-to-nearest hopping term $t' = 0.0375$ eV). In the left panels of the Fig. 3.14 the DCA self-energy for the anti-nodal and the nodal momentum is shown, together with its corresponding parquet decomposition. Please note, as it was also stated in Ref. [90], that

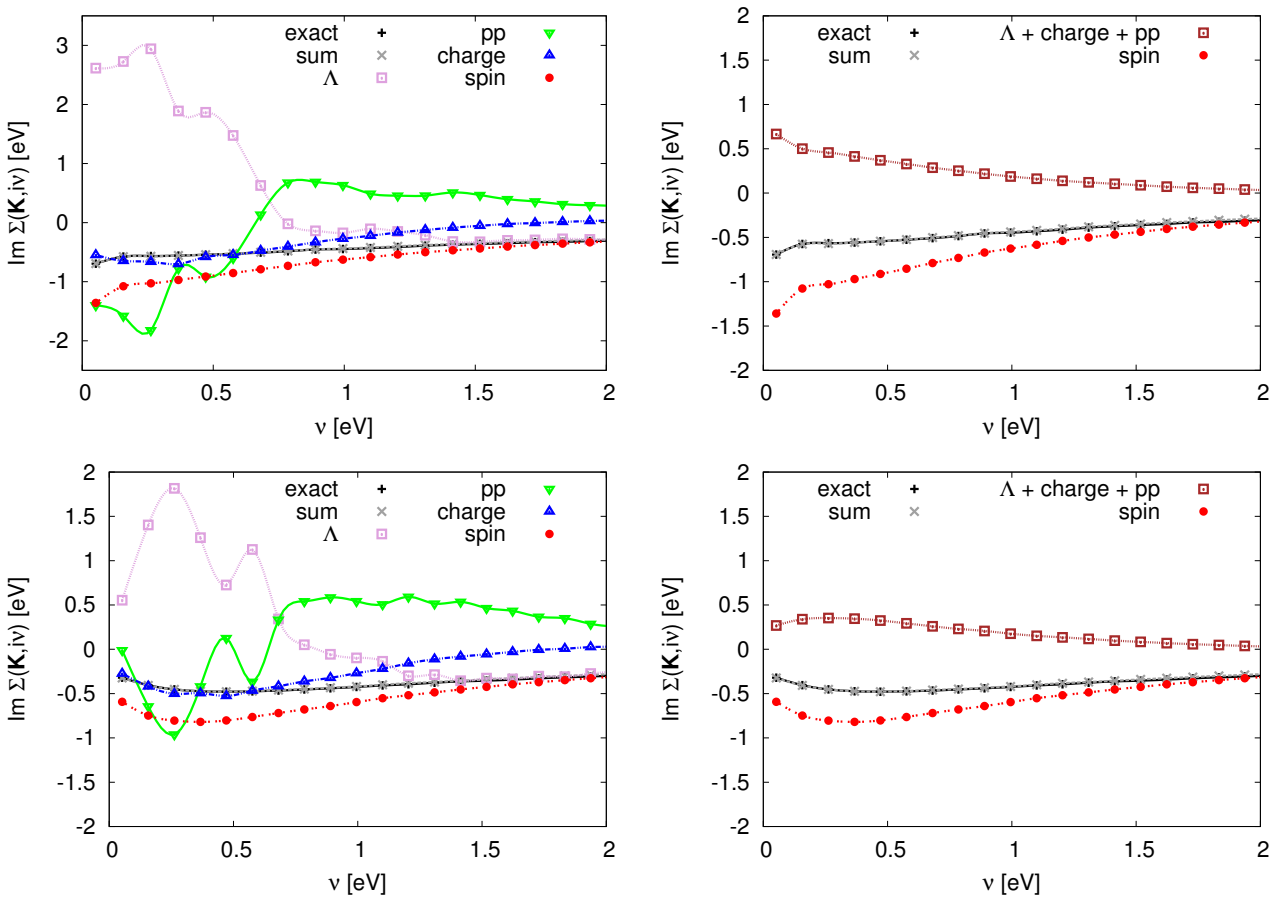

Figure 3.14: Parquet decomposition of the DCA self-energy $\Sigma[\vec{k}, i\nu]$ with $N_c = 8$ for the low-T, underdoped case $n = 0.94$ with $U = 1.75$ eV and $\beta = 60$ eV^{-1} (see text). Left upper panel: parquet decomposition for the antinodal DCA self-energy [$\vec{k} = (\pi, 0)$]; right upper panel: Bethe-Salpeter decomposition of the antinodal DCA self-energy. Left lower panel: parquet decomposition of the nodal[$\vec{k} = (\frac{\pi}{2}, \frac{\pi}{2})$] DCA self-energy. Right lower panel: Bethe-Salpeter decomposition of the nodal DCA self-energy.

the positive (i.e., non Fermi-liquid) slope of Im $\Sigma(\vec{k}, i\nu)$ in the lowest frequency region for $\vec{k} = (\pi, 0)$ indicates a pseudogap spectral weight suppression at the antinode. The parquet decomposition of the two self-energies is, however, very similar: The strong oscillations of the various channels clearly demonstrate that in the parameter region where a pseudogap behavior is found in DCA, the parquet decomposition displays already strong oscillations. It is also interesting to notice that, similarly as is was discussed in the previous section, also in this case, the spin channel contribution of the parquet decomposition is the only one displaying a well-behaved shape, with values of the order of the self-energy and no frequency oscillations. Consequently, also for the DCA self-energy in the pseudogap regime, a Bethe-Salpeter decomposition in the spin-channel of the self-energy remains valid (see right panel of Fig. 3.14). As discussed in the previous section, this might be inter-

preted as an hallmark of the predominance of the spin-scattering processes in a non-perturbative regime, where a well-behaved parquet decomposition is no longer possible. In this perspective, the physical interpretation would match very well the conclusions derived about the origin for the pseudogap self-energy of DCA by means of the recently introduced fluctuation diagnostics method (see Sec. 3.4). At present, hence, the post processing of a given numerical self-energy provided by the fluctuation diagnostics procedure appear the most performant, because -differently from the parquet decomposition- it remains applicable, without any change, also to non-perturbative cases (see following Sec. 3.4).

3.4 Fluctuation diagnostics

Parts of this section (marked by a vertical sidebar) have already been published in the APS journal Phys. Rev. Lett. **114**, 236402 (2016).

Correlated electron systems display some of the most fascinating phenomena in condensed matter physics, but their understanding still represents a formidable challenge for theory and experiments. For photo-emission [107] or STM [108,109] spectra, which measure single-particle quantities, information about correlation is encoded in the electronic self-energy Σ. However, due to the intrinsically many-body nature of the problems, even an exact knowledge of Σ is not sufficient for an unambiguous identification of the underlying physics. A perfect example of this is the pseudogap observed in the single-particle spectral functions of underdoped cuprates [110], and, more recently, of their nickelate analogues [111]. Although relying on different assumptions, many theoretical approaches provide self-energy results compatible with the experimental spectra. This explains the lack of a consensus about the physical origin of the pseudogap: In the case of cuprates, the pseudogap has been attributed to spin-fluctuations [93,112–115], preformed pairs [116–120], Mottness [121,122], and, recently, to the interplay with charge fluctuations [123–126] or to Fermi-liquid scenarios [127]. The existence and the role of ($d-$wave) superconducting fluctuations [116–120] in the pseudogap regime are still openly debated for the basic model of correlated electrons, the Hubbard model.

Experimentally, the clarification of many-body physics is augmented by a **simultaneous investigation at the two-particle level**, i.e., via neutron scattering [128], infrared/optical [129] and pump-probe spectroscopy [130], muon-spin relaxation [131], and coincidence two-particle spectroscopies [132–134]. Analogously, theoretical studies of Σ can also be supplemented by a corresponding analysis at the two-particle level. In this section, the influence of the two-particle fluctuations on Σ is (again as in Sec. 3.3) studied via its equation of motion. However, this time, in order to overcome the limitations of the parquet decomposition, the method of **"fluctuation diagnostics"**

is used to identify the role played by different collective modes in the pseudogap physics.

3.4.1 The fluctuation diagnostics method

Emphasis should be put on the fact that all concepts and equations below are applicable within any theoretical approach in which the self-energy and the two-particle scattering amplitude are calculated without a priori assumptions of a predominant type of fluctuations. This includes quantum Monte-Carlo (QMC) methods (e.g., lattice QMC [136]), functional renormalization group [135], parquet approximation [61, 137, 138], and cluster extensions of the dynamical mean field theory (DMFT) (see Sec. 2.2.4.1) such as the cellular-DMFT or the dynamical cluster approximation (DCA). Within diagrammatic extensions [20, 43, 45, 46] of DMFT, the fluctuation diagnostics is applicable if parquet-like diagrams are included [46, 60, 139]. The outputs of these techniques can be then post-processed by means of the fluctuation diagnostics with a comparably lower numerical effort.

The self-energy describes all scattering effects of one added/removed electron, when propagating through the lattice. In correlated electronic systems, these scattering events originate from the Coulomb interaction among the electrons themselves, rather than from the presence of an external potential. Therefore, Σ is entirely determined by the full two-particle scattering amplitude (vertex) F (see Sec. 2.3.1). The formal relation between F and Σ is the Dyson-Schwinger equation of motion (EOM) (Eq. (2.27)), which is recalled here:

$$\Sigma(k) = \frac{Un}{2} - \frac{U}{\beta^2} \sum_{k'q} F_{\uparrow\downarrow}^{kk'q} G(k') G(k'+q) G(k+q)$$

Therein, $F_{\uparrow\downarrow}$ is the full scattering amplitude (vertex) between electrons with opposite spins: It consists of repeated two-particle scattering events in *all* possible configurations compatible with energy/momentum/spin conservation. Therefore it contains the complete information of the two-particle correlations of the system. Yet, much of the information encoded in $F_{\uparrow\downarrow}$ about the *specific* physical processes determining Σ is washed out by averaging over all two-particle scattering events, i.e., by the summations on the r.h.s. of Eq. (2.27). Hence, an unambiguous identification of the physical role played by the underlying scattering/fluctuation processes requires a "disentanglement" of the EOM. The most obvious approach would be a direct decomposition of the full scattering amplitude $F_{\uparrow\downarrow}$ of the EOM in all possible fluctuation channels, the parquet decomposition introduced in Sec. 3.3. As analyzed there, this approach works well in the weakly correlated regime (small U, large doping, high T), whereas for stronger correlations it suffers from intrinsic divergences.

In this section an alternative route that can be followed to circumvent this problem is presented.

The idea exploits the freedom of **employing formally equivalent analytical representations of the EOM.** For instance, by means of SU(2) symmetry and "crossing relations" (see, e.g., [51, 56, 140]), $F_{\uparrow\downarrow}$ in the EOM can be expressed in terms of the corresponding vertex functions of the spin/magnetic $F_{\mathsf{s}} = F_{\uparrow\uparrow} - F_{\uparrow\downarrow}$ and charge/density $F_{\mathsf{c}} = F_{\uparrow\uparrow} + F_{\uparrow\downarrow}$ sectors. Analogously, a rewriting in terms of the particle-particle sector notation is done via $F_{pp}(k, k', q) = F_{\uparrow\downarrow}(k, k', q - k - k')$. Inserting these results in the EOM and performing variable transformations, one recovers the EOM, with $F_{\uparrow\downarrow}$ replaced by F_{s}, F_{c} or F_{pp}. These three expressions,

$$\begin{aligned} \Sigma(k) - \Sigma_{\mathsf{H}} = & \quad \frac{U}{\beta^2} \sum_{k',q} F_{\mathsf{s}}^{kk'q} G(k') G(k'+q) G(k+q) \\ = & -\frac{U}{\beta^2} \sum_{k',q} F_{\mathsf{c}}^{kk'q} G(k') G(k'+q) G(k+q) \\ = & -\frac{U}{\beta^2} \sum_{k',q} F_{\mathsf{pp}}^{kk'q} G(k') G(q-k') G(q-k) \end{aligned} \tag{3.12}$$

yield the same result for Σ after all internal summations are performed (Σ_{H} denotes the constant Hartree term $\frac{Un}{2}$). Crucial physical insight can be gained at this stage, by performing *partial* summations. One can, e.g., perform all summations, except for the one over the transfer momentum $\vec{q}$. This gives $\widetilde{\Sigma}_{\vec{q}}(k)$, i.e. the contribution to Σ for fixed $\vec{q}$, so that $\Sigma(k) = \sum_{\vec{q}} \widetilde{\Sigma}_{\vec{q}}(k)$. The vector $\vec{q}$ corresponds to a specific spatial pattern given by the Fourier factor $e^{i\vec{q}\vec{R}_i}$. For a given representation such a spatial structure is associated to a specific collective mode, e.g., $\vec{q} = (\pi, \pi)$ for antiferromagnetic or charge-density-wave (CDW) and $\vec{q} = (0, 0)$ for superconducting or ferromagnetic fluctuations. Hence, if one of these contributions dominates, $\widetilde{\Sigma}_{\vec{q}}(k)$ **is strongly peaked** at the $\vec{q}$-vector of that collective mode, provided that the corresponding representation of the EOM is used. On the other hand, in a different representation, *not* appropriate for the dominant mode $\widetilde{\Sigma}_{\vec{q}}(k)$ will display a weak $\vec{q}$ dependence. These heuristic considerations can be formalized by expressing F through its main momentum and frequency structures (see Sec. 3.4.5). Hence, in cases where the impact of the different fluctuation channels on Σ is not known *a priori*, the analysis of the $\vec{q}$-dependence of $\widetilde{\Sigma}_{\vec{q}}(k)$ in the alternative representations of the EOM will provide the desired diagnostics.

3.4.2 Results for the attractive Hubbard model

To demonstrate the applicability of the fluctuation diagnostics, one may start from a case where the underlying, dominant physics is well understood, e.g. the **attractive Hubbard model**, $U < 0$. This model captures the basic mechanisms of the BCS/Bose-Einstein crossover [141–145] and has been intensively studied both analytically and numerically, e.g., with QMC [146–148] and

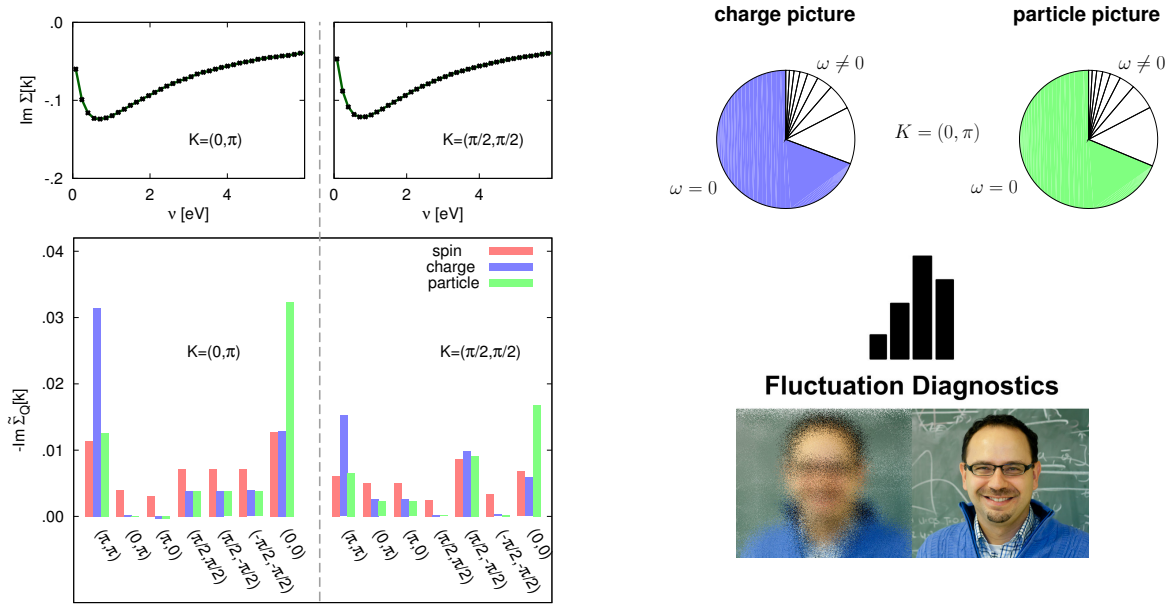

Figure 3.15: Fluctuation diagnostics of Im $\Sigma(\vec{k}, \nu)$ (first row) for the attractive Hubbard model. The histogram shows the contributions of Im $\widetilde{\Sigma}_{\vec{q}}(\vec{k}, \pi/\beta)$ from different values of $\vec{q}$ in the spin, charge and particle-particle representations for the attractive 2D Hubbard model (see text). The pie charts display the relative magnitudes of $|\text{Im}\widetilde{\Sigma}_{\omega}(\vec{k}, \pi/\beta)|$ for the first eight Matsubara frequencies $|\omega|$ in the charge and particle-particle picture, respectively.

DMFT [149–152]. Because of the local attractive interaction, the dominant collective modes are necessarily $s-$wave pairing fluctuations [$\vec{q} = (0, 0)$] in the particle channel, and, for filling $n \sim 1$, CDW fluctuations [$\vec{q} = (\pi, \pi)$] in the charge channel.

Presented here are DCA results computed on a cluster with $N_c = 8$ sites for a 2D Hubbard model with the following parameter set: $t = 0.25$ eV ($t' = 0$), $U = -1$ eV, $\mu = -0.53$ eV and $\beta = 40$ eV^{-1}. This leads to the occupancy $n = 0.87$, for which, at this T, no superconducting long-range order is observed in DCA, and to the self-energy shown in Fig. 3.15 (upper left panel) which exhibits a metallic behavior with weak $\vec{k}$-dependence. The lower left and upper right panels of Fig. 3.15 show the fluctuation diagnostics for Σ. The histogram depicts the different contributions to Im $\Sigma[\vec{k}, \nu]$ for $\vec{k} = (0, \pi)$ and $(\pi/2, \pi/2)$ (lower left panel of Fig. 3.15) at the lowest Matsubara frequency ($\nu = \pi/\beta$) as a function of the momentum transfer $\vec{q}$ within the three representations (spin, charge and particle). Large contributions for $\vec{q} = (\pi, \pi)$ in the charge representation (blue bars) and for $\vec{q} = (0, 0)$ in the particle-particle one (green bars) can be observed. At the same time, no $\vec{q}$ dominates in the spin picture. Hence, the fluctuation diagnostics correctly identifies the key role of CDW and $s-$wave pairing fluctuations in this system. This outcome is supported by a complementary analysis in frequency space (pie-chart in Fig. 3.15): Defining $\widetilde{\Sigma}_{\omega}(\vec{k}, \nu)$ as contribution to the self-energy where the EOM all summations except the one over the transfer frequency ω are performed, one

observes a largely dominant contribution at $\omega = 0$ ($\sim 70\%$) both in the charge and particle-particle pictures. This proves that the corresponding fluctuations are **well-defined and long-lived.**

3.4.3 Results for the repulsive Hubbard model

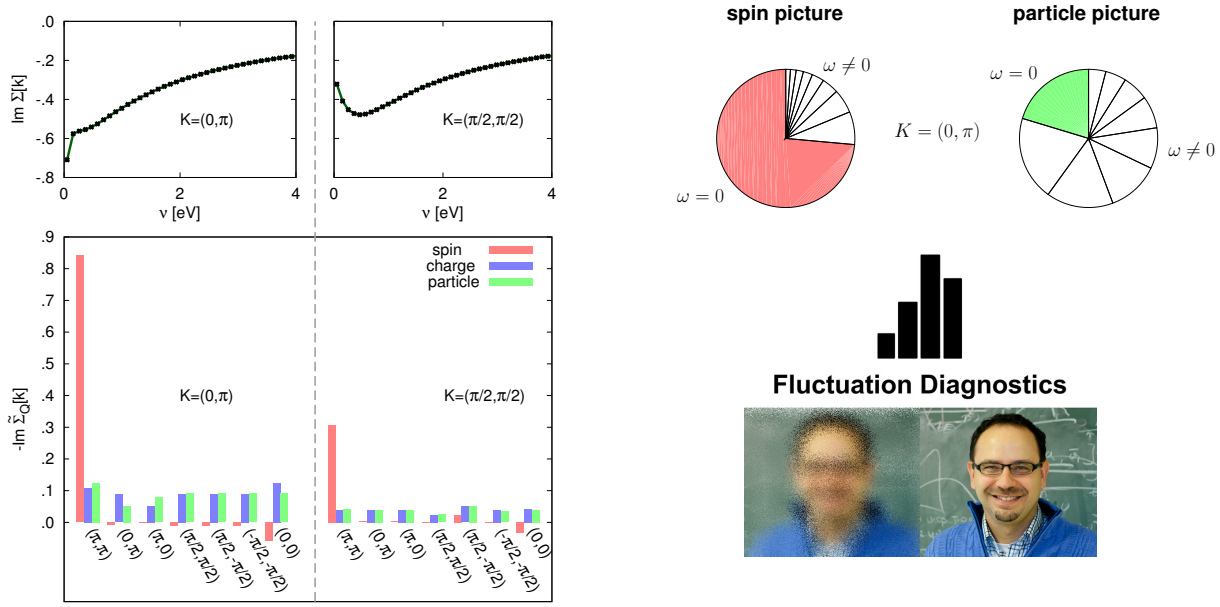

Figure 3.16: As for Fig. 3.15: Fluctuation diagnostics of the electronic self-energy, for the case of the repulsive Hubbard model.

The fluctuation diagnostics is now applied to the much more debated physics of the repulsive Hubbard model in 2D, focusing on the **analysis of the pseudogap regime.** As before, DCA calculations with a cluster of $N_c = 8$ sites are analyzed. Σ and F have been calculated using the Hirsch-Fye and Continuous Time QMC methods (see Sec. 2.2.2.3), accurately cross-checking the results. In the view of a crude modellization of the cuprate pseudogap regime, the parameter set $t = 0.25$ eV, $t' = 0.0375$ (next nearest neighbor hopping), $U = 1.75$ eV, $\mu = 0.6$ eV (corresponding to $n = 0.94$) and $\beta = 60$ eV^{-1} is utilized. For these parameters, the self-energy (see upper left panel of Fig. 3.16) displays strong momentum differentiation between the "antinodal" [$\vec{k} = (0, \pi)$] and the "nodal" [$\vec{k} = (\pi/2, \pi/2)$] momentum, with a pseudogap-like behavior at the antinode [153, 154].

The fluctuation diagnostics is performed in Fig. 3.16, where the contributions to Im $\Sigma[\vec{k}, \pi/\beta]$ for $\vec{k} = (0, \pi)$ and $(\pi/2, \pi/2)$ (upper panels) as a function of the transfer momentum $\vec{q}$ in the three representations are shown. This illustrates clearly the underlying physics of the pseudogap. In the spin representation (red bars in the histogram), the $\vec{q} = (\pi, \pi)$ contribution dominates, and contributes more than 85% and 80% of the result for $\vec{k} = (0, \pi)$ and $\vec{k} = (\pi/2, \pi/2)$, respectively. Conversely,

all the contributions at other transfer momenta $\vec{q} \neq (\pi, \pi)$ are about an order of magnitude smaller. The dominant $\vec{q} = (\pi, \pi)$-contribution is also responsible for the momentum differentiation, being almost twice as large for the antinodal self-energy. Performing the same analysis in the *charge* (blue bars) or particle-particle (green bars) representation, one obtains a completely different shape of the histogram. In both cases, the contributions to Σ are almost uniformly distributed among all transfer momenta $\vec{q}$.

Hence, no important contributions to Σ are found from charge or pairing modes, while the histogram in the **spin-representation marks the strong impact** of antiferromagnetic fluctuations [93, 112–115, 155–157]. This picture is further supported by the complementary frequency analysis. The pie chart in Fig. 3.16 is dominated by the $\omega = 0$ contribution in the spin picture, reflecting the long-lived nature of well-defined spin-fluctuations. At the same time, in the particle (and charge, not shown) representation, the contributions are more uniformly distributed among all ω's, which corresponds to short-lived pairing (charge) fluctuations.

3.4.4 Physical interpretation of the pseudogap

From the results of the preceding section, some general conclusions on the physics underlying a pseudogap can be drawn. These considerations are relevant for the underdoped cuprates, up to the extent their low-energy physics is captured by the 8-site DCA for the repulsive 2D Hubbard model. By means of fluctuations diagnostics, in Fig 3.16, a well-defined [$\vec{q} = (\pi, \pi)$] collective spin-mode is identified to be responsible (on the 80% level) both for the momentum differentiation of Σ and for its pseudogap behavior at the antinode: The large values of $\widetilde{\Sigma}_{\vec{q}}$ at $\vec{q} = (\pi, \pi)$ and $\widetilde{\Sigma}_{\omega}$ at $\omega = 0$ are the distinctive hallmarks of long-lived and extended (antiferromagnetic) spin-fluctuations. At the same time, the rather uniform $\vec{q}$- and ω-distribution of $\widetilde{\Sigma}_{\vec{q}}$ and $\widetilde{\Sigma}_{\omega}$ in the charge/particle pictures shows that the well-defined spin mode can be *also* viewed as *short-lived* and *short-range* charge/pair fluctuations. The latter cannot be interpreted, hence, in terms of *preformed* pairs. This scenario matches very well the different estimates of fluctuation strengths in previous DCA studies [154, 157, 158]. The general applicability of the results has to be emphasized: A well defined mode in one channel appears as short-lived fluctuations in other channels. This dichotomy is not visible in Σ, which makes the fluctuations diagnostics a powerful tool for identifying the most convenient viewpoint to understand the physics responsible of the observed spectral properties.

Attention should be paid to the still open question about the impact of superconducting d-wave fluctuations on the normal-state spectra in the pseudogap regime of the Hubbard model. The instantaneous fluctuations are defined as $\langle \Delta_d^\dagger \Delta_d \rangle$, with $\Delta_d^\dagger = \sum_{\vec{k}} f(\vec{k}) c^\dagger_{\vec{k}\uparrow} c^\dagger_{-\vec{k}\downarrow}$ and $f(\vec{k}) = \cos k_x - \cos k_y$. These $\vec{q} = 0$ fluctuations are certainly strong in proximity of the superconducting phase, but they were also found [154] to be significant over short distances in the pseudogap regime. Their in-

tensity gets stronger as U is increased, beyond the values where superconductivity exists. The expression for $\tilde{\Sigma}_{\vec{q}=(0,0)}$ in the particle picture is closely related to $\langle\Delta_d^\dagger\Delta_d\rangle$, except that the factor $f(\vec{k})$ is missing in $\tilde{\Sigma}_{\vec{q}}$. One might therefore have expected that large $\vec{q}=0$ pair fluctuations, irrespectively of their lifetime, would have contributed strongly to Σ. For unconventional superconductivity, e.g., $d-$wave, this does not happen. The reason is the angular variation of $f(\vec{k})$. For strong pair fluctuations, the variations of $f(\vec{k})$ make the contributions to the fluctuations add up, while the contributions to Σ then tend to cancel. This explains why suppressing superconductivity fluctuations [20, 43, 154, 158–161] does not affect the description of the pseudogap of the Hubbard model. In the case of a purely local interaction such as in the EOM, enhanced $\langle\Delta_d^\dagger\Delta_d\rangle$ fluctuations are mostly averaged out by the momentum summation.

The diagnosis of dominant spin-fluctuations in the DCA self-energy in the underdoped 2D-Hubbard model does not represent per se the conclusive scenario for the cuprate pseudogap. However, important information about the realistic modeling of cuprates can be already extracted: If definitive experimental evidence for an impact of supposedly "secondary" (e.g., charge) fluctuations on the pseudogap is found, extensions of the modellization will be unavoidable for a correct pseudogap theory: Non-local interactions (e.g., extended Hubbard model) or explicit inclusion of the oxygen orbitals (e.g., Emery model) might be required. In fact, such extensions represent in itself an intriguing playground for future fluctuation diagnostics applications.

3.4.5 Fluctuation decomposition of the vertex

The physical interpretation of the numerical results presented in the previous section, is supported by a precise analytical derivation valid for the **weak-coupling regime.** Specifically one may consider in the following an approximation for the vertex function F_r, $r=$ c,s,pp, entering in the EOM. In this approximation, one retains all principal frequency and momentum structures of the vertex functions, i.e. (beyond the bare interaction U) the main and secondary diagonal and the constant background (see [51, 162]). Physically, these main features of F correspond to the different susceptibilities (response-functions) $\chi_\mathsf{r}(\vec{q},\omega)$, r $=$ c,s,pp. In the weak-coupling approximation the vertex F will be now expressed as [51]

$$F_\mathsf{c}^{kk'q} \approx U + U^2\left[-\chi_\mathsf{c}(q) + \frac{3}{2}\chi_\mathsf{s}(k'-k) + \frac{1}{2}\chi_\mathsf{c}(k'-k) - \chi_\mathsf{pp}(k+k'+q)\right] \tag{3.13a}$$

$$F_\mathsf{s}^{kk'q} \approx -U - U^2\left[\chi_\mathsf{s}(q) + \frac{1}{2}\chi_\mathsf{s}(k'-k) - \frac{1}{2}\chi_\mathsf{c}(k'-k) + \chi_\mathsf{pp}(k+k'+q)\right] \tag{3.13b}$$

$$F_\mathsf{pp}^{kk'q} \approx U + U^2\left[-\frac{1}{2}\chi_\mathsf{c}(q-k-k') + \frac{1}{2}\chi_\mathsf{s}(q-k-k') + \chi_\mathsf{s}(k'-k) - \chi_\mathsf{pp}(q)\right]. \tag{3.13c}$$

As mentioned above, such an approximation can be rigorously justified only in the weak-coupling regime, i.e., for small interaction values U ($U \ll t$). At stronger interactions additional structures appear in the vertex functions such as a "cross" discussed in Ref. [51]. The latter emerges from third-order diagrams ("eye"-diagrams) which eventually become relevant at stronger coupling. In the weak-coupling limit, however, Eqs. (3.13) allow for an immediate understanding of how different fluctuations contribute to the self-energy. In this respect, one should recall that each susceptibility $\chi_r(\vec{q},\omega)$ has a clear physical meaning: They describe the (linear) response of the system with respect to an external forcing field, which is associated to the specific channel r ($r=ch \rightarrow$ chemical potential, $r=sp \rightarrow$ (staggered) magnetic field, $r=pp \rightarrow$ pairing field). They become obviously very large in the vicinity of a corresponding second order phase transition. More specifically, the static susceptibility $\chi_r(\vec{q},\omega=0)$ gets strongly enhanced at a specific momentum, $\vec{q}_0$, if the system exhibits large fluctuations in the channel r, which are associated with the spatial pattern defined by $e^{i\vec{q}_0\cdot\mathbf{R}_i}$ (see discussion in the main text). Hence, one can generally expect that the susceptibilities $\chi_r(q)$ (at $\omega=0$ and $\vec{q}=\vec{q}_0$) yield the most relevant contributions to the self-energy, if the system exhibits large fluctuations in the corresponding channel(s) r [see Eqs. (3.13) and the EOM]. In the following, these considerations are applied to the cases of the repulsive ($U>0$) and the attractive ($U<0$) Hubbard model discussed in the previous section.

Assuming that in the repulsive Hubbard model antiferromagnetic [$\vec{q}=\mathbf{\Pi},\mathbf{\Pi}=(\pi,\pi)$] spin-fluctuations dominate (this is most likely the case at half-filling), one can analyze how, in this situation, the different frequency ($\widetilde{\Sigma}_\omega$) and momentum ($\widetilde{\Sigma}_{\vec{q}}$) contributions to the self-energy, as depicted in the histograms/pie charts for the self-energy decomposition in Fig. 3.16, are interpreted in terms of the approximate form for the vertex F_r in Eqs. (3.13). In a spin dominated situation, the most relevant contributions to F_r will originate from $\chi_s(\vec{q}=\mathbf{\Pi},\omega=0)$. Following the above considerations and replacing the exact vertex functions F_r by their approximate forms (3.13) in the calculation of $\widetilde{\Sigma}_{\vec{q}}$ and $\widetilde{\Sigma}_\omega$ one, hence, arrives at the following conclusions:

- In the **spin-picture**, χ_s appears as a function of $\vec{q}$ and ω in F_{sp} [see Eqs. (3.13b)], independent of k'. In this situation *each* term in the k'-sum in the EOM includes the large contribution $\chi_s(\vec{q}=\mathbf{\Pi},\omega=0)$ to $\widetilde{\Sigma}_{\vec{q}}$ and $\widetilde{\Sigma}_\omega$. On the other hand, for $\vec{q}\neq\mathbf{\Pi}$ or $\omega\neq0$ the largest contribution to the k' summation stems from the *single* term proportional to $\chi_s(k'-k)$ in Eq. (3.13b), evaluated for $(\vec{k}'-\vec{k})=\mathbf{\Pi}$ and $\nu'-\nu=0$. This explains the rather small values of $\widetilde{\Sigma}_{\vec{q}}$ and $\widetilde{\Sigma}_\omega$ for $\vec{q}\neq\mathbf{\Pi}$ or $\omega\neq0$, respectively, in the spin picture. Please note that this situation corresponds to histograms and pie charts, very similar to those observed for the DCA calculation of Fig. 3.15.

- At the same time, in the **charge and particle-particle representations**, χ_s appears only as a function of $k'-k$ (or $q-k-k'$), see Eqs. (3.13a) and (3.13c). Therefore, when performing the partial summations over k' in the EOM, only the *single* contribution for $\vec{k}'-\vec{k}=\mathbf{\Pi}$ and

$\nu' - \nu = 0$ ($\vec{q} - \vec{k} - \vec{k}' = \mathbf{\Pi}$ and $\nu - \nu' - \omega = 0$) is large in this sum. On the other hand, such a contribution appears for *each* value of $\vec{q}$ and ω. This explains well the fact that in the charge and the particle-particle pictures the contributions $\widetilde{\Sigma}_{\vec{q}}$ and $\widetilde{\Sigma}_{\omega}$, respectively, to the self-energy are uniformly distributed among all values of $\vec{q}$ and ω as it is observed in the histograms and pie chart (only particle-particle) in Fig. 2. It should be stressed, that χ_{s} *does* contribute to F_r in the charge and particle-particle picture, but only as a function of $k' - k$ rather than q. Hence, one can argue that in the charge and particle-particle representation spin fluctuations are seen from a not "convenient" perspective. From this specific point of view, a well-defined collective spin-mode will appear as short-range (or even local) and short-lived charge or particle-particle fluctuations, as indicated by the democratic distribution of $\widetilde{\Sigma}_{\vec{q}}$ and $\widetilde{\Sigma}_{\omega}$ among all values of $\vec{q}$ and ω.

Obviously the above analysis is applicable also to the attractive Hubbard model ($U < 0$): In this situation charge and particle-particle fluctuations are expected to dominate while spin fluctuations are strongly suppressed. Hence, $\chi_{\mathsf{c}}(\vec{q} = \mathbf{\Pi}, \omega = 0)$ and $\chi_{\mathsf{pp}}(\vec{q} = \mathbf{0}, \omega = 0)$, $0 = (0, 0)$, are enhanced:

- In the **spin picture** these arguments for χ_{c} and χ_{pp} appear for *only one* value of k' when performing the k' summation.
- On the contrary, in the **particle-particle picture**, χ_{c} (or χ_{pp}) is a function of $\vec{q}$ and ω and the above mentioned large contribution to $\widetilde{\Sigma}_{\vec{q}}$ and $\widetilde{\Sigma}_{\omega}$ appears for *each* value of k'. Hence, $\widetilde{\Sigma}_{\vec{q}}$ and $\widetilde{\Sigma}_{\omega}$ get strongly peaked at $\vec{q} = \mathbf{\Pi}$ and $\omega = 0$, respectively, in the charge description and $\vec{q} = \mathbf{0}$ and $\omega = 0$ in the particle-particle description, while in the spin picture $\widetilde{\Sigma}_{\vec{q}}$ is almost independent of $\vec{q}$.

The above discussion based on the vertex decomposition in Eqs. (3.13) is rigorously justified only for small values of U where corrections beyond Eqs. (3.13) are negligible. This highlights the importance of the fluctuation diagnostics approach which is applicable for all values of the interaction. In fact, the fluctuation diagnostics for the DCA self-energy in the pseudogap regime of the repulsive two-dimensional Hubbard model gives gives histograms/pie charts for $\widetilde{\Sigma}_{\vec{q}}$ and $\widetilde{\Sigma}_{\omega}$ dominated by $\vec{q} = \mathbf{\Pi}$ and $\omega = 0$ in the spin representation, indicating the dominant role played by a well defined and long-lived ($\vec{q} = \mathbf{\Pi}$, $\omega = 0$) spin collective mode. This hold even in a regime, where Eqs. (3.13) break down. Specifically, while the main bosonic structures of F described in Eqs. (3.13) give a significant contribution to the self-energy even in the non-perturbative regime, the momentum differentiation observed in the histograms originates from contributions *beyond* Eqs. (3.13).

4

Spectral analysis at the one-particle level: from 3D to 1D

"It is as though a star throws the whole secret history of its being into its spectrum, and we have only to learn how to read it aright in order to solve the most abstruse problems of the physical Universe."

- Herbert Dingle (English astronomer and philosopher, *1890 - †1978)

The dynamical mean field theory (DMFT) accounts for temporal fluctuations of a strongly correlated system, neglecting its spatial correlations beyond mean-field. DMFT is an exact theory in the limit of infinite dimensionality, however, it can be used as a powerful approximation for finite dimensional systems. For three-dimensional bulk systems DMFT calculations are usually accurate, although quantitative corrections have to be taken into account, especially in the vicinity of second order phase transitions, where non-local correlations become more dominant. The situation dramatically changes in two-dimensional systems, where non-local correlations ought to be included in order to obtain a qualitative correct physical description. Of course, if the dimensionality is reduced to the even more extreme case of one dimension, the physics of DMFT can be completely overturned. In this Chapter, a diagrammatic extension of DMFT, the dynamical vertex approximation (DΓA) is exploited to analyze the spectral properties of Hubbard systems when the dimensionality is progressively reduced. This will allow to identify, in general, how spatial and temporal correlations appear in the electronic self-energy for different dimensions, suggesting future algorithmic improvements. Starting at three dimensions, the impact of second-order phase transitions on Fermi-liquid properties is studied and the space-time separability of the self-energy is discussed. In two dimensions, an alternative parametrization of the (spatial part of the) self-energy is applied, that leads to a remarkable collapse of this quantity onto a single curve. Eventually, in the most challenging case of one dimension, the DΓA and DMFT are benchmarked against the exact solutions available for finite Hubbard nano-rings.

4.1 Separability of local and non-local correlations in three dimensions

Parts of this section (marked by a vertical sidebar) have already been published in the *APS journal* Phys. Rev. B **12**, 121107(R) (2015).

Several iconic phenomena of the many-body problem, such as the Kondo effect or the Mott metal-insulator transition, can be described by local correlation effects. This explains the great success of DMFT for our understanding of numerous correlated materials (see Sec. 2.2). However, DMFT ad hoc assumes the electron self-energy to be independent of momentum. This is known to fail in low dimensions, e.g. for the Luttinger liquid in 1D, or the strong momentum space differentiation in (quasi) 2D systems. However, even in three dimensions, the major realm of practical DMFT applications, signatures of local spatial correlations are apparent, e.g., in the presence of second order phase transitions: In the 3D Hubbard model, nearest-neighbor spin-spin-correlation functions [163, 191], non-mean-field critical exponents [171], and deviations from a non-local correlations' picture of the entropy [163, 191] indicate a paramount effect of local antiferromagnetic fluctuations in a large region of the phase-diagram.
Complementary to these manifestations of self-energy effects that are local in space, one might also investigate their structure in the time domain. While exchange contributions to the electron self-energy are static by construction, correlation effects are *a priori* both momentum- and energy-dependent. Recently it has been proposed that the quasi-particle weight $Z_{\vec{k}} = (1 - \partial_\omega \mathrm{Re}\Sigma(\vec{k}, \omega))^{-1}_{\omega=0}$, accounting for the low-energy dynamics in the (retarded) self-energy Σ of metals, is essentially momentum-independent in the iron pnictides [164], as well as metallic transition metal oxides [165]. Yet, the basis for the mentioned empirical finding of the non-locality of $Z_{\vec{k}}$ was the weak-coupling GW approach [166–168], where spin fluctuations are completely neglected. However, large dynamical spin fluctuations have been found in the iron pnictides both theoretically [73, 169] and experimentally [169]. Moreover, these fluctuations were shown to constitute the leading contribution to local self-energies in the (extended) Hubbard model [170–172].

In this section, the **analysis of local and non-local correlations in spectral properties** of metals is put on solid grounds (see also the recent analysis presented in [68]). To this aim the dynamical vertex approximation (see Sec. 2.3) is applied to the 3D Hubbard model (Eq. (2.6)) on a cubic lattice away from half-filling. This allows for a precise study of the electron self-energy *beyond* the weak-coupling regime. Energies in this section will be measured in units of the half-bandwidth $W/2 = 6t \equiv 1$. An interaction value of $U = 1.6$ is chosen, which, at half filling, $n = 1$, yields a Mott insulator with maximal Néel temperature [171]. Thus, the crossover regime between weak-coupling (where the perturbative GW approximation is most justified and magnetism controlled by Fermi surface instabilities) and the Mott-Heisenberg physics at large interaction strengths, is

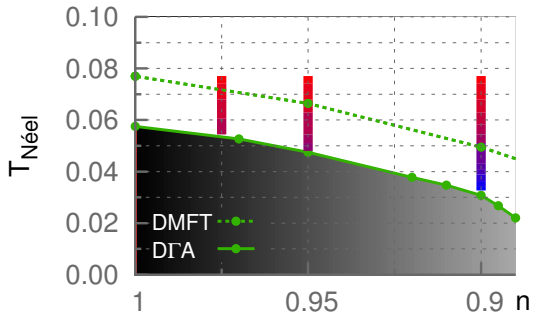

Figure 4.1: Phase diagram of the 3D Hubbard model within DMFT and DΓA for U=1.6. The solid (dashed) line indicates the DΓA (DMFT) Néel temperature, determined from the divergence of the spin susceptibility. The vertical bars at fixed filling n indicate the temperature paths followed in Fig. 4.2. The system is Mott-insulating at half-filling ($n = 1$). All energies here are measured in units of the half-bandwidth.

considered. It was shown (for half-filling) that the effect of local fluctuations is strongest in this intermediate regime [20, 171].

4.1.1 Results

Fig. 4.1 shows the phase diagram of the 3D Hubbard model as a function of filling n and temperature T (see Sec. 6.3 for higher dopings). As a clear signature of local fluctuations, the Néel temperature is reduced by at least 30% in DΓA with respect to the DMFT result. To elucidate the influence of these manifestly non-local effects in the two-particle AF susceptibility onto the one-particle electronic structure, the DΓA self-energy is analyzed when approaching the spin density wave (SDW) instability at constant filling.

In a first step, effects near the Fermi level are investigated and a low-energy expansion of the self-energy on the real frequency axis ω is performed ("Landau Fermi-liquid expansion"):

$$\Sigma(\vec{k},\omega) = \mathrm{Re}\Sigma(\vec{k},\omega=0) + (1-1/Z(\vec{k}))\omega + \imath\Gamma(\vec{k})(\omega^2+\pi^2T^2) + \cdots , \tag{4.1}$$

where

$$\gamma(\vec{k}) = -\mathrm{Im}\Sigma(\vec{k},\omega=0) = \Gamma(\vec{k})\pi^2T^2 + \mathcal{O}(T^4)$$

is the **scattering rate**, and $Z(\vec{k})$ can be identified as the **quasi-particle weight in the Fermi liquid regime.** In the limit of infinite dimensions, non-local self-energy diagrams vanish, and Z and γ are momentum independent [16]. The DMFT self-consistency condition then yields, via

$$\Sigma(k,\omega) = \mathbf{Re\Sigma(k,\omega=0)} \quad + \quad (1-1/\boldsymbol{Z(k)})\,\omega \quad - \quad \imath\boldsymbol{\Gamma(k)}\left(\omega^2+\pi^2T^2\right) \quad + \cdots$$

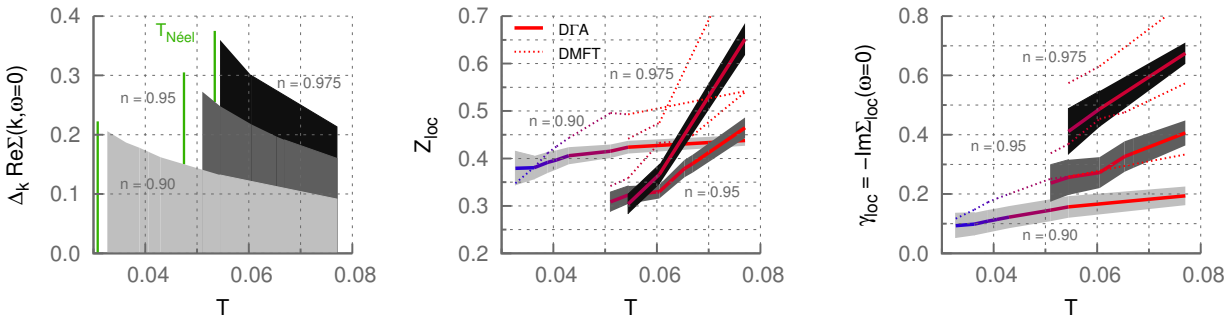

Figure 4.2: Low-energy expansion of the DΓA self-energy and momentum dependence of the expansion coefficients. The shaded areas (light gray, gray, black) indicate the standard deviation of the expansion coefficients in the Brillouin zone with respect to their local values a_{loc}, as a function of temperature for different fillings ($n = 0.9$, $n = 0.95$, $n = 0.975$).

the Dyson equation (2.12), the exact non-interacting propagator of an effective Anderson impurity problem [15]. In finite dimensions this is no longer true. Therefore, besides the approximation of assuming the self-energy to be purely local, this local self-energy does not need to coincide with the local projection of the exact (non-local) lattice self-energy. In fact, the momentum average

$$a_{\text{loc}} = \frac{1}{N_{\vec{k}}} \sum_{\vec{k}} a(\vec{k})$$

(with $N_{\vec{k}}$ the number of $\vec{k}$-points) of the DΓA quasi-particle weight and scattering rate, Z_{loc} and γ_{loc}, deviate notably from the DMFT prediction (Fig. 4.2, middle and right panel). As expected [20], the inclusion of antiferromagnetic fluctuations reduces the quasi-particle weight Z. Please note that the temperature evolution of Z_{loc}, and its change in hierarchy (Z smallest at low doping, $1-n$, for small T; while for high T, Z is largest for small doping) follows the same trends as the inverse of the effective mass of the 3D electron gas [173].

For the chosen parameter set, the scattering rate γ in DMFT is large enough to induce a large violation of the pinning condition $\text{Im}G_{\text{loc}}(\omega=0) = \text{Im}G^{U=0}_{\text{loc}}(\omega=0)$, valid for local self-energies with vanishing imaginary part at the Fermi level [174]. Moreover, the temperature dependence of γ evidently involves corrections [175] to the low-energy Fermi liquid behavior, as neither DMFT nor DΓA yield a T^2 behavior. Therewith the interpretation of the expansion coefficient Z as quasi-particle weight breaks down. Nevertheless, in the following the solutions $\vec{k}_F$ of the quasi-particle equation, $\det(\mu - \epsilon_{\vec{k}} - \text{Re}\Sigma(\vec{k},0)) = 0$ are conventionally indicated as “Fermi surface”, with the chemical potential μ and the one-particle dispersion $\epsilon_{\vec{k}}$. This can be motivated by the (co)existence of quasi-particle-like excitations even above the Fermi liquid coherence scale [175]. In DΓA, spectral weight

at the Fermi level is further depleted compared to DMFT [20,171] and effective masses are reduced (see below). Hence, the local electron-electron scattering contributions to quasi-particle lifetimes decrease, explaining why $\gamma^{\text{DMFT}} > \gamma_{\text{loc}}^{D\Gamma A}$. When approaching the SDW state, however, non-local spin fluctuations provide an additional scattering mechanism: While $\gamma \to 0$ for $T \to 0$ in DMFT, the inverse life-time in DΓA levels off. Concomitantly, and analogous to the incoherence crossover at high-T via local electron-electron scattering, the emerging low-T scattering in DΓA, causes $Z^{D\Gamma A}$ to saturate towards the SDW state.

In the following, the momentum dependence of the self-energy is analyzed by calculating the **standard deviation of the expansion coefficients** $a(\vec{k}) = \text{Re}\Sigma(\vec{k}, \omega{=}0)$, $Z(\vec{k})$, $\gamma(\vec{k})$ with respect to their local values:

$$\Delta_{\vec{k}} a(\vec{k}) = \sqrt{1/N_{\vec{k}} \sum_{\vec{k}} \left| a(\vec{k}) - a_{\text{loc}} \right|^2}.$$

One can see that non-local fluctuations manifest themselves very differently in the individual coefficients (from left to right in Fig. 4.2):

(i) The momentum dependence of the **static part** of the self-energy $\text{Re}\Sigma(\vec{k}, \omega{=}0)$, as measured by the above standard deviation, increases substantially towards the spin ordered phase, and grows sharply when approaching the Mott insulator at half-filling; $\Delta_{\vec{k}}\text{Re}\Sigma(\vec{k}, \omega = 0)$ reaches values as large as 20-40% of the half-bandwidth $W/2$ –a large effect that is fully neglected in DMFT.

(ii) The standard deviation in momentum space of the **quasi-particle weight**, $\Delta_{\vec{k}} Z(\vec{k})$ (depicted as shaded areas around the local values in Fig. 4.2(b)), is small in all considered cases. Indeed the largest absolute deviation amounts to only 0.07. In particular, $\Delta_{\vec{k}} Z(\vec{k})$ does not dramatically increase upon approaching the Néel temperature, in stark contrast to the discussed static part of the self-energy.

(iii) The momentum dependence of the **scattering rate** γ, Fig. 4.2(c), remains always moderate. Specifically, the momentum variation increases on absolute values when approaching the Mott insulator at half-filling, although the relative importance $\Delta_{\vec{k}}\gamma(\vec{k})/\gamma$ actually decreases.

Summarizing, one finds that while spin and charge fluctuations, that develop upon approaching the spin-ordered or Mott-insulating state, can renormalize significantly the value of the quasi-particle weight Z, they do not introduce any sizable momentum differentiation in it. This is in strong opposition to the pronounced non-local effects in the static part of the self-energy. The latter will, however, strongly modify the mass m^* of the quasi-particles, as e.g. extracted from Shubnikov-de Haas or photo-emission experiments. Indeed the effective mass enhancement m^*/m is defined by

$\vec{k}=\vec{k}_F$	k_0	$\nabla_k\epsilon_{\vec{k}}$	$\nabla_k\mathrm{Re}\Sigma(\vec{k},0)$	Z	$1/Z$	m^*/m
$\vec{k}_1=(k_0,k_0,0)$	2.16	0.55	0.30	0.45	2.20	1.42
$\vec{k}_2=(k_0,0,\pi)$	$\pi/2$	0.67	0.20	0.45	2.23	1.72
$\vec{k}_3=(k_0,k_0,k_0)$	$\pi/2$	0.99	0.35	0.41	2.44	1.81

Table 4.1: Effective masses on the Fermi surface. Contributions to m^*/m from dynamical (Z) and static ($\nabla_k\mathrm{Re}\Sigma(\vec{k},0)$) renormalizations for three $\vec{k}_F$, see also Fig. 4.3. In DMFT: $m^*/m = 1/Z = 1/0.44 = 2.26$. U=1.6, T=0.043.

the ratio of group velocities of the non-interacting and interacting system, respectively:

$$\left(\frac{m^*}{m}\right)^{-1}\Bigg|_{\vec{k}_F} = Z(\vec{k}_F)\left[1+\frac{\hat{e}_{\vec{k}_F}\cdot\nabla_k\mathrm{Re}\Sigma(\vec{k},\omega=0)}{\hat{e}_{\vec{k}_F}\cdot\nabla_k\epsilon_{\vec{k}}}\right]_{\vec{k}=\vec{k}_F} \tag{4.2}$$

where $\epsilon_{\vec{k}}$ is the non-interacting dispersion and $\hat{e}_{\vec{k}_F}$ is the unit-vector perpendicular to the Fermi surface for a given $\vec{k}_F$. Thus, besides the enhancement of m^* via Z (which are shown to be quasi local, see also Tab. 4.1), there is a contribution to m^* from the momentum dependence of the static self-energy. The sign of the derivative $\nabla_k\mathrm{Re}\Sigma$ is always positive, thus the effect of non-local correlations is to *reduce* the effective mass. In Tab. 4.1 the individual components to m^*/m for three Fermi vectors $\vec{k}_F$ (on the Fermi surface, Z and γ are maximal (minimal) for $\vec{k}_2$ ($\vec{k}_3$)) are given. One finds m^*/m to be notably momentum-dependent: $m^*/m = 1.4$ for $\vec{k}_1$, while for $\vec{k}_3$ $m^*/m = 1.8$ –a value larger by 30%. However, it is dominantly the **spatial variation** of the self-energy ($\nabla_k\mathrm{Re}\Sigma$), not a non-local dependence in its dynamics (Z), that causes this momentum differentiation. Depending on $\vec{k}_F$, local correlation effects reduce the effective mass down to 55-75% of its dynamical contribution, $1/Z$. In realistic GW calculations even larger reductions were found for iron pnictides [164]. Besides the change in the (local) quasi-particle weight, this is a second, significant effect not accounted for in non-local approaches, such as DMFT.

Having so far concentrated on effects at the Fermi level, a natural question is: Up to which energy scale do dynamical correlations remain essentially local? Fig. 4.3 shows the Fermi surface within DΓA for $n = 0.9$ and the real parts of the self-energies along a path in the Brillouin zone. Congruent with the quasi-particle weight being quasi local, the slopes of the self-energies at the Fermi level are the same for all momenta and the curves differ by a static shift only. To quantify this observation, Fig. 3 (right) shows the standard deviation $\Delta_{\vec{k}}Z(\vec{k},\omega)$, where the Z-factor is formally extended to finite frequencies: $Z(\vec{k},\omega) = 1/(1-\partial_\omega\mathrm{Re}\Sigma(\vec{k},\omega))$. $\Delta_{\vec{k}}Z(\vec{k},\omega)$, a measure for the momentum dependence of dynamical correlations, is negligible in the energy window $[-0.25:0.6]$. Given the bandwidth renormalization $W \to Wm/m^*$, with the above effective mass ratio, non-local correlations are effectively static over most of the *interacting* quasi-particle dispersion.

Fig. 4.3 also shows GW results: While the slope of the self-energy is constant throughout the Brillouin zone within the linear Fermi liquid regime (the extension of which GW overestimates), also the static part shows only a weak momentum-dependence. The comparatively large variations of $\mathrm{Re}\Sigma(\vec{k},\omega{=}0)$ in DΓA therefore emphasize the pivotal influence of spin fluctuations (neglected by GW) onto (static) non-local correlations.

4.1.2 Implication on many-body schemes

The central findings of the above analysis for correlated metals in 3D are:

1. Within most of the quasi-particle bandwidth non-local correlations are static. Conversely dynamical correlations are local. Hence, the self-energy of 3D systems is *separable* into local and dynamical contributions

$$\Sigma(\vec{k},\omega) = \Sigma^{\text{non-loc}}(\vec{k}) + \Sigma^{\text{loc}}(\omega) \tag{4.3}$$

   providing an *a posteriori* justification for the application of a DMFT-like method to describe $\Sigma^{\text{loc}}(\omega)$ in 3D. It should be stresses, however, that since e.g. $Z^{\text{DMFT}} \neq Z^{D\Gamma A}_{\text{loc}}$, ways to improve the DMFT impurity propagator (e.g. by incorporating $\Sigma^{\text{non-loc}}(\vec{k})$ in the DMFT self-consistency) need to be pursued.

2. Static correlations have a large momentum-dependence, calling for a description of $\Sigma^{\text{non-loc}}$ beyond, say, DFT. This can e.g. be achieved with the GW+DMFT approach [165, 176], or the recently proposed QSGW+DMFT [164]. Exploiting Eq. (4.3), these can be simplified, as is the strategy in DMFT@(local GW). Yet, already the GW can profit: Here, one can propose to

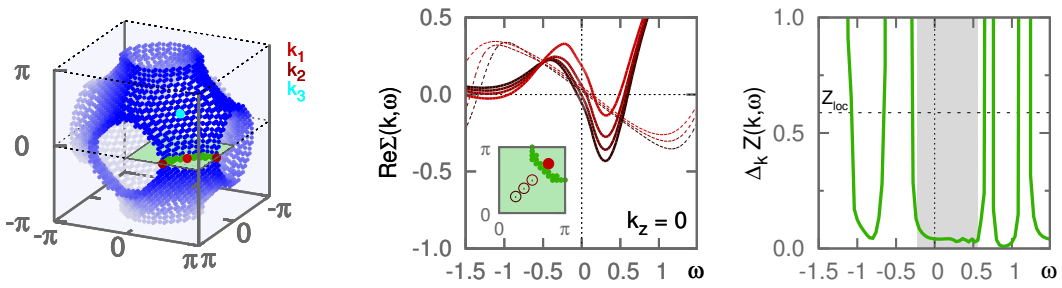

Figure 4.3: DΓA Fermi surface and momentum dependence of the self-energy. Shown is the Fermi surface computed in DΓA for $n = 0.9$, $U = 1.6$, $T = 0.043$ (left). There, the green squares indicates the cut of the Brillouin zone that contains the path $(k, k, 0)$ for which the real parts of the DΓA self-energies (middle panel) are shown. Indicated are also the $\vec{k}$-points of Tab. 4.1. The maximal (minimal) Z and γ on the Fermi surface occur at $\vec{k}_2$ ($\vec{k}_3$).

replace Hedin's

$$\Sigma_{GW}(\vec{k},\omega) = 1/N_{\vec{q}} \sum_{\vec{q},\nu} G(\vec{k}+\vec{q},\omega+\nu) W(\vec{q},\nu)$$

with

$$\widetilde{\Sigma}_{GW}(\vec{k},\omega) = \Sigma_{GW}^{\text{loc}}(\omega) + \Sigma_{GW}^{\text{non-loc}}(\vec{k}),$$

where

$$\Sigma_{GW}^{\text{loc}}(\omega) = \sum_{\nu} G^{\text{loc}}(\omega+\nu) W^{\text{loc}}(\nu),$$

$$\Sigma_{GW}^{\text{non-loc}}(\vec{k}) = \frac{1}{N_{\vec{q}}} \sum_{\vec{q},\nu} G(\vec{k}+\vec{q},\nu) W(\vec{q},\nu) - \Sigma_{GW}^{\text{loc}}(\omega=0)$$

for GW calculations of metals. This physically motivated scheme is referred to as **"space-time-separated GW"**. Avoiding the $\vec{q}$- and ω-convolution, respectively, reduces the numerical expenditure, typically gaining more than an order of magnitude. If the dominant non-local self-energy derives from *exchange* effects, Eq. (4.3) holds and SEX+DMFT [177] can be employed. In the (one-band) Hubbard model, however, non-local self-energies are not exchange-driven. Still, $\Sigma^{\text{non-loc}}$ is significant, and in particular beyond a perturbative description like GW. Consequently, at least in the vicinity of second order phase transitions, a methodology beyond (QS)GW+DMFT is required. *Ab initio*-DΓA [178] or realistic applications of other diagrammatic extensions [43,45,46,203] of DMFT might provide a framework for this. That Eq. (4.3) holds beyond weak coupling, however, nourishes the hope that a much less sophisticated electronic structure methodology can be devised in 3D.

However, also in 3D, momentum-dependent quasi-particle weights can be generated. In fact, this is the typical situation in heavy fermion systems below their (lattice) Kondo temperature. There, the hybridization amplitude for spin singlets between atomic-like f-states and conduction electrons is modulated on the Fermi surface, as it can be rationalized with mean-field techniques [179]. Thus, even a local quasi-particle weight of the f-states yields a momentum-space anisotropy of Z via the change in orbital character. This effect has also been held responsible for anisotropies in some Kondo insulators [181]. Beyond this scenario, however, strong inter-site fluctuations in the periodic Anderson model (see Eq. (2.8) and [180]) suggest actual non-local correlation effects to be of crucial relevance to heavy fermion quantum criticality [182, 183]. A further source of non-trivial non-local correlation effects in 3D are multi-polar Kondo liquids [179, 184, 185]. To elucidate the latter two phenomena, an application of DΓA to e.g. the periodic Anderson model is called for.

Non-local renormalizations that are dynamical also occur **in lower dimensions**, as e.g. shown theoretically for 2D [39, 43, 46, 186, 187]. In the next section, therefore, the structure of the self-energy for the Hubbard model in two dimensions is analyzed in detail.

4.2 Self-energies and their parametrization in two dimensions

Most of the figures in this section have already been published in the APS journal Phys. Rev. B **93**, 195134 (2016).

The results of the previous section showed that, for certain energy windows, the self-energy $\Sigma(\nu, \vec{k})$ for the Hubbard model in three dimensions can be separated in a local (but frequency-dependent) and a non-local (but frequency-independent) part,

$$\Sigma(\vec{k}, \omega) = \Sigma^{\text{loc}}(\vec{k}) + \Sigma^{\text{non-loc}}(\omega). \tag{4.4}$$

In two dimensions, however, local and non-local fluctuations are believed to be fundamentally interwoven, so that such a decomposition usually cannot be achieved. However, as will be shown in this section, the self-energy of the Hubbard model in two dimensions exhibits a surprising, quite different property: away from the Fermi surface, the self-energy $\Sigma(\nu, \vec{k})$, parameterized by the frequency ν and momentum vector $\vec{k}$, **collapses onto a different parametrization of frequency ν and (non-interacting) electron dispersion** $\epsilon_{\vec{k}}$, i.e.

$$\Sigma = \Sigma(\nu, \vec{k}) \rightarrow \Sigma(\nu, \epsilon_{\vec{k}}). \tag{4.5}$$

This is a quite remarkable feature, since, in two spatial dimensions, this self-energy parametrization only requires two parameters instead of three. Of course, this energy-parametrization is not exact: notable deviations from the ("exact") momentum-parametrization occur in the (per definition, $\vec{k}$-selective) pseudogap phase and strongly asymmetric lattices, where the x/y-symmetry is broken. However, for a wide range of parameters, the energy-parametrization works remarkably well.

In the following, first, the behavior of self-energies in the half-filled Hubbard model on a simple square lattice (Eq. (2.6)) in momentum- and energy-parametrization is studied by means of two complementary cutting-edge many-body methods: of the dynamical vertex approximation (see Sec. 2.3) and (finite-size) Blankenbecler-Sugar-Scalapino quantum Monte-Carlo (BSS-QMC) simulations. BSS-QMC shares some similarities with Hirsch-Fye QMC (see Sec. 2.2.2.3) on a finite lattice [136]. Later, the proposal of the energy-parametrization is attempted to be transferred to anisotropic and doped systems.

4.2.1 Collapse of $\vec{k}$-dependence on a $\varepsilon_{\vec{k}}$-dependence

In a first step it is illustrative, to investigate the self-energy in the (original) momentum-parametrization $\Sigma(\nu, \vec{k})$ for a representative set of parameters in BSS-QMC. Fig. 4.4 shows the (imaginary part) of the 2D self-energy for $U = 4t$, $\beta t = 5.6$, on a simple square (isotropic, nearest-neighbor

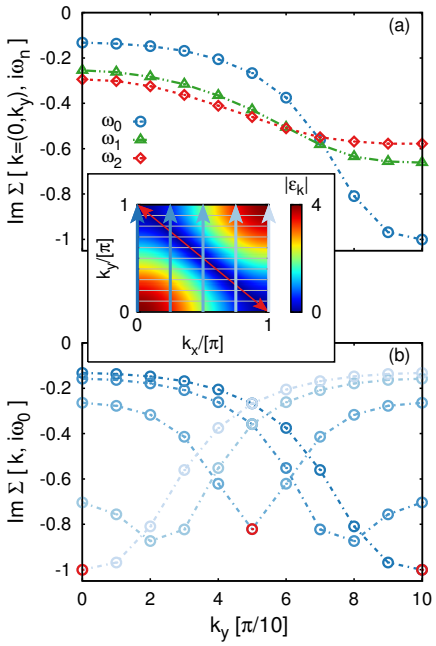

Figure 4.4: (taken from [188]) Imaginary part of the self-energy $\Sigma(\nu, \vec{k})$ from BSS-QMC for $U = 4t$, and $\beta t = 5.6$ at (a) the first three Matsubara frequencies and $k_x = 0$; (b) at the first Matsubara frequency along the (brightness-coded) five momentum paths shown in the inset. The red points in (b) correspond to the nodal and antinodal point, which are emphasized alike in the inset by the red diagonal arrow.

hopping only) lattice and half-filled system (anisotropic and doped cases can be found in the following subsections). The upper panel (a) depicts its momentum-dependence for the fixed momentum slice $\vec{k} = (k_x = 0, k_y)$ and the first three Matsubara frequencies ($i\nu_0$, $i\nu_1$ and $i\nu_2$). For this parameter set (half-filling, intermediate coupling and temperature) the self-energy exhibits a pseudogap, which can be anticipated from the high degree of momentum-differentiation of the self-energy's imaginary part, looking at the first Matsubara frequency $i\nu_0$: its value varies by a factor of 10 along this highly symmetric cut over the Brillouin zone, making DMFT obviously not applicable for a correct description of the self-energy here. This big variation can be seen also for other paths along the Brillouin zone (which are shown color coded in the center of Fig. 4.4) in the lower panel of Fig. 4.4 for the first Matsubara frequency.

In a next step, the self-energy data are plotted as a function of the non-interacting dispersion relation, which, in the case of the simple square lattice, reads

$$\epsilon_{\vec{k}} = -2t\left(\cos(k_x) + \cos(k_y)\right).$$

Fig. 4.5 shows the imaginary (a) and real (b) part of the self-energy for the same parameter set as

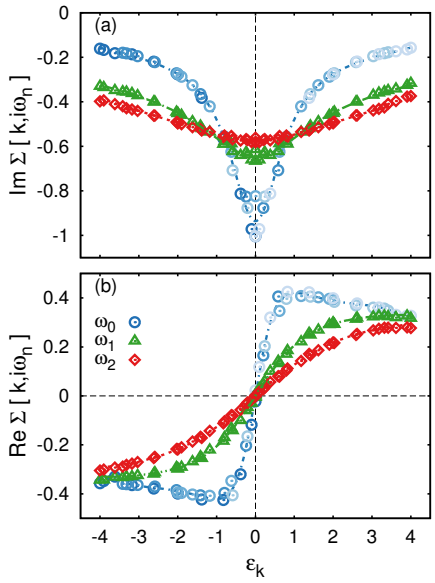

Figure 4.5: (taken from [188]) Imaginary (a) and real (b) part of the self-energy $\Sigma(\nu, \vec{k})$ vs. the non-interacting dispersion $\varepsilon_{\vec{k}}$ from BSS-QMC at $U = 4t$ and $\beta t = 5.6$. Different (k_x, k_y) points with the same $\varepsilon_{\vec{k}}$ collapse onto a single curve.

above, however, this time, as a function of $\epsilon_{\vec{k}}$. In particular, the frequencies are indicated by open circles ($i\nu_0$), triangles ($i\nu_1$) and diamonds ($i\nu_2$), respectively. Close inspection of the plots yields their following features:

- The pseudogap feature, i.e. the quite big momentum variation (especially pronounced comparing the nodal ($\vec{k} = (\pi/2, \pi/2)$) and antinodal points ($\vec{k} = (\pi, 0)$)) at the Fermi level $\epsilon_{\vec{k}} = 0$, remains. This is a physical result, also confirmed by recent BSS-QMC [189] and DΓA studies [187, 190].

- However, going slightly away from the Fermi-surface, quite accurately, the data sets for both imaginary and real part collapse onto a single line. This collapse is quite independent of the cluster size and geometry [188], although the collapse is better for larger systems and the convergence is quite fast with system size. This finding suggest the collapse to survive in the thermodynamic limit (see Sec. 4.2.2).

- Most importantly from the applicational point of view, the collapse survives, irrespectively of the interaction strength as can be deduced from Fig. 4.6, where the same analysis as before has been conducted for different values of the Coulomb interaction. Please note, that the large-U-regime shows a stronger dependence on the non-interacting dispersion, however, the collapse onto a single curve is untouched.

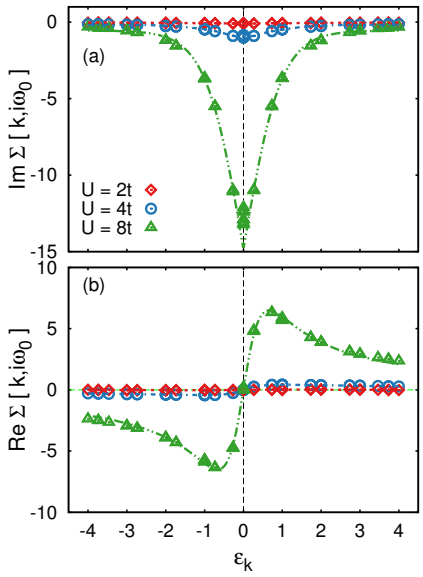

Figure 4.6: (taken from [188]) Imaginary (a) and real (b) part of the self-energy $\Sigma(i\nu_0, \vec{k})$ for different U-values and $\beta t = 5.6$.

4.2.2 Comparison to DΓA

In the previous Sec. 4.2.1 it has been shown that the self-energy $\Sigma(\nu, \vec{k})$ obtained by means of BSS-QMC collapses onto $\Sigma(\nu, \epsilon_{\vec{k}})$ when leaving the vicinity of the Fermi edge. However, only spatial fluctuations with extensions up to the size of the cluster used are incorporated in the BSS-QMC self-energy. In order to test whether the universal parametrization of the self-energy via the non-interacting dispersion $\varepsilon_{\vec{k}}$ also holds in the thermodynamic limit (including spatial correlations on every length scale), self-energy calculations by means of the ladder-DΓA (introduced in Sec. 2.3.2) were performed.

Fig. 4.7 shows density plots of the value of the imaginary part (in units of $4t$) of the DΓA self-energy for $\beta t = 5$ and $U = 2t$ for the first (left panel) and fourth (right panel) Matsubara frequency in the (irreducible) Brillouin zone. As one can see, for frequencies close to the frequency Fermi edge ($i\nu_0$), this value strongly varies across the Brillouin zone, reflecting again the pseudogapped behavior in this parameter regime. Leaving the frequency Fermi edge and going to $i\nu_3$, however, the distribution becomes much more homogeneous, which is a first indication, that the collapse of the self-energy could still survive in the thermodynamic limit. That this is indeed the case, can be deduced by inspecting Fig. 4.8(a), which presents the imaginary part of $\Sigma(i\nu_0, \epsilon_{\vec{k}})$ (now again in units of t) for $U = 2t$ and $\beta t = 5$. The dotted circles recall the BSS-QMC data for certain points $\vec{k}$ of the Brillouin zone, whereas the dark-blue triangles mark the values for the DΓA self-energy at identical of similar $\vec{k}$-points. The light-blue data points in the background reveal data for all available

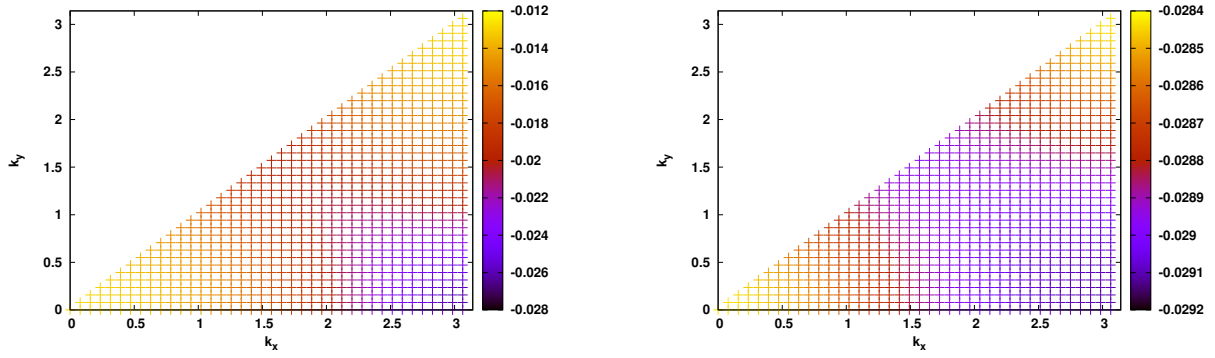

Figure 4.7: Value of the imaginary part (in units of $4t$) of the DΓA self-energy for $\beta t = 5$ and $U = 2t$ for the first (left panel) and fourth (right panel) Matsubara frequency in the (irreducible) Brillouin zone.

$\vec{k}$-points of the DΓA calculation. Whereas one can observe a quantitative difference between the two self-energy curves of DΓA and BSS-QMC, the remarkable qualitative feature of the collapse of $\Sigma(i\nu_0, \epsilon_{\vec{k}})$ survives in the thermodynamic limit. In particular, the behavior of $\Sigma(i\nu_0, \epsilon_{\vec{k}})$ in DΓA resembles the one in BSS-QMC in view of the fact that leaving the Fermi edge $\varepsilon_{\vec{k}} = 0$, the spread of the data points gets drastically diminished. Again, the relatively big spread at the Fermi edge of the DΓA self-energy can be explained physically by the onset of the opening of a pseudogap in this region of the (DΓA) phase diagram [20, 187, 190]. Lowering the temperature to $\beta t = 10$ the spread at the Fermi level increases, however, the collapse away from the Fermi edge persists [Fig. 4.8(b)].

Leaving the vicinity of the Fermi edge by choosing a higher Matsubara frequency, the collapse becomes even more drastic as can be seen in the first row of Fig. 4.9, where the imaginary part of $\Sigma(i\nu_n, \epsilon_{\vec{k}})$ is plotted for $U = 4t$ and $\beta t = 2$ for the first [Fig. 4.9(a)] and second [Fig. 4.9(b)] Matsub-

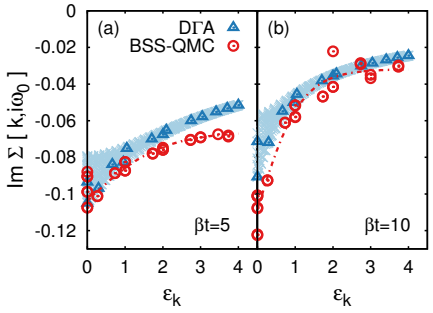

Figure 4.8: (taken from [188]) Imaginary part of the self-energy $\Sigma(\vec{k}, i\omega_0)$ for $U = 2t$ and two different temperatures: (a) $\beta t = 5$ and (b) $\beta t = 10$. The (light blue) continuum of data points represent all different DΓA momenta for a given $\varepsilon_{\mathbf{k}}$. For a better comparison of DΓA with BSS-QMC, we highlighted data points in the DΓA calculation (dark-blue triangles) that correspond to the BSS-QMC data (red circles) with similar $\vec{k}$-points.

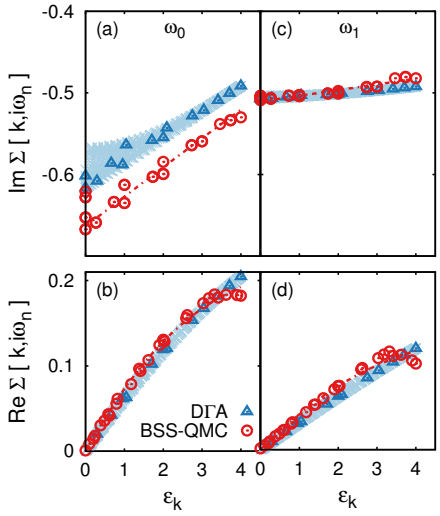

Figure 4.9: (taken from [188]) The self-energy for $U = 4t$, $\beta t = 2$ and the first (left) and second (right) Matsubara frequencies comparing BSS-QMC (red circles) and DΓA (light blue; and dark blue triangles for similar momenta as the red circles).

ara frequency respectively. One can observe that especially for $\varepsilon_{\vec{k}} \to 0$ the spread of Im $\Sigma(i\nu_1, \epsilon_{\vec{k}})$ is much smaller than the one of Im $\Sigma(i\nu_0, \epsilon_{\vec{k}})$, again a feature of the onset of the pseudogap phase. Additionally, the collapse of the real part of the self-energy [lower row of Fig. 4.9(b)] supports the significance of the energy-parametrization of the self-energy.

Eventually, from the above data and discussion, one can conclude, that the switch from the finite-size cluster in BSS-QMC to the thermodynamic limit in DΓA does not impact the qualitative phenomenon of the collapse of the self-energy $\Sigma(\nu, \epsilon_{\vec{k}})$ in energy-parametrization.

Of course, a valid criterion for the practical applicability of exploiting the self-energy collapse is its transferability to other lattice geometries than the simple square lattice one, as is discussed in the next subsection.

4.2.3 Anisotropic Case

One may leave the highly symmetric geometry of the simple square lattice by introducing an **anisotropic hopping** ratio $0 \leq \alpha \leq 1$ with $\alpha = \frac{t_x}{t_y}$. The kinetic energy scale shall be fixed, so $t_y = \sqrt{2t^2/(\alpha^2+1)}$. The main panels of Fig. 4.10 show BSS-QMC results for $\alpha = 1$, $\alpha = 0.8$ and $\alpha = 0.6$ ($U = 4t$ and $\beta t = 5.6$). Please note the following points:

- Increasing the anisotropy α of the lattice results in an increase of the spread of the curves, i.e. the **collapse gets continuously lifted**, both in the imaginary and real parts of the self-energy. However, in the limit of purely one-dimensional hopping (inset, $\alpha = 0$), the collapse

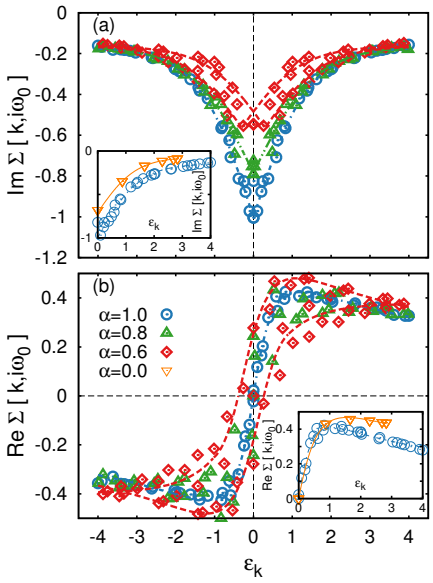

Figure 4.10: (taken from [188]) Imaginary (a) and real (b) part of the self-energy $\Sigma(i\nu_0, \vec{k})$ from BSS-QMC at $U = 4t$ and $\beta t = 5.6$ but for various degrees of anisotropies α.

naturally revives, because, also in momentum-parametrization, the spatial parameter space is only one-dimensional.

- Due to the absence of the high symmetry of the simple square geometry, the Fermi surface is modified stronger. This modification is strongly momentum-dependent. This dependency is, in turn, transferred to the real part of the self-energy, and is much more pronounced than the one of the imaginary part (where the self-energy collapse still works reasonably well for $\alpha = 0.8$).

Concluding, the collapse for the self-energy in energy-parametrization as shown in Sec. 4.2.1 strictly only applies for the case of very weak or very strong anisotropies. However, one can try to deform the Fermi surface also by introducing more/less charge carriers into the system as is done in the next section.

4.2.4 Doping

For practical applications of many-body techniques, doped systems are of high interest (e.g. for the description of high-temperature superconductors), but challenging, especially for BSS-QMC simulations as they suffer from the notorious sign-problem, due to the broken particle-hole symmetry. This results in a high numerical effort, and consequently, the lattice sizes have to be reduced (in this case to $L = 8 \times 8$). Fig. 4.11 shows self-energy data for the isotropic case for several doping levels ($n=t$ represents half-filling here). One can observe the following points:

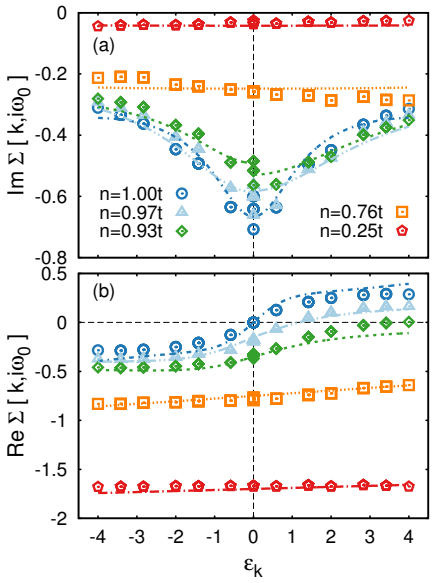

Figure 4.11: (taken from [188]) Imaginary (a) and real (b) part of the self-energy $\Sigma(i\nu_0, \vec{k})$ from BSS-QMC at $U = 4t$, $\beta t = 3.6$ and $L = 8 \times 8$ for doped systems.

- The spread in the imaginary part of the self-energy, although becoming asymmetric with respect to $\epsilon_k = 0$, quickly disappears with doping, so that a parametrization as in the half-filled case remains possible.
- As in the case of anisotropy, the deviation from a smooth energy-parametrization of the self-energy results from Fermi-surface deformations.

Concluding this section about self-energies in two dimensions, one can summarize that a collapse of the self-energies $\Sigma = \Sigma(\nu, \vec{k}) \rightarrow \Sigma(\nu, \epsilon_{\vec{k}})$ can be observed for the isotropic square lattice in and out of half-filling. This collapse, however, is limited in the cases of pseudogaps and strongly anisotropic lattices. Reducing the dimensionality of the system further and switching to one dimension, the (one-dimensional) energy-parametrization introduced above becomes of course exact due to the one-dimension momentum parameter-space. However, as non-local fluctuations are becoming even more dominant in one dimension and exact solutions exist here to compare with, the case of one spatial dimension provides an ideal benchmark for quantum many body theories aiming at the inclusion of non-local correlations and identifying the impact of non-local correlations on spectral functions. Therefore, in the next section, the DΓA is applied to the simplest non-trivial one-dimensional correlated structures, i.e. finite-size Hubbard nanorings and its results are compared to the ones of other many-body techniques as well as to the ones of the exact solution.

4.3 Application of the DΓA to Hubbard nano-rings in one dimension

Parts of this section (marked by a vertical sidebar) have already been published in the APS journal Phys. Rev. B **91**, 115115 (2015).

As this work was done in a collaboration, parts of it appeared also in A. Valli, PhD thesis, TU Wien (2013).

Please note that, due to the one-dimensional problems discussed in this section, here, the index k is a plain momentum-index instead of a general four-index.

Models and materials with reduced dimensionality typically show enhanced correlation effects *beyond* the limit of standard density-functional or perturbation theory-based schemes, calling for corresponding developments of theoretical tools. From a general point of view, the challenge for a theoretical description is much bigger than in bulk systems: In three dimensions (3D), even in the presence of strong electronic correlations, very accurate material calculations can be performed by means of the dynamical mean-field theory (DMFT), [15] combined with *ab-initio* methods. [18, 70] This is possible, because DMFT captures, non-perturbatively, the purely *local* part of electronic correlations, which drives most important phenomena of correlated electrons in the bulk, such as, e.g., the Mott-Hubbard metal-insulator transition (MIT). Formally, DMFT becomes exact in the limit of infinite dimensions [16] where all non-local correlations in space are averaged out. Corrections to DMFT in finite-dimensional systems originate from non-local correlations. While in 3D deviations from the DMFT description become predominant only in specific parameter regimes, [171, 191] e.g., in the proximity of a second order phase transition, [171] the situation is completely different in case of lower dimensions. In fact, reducing the dimensionality magnifies effects of non-local correlations, undermining the main assumption of DMFT.

As for the theoretical description of electronic correlations at the nanoscale, several algorithmic implementations based on DMFT have recently been implemented under the name of **nano or real-space DMFT** [192–196]. Despite some technical differences, all these algorithms essentially extend the DMFT scheme to finite-size and possibly non-translational invariant systems. The common idea consists in solving simultaneously several single impurity problems for calculating, separately, the local self-energies of the different sites composing the system of interest, while the DMFT self-consistency is then enforced at the level of the whole nanostructure. This way, a number of interesting results have been obtained both for model [193, 197, 198] and realistic studies [199–202]. However, the applicability of these DMFT-based methods is restricted to the weakly correlated and/or the high-temperature regime, where the effects of non-local correlations are weaker [20, 171, 191] and can be, to a certain extent, neglected. Such limitations were also openly discussed in the previous literature, [195, 197] where numerical comparisons between DMFT-based calculations and exact solutions (where available) have shown large deviations al-

ready in the intermediate coupling regime.

A promising theoretical answer to this challenging situation has already been proposed, but not implemented, in Ref. [195]: The application of diagrammatic extensions [43, 45, 46, 203] of DMFT such as the dynamical vertex approximation (DΓA) [20] for nanoscopic systems (nano-DΓA). The basic idea of DΓA is the following: Instead of assuming the locality of the one-particle self-energy [$\Sigma(\nu, \vec{k}) = \Sigma(\nu)$], as in DMFT, one raises the assumption of the locality to a *higher* level of the diagrammatics, i.e., from the one- to the two-particle irreducible vertex (Λ) (see Sec. 2.3 and [171, 204]). Once local vertex functions are computed, e.g., with the same impurity solvers used for the standard DMFT [20, 51, 80, 84, 204, 205], non-local correlation effects can be directly included through diagrammatic relations, e.g., in the most general case, through the parquet equations (2.28).

In the specific case of the DΓA implementation for nanoscopic systems [195], the nano-DΓA algorithm requires a separate calculation of the local irreducible vertex function for each inequivalent site of the nanostructure. The inclusion of the non-local effects should be performed at the level of the whole nanostructure via a self-consistent solution of the parquet equations. This procedure is less demanding than the exact treatment of the corresponding quantum Hamiltonian: the exponential scaling with the number of sites required for a diagonalization of the Hamiltonian, is replaced by a polynomial effort to solve the parquet equations. Moreover, the necessity of calculating the vertex functions only locally, mitigates secondary (but important) numerical problems such as the sign-problem in quantum Monte Carlo (QMC) solvers.

The importance of the results presented in the following is twofold, and goes beyond the demonstration of a full applicability of the algorithm proposed in Ref. [195]: Physically, the calculations allow to understand the interplay of local and non-local correlations in spectral and transport properties of finite systems of different sizes; from a methodological perspective, the application of a full (parquet-based) DΓA scheme to these nanoscopic systems represent one of the most severe benchmarks conceivable for this theoretical approach. In fact, the accuracy of a DΓA calculation depends on the correctness of the locality assumption for the two-particle irreducible vertex functions. Heuristically, this assumption looks plausible for 3D and 2D systems with local interactions, where strong spin, charge, and pair fluctuations are already generated by the corresponding collective modes built on local irreducible vertices. Numerically, a direct verification of the DΓA assumption is difficult in 2D or 3D: While the irreducible vertex surely displays a strong frequency dependence (see [51, 204] and Sec. 3.1.1), taken into account by the DΓA, its independence on momentum has been shown explicitly only in few calculations [22, 206] beyond DMFT, where the momentum-dependence was found to be weak. In this section, the focus is, instead, on systems where an exact numerical solution is available, so that both, the DΓA performances and assump-

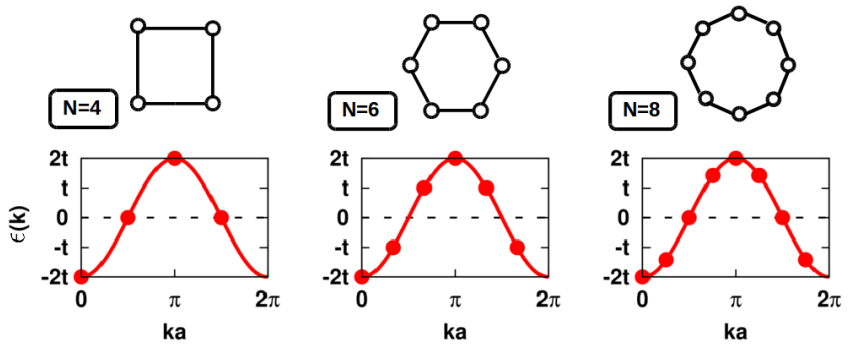

Figure 4.12: Energy-momentum dispersion relation $\epsilon(k)$ with respect to the Fermi level μ (dashed line) for nano-rings with $N = 4, 6, 8$ sites. The symbols denote the discrete eigenstates corresponding to the allowed values of the momentum: $k = 2\pi n/N$, with $n \in \mathbb{N}$.

tions, can be tested. The low connectivity and the peculiarity of 1D physics represent the most challenging situation for DΓA. In this perspective, this numerical analysis will also allow to draw conclusions, on a more quantitative ground, on the physical content of parquet-based approximations.

4.3.1 Modelling the nano-rings

The correlated nanoscopic rings considered in the following consist of N isolated correlated atoms, arranged in a **chain with periodic boundary conditions**, and described by the Hubbard Hamiltonian

$$H = -t \sum_{\sigma} \sum_{i=1}^{N} \left(c^{\dagger}_{i\sigma} c_{i+1\sigma} + c^{\dagger}_{i+1\sigma} c_{i\sigma} \right) + U \sum_{i=1}^{N} n_{i\uparrow} n_{i\downarrow} \tag{4.6}$$

where $c^{\dagger}_{i\sigma}$ ($c_{i\sigma}$) denote the creation (annihilation) operators of an electron on site i with spin σ, fulfilling the periodic boundary conditions $c_{(i+N)\sigma} = c_{i\sigma}$. Due to the translational invariance of the system, granted by the periodic boundary conditions of the ring, it is convenient to formulate the hopping term in the reciprocal space, yielding a tight-binding dispersion $\epsilon(k) = -2t\,\cos(ka) - \mu$, where μ is the chemical potential. In the following, the lattice spacing $a = 1$ and rings with $N = 4, 6, 8$ sites are considered in the half-filled case, i.e., $\mu = U/2$, where electronic correlations stemming from the local Hubbard interaction are expected to be most effective. Under these conditions, all rings display a particle-hole symmetric density of states, and in particular, in the non-interacting case ($U = 0$) the systems display either a "band" gap (as in the case of the $N = 6$ sites ring) or a 2-fold degenerate state at the Fermi level (as in the case of $N = 4, 8$ sites rings). The rings considered and the corresponding dispersions $\epsilon(k)$ are shown in the upper and lower panel of Fig. 4.12, respectively.

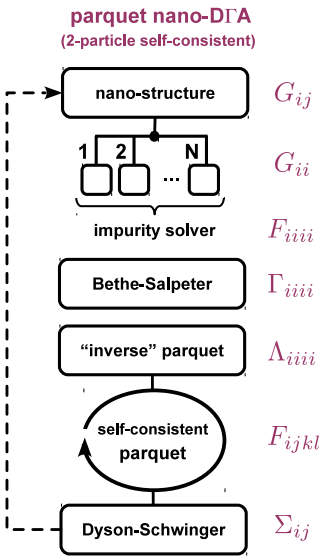

Figure 4.13: Flowchart of the parquet implementation of the nano-DΓA. See text for a related discussion.

4.3.2 Parquet-based implementation of the nano-DΓA

It should be recalled from Sec. 2.3 that the idea of DΓA is to apply the locality assumption of DMFT at an higher level of the diagrammatics: While in DMFT all one-particle irreducible (1PI) one-particle diagrams (i.e., the self-energy Σ) are assumed to be purely local, DΓA confines the locality to the two-particle irreducible (2PI) two-particle diagrams, i.e., the fully irreducible vertex Λ is approximated by all local Feynman diagrams. Hence, in the DΓA framework, the purely local, but frequency-dependent 2PI vertex $\Lambda^{\nu\nu'\omega}_{iiii}$ is calculated for a site i and then used as the input for the parquet equations. In practice, this vertex is obtained by solving the Anderson impurity model (AIM) numerically. Hence, non-local correlations on top of the DMFT solution are generated in *all* scattering channels by the (numerical) solution of the parquet equations (2.28) without any restriction to specific (ladder) subsets of diagrams (see Sec. 2.3.2.1). For the sake of clarity, it should be emphasized that this is different from the so-called parquet approximation (PA, see also Sec. 2.3.1). In fact, the PA corresponds to approximating the 2PI vertex with the bare interaction of the theory (e.g., $\Lambda = U$) in a merely perturbative fashion. On the contrary, in DΓA all non-perturbative DMFT correlations, which control, e.g., the physics of the Mott-Hubbard transition, are actually included through the frequency dependent $\Lambda^{\nu\nu'\omega}$, and non-local correlations beyond DMFT are generated via the solution of the parquet equations.

The specific implementation of the parquet-based DΓA scheme for the case of nanoscopic systems, such as the Hubbard nano-rings, is briefly sketched in the flowchart of Fig. 4.13, and incorporates all main aspects of the original proposal of Ref. [195]. The DMFT scheme for a nanoscopic

system with N constituents (e.g., atoms), which is self-consistent at the one-particle level only. Its first step consists in mapping the full problem onto a set of auxiliary AIMs, one for each of the N sites of the nanostructure. Each auxiliary problem is characterized by a dynamical Weiss field (i.e., the non-interacting Green function of the AIM) $\mathcal{G}_{0i}(\nu)$. The numerical solution of the AIM yields the local Green function $G_{ii}(\nu)$ and the local DMFT self-energy $\Sigma_{ii}(\nu) = \mathcal{G}_{0,ii}^{-1}(\nu) - G_{ii}^{-1}(\nu)$. Through the Dyson equation the local (yet site-dependent) DMFT self-energies determine the new non-local Green function G_{ij}, and the self-consistency is realized at the level of the whole nanostructure.

In the case of the DΓA this procedure is raised to the two-particle level. For each inequivalent AIM, the local 2PI vertex function has to be computed. Once all inequivalent local 2PI vertices Λ_{iiii} are obtained for each site i, they are used as an input for the solution of the parquet equations for the whole nanoscopic system. This yields the non-local full two-particle vertex function F_{ijkl} and, through the Dyson-Schwinger equation, the non-local self-energy in real space:

$$\Sigma_{ij} = \frac{Un}{2}\delta_{ij} - \frac{U}{\beta^2}\int \sum_{klm} G_{ik}G_{il}G_{im}F^{\uparrow\downarrow}_{klmj}, \tag{4.7}$$

where the integral symbol, as above, denotes a summation over all the internal degrees of freedom, while the sum over the spatial indices of the nanoscopic system is explicit. Please note that the local Hartree shift of the self-energy $\Sigma_{\mathrm{H}} = Un/2$ is already included in the definition of the chemical potential. The set of equations (Parquet (2.28), Bethe-Salpeter (2.29) and Dyson-Schwinger equations (4.7)) can be solved self-consistently until the non-local self-energy (4.7) is converged [61, 140]. The flowchart of the parquet DΓA is shown schematically in Fig. 4.13. Finally, after having determined Σ_{ij} one can either skip the outermost loop, i.e., updating the AIM and simply start from $\mathcal{G}_{ii}$ of DMFT, as is done for the results of the current section, or one can perform fully self-consistent calculations; In the latter case the $\mathcal{G}_{ii}$ of the corresponding inequivalent AIMs has to be adjusted to yield the given DΓA G_{ii} from the previous iteration before recalculating the 2PI vertex (which is defined diagrammatically in terms of U and G_{ii}). One then needs to iterate this scheme until convergence.

4.3.3 Results

In the following numerical results for all Hubbard nano-rings discussed in Sec. 4.3.1 are presented, characterized by the dispersions $\epsilon(k)$ shown in Fig. 4.12 (lower panels). For each system different approximations, i.e., **DMFT, PA, and parquet DΓA**, are compared to the **exact QMC** solution. Each method employed is associated to a specific diagrammatic content, as discussed in Sec. 4.3.2 and 2.3.1, which allow for an understanding of the relevance of specific subsets of Feynman diagrams for the description of the systems considered. Later, in Sec. 4.3.4, another comparison

of the self-energies will be employed with the ones obtained within the **ladder approximation of the DΓA** scheme introduced in Sec. 4.3.4.

Results are discussed for the electronic self-energy $\Sigma(\nu,k)$, the local Green function in imaginary time $G_{ii}(\tau)$, and the two-particle irreducible local (i.e., DMFT) vertex function $\Lambda^{\nu\nu'\omega}_{iiii}$. The analysis of the self-energy allows to resolve a k-selective behavior in the (discrete) reciprocal space. In particular, low-energy parameters are analyzed (for three dimensions, see Sec. 4.1.1 and Eq. (4.1)), i.e., the scattering rate $\gamma(k) \equiv -2\mathrm{Im}\Sigma(\nu, k \to 0)$, which corresponds to a damping or to the inverse lifetime of quasi-particle excitations in the Fermi liquid regime, and the (static) renormalization of the bare dispersion $\Delta(k) \equiv \mathrm{Re}\Sigma(\nu \to 0, k)$. The effect of the local and non-local self-energy on the low-energy spectral properties of the system are discussed, which can be deduced by the local Green function, and is related to the k-resolved spectral function $A(\nu,k)$ by

$$G_{ii}(\tau) = \sum_k \int_{-\infty}^{\infty} d\nu \frac{\mathrm{e}^{-\tau\nu}}{1+\mathrm{e}^{\beta\nu}} A(\nu,k). \tag{4.8}$$

The value of the Green function at $\tau = \beta/2$ represents an estimate of the value of the local spectral function at the Fermi level (averaged over an energy window proportional to the temperature T), i.e.,

$$-\beta G_{ii}(\beta/2) \approx \pi \sum_k A(0,k). \tag{4.9}$$

In order to understand the non-local self-energy corrections beyond mean-field, the results will be related to the frequency structure of the local 2PI vertex (Λ_{iiii}), which is the input for the parquet equations of the DΓA. To this end, the generalized susceptibility of the AIM is computed and the 2PI vertex is obtained following the steps discussed in Sec. 4.3.2.

4.3.3.1 $N=6$: "insulating" ring

In Fig. 4.14the local DMFT self-energy are compared with the k-resolved self-energy for representative k points[1] in the discrete Brillouin zone (DBZ), namely $k=0$ and $k=\pi/3$, obtained by means of PA, DΓA and exact QMC solution. Concerning the imaginary part of the self-energy Im $\Sigma(\nu,k)$, one can note that all the approximations employed provide a qualitative and quantitative agreement with the exact solution. The system displays a low scattering rate γ_k, which is consistent with the picture of an insulating ground state reminiscent of the band gap of the non-interacting spectral function (renormalized by electronic correlations), rather than driven by a Mott MIT. More specifically, the exact QMC self-energy displays a weak k-dependence at low frequencies, resulting in a slightly different scattering rate γ_k for different k points in the DBZ. While this feature cannot

[1] Due to the particle-hole symmetry and to the degeneracy of the non-interacting eigenstates, the other components of the k-resolved self-energy can display, at most, a sign change with respect to the ones shown here.

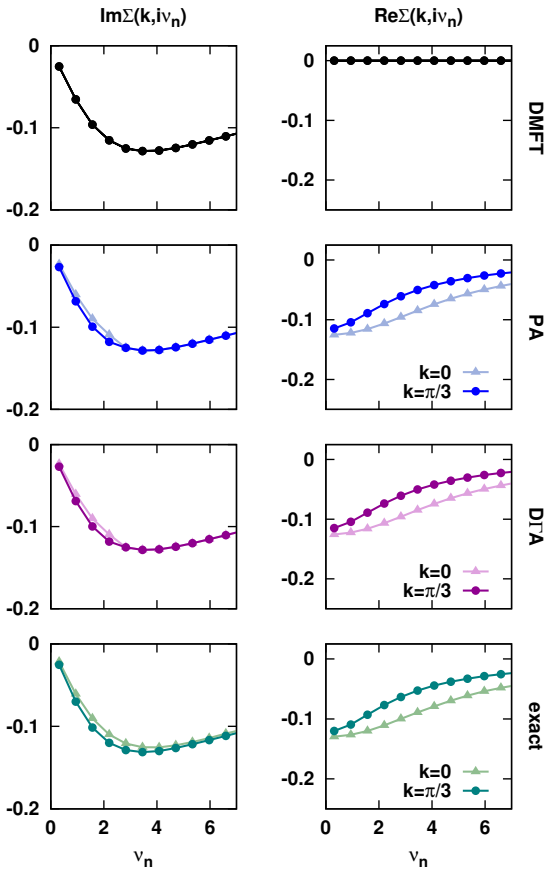

Figure 4.14: Comparison between the local DMFT self-energy in Matsubara representation and the k-resolved PA, DΓA, and the exact self-energy, for representative k-points in the DBZ. In this case, including the full frequency dependence of Λ results in negligible corrections to the static PA. Parameters: $N=6$, $U=2t$ and $T=0.1t$.

be reproduced within DMFT by definition, it is well captured including non-local correlations beyond mean-field. Concerning the real part of the self-energy, one can observe that within DMFT Re $\Sigma(\nu)=0$, i.e., all contributions averaging out in the local picture, except for the Hartree term, which is included in the redefinition of the chemical potential, i.e., $\mu \to \mu - U/2$ at half-filling. On the contrary, including non-local correlations beyond mean-field a sizable k-dependent self-energy Re $\Sigma(\nu, k)$ is found. In all cases the exact self-energy is quantitatively well reproduced.

Fig. 4.15 shows the effect of non-local correlations on the local Green function $G_{ii}(\tau)$. In the case of the $N=6$ sites ring, the interpretation of the results is straightforward. In fact, all methods predict an insulating solution, and this is reflected by $G_{ii}(\beta/2) \approx 0$. However, at a closer look one can notice that the DMFT predicts more spectral weight $A(0)$, or equivalently a smaller value of the spectral gap, than the other methods. It is interesting to notice that, considering specifically $A(0)$,

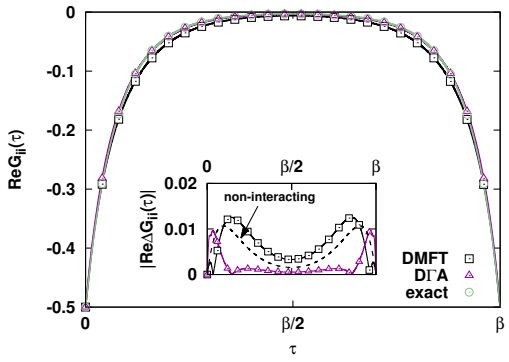

Figure 4.15: Comparison of the local Green function $G_{ii}(\tau)$ obtained from the corresponding DMFT, DΓA and exact self-energy. The inset shows the difference $\Delta G_{ii}(\tau)$ between the corresponding approximation and the exact solution. Parameters: $N=6$, $U=2t$ and $T=0.1t$.

the DMFT is worse than the non-interacting case, while obviously DMFT is superior in several other respects, e.g., lifetime of one-particle excitation. This is clearly shown in the inset of Fig. 4.15, where plot the difference $\Delta G_{ii}(\tau)$ of the local Green function for the different approximations with respect to the one of the exact solution is plotted. Hence, one can "disentangle" the roles played by local and non-local correlations on an insulator considering that, in an insulator

i) taking into account only local correlations within DMFT reduces the non-interacting spectral

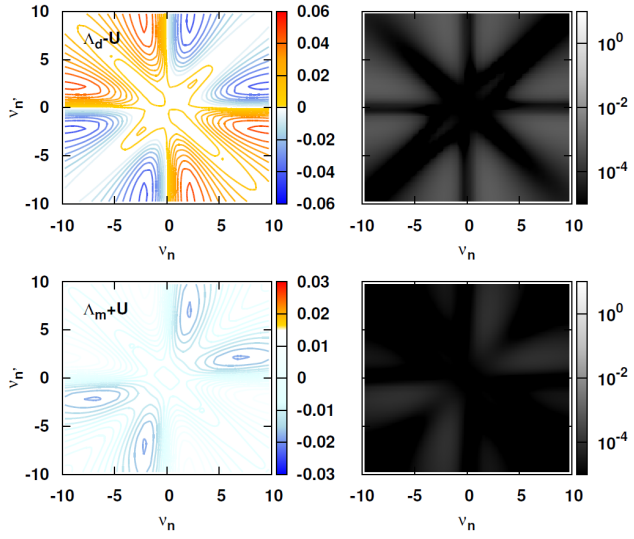

Figure 4.16: Local two-particle fully irreducible vertex calculated in DMFT in the (particle-hole) density and magnetic channels with respect to the static asymptotics, i.e.: $\Lambda_d - U$ (upper row) and $\Lambda_m + U$ (lower row), as a function of the two fermionic frequencies ν_n and $\nu_{n'}$, for bosonic frequency $\omega = 0$. The isoline plot (left panels) highlights the frequency and sign structure of the vertex, while the gray-scale density plot (right panels) shows its logarithmic intensity. Parameters: $N=6$, $U=2t$, and $T=0.1t$.

gap, [207] and

ii) the non-local correlations in the exact solution display the opposite trend, as correctly described by the DΓA.

Indeed, the analytic continuation of the Green function by means of the maximum entropy method (not shown) confirms the expectations, yielding a spectral gap $\Delta \approx 1.9t$ within DMFT and $\Delta \approx 2.2t$ within DΓA and the exact solution, to be compared to the non-interacting value $\Delta_0 = 2t$.

One can understand the results obtained for both the self-energy and the local Green function within the different approximations, by taking a closer look at the local fully irreducible vertex calculated from the DMFT Green function. The isolines and the density plot in the left and right panels of Fig. 4.16, respectively, highlight the sign and the logarithmic intensity of the frequency structure of $\Lambda_{d,m}$. The fully irreducible vertex displays the typical **butterfly structure** see [51] or Sec. 3.2.1) with positive and negative lobes decaying to the bare interaction value at high frequency (beyond the frequency range shown here). The frequency structure of the 2PI vertex beyond the static asymptotics is negligible with respect to the bare interaction $U = 2t$. This is a consequence of the spectral gap, resulting in insulating Green functions already within DMFT. The inversion of sign at low frequencies in the first and third quarter of the (ν, ν') plane originates, instead, from the precursor lines of the Mott transition discussed in Sec. 3.1.1. The negligible frequency structure of the local 2PI vertex explains why the DΓA self-energy does not deviate from the plain PA result in this case. On the other hand, the quantitative agreement with the exact QMC solution, suggests that the local DΓA assumption of the 2PI is justified in this system. The direct numerical analysis of the exact 2PI vertex confirms that, besides a structure in momentum space, its overall values yield moderate corrections to the bare interaction $U = 2t$ (not shown).

4.3.3.2 $N = 4$ and $N = 8$: "correlated metallic" rings

In contrast to the previous system, both the $N = 4$ and $N = 8$ sites rings are characterized by the presence of a (doubly degenerate) eigenstate at the Fermi level of the non-interacting density of states. For this reason one could expect them to display a similar behavior, and a different low-energy physics with respect to the $N = 6$ sites ring. As will be shown, this is only partially true. First, the k-resolved self-energy of the $N = 4$ ring, shown in Fig. 4.17 for representative k points in the DBZ, namely $k = 0$ and $k = \pi/2$ (the latter at the Fermi surface), will be discussed. In this case the DMFT self-energy displays a non-Fermi liquid behavior, characterized by a large yet finite scattering rate γ (obviously independent on k). As one can see below, the system is not gapped in DMFT. The DMFT picture, however, is substantially changed by non-local correlations, as reflected in a strong k-dependent behavior of the self-energy, found within all approximations considered. In particular, away from the Fermi surface (e.g., at $k = 0$) all approximations yield a low scattering rate

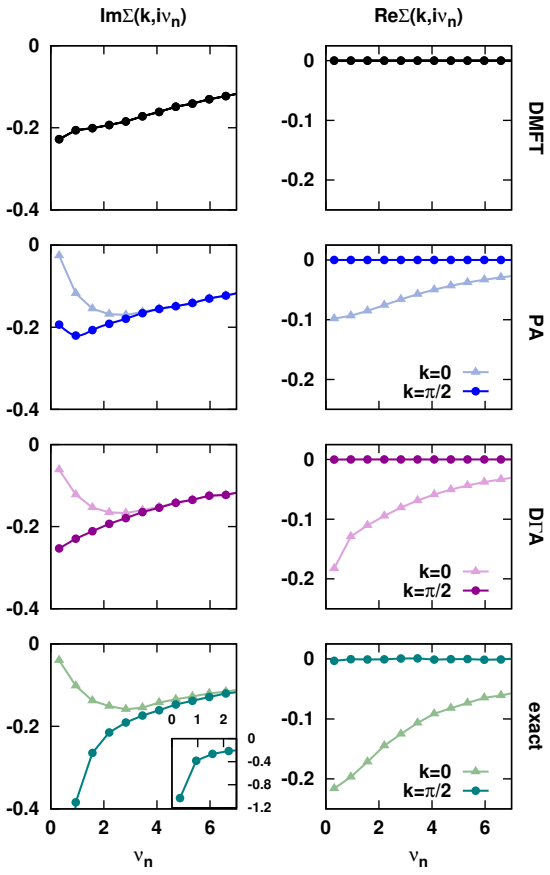

Figure 4.17: As in Fig. 4.14 but for the $N=4$ ring. In contrast to the previous case, including the full frequency dependence of Λ leads to a substantial improvement of the DΓA over the static PA. The inset shows the low-energy tendency toward a divergence of the exact self-energy for $k=\pi/2$.

$\gamma_{k=0}$ due to the bending towards zero of $\mathrm{Im}\Sigma(\nu,k)$. The situation is drastically different at the Fermi surface (e.g., at $k=\pi/2$), where in the exact solution, the divergent tendency of the self-energy marks the opening of a gap in the spectral function. Taking into account all scatting channels within the parquet DΓA formalism leads to an improvement with respect to the DMFT results. While the PA yields a sizable scattering rate $\gamma_{k=\pi/2}\approx 0.4$, including the frequency dependence of the fully irreducible vertex within DΓA further enhances $\gamma_{k=\pi/2}$ and reproduce correctly the qualitative trend of the exact self-energy, as well as an overall better description of the Re $\Sigma(k,\nu)$ with respect to PA and DMFT. The quantitative difference between the parquet DΓA and the exact solution may originate either from the momentum dependence of the 2PI vertex, neglected in DΓA, or by the lack of self-consistency.

Further insights can be obtained by considering the spin propagator $\chi_s^{\omega}(q)$, in particular at $\omega=0$.

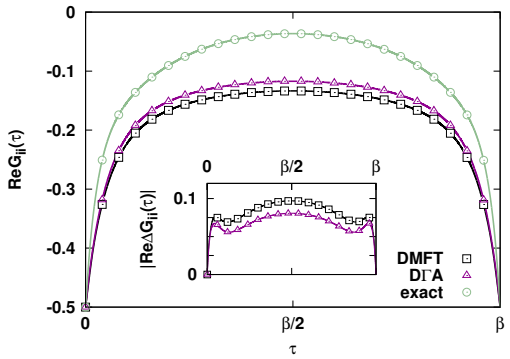

Figure 4.18: As in Fig. 4.15 but for the $N=4$ ring.

Within DMFT, we find that $\chi_s(q=\pi)<0$. The unphysical value of the susceptibility indicates that the system is **below the Néel temperature of DMFT** (see also Sec. 6.3), i.e., $T<T_N^{\mathrm{DMFT}}$, while no ordering is expected at finite temperature. Including non-local spatial correlations within the parquet DΓA scheme reduces T_N [159]. However, it is plausible that the local physics described by DMFT, and hence the information encoded into the 2PI vertex of DMFT, can be very different from the local physics of the exact solution.

What are the effects of local and non-local correlations on the Green function? Both in DMFT and DΓA, a sizable value of $G_{ii}(\beta/2)$ indicates a metallic spectral function, while in the exact solution this quantity is strongly suppressed, revealing an insulating nature. In this respect, one should note that, even in the insulating state, a value of $G_{ii}(\beta/2)=0$ can only be achieved at $T=0$, while here one observes a finite value due to the average over an energy window due to the broadening of the Fermi distribution at finite temperature. The combined information of a sizable value of $G_{ii}(\beta/2)$ and the large scattering rate γ_k at the Fermi surface (i.e., $k=\pi/2$) in the corresponding self-energy in Fig. 4.17 suggest the presence of a local minimum in the spectral function at the Fermi level (pseudogap). Hence, one can conclude that the DΓA, in its full parquet-based implementation, yields a quantitative improvement over the DMFT description, however, the non-local correlations stemming from the 2PI local vertex of DMFT are not yet strong enough to completely open a well-defined gap in the spectral function, which is instead present in the exact solution.

A deeper understanding of the above results can be obtained by the analysis of the frequency and momentum structure of the 2PI vertex. The local 2PI vertex is shown in Fig. 4.19. The most striking feature of the vertex of the $N=4$ sites ring is the strongly enhanced low-frequency structure which now exhibits strong deviations from the bare interaction $U=2t$. In fact, the vertex corrections are orders of magnitude larger than for the $N=6$ insulating ring, and the low-frequency structure is also more complex. In particular, one can observe additional negative "spots" (of highest intensity) which are generated by the change of sign of several eigenvalues of the generalized local suscep-

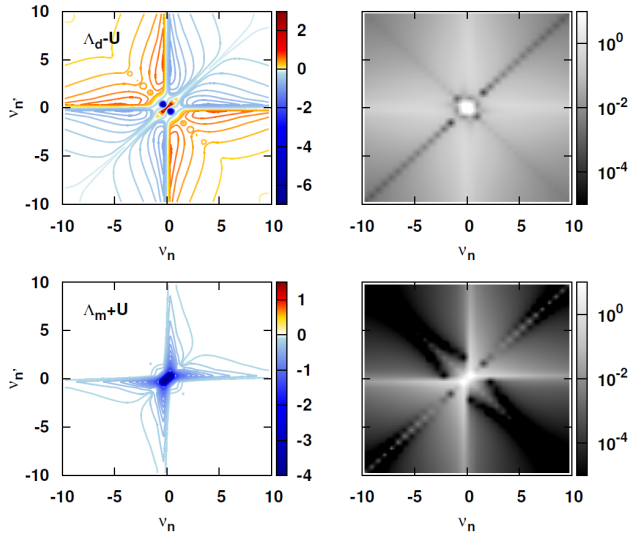

Figure 4.19: As in Fig. 4.16 but for the $N=4$ ring.

tibility (see Sec. 3.1.1). This low-frequency structure of the local 2PI vertex is responsible for a k-selective enhancement of the DΓA self-energy over the one obtained within the PA.

The direct numerical evaluation of the exact 2PI vertex, shown in Fig. 4.20, allows to understand the role of its momentum structure. The q-resolved exact fully irreducible vertex $\Lambda(q) = \frac{1}{N_k^2} \sum_{kk'} \Lambda_{kk'q}$ shows that $\Lambda(q)$ displays a change in both sign and magnitude for different values of q (the vertex is identical at $q = \pm\pi/2$ due to symmetry reasons). Such a large frequency and momentum dependence of the exact 2PI vertex can be possibly interpreted in terms of a proximity to a non-perturbative instability of the Bethe-Salpeter equations (see Sec. 3.1.1). The strong momentum dependence of the fully irreducible vertex is certainly one of the reasons of the failure of the present DΓA calculation to open a spectral gap at the Fermi level of the $N=4$ sites ring. However, an important piece of information is also enclosed in the exact local vertex $\Lambda = \frac{1}{N_q} \sum_q \Lambda(q)$. As shown in Fig. 4.20, the exact local Λ displays a complex frequency structure, which is not fully captured by the local Λ of DMFT (cf. with Fig. 4.19). This suggests that, in this case, DMFT does not provide a good description of the two-particle local physics of the system. For this reason, performing a full self-consistency at the two-particle level, i.e., updating the local Λ including the effect of non-local correlations, is expected to lead to improvements over the present DΓA results. This idea is also supported by the calculations performed within the ladder approximation of the DΓA, discussed in Sec. 4.3.4 in comparison with the parquet DΓA.

Finally, the results for the $N=8$ sites ring are discussed, where the presence of additional structures in the non-interacting density of states, besides the (doubly degenerate) eigenstate at the Fermi level and the one at the band edge lead to a somewhat different physical situation. The

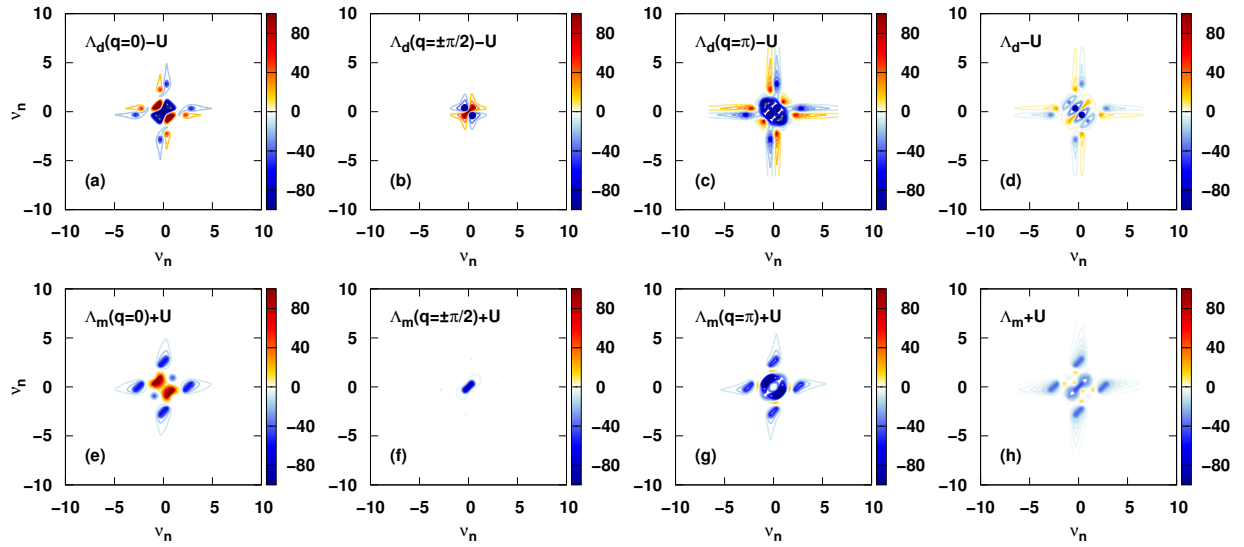

Figure 4.20: Exact fully irreducible vertex in the (particle-hole) density and magnetic channels with respect to the static asymptotics, i.e.: $\Lambda_d - U$ (upper row) and $\Lambda_m + U$ (lower row), as a function of the two fermionic frequencies ν_n and $\nu_{n'}$, for bosonic frequency $\omega = 0$. The q-resolved vertex $\Lambda(q)$ (panel a, b, c, e, f, and g) corresponds to the fully irreducible vertex averaged over k and k', while the local Λ (panel d and h) is averaged over q as well. In addition to the non-trivial momentum structure of $\Lambda(q)$, neglected within the parquet DΓA, it is worth noting that the complex frequency structure of the local Λ is not captured from the DMFT vertex (cf. Fig. 4.19). This suggests that a full self-consistency at the two-particle level, via a corresponding redefinition of the AIM, might improve the present DΓA results. Parameters: $N = 4$, $U = 2t$, and $T = 0.1t$.

k-resolved self-energy is shown in Fig. 4.21. As N increases, the number of inequivalent k points in the DBZ increases with respect to the previous cases. By symmetry it is sufficient to consider $k = 0$, $k = \pi/4$, and $k = \pi/2$ (the latter at the Fermi surface). In this case, in contrast to the $N = 4$ sites ring, the DMFT self-energy shows a metallic bending, with a (k-independent) scattering rate $\gamma \approx 0.1$. The comparison with the exact solution shows that the largest corrections with respect to DMFT are the enhanced scattering rate at the Fermi surface, $\gamma_{k=\pi/2}$, and the renormalization of the dispersion $\Delta_{k=0,\pi/4} = \text{Re}\,\Sigma(\nu \to 0, k)$. The PA and the DΓA give rise to similar non-local correlations, displaying a strong k-dependent scattering rate at the Fermi surface $\gamma_{k=\pi/2} \approx 0.3$. The large scattering rate reflects physically in the Green function through a suppression of $G_{ii}(\beta/2)$, and hence of the low-energy spectral weight, with respect to DMFT, as shown in Fig. 4.22. Although DΓA provides an overall better description of the low-energy physics of the system with respect to DMFT, also in this case the parquet-based approximations **fail to reproduce the divergent behavior of** Im $\Sigma(\nu, k = \pi/2)$.

As for the interpretation of the results, from the similarity of the PA and DΓA results for the $N = 8$

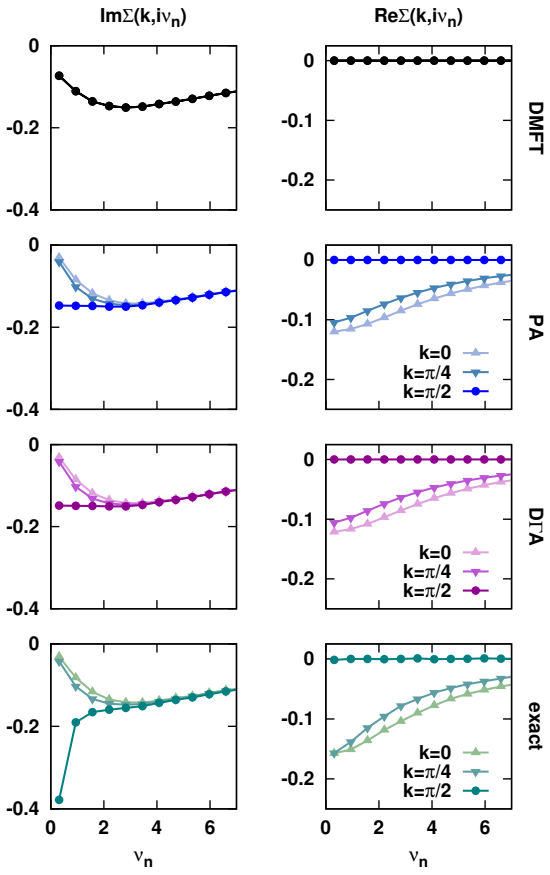

Figure 4.21: As in Fig. 4.14 but for the $N = 8$ ring. In this case, including the full frequency dependence of Λ results in negligible corrections to the self-energy, and the DΓA results does not deviate appreciably from the one obtained within the static PA.

sites ring one would not expect a strong frequency dependence of the local 2PI vertex, as confirmed from the numerical data shown in Fig. 4.23. The 2PI vertex qualitatively resembles the

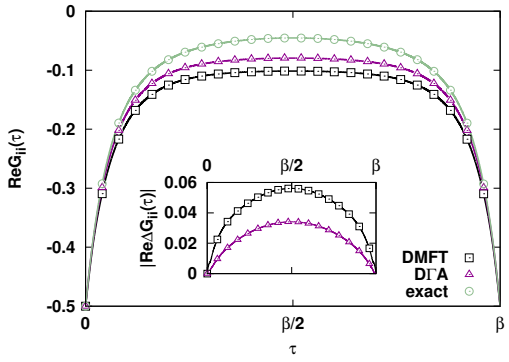

Figure 4.22: As in Fig. 4.15 but the $N=8$ ring.

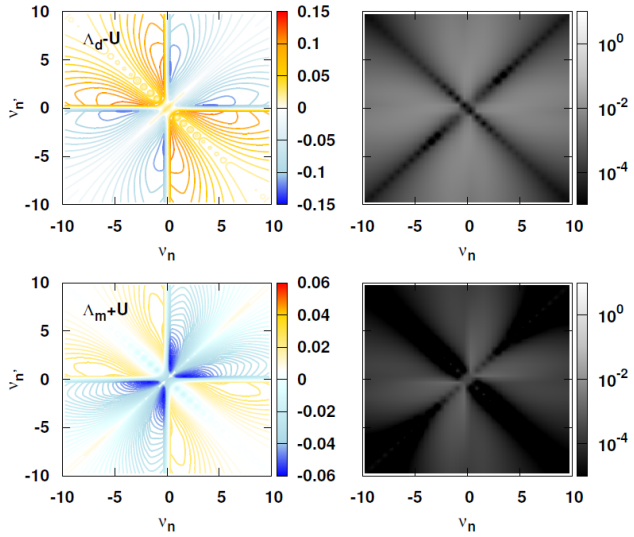

Figure 4.23: As in Fig. 4.16 but for the $N=8$ ring.

one of the $N=6$ sites ring, with the difference that there is no suppression of the low-frequency structure. On the other hand, the difference between DΓA and the exact solution might suggest an important momentum structure of the 2PI vertex. Unfortunately in this case a direct analysis is not feasible, due to the extremely high computational effort required to calculate the exact momentum-dependent two-particle vertex functions for the $N=8$ site ring. While a strong momentum dependence of the exact 2PI vertex is possible, also in this case the deviation observed between the parquet DΓA and the exact solution might be induced by the poor approximation of the local physics of the system provided by the 2PI vertex of DMFT. This scenario, supported by the qualitatively correct behavior found within the Moriya corrected ladder approximation in the next section, suggests that the parquet DΓA results might be further improved performing a **fully self-consistent calculation**.

4.3.4 Relation to the ladder approximation

The ladder approximation is obtained by replacing the solution of the parquet equations in the flowchart of Fig. 4.13 with a simpler calculation at the level of Bethe-Salpeter equations (see Sec. 2.3.2.2). Hence, in ladder-DΓA the non-local corrections to the local physics will be generated only in (a) selected channel(s). In practice, this corresponds to an essential simplification of the algorithm, because in ladder DΓA only the corresponding irreducible vertex in the selected channel (e.g., spin) needs to be extracted from the AIM, and used to calculate the DΓA self-energy via the Bethe-Salpeter equation.

The application of the ladder approximation is well justified in case the system displays predomi-

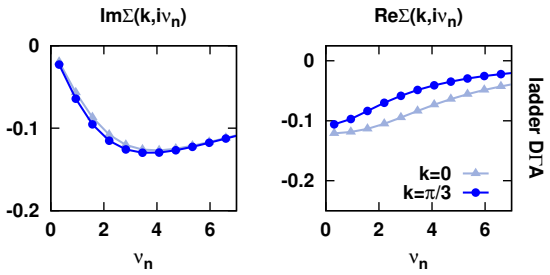

Figure 4.24: k-resolved ladder DΓA self-energy in Matsubara representation, for representative k-points in the DBZ. The ladder resummation was supplied with the Moriyaesque correction to the spin propagator. Parameters: $N=6$, $U=2t$ and $T=0.1t$.

nating fluctuations in a given scattering channel, which is known *a priori*, e.g., in the case of the antiferromagnetic instability in the 3D Hubbard model at half-filling [171]. However, the significant numerical simplification of avoiding the solution of the direct and inverse parquet equations comes at the price of a more approximative approach, which is mitigated by performing the so-called Moriya-correction (see Sec. 2.3.2.2). In the case of the $N=6$ sites ring, the ladder DΓA self-energy, shown in Fig. 4.24, is in good agreement with both the parquet DΓA and the exact results (cf. also Fig. 4.14 for a direct comparison). Slight deviations suggest that, although at half-filling the physics is expected to be dominated by spin fluctuations, in low-dimensions considering all the scattering channels (and their interplay) on the same footing, via the solution of the parquet equations, leads to quantitative corrections in this parameter regime. The situation is different in the cases of the $N=4,8$ sites rings. In particular, the ladder DΓA self-energy, shown in Figs. 4.25 and 4.26, is able to capture the large scattering rate at the Fermi surface $\gamma_{k=\pi/2}$ of the exact solution, **improving over the parquet-DΓA results**. This unexpected result is likely to be attributed to the ability of the Moriyaesque corrections to **mimic the self-consistency of the local (irreducible)**

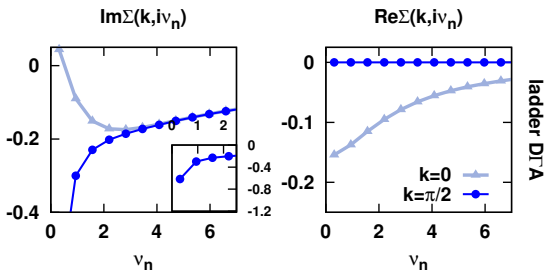

Figure 4.25: As in Fig. 4.24 but for the $N=4$ ring The non-causal self-energy for $k=0$ (gray dashed line) observed in this case is an extreme consequence of the breakdown of the ladder approximation far from the Fermi surface, as discussed in the text. The inset shows the low-energy tendency toward a divergence of the ladder DΓA self-energy for $k=\pi/2$.

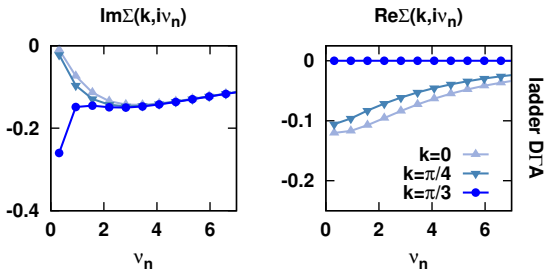

Figure 4.26: As in Fig. 4.24 but for the $N=8$ ring.

vertex. This suggests that also the full parquet DΓA might be able to reproduce the divergent trend of the self-energy at the Fermi surface with a better starting point for the local fully irreducible vertex than the one provided by DMFT. This would definitely be achieved by performing fully self-consistent DΓA calculations.

The ladder DΓA calculations performed here also pointed out an important issue, i.e., the **failure of the ladder approximation far away from the Fermi surface.** This is indicated for the $N=4$ sites ring by the **non-causal self-energy** obtained at the lowest Matsubara frequency for $k=0$. Several tests in this case ruled out the possibility that the non-analyticity of the self-energy is a physical artifact due to numerics (e.g., due to the finite frequency mesh).

By exploiting the (hitherto) unique possibility of having at disposal both ladder- and parquet DΓA self-energy and vertex results, a decomposition of the DΓA self-energy, by separating the contributions coming from the different channels, following a similar "philosophy" as in the parquet-decomposition of the electronic self-energy introduced in Sec. 3.3. The assumption, under which a simplification of the parquet DΓA algorithm to the ladder DΓA is possible, is that the (k-dependent) non-local corrections to the DMFT self-energy are dominated by the contribution of a specific channel (e.g., at half-filling, the spin channel). The parquet decomposition of the ladder DΓA self-energy, shown in the left and middle panels of Fig. 4.27, demonstrate that this is indeed the case for the calculations of the self-energy at the Fermi level ($k=\pi/2$). On the other hand, one can also see that, in the case of the $N=4$ sites ring, the **ladder assumption does not apply any longer far from the Fermi surface**. In fact, as shown in Fig. 4.27, at $k=0$ the contribution of the spin-channel to the DΓA self-energy is strongly reduced with respect to the $k=\pi/2$, becoming comparable with the contributions of the other channels. This means that the error introduced by ladder assumptions might become even larger than the value of Im $\Sigma(k)$ itself, which is often strongly reduced by non-local correlation far from the Fermi surface. It is important to emphasize that the overall trend of a strong reduction of Im $\Sigma(k=0)$ due to non-local correlation, which is also visible in the exact results, is correctly captured even by the ladder DΓA calculations. However, quantitatively, the

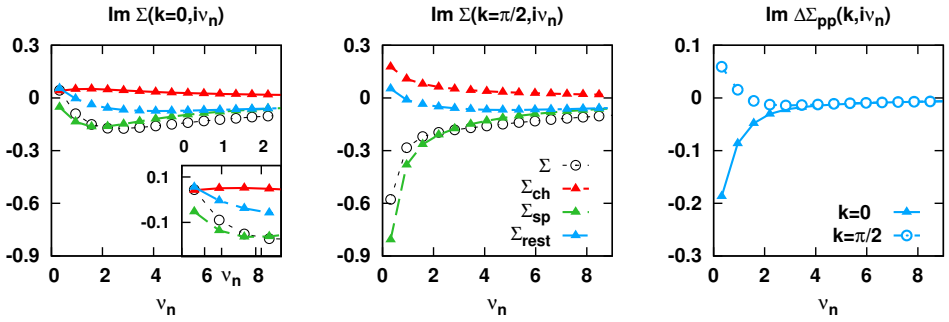

Figure 4.27: [Left and middle panels] Parquet decomposition of the ladder-DΓA self-energy, where Im $\Sigma(\nu, k)$ has been resolved in its contributions from the spin channel, the charge channel, and all the rest. Within the ladder approximation, at $k = \pi/2$ the contribution of the spin channel is dominant, while at $k = 0$ all contributions are similar in magnitude. The inset shows the low-energy behavior of the different self-energy contributions at $k = 0$. [Right panel] Non-local parquet DΓA correction to the DMFT self-energy computed in the particle-particle scattering channel $\Delta\Sigma_{pp}$. Its strong k-dependence, neglected within the ladder approximation is at the origin of the causality violation of the ladder-DΓA self-energy at $k = 0$ (cf. Fig. 4.25). Parameters: $N = 4$, $U = 2t$ and $T = 0.1t$.

breakdown of the ladder assumption for this k-point leads to a large relative error on Im $\Sigma(k = 0)$, and eventually to an **analyticity violation**, preventing the applicability of the ladder-DΓA for this k-point. This explanation is numerically supported by the comparison with the corresponding decomposition of the full parquet DΓA self-energy. Specifically, in the right panel of Fig. 4.27 the momentum dependence of the "secondary" (particle-particle) channel contribution to Im $\Sigma(\nu, k)$ is shown. At $k = 0$, the correction with respect to DMFT (neglected in ladder DΓA) is actually of the same order, if not larger, than the contribution of the "dominant" channel and/or of the overall value of Im $\Sigma(k = 0)$, shown in the left panel of Fig. 4.27. Although the deterioration of accuracy of the ladder approximation far from the Fermi surface may be expected as a general trend, the error introduced is often not significant. For instance, in the parameter regime considered for the $N = 8$ sites ring, causality is preserved. As the particle-hole channel is dominant in the vicinity of the Fermi level, neglecting the particle-particle channel is justified for this (most relevant) part of the DBZ, and the ladder approximation can still be employed.

Recently, an alternative route for performing λ-corrections was proposed which potentially could overcome the non-analyticity of the ladder-DΓA far away from the Fermi surface (for details see [68]).

5

The Mott-Hubbard transition and its fate in 2D

“Non temer; ché ’l nostro passo
non ci può tòrre alcun: da tal n’è dato.“

”Do not be afraid; our fate
Cannot be taken from us; it is a gift.”

- Dante Alighieri (Italian writer and philosopher, *1265 - †1321),
Inferno, Canto **VIII**, 104-105 (1313).

One of the most intriguing and prototypical phenomena in strongly correlated many-body systems is, without a doubt, the Mott-Hubbard metal-insulator transition (MIT). The first coherent theoretical description of this MIT has represented one of the biggest successes of the dynamical mean field theory (DMFT). Formally, DMFT becomes exact only in the limit of lattices with infinite coordination numbers (or dimensions), but it still provides an accurate description of the Mott-Hubbard MIT in the case of three-dimensional bulk materials. However, if considering systems with lower dimensionality (such as layered or two-dimensional compounds), spatial fluctuations must be included, which are neglected by DMFT. In this Chapter, the theoretical description of the Mott-Hubbard MIT is revisited for the two-dimensional half-filled Hubbard model on a square lattice. First, the basic mechanism of the MIT is explained and the differences to a common band insulator are clarified. Then, the DMFT results for the MIT, where only local correlations are included, are discussed, . Afterwards the physics of two dimensions is studied by successively including spatial correlations on longer and longer length scales by means of cluster extensions of DMFT. Eventually, the actual thermodynamic MIT is shown to vanish in favor of a metal-insulator crossover once spatial correlations on all length scales are included by means of the dynamical vertex approximation. Spin-fluctuations in the paramagnetic phase (Slater-paramagnons) are identified as the microscopic mechanism for opening up a spectral gap at every (finite) value of the Hubbard repulsion at low enough temperature.

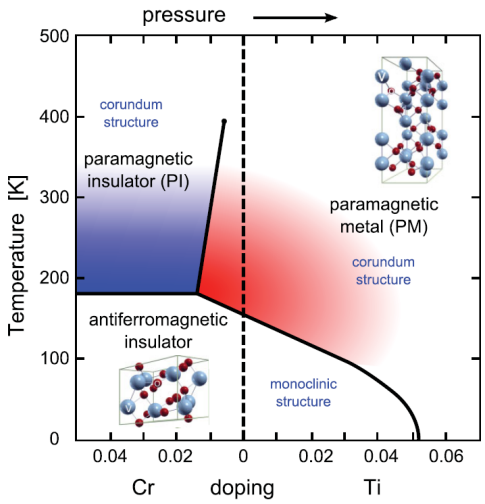

Figure 5.1: Phase diagram of V_2O_3, a prototypical material which exhibits a Mott metal-insulator transition, upon the application of pressure or doping (taken from [71]).

5.1 The Mott metal-insulator transition

An exemplary textbook phenomenon in strongly correlated electron systems is the Mott-Hubbard metal-insulator transition (MIT) [69]. Opposing a **band insulator**, whose origin of insulating behavior is the lack of free charge carriers, i.e., ultimately, the Pauli principle, the insulating state of the **Mott phase is entirely triggered by the Coulomb repulsion** between the electrons: In general, this transition can be regarded as the result of a competition of kinetic and potential energies in the electronic system.

Fig. 5.1 shows the phase diagram of V_2O_3, a textbook material exhibiting a Mott-Hubbard MIT. At high temperatures (200-400 Kelvin), a transition between a paramagnetic metal and a paramagnetic insulator is **triggered by** applying either chromium **doping or pressure** to the system. Not surprisingly, due to the many-body nature of the transition, **single-particle approaches** (such as density functional theory, see, e.g., [208]) **fail to predict** the existence of such a transition. This breakdown of the single-particle picture can be easily understood by taking a look at the single-particle density of states (DOS, here loosly regarded as equivalent to the spectral function). A typical DOS of a band insulator is depicted in the left panel of Fig. 5.2. VB and CB denote valence and conduction band, respectively. The spectral weight of the conduction band is fixed to two states per site. Upon doping, states are just shifted with respect to the chemical potential μ, so that the integral up to the chemical potential yields the filling n.

The behavior upon doping is dramatically different for the Mott insulator (right panel of Fig. 5.2).

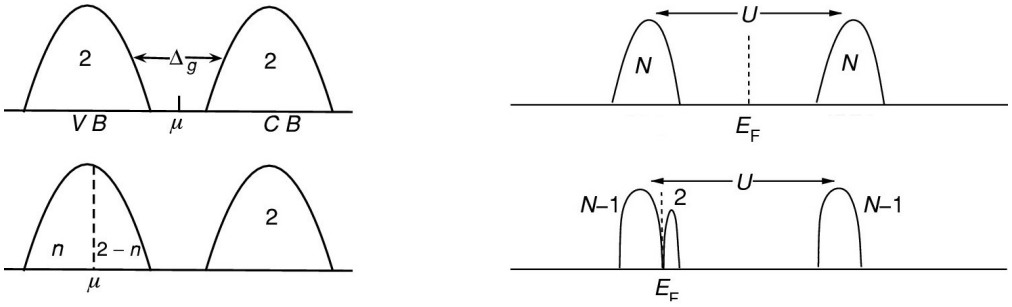

Figure 5.2: Typical single-particle spectral functions of a rigid band insulator (left panel) and Mott insulator (right panel), respectively, upon doping (taken from [209]).

In the half-filled case (and for large coupling strengths U), one can identify an upper and a lower so-called **Hubbard band**, separated by an energy scale of order U. Here, doping the system results in **rearranging** of the electronic states: The **spectral weight** of the lower Hubbard band, in contrast to a rigid shift in the band picture, **depends on the filling**. It thus becomes immediately clear that a single-particle picture is totally inadequate to describe the Mott insulating state. This is why many-body techniques (such as the DMFT) must be exploited in order to correctly capture the physical mechanisms of the Mott-Hubbard MIT.

5.2 The description of the MIT by means of the DMFT

As stated in the previous section, the essence of the MIT lies in its competition of kinetic and potential energies of electrons on a lattice. One of the simplest modellizations of this physical situation is encoded in the (single-band, half-filled) Hubbard model, introduced in Sec. 2.1, which has been intensively studied aiming at a basic description of a Mott-Hubbard MIT. Early approaches consisted in

- Green function decoupling techniques (**"Hubbard picture"**, [210]), which could describe the continuous splitting of the (Hubbard) bands triggered by the purely local Coulomb interaction.
- Gutzwiller variational wave functions (**"Brinkman-Rice picture"**, [211]), that cover the vanishing quasiparticle peak in the single-particle spectrum approaching the MIT.

Both approaches can thus be regarded as complementary to each other. However, the first theory, which could consistently describe both features of the MIT (i.e. the separation of the Hubbard band *and* the vanishing of the quasiparticle peak) was the **dynamical mean field theory (DMFT)** (see Sec. 2.2). The main panel of Fig. 5.3 shows DMFT results for the half-filled Hubbard model (Eq. (2.6)) on the Bethe lattice[1] [33]. The phase diagram is given as a function of the temperature T

[1] In DMFT, due to its mean-field nature, the lattice type only enters via the non-interacting density of states. When rescaling all energies by the second moment of the respective energy dispersion, physical quantities become easily

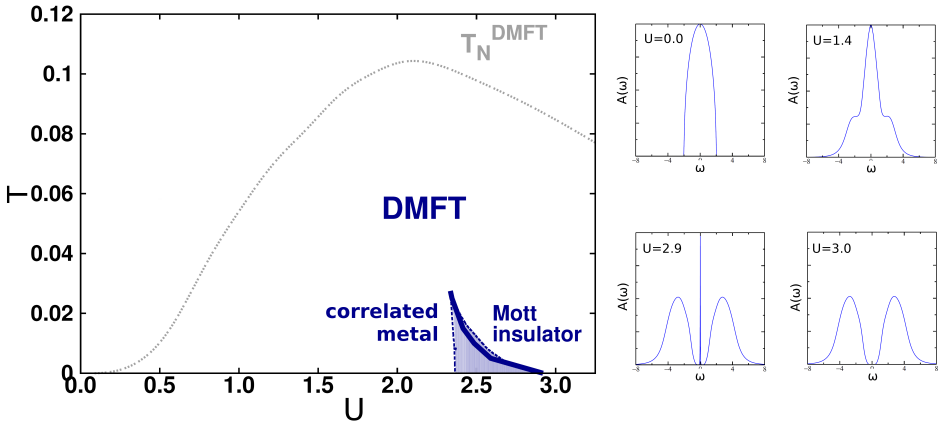

Figure 5.3: Main panel: DMFT phase diagram of the half-filled single-band Hubbard model on a Bethe lattice (semi-elliptic density of states, data taken from [33]). Right panel: Spectral functions at $T = 0$ for several interaction values, calculated by NRG for the Bethe lattice (from [85]). All energies are measured in units of $4t \equiv 1$, i.e. the bandwidth to the two-dimensional square lattice.

and U, i.e. the value of the Hubbard interaction[2]. The dashed grey line indicates the transition from the paramagnetic to an antiferromagnetic ordered state, however, the DMFT was performed by enforcing $SU(2)$ symmetry of the paramagnetic phase, so that this transition does not affect the DMFT spectral properties. Having excluded the magnetic order, the phase diagram reveals a **first order metal-insulator transition** exhibiting a **coexisting region** (blue shaded area) terminating at a **critical point** of second order. The bold blue line is indicating the minimum of the free energy. For temperatures above the one of the critical endpoint **crossover regions** exist (not shown, see e.g. [33, 212, 213]).

The evolution from the non-interacting limit to a Mott insulator can be illustrated best by taking a look at the single-particle spectral function. The right panel of Fig. 5.3 shows the numerical results obtained at $T = 0$ in DMFT, using numerical renormalization group (NRG) as impurity solver [85]. Starting at the non-interacting limit ($U = 0.0$) the system is clearly metallic with a quasiparticle peak at the Fermi level $\omega = 0$. However, when increasing the interaction, first shoulder formation sets in ($U = 1.4$), whose intensity grows at higher interaction values, e.g. $U = 2.9$. Also, at this high interaction strength, the separation of the Hubbard bands as well as the vanishing of the quasiparticle peak can be observed (**three peak structure**). Eventually, by increasing the interaction value further, the quasiparticle peak vanishes and the lower and upper Hubbard bands are separated by an energy scale of $U = 3.0$.

comparable, despite low-temperature features induced by the specific form of the density of states (e.g. van-Hove singularities). Specifically for the Mott-Hubbard MIT, after rescaling, the transition curves for Bethe and square lattice lie on top for all practical purposes, cf. [33, 214].

[2] All energies in this section are measured in units of $4t$.

It is worth noting, that beyond this "standard" description of the DMFT MIT in terms of one-particle quantities, the non-perturbative nature of the MIT is reflected also in higher particle correlation functions. For instance, at $T = 0$, also the local spin-spin susceptibility $\chi_{\text{loc}}(\omega = 0)$ diverges, signalling the formation of local magnetic moments. Even more surprisingly, however, one does not even have to abandon the (correlated) metallic phase to detect the influence of the MIT: As discussed in Sec. 3.1, well inside the metallic phase, the charge-irreducible vertex $\Gamma_{\text{c}}^{\nu\nu'\omega}$ displays **singularities** in its low-frequency structure, which can be regarded as precursors of the MIT.

DMFT has been extremely successful in the description of the MIT in infinite dimensions which also provides a good approximation for three-dimensional bulk systems. However, as can be deduced from Chapter 4, when reducing the dimensionality of the system to, e.g., two dimensions, **spatial correlations** cannot be neglected. Therefore, in the following section, the physics of the MIT is revisited in the case of two dimensions by analyzing the progressive inclusion of spatial correlations. First, the influence of short-ranged spatial correlations is analyzed by means of a cluster extension of DMFT. Afterwards, spatial correlations on every length scale are accounted for by the dynamical vertex approximation, unravelling the (somewhat sad) fate of the Mott-Hubbard MIT in two dimensions.

5.3 Inclusion of non-local correlations in 2D

Parts of this section (marked by a vertical sidebar) and the data shown have already been published in the APS journal Phys. Rev. B **91**, 125109 (2015) *and the* Journal of Magnetism and Magnetic Materials **400**, 107-111 (2015).

As already stated in the previous chapter, in two dimensions the dynamical mean field approximation of neglecting spatial correlations breaks down completely due to the significant violation of the central limit theorem hypothesis in systems with reduced dimensionality. At the same time, two-dimensional systems are of huge research interest, because they exhibit fascinating examples of condensed matter phenomena, the most prominent of which, arguably, are high-temperature superconductors. For the specific material class of copper-oxide compounds, the so-called cuprates, the two-dimensional Hubbard model (see Eq. (2.6)) is believed to represent the minimal model for being able to capture their physics (at least on a qualitative level). Therefore, a clear-cut investigation of the model's properties starting from the fundamental case of the **(completely unfrustrated) two-dimensional, half-filled Hubbard model on a simple square lattice**, is called for.

In a first step, **short-ranged spatial correlations** can be included by means of a cluster extension of DMFT, the cellular DMFT (see Sec. 2.2.4.1 and [214]). Fig. 5.4 shows results of a CDMFT

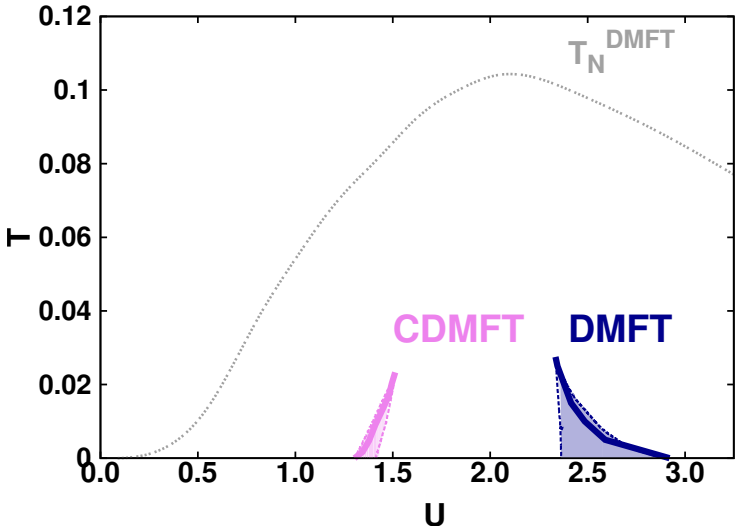

Figure 5.4: Comparison of MIT data from DMFT [33] and CDMFT [214] (for a two-dimensional plaquette cluster of size $N_c = 4$). The CDMFT introduces short-ranged spatial correlations up to the cluster size on top of the local correlations, which are treated exactly in DMFT.

calculation for a plaquette cluster (i.e. $N_c = 4$ cluster sites). Comparing to DMFT, the introduction of short-ranged spatial correlations leads to:

- A **reduction of the critical value of** U. For DMFT, the critical value $U_{c2}^{\mathrm{DMFT}} \approx 3.0$ for the second line confining the coexistence region at $T = 0$ gets significantly reduced in CDMFT, $U_{c2}^{\mathrm{CDMFT}} \approx 1.45$. This reflects the fact that short-ranged spatial correlations are able to destroy the metallic phase at intermediate couplings and low temperatures, allowing for more scattering possibilities for the electronic quasiparticles.

- The size of the **coexistence region shrinks** with respect to the one in DMFT and **its shape** (including the line of minimal free energy) is qualitatively modified. Specifically, the slope of the free energy line $\mathcal{F} = \mathcal{U} - TS$ is reversed. The latter effect can be easily understood by by taking a look at the Clausius-Clapeyron equation for the DMFT data [19]

$$\frac{dU}{dT} = \frac{\Delta S}{\Delta D},$$

where ΔS is the difference of entropies of metal and insulator and ΔD is the difference in the number of doubly occupied sites of the two phases. For DMFT, a possible (non-local) exchange coupling $J \propto -\frac{t^2}{U}$ vanished due to the limit of infinite dimensions, so that the entropy of the insulating state $S_{\mathrm{ins}} = \log(2)$ per electron even at low temperatures $T \to 0$. For the metal, Landau Fermi-liquid theory predicts $S_{\mathrm{met}} \propto T$, which means for $T \to 0$ that $S_{\mathrm{met}} < S_{\mathrm{ins}} \Rightarrow \Delta S < 0$ at low temperatures. Of course, the number of doubly occupied sites in the insulating phase is smaller than in the metallic one, i.e. $\Delta D > 0$, which implies an

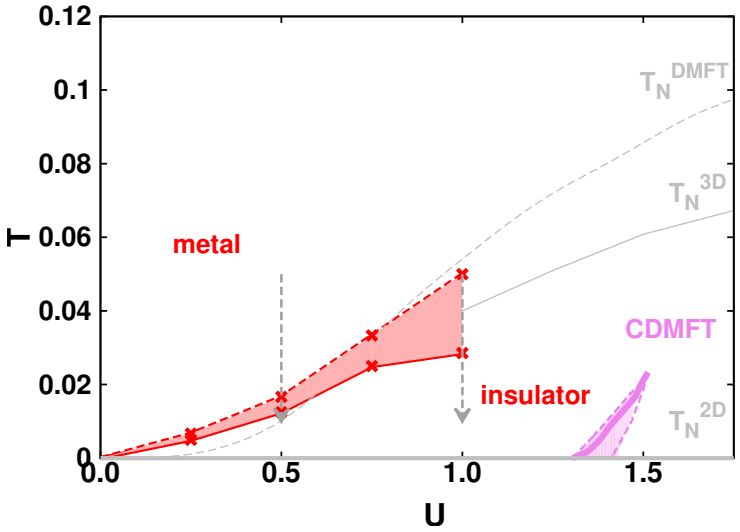

Figure 5.5: Phase diagram of the half-filled Hubbard model on a simple square lattice determined by ladder-DΓA. The MIT vanishes as a transition in favor for a Mott-Hubbard crossover at small interaction values. The antiferromagnetic ordering temperature is quenched to $T_N^{2D} = 0$, fulfilling the Mermin-Wagner theorem. Shown is also the DΓA antiferromagnetic transition temperature in 3D T_N^{3D} as well as the DMFT one T_N^{DMFT}.

overall negative slope of the Clausius-Clapeyron equation in DMFT. On the other hand, a finite-sized cluster leads to a finite exchange coupling[3] $J > 0$, which gives an entropy of the insulator: if it is vanishing faster than linearly for $T \to 0$ [19], this implies that $\Delta S > 0$ for low temperatures, hence the positive slope in CDMFT.

The inclusion of short-ranged spatial correlations, hence, already leads to significant quantitative corrections with respect to the DMFT description, which only takes temporal fluctuations into account. However, this picture of the MIT in the two-dimensional unfrustrated case becomes completely overturned when considering also **long-ranged spatial correlations** by means of, e.g., the dynamical vertex approximation (DΓA) (see Sec. 2.3). Fig. 5.5 shows the phase diagram in DΓA[4]. The red shaded area marks the region, where the Fermi-surface is gradually gapped out, indicating the onset of a **pseudogap phase** or, equivalently, a mere crossover region instead of a thermodynamic transition at small interactions. The results, thus, indicate that at low enough temperatures, the system will **always be displaying an insulating behavior, regardless of the interaction** strength U. For every (weak-coupling) U a gradual opening of the spectral gap can be easily demonstrated by taking a look at the imaginary parts of the self-energies on the Matsubara axis. In Fig. 5.6 these are shown for two temperature cuts (fixed interaction strengths) $U = 0.5$ (up-

[3]This is due to the possibility of (non-degenerate) short-ranged singlet formation within the cluster, which cannot occur, evidently, in DMFT.

[4]Here, the ladder-DΓA in the spin-channel with λ-corrections applied only to the spin-channel has been used (see Sec. 2.3.2.2).

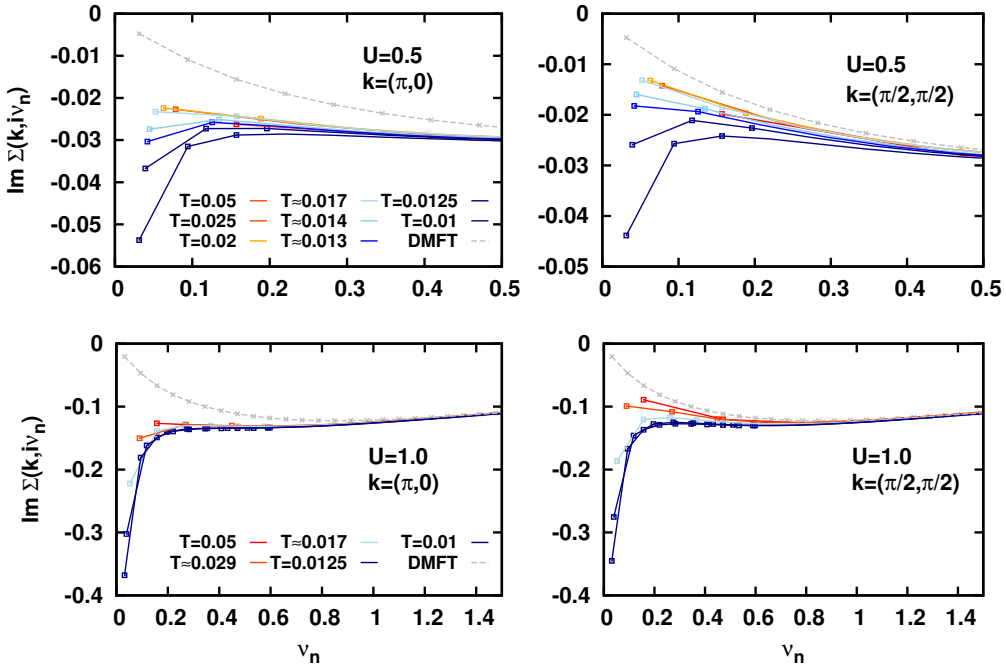

Figure 5.6: (taken from [190]) Imaginary parts of the DΓA self-energy Σ vs Matsubara frequency ν_n for the half-filled Hubbard model at the antinodal (left) and nodal (right) point of the Fermi surface at $U = 0.5$ (upper panels) and $U = 1.0$ (lower panels) and different temperatures. The DMFT results at $T = 0.01$ are provided for comparison.

per panels) and $U = 1.0$ (lower panels) indicated by the vertical arrows in the phase diagram of Fig. 5.5) and two representative points on the Fermi surface [the antinodal point $\vec{k} = (\pi, 0)$ (left panels) and the nodal point $\vec{k} = (\pi/2, \pi/2)$ (right panels)]. For $U = 0.5$ and high temperatures, $T > 0.017$, the self-energy shows clearly a low-frequency metallic behavior at every point on the Fermi surface from the nodal to the antinodal one. Upon cooling along the gray arrow in Fig. 5.5, first the low-frequency self-energy shows a downturn for $\nu \to 0$ at the antinodal point of the Fermi surface [$k = (\pi, 0)$], i.e., an non Fermi-liquid behavior below $T = 0.017$. For $0.017 > T \geq 0.0125$ however, the nodal point of the Fermi surface [$k = (\pi/2, \pi/2)$] does not show this insulating-like behavior yet. Only for $T < 0.0125$ the low-frequency self-energy acquires an insulating behavior *even at the nodal point*, indicating a complete destruction of the Fermi-liquid excitations over the whole Fermi surface: For $T < 0.0125$ one obtains an insulator with the whole Fermi surface gapped, whereas for $0.017 > T \geq 0.0125$ a pseudogap is opened with only parts of the Fermi surface gapped. Hence, upon cooling along the grey arrow in the phase diagram Fig. 5.5, one first crosses the dashed red line which marks the temperature where the first point of the Fermi surface [$k = (\pi, 0)$] shows a non Fermi-liquid, insulating behavior. At lower temperatures, one crosses a second (solid-red) line at which the whole Fermi surface gets gapped. The red-shaded region inbetween hence displays a pseudogap behavior. The analogous analysis for $U = 1.0$ can be found in the lower panels of

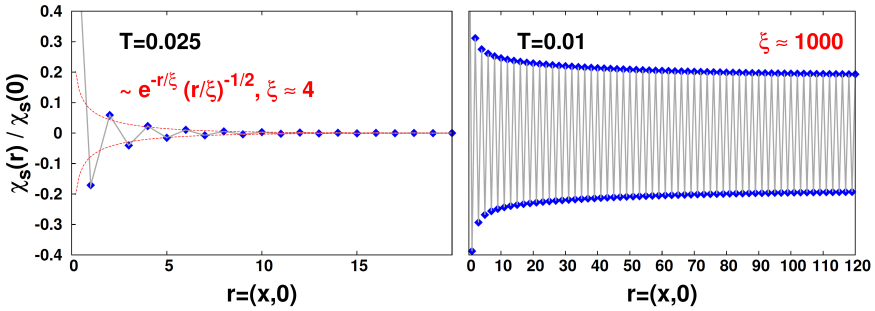

Figure 5.7: (taken from [187]) Real-space dependence of the DΓA spin correlation function $\chi_s(\vec{r})/\chi_s(\vec{0})$ for $U = 0.5$ and $T = 0.025$ (left panel) and $T = 0.01$ (right panel). Shown is the cut $\mathbf{r} = (x, 0)$ where x is given in units of the lattice spacing $a = 1$. The solid line (grey, guide to the eye) interpolates between the values at different lattice vectors (blue diamonds).

Fig. 5.6. It corresponds to the second gray arrow in Fig. 5.5. In this case, one can identify a larger pseudogap region located at higher temperatures: For $0.05 > T > 0.025$ the nodal self energy is still metallic whereas the antinodal one is already insulating. As already explained in Sec. 3.3 in the context of the parquet decomposition of the self-energy, no conclusions about the physical origin of a self-energy can be drawn from the shape of the self-energy alone - for that, a two-particle correlation analysis is needed. In Fig. 5.7, the (normalized) static spin-spin correlations function in real space $\chi_{s(\omega=0,\vec{r})}$ for a one-dimensional cut $\vec{r} = (x, 0)$ at fixed interaction $U = 0.5$ is shown. Already for a temperature $T = 0.025$ (left panel) above the red shaded region in Fig. 5.5, its oscillating, sign-changing behavior is a clear indication of **antiferromagnetic spin-fluctuations**. Their corresponding correlation length can be extracted by fitting the numerical results with the real-space form of an Ornstein-Zernicke correlation function (see also Sec. 2.3.2.2)

$$|\chi_s(\omega = 0, \vec{r} = (x, 0))| \sim e^{-x/\xi}(r/\xi)^{-1/2}. \tag{5.1}$$

This yields $\xi \approx 4$, i.e. correlations extended over about four lattice sites, for $T = 0.025$. The situation changes very dramatically, however, when lowering the temperature *below* the crossover region in the phase diagram, as is done in the right panel of Fig. 5.7 for $T = 0.01$. The oscillating nature of the (antiferromagnetic) spin-fluctuations persists, but their correlation length now explodes to about $\xi \approx 1000$ lattice sites. This means that, by lowering the temperature, spin fluctuations get progressively more (actually exponentially) extended in space. Once this happens, the electron moves in a quasi-ordered antiferromagnetic background and the corresponding scattering becomes so strong that all points of the Fermi-surface gap out approaching the perfectly gapped spectral function at the antiferromagnetically, long-ranged ordered ground-state. In other words, **long-ranged antiferromagnetic paramagnons** open the spectral gap responsible for the insulating state at low temperatures.

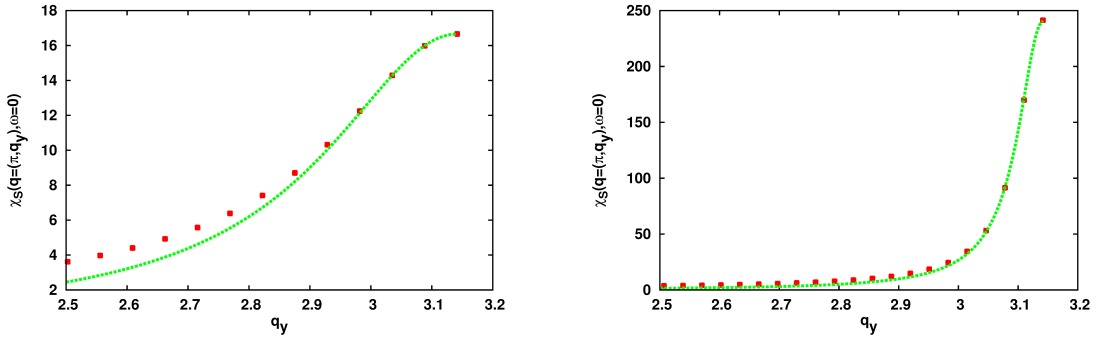

Figure 5.8: Extraction of the correlation length from a momentum-cut $\vec{q} = (\pi, q_y)$ of the static spin-spin susceptibility in momentum space $\chi_{\mathrm{s}}(\vec{q}, \omega = 0)$ for $T = 0.025$ (left panel) and $T \approx 0.014$ (right panel). The red points indicate the results from ladder-DΓA, the green lines the fits according to Eq. (5.2).

Further insight can be gained by analyzing the spin susceptibility in momentum space via the Ornstein-Zernicke relation

$$\chi_{\mathrm{s}}(\omega = 0, \vec{q}) \sim \frac{1}{(\vec{q} - \vec{Q})^2 + \xi^{-2}}, \tag{5.2}$$

where $\vec{Q}$ is the ordering vector of the underlying magnetic transition. In this case of the unfrustated, half-filled Hubbard model on a square lattice, due to the **perfect nesting** of its Fermi surface with the nesting vector $\bar{Q} = (\pi, \pi)$, the antiferromagnetic ordering of the ground-state[5] ($T_N^{2D} = 0$) is perfectly checkerboard-like $\vec{Q} = (\pi, \pi)$.

In Fig. 5.8 the corresponding fits for $U = 0.5$ and two different temperature values ($T = 0.025$ in the left panel, $T \approx 0.014$ in the right panel) and a momentum cut $\vec{q} = (\pi, q_y)$ are shown. As is immediately clear from Eq. (5.2) the width of the peak around $\vec{Q} = (\pi, \pi)$ is a direct measure of the (inversely quadratic) correlation length ξ^{-2}, which increases by lowering the temperature at fixed interaction value. In order to improve the understanding of the temperature dependence of the correlation length, in Fig. 5.9 the T-dependence of the inverse correlation length $\xi^{-1}(T)$ is shown for two interaction values $U = 0.5/0.75$. One can see that, starting at high temperatures the curves follow a **bosonic mean-field behavior** (see Chapter 6) of $\xi \propto T^{-0.5}$, whereas at low temperatures, the influence of the ordered phase (at $T = 0$) is altering this behavior qualitatively through the corresponding long-range spin fluctuations: The temperature-dependence of ξ is changed into an exponential growth $\xi \propto e^{c/T}$, which is actually expected for a phase transition at zero temperature

[5] For this model, the Mermin-Wagner theorem, which is also respected by the (λ-corrected) ladder-DΓA (see [20]), prohibits ordering at finite temperatures [215].

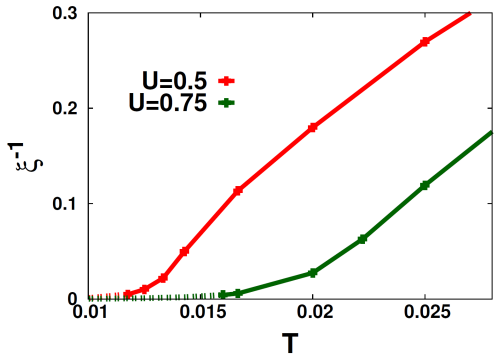

Figure 5.9: (taken from [187]) T-dependence of ξ^{-1} for different interaction values. A crossover to an exponential behavior is observed at T consistent with the onset of the insulating behavior (pink/green colored areas for $U = 0.5/0.75$).

in two dimensions (see also, e.g., [159]).

5.4 Slater vs. Heisenberg mechanism for magnetic fluctuations

The last question to address in this chapter about the MIT in two dimensions is the microscopic mechanism through which the antiferromagnetic fluctuations responsible for the destruction of the Fermi surface stem from, is stabilized (see also [216]).

Bearing in mind that the system's Hamiltonian reads

$$H = -t \sum_{(i,j),\sigma} c^{\dagger}_{i,\sigma} c_{j,\sigma} + U \sum_{i} n_{i\uparrow} n_{i\downarrow} \tag{5.3}$$

and its (non-interacting) Fermi surface is perfectly nested by $\bar{Q} = (\pi, \pi)$, two scenarios are conceivable:

1. In the weak-coupling regime (U much smaller than the bandwidth), the quasiparticles in the paramagnetic high-temperature phase are far from being localized (itinerant quasiparticles). When lowering the temperature, at the magnetic transition, the bound state and the phase-coherence (i.e. coherent alignment of spins) set in simultaneously. Energetically, this results in a simultaneous **gain in potential energy** (due to the onset of magnetism) and loss in kinetic energy (due to the binding). The spatial pattern of the incipient order, due to the weakness of the Coulomb interaction, is typically determined by the Fermi surface nesting properties. This first scenario is named **Slater mechanism** and is clearly an analogon to the Stoner-Wohlfahrt theory of (ferromagnetic) band magnetism [217].

2. In the strong coupling regime, at a certain temperature, there already exist preformed local

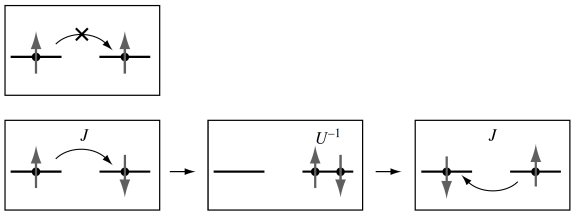

Figure 5.10: (taken from [23]) The Heisenberg superexchange mechanism for antiferromagnetic order. Due to the Pauli exclusion principle, virtual hopping procceses are only possible, if the spins are aligned antiferromagnetically. The exchange coupling $J \sim t^2/U$.

magnetic moments, which, however, are still incoherently ordered, i.e. their spin orientations are not related mutually. However, as they are already localized, their potential energy already reached saturation (few or no double occupancies). When lowering the temperature, the system can still **gain kinetic energy** due to (virtual) **Heisenberg superexchange processes**, i.e. by introducing "phase-coherence" as depicted in Fig. 5.10. This energy gain, however, is only accessible for antiferromagnetically arranged spins due to the Pauli exclusion principle. Hence, this kind of order is favored at low temperature and the corresponding magnetism is stabilized by a gain in kinetic energy. This scenario is coined **Heisenberg mechanism**, which is realized, e.g., in the half-filled Hubbard model in three (or higher) dimensions at strong coupling.

Turning again to the ladder-DΓA results in 2D, one can observe a slight reduction of the potential energy $U\langle n_\uparrow n_\downarrow\rangle$ of about 1% traversing the pseudogap region at $U = 0.5$ in Fig. 5.5. This gain in potential energy occurs in the presence of very extended and strong spatial correlations as can be deduced from Fig. 5.8, which implies that the physics should largely reflect the one of the ordered phase [219]. Hence, the DΓA results lead to the conclusion, that the Slater mechanism is generating the strong fluctuations (Slater paramagnons) which are ultimately responsible for opening the gap at weak coupling, opposing conclusions drawn in other work (see, e.g. [218]). In fact, the intrinsic nature of the antiferromagnetic fluctuations appears to be driven by the nature of the corresponding long-range ordered ground-state. As the antiferromagnetism of the latter gradually evolves from Slater-like to Heisenberg-like with increasing interaction, it is evident to expect the same to happen to the corresponding fluctuations at finite temperatures.

For a more extensive study of the impact of non-local correlations over different energy scales on the energetics and spectral functions in the half-filled Hubbard model, the reader is referred to the recent work by G. Rohringer and A. Toschi [68].

6

Magnetic phase diagram, quantum criticality and Kohn anomalies in 3D

"I happen to have discovered a direct relation between magnetism and light, also electricity and light, and the field it opens is so large and I think rich."

- Michael Faraday (English physicist, *1791 - †1867)

The phase diagrams of correlated electron materials display a vast variety of different states of matter. One of the most frequently appearing are magnetically ordered phases, which often can only be understood by using a full quantum many-body description. The situation can be made even more interesting by exploiting a non-thermal parameter to suppress the finite-temperature transitions, leading to a quantum critical point at zero temperature. Although this limit cannot be reached experimentally, the existence of a quantum critical point can severely influence the system's excitation spectrum at finite temperatures and is often associated with exotic phenomena. In spite of its intrinsic interest, however, a consistent theory has not been established yet. One of the reasons is the theoretically quite challenging intermingling of temporal and spatial correlations, both of which must be taken into account for the description of a quantum phase transition. In this Chapter quantum critical properties of the fundamental model of electronic correlations, the Hubbard model in three dimensions, are studied by means of the DΓA, which is particularly suitable for this purpose. First, the magnetic phase diagram of the Hubbard model on a simple cubic lattice is computed at and out of half-filling. Then its (classical and quantum) critical regions and exponents are analyzed: Quite unexpectedly, the quantum critical properties are found to be driven by the model's Fermi surface properties (Kohn points), even in presence of strong correlations: The temperature dependences of the magnetic susceptibility and of the correlation length in the vicinity of the quantum critical point largely violate the prediction of the conventional Hertz-Millis-Moriya theory of quantum criticality.

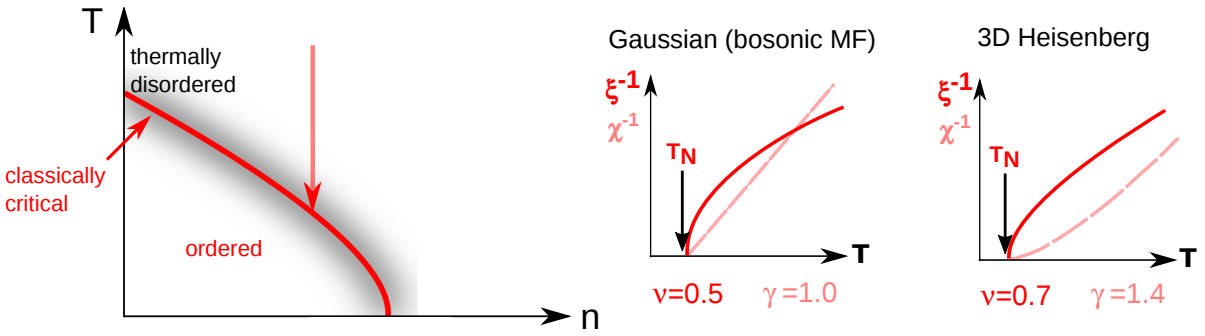

Figure 6.1: (readapted from [9] and [220]) Generic phase diagram of a system exhibiting a finite temperature (classical) phase transition as a function of temperature T and a non-thermal control parameter n (left panel). Classical critical exponents predicted by bosonic mean field theories (like DMFT) and renormalization group calculations for the critical exponents of the 3D Heisenberg model, which constitutes the universality class for a finite temperature magnetic phase transition of the 3D Hubbard model (right panel). The gray shaded region marks the classically critical regime.

Parts of this chapter are available as a preprint arXiv:1605.06355 (2016).

6.1 Classical and quantum criticality in three dimensions

In order to study the phenomenon of (classical and quantum) magnetic phase transitions in strongly correlated electron systems, in this chapter, the focus is on the **Hubbard model in three dimensions on a simple cubic lattice** [see Eq. (2.6), energies in this chapter are measured in units of $2\sqrt{6}t$, see footnote 1 in Chap. 5]. Contrary to the two-dimensional case (discussed in Chapter 5), in three dimensions magnetic ordering is not prohibited at finite temperatures by the Mermin-Wagner theorem [215]. This makes the magnetic phase diagram even richer than the one in two dimensions. Before analyzing the results of DMFT and DΓA for this model in the following sections, a qualitative description of the expected critical behavior in this system is given at a general level.

6.1.1 Classical critical behavior in three dimensions

The left panel of Fig. 6.1 shows a generic phase diagram for a system exhibiting a second order finite temperature **classical phase transition** [e.g. the transition from a paramagnetic (PM) to an antiferromagnetically (AF) ordered phase[1]] as a function of temperature and a non-thermal control parameter n (which hereafter will be the density varied by means of hole-doping). This phase transition, due to its classical nature, is **triggered by temperature**, i.e. above the ordering

[1] Although the analysis presented in this section is quite general, the terminology used for phase transitions here is suited to magnetic ones, respecting the focus of this chapter.

temperature (Néel temperature T_N for the AF) the order is destroyed by thermal fluctuations giving rise to a thermally disordered phase. However, below T_N, these thermal fluctuations are not sufficient to completely suppress the ordering tendency of the system and an ordered phase emerges.

Due to the second order (continuous) nature of the phase transition, if one gradually reduces the temperature, starting from the thermally disordered (high-temperature) regime one will cross a classically critical regime, where the system exhibits universal behavior. Universality manifests itself in the emergence of critical exponents (e.g. in the temperature dependence of relevant physical observables such as the magnetic susceptibility), that are identical for systems within the same **universality class**, the latter being determined by the general symmetry properties and the dimensionality of the Hamiltonian and order parameter (see, e.g., [11]).

Commonly investigated critical exponents are the ones controlling the temperature dependence of the physical (non-uniform static spin) susceptibility $\chi_{\mathsf{s}}(\omega = 0, \vec{q} = \vec{Q})$ at the vector $\vec{Q}$, where the susceptibility reaches its maximum[2]

$$\chi_{\mathsf{s}}(\omega = 0, \vec{q} = \vec{Q})\big|_{T \to T_N} \sim \left| \frac{T - T_N}{T_N} \right|^{-\gamma} \tag{6.1}$$

and the temperature dependence of the (spin) correlation length ξ

$$\xi\big|_{T \to T_N} \sim \left| \frac{T - T_N}{T_N} \right|^{-\nu} . \tag{6.2}$$

The correlation length can be extracted from the Ornstein-Zernicke form of the corresponding correlation function close to a transition (see also Eq. (2.60))

$$\chi_{\mathsf{s}}(\omega = 0, \vec{q}) = \frac{A}{\left|\vec{q} - \vec{Q}\right|^2 + \xi^{-2}} \tag{6.3}$$

and can be, thus, associated with the inverse width of the peak around the maximum of the correlation function $\chi_{\mathsf{s}}(\omega = 0, \vec{q})$ at $\vec{q} = \vec{Q}$. Please note that, as $\gamma > 0, \nu > 0$, both observables in Eq. (6.1) and (6.2) obviously **diverge** at the transition temperature $T = T_N$. This divergence, in fact, marks the occurrence of the phase transition and can be used to determine the transition temperature. Furthermore please recall that not all physical observables (like, e.g., the transition temperature)

[2] This corresponds, thus, to the ordering vector at $T = T_N$. For the moment, the temperature-dependence of $\vec{Q}$ is neglected. See, however, the discussion at the end of this chapter.

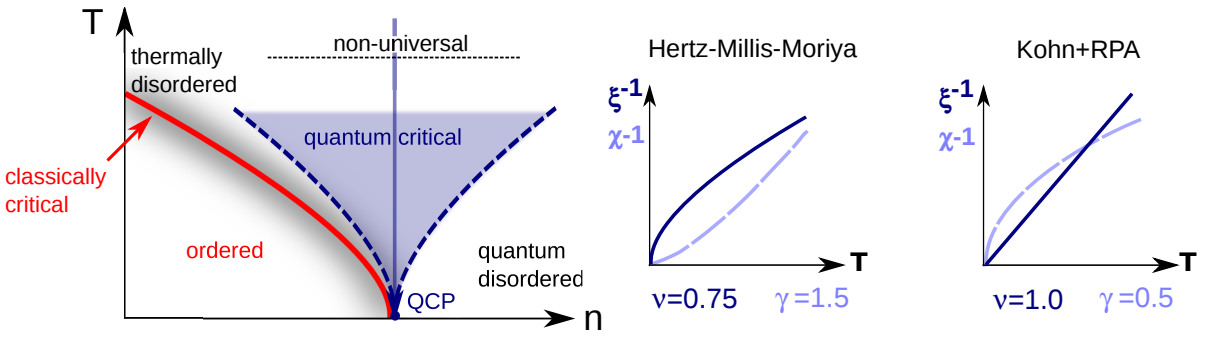

Figure 6.2: (readapted from [9] and [220]) Generic phase diagram of classical as well as quantum phase transitions. At the quantum critical point (QCP) at $(T = 0, n = n_c)$, an abrupt change of the ground state of the system takes place (left panel). The blue shaded region marks the quantum critical regime, where the (quantum) critical exponents γ and ν show universal behavior. The temperature dependences of magnetic susceptibility and correlation length in this region, calculated from Hertz-Millis-Moriya theory (for $d = 3$, SDW ordering and $z = 2$) and in presence of Kohn anomalies at the Fermi surface, are shown (right panel).

display universal behavior, even in the critical regime.

Depending on the types of fluctuations included in the theoretical description, different predictions for the critical exponents of the universality class for classical magnetic phase transitions of the selected model are conceivable. Specifically, in case of the three-dimensional Hubbard model (which at least for $n = 1$ and $U \gg t$ falls in the same universality class as the three-dimensional Heisenberg model), one obtains (see right panels of Fig. 6.1):

- For a **bosonic mean-field theory** (like the DMFT), that neglects all spatial correlations (see Sec. 2.2), the predicted critical exponents are $\gamma = 1$ and $\nu = 0.5$ and, therefore, coincide with the exponents yielded by a Ginzburg-Landau theory including Gaussian fluctuations (see [23]).
- On the other hand, for a **three-dimensional Heisenberg model**, renormalization group calculations [221] as well as quantum Monte Carlo studies [222], including spatial correlations yield $\gamma \approx 1.4$ and $\nu \approx 0.7$. These exponents should also hold (at least in the strong-coupling limit) for classical magnetic phase transitions of the Hubbard model in three dimensions.

Quite generically, the transition temperature T_N can be varied by tuning the non-thermal control parameter n (see Fig. 6.1). Eventually, at large enough n, the finite-temperature ordering tendency of the system is completely suppressed, leading to a quantum critical point.

6.1.2 Quantum critical behavior in three dimensions

Opposing finite temperature phase transitions, which are triggered by temperature, quantum phase transitions, i.e. changes in the ground state of a system at $T = 0$, can occur by tuning a (non-thermal) control parameter n. Although in this chapter the focus is on purely magnetic phase transitions and, specifically, n is representing the doping level of the system, this concept is quite general[3].

The left panel of Fig. 6.2 shows, how the generic phase diagram for classical phase transitions (Fig. 6.1) is amended by a **quantum critical point (QCP)**. Starting from the classically ordered phase at $T = 0$ and progressively increasing n, the ordered phase disappears in favor of a quantum disordered regime. In this regime, the order is destroyed by quantum fluctuations instead of thermal fluctuations at finite temperatures. Between the ordered and quantum disordered regimes, exactly at the QCP at the critical doping n_c, an abrupt change in the ground state of the system takes place.

Despite the fact that the QCP is located at $T = 0$, its sheer existence has a strong influence on the excitation spectrum of the system at finite temperatures, giving rise to the emergence of a very important region in the (T, n) phase diagram, the quantum critical regime (funnel-shaped region in Fig. 6.2). Analogously to the classically critical regime, in the quantum critical regime the system can exhibit universal behavior, e.g. in terms of critical exponents: Because of the vanishing of the ordering temperature, in the quantum critical regime, the corresponding power laws describing the temperature dependence of the observables of interest become [9]

$$\chi_{\mathsf{S}}(\omega = 0, \vec{q} = \vec{Q}) \sim T^{-\gamma} \tag{6.4}$$

for the spin susceptibility and

$$\xi \sim T^{-\nu} \tag{6.5}$$

for the magnetic correlation length. Please note, that despite the equivalence in the notation, the critical exponents γ and ν for the quantum phase transition can be completely different from the classical ones described in Sec. 6.1.1.

Furthermore, at $T = 0$ for instance the correlation length can also be expressed as a function

[3] For instance, in heavy-fermion compounds, n most commonly represents the ratio of the RKKY interaction strength and the Kondo interaction (see, e.g. [223, 224]), which can be controlled by applying pressure, doping or a magnetic field to the system. For a simple Ising spin chain, n could be the transverse external magnetic field (see [8]).

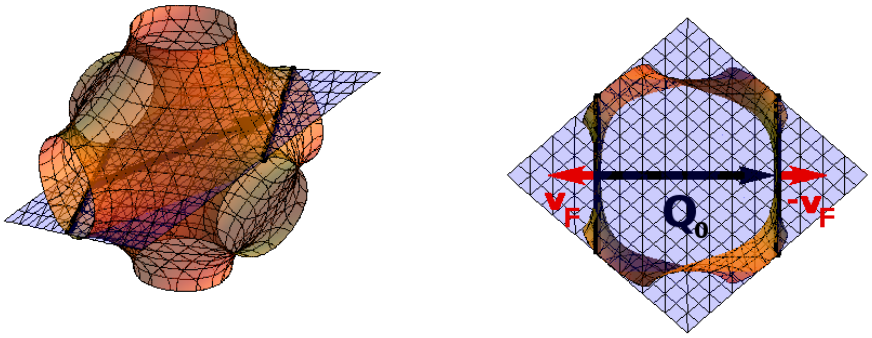

Figure 6.3: (taken from [220]) Visualization of (one out of four pairs of) Kohn lines in the $3d$ Brillouin zone of the simple cubic lattice with nearest-neighbor hopping and the connecting SDW vector $\mathbf{Q_0}$. The left panel shows a $2d$ cut with the Kohn-line, the right one the corresponding (opposite) Fermi-velocities.

of the deviation of the non-thermal control parameter n from its critical value n_c [9]:

$$\xi \sim |n - n_c|^{-\nu^*}. \tag{6.6}$$

Here, ν^* denotes another (quantum-)critical exponent that can be different from ν in general. As at $T = 0$ temporal fluctuations become non-negligible, also the (imaginary) **correlation time** diverges at the quantum phase transition [9]:

$$\xi_\tau \sim |n - n_c|^{-z\nu^*}, \tag{6.7}$$

defining z, the so-called **dynamical critical exponent**. Interestingly, according to the most known theoretical descriptions [9], quantum-critical systems of spatial dimension d can behave like classical systems with enhanced effective dimensionality

$$d_{\text{eff}} = d + z, \tag{6.8}$$

which is determined by this dynamical critical exponent and may boost the system above its upper critical dimension.

More specifically, the conventional theory for the description of quantum phase transitions in fermionic systems is the **Hertz-Millis-Moriya (HMM) theory** [12–14,66,225]. It essentially amends the (perturbative) Landau-Ginzburg-Wilson (LGW) theory [11] by plainly including temporal fluctuations of the quantum regime. As already mentioned in Chap. 1, Hertz studied itinerant electron

systems by applying a renormalization group (RG) treatment to model systems and concluded that at zero temperature, static and dynamic properties are interwoven. Later, Millis analyzed how the existence of a quantum phase transition affects properties of these systems at finite temperatures. For a magnetic metallic system (spin-density wave (SDW)), the HMM theory predicts $z = 3$ for a ferromagnetic and $z = 2$ for an antiferromagnetic type of ordering, respectively. In case of a three-dimensional metallic spin-density wave (which will be considered in this chapter), $d_{\text{eff}} = d + z = 5$, and the HMM theory yields the critical exponents $\gamma = 1.5$ and $\nu = 0.75$, see middle panel of Fig. 6.2 [9].

Despite many successes of the HMM theory, most quantum critical materials are strongly correlated so that approaches based on perturbation theory or an RG extension thereof become at least questionable, e.g. for QCPs in transition metals under pressure, such as $Cr_{1-x}V_x$ [226–229] and heavy fermion compounds under pressure or in a magnetic field, such as in $CeCu_{6-x}Au_x$ [230] and $YbRh_2Si_2$ [231, 232]. Furthermore, it has been established that one effect of strong correlations, namely the breakdown of the "large" Fermi-surface containing both conduction and f-electrons and the associated local quantum criticality [233, 234], may lead to different critical exponents.

Another, yet different kind of source for the **break down** of the HMM theory stems from **Fermi surface features**: While it is known that in presence of an isotropic, perfectly nested Fermi surface ($\vec{Q} = 2k_{\text{F}}$) the HMM theory may no longer be applicable [9], little is known about how this situation can be realized in a concrete case of interest. In fact, as it is demonstrated in Sec. 6.3 and Ref. [220] for the case of three dimensions, it may break down if the system's Fermi surface exhibits the peculiar features of **Kohn points or lines**. Kohn lines are defined as continuous lines of (Kohn) points on the Fermi surface, connected by the SDW vector $\mathbf{Q}_0$ and having opposite Fermi velocities. To illustrate the concept of Kohn lines, Fig. 6.3 shows a pair of them for the (non-interacting) Fermi surface of the simple cubic unfrustrated lattice. The existence of such Kohn lines affects the physical susceptibilities drastically, such that the critical exponents can be strongly altered as well as their mutual relations can be strongly violated. For the case considered in this Chapter (the unfrustrated Fermi surface in three dimensions), the values of the critical exponents change into $\gamma = 0.5$ and $\nu = 1.0$ (see right panel of Fig. 6.2). In fact, this can be foreseen from a purely analytical random phase approximation (RPA) analysis of the quantum critical spin susceptibility (see [235]): The expression for the temperature-dependent non-uniform bare susceptibility in the presence of Kohn anomalies is given by

$$\chi^0_{\text{s}}(\omega = 0, \vec{q} + \vec{Q_T}) \simeq \left[\chi^{-1}_{0,\text{s}}(\omega = 0, \vec{Q}_0)_{T=0} + AT^{1/2} + BT^{-3/2}q_z^2\right]^{-1}. \tag{6.9}$$

Here $\vec{Q}_T = \vec{Q}_0 + (0, 0, \delta Q_z)$, with $\delta Q_z = -2CT$ describing a shift of the wave vector with the temperature and A, B, C are positive factors, containing weak, $\ln\ln(1/T)$, corrections. Adopting

the random phase approximation

$$\chi_{\mathsf{s}}^{\mathsf{RPA}}(\omega=0,\vec{Q}) = \frac{1}{\chi_{\mathsf{s}}^{0}(\omega=0,\vec{Q}) - U}, \tag{6.10}$$

one arrives at the critical exponents given above. The same preliminary analysis also suggests that in such cases a univocal definition of the dynamical exponent z might become problematic: The frequency dependence of $\chi^{\mathsf{RPA}}(\omega,\vec{q})$ in the presence of Kohn anomalies will acquire a rather complicated form ([236,237], see [238] for the critical exponents in two dimensions), not characterized by the single exponent z appearing in the expression of the HMM theory

$$\chi_{\mathsf{s}}^{\mathsf{HMM}}(\omega,\vec{q}+\vec{Q}) \propto \frac{1}{\vec{q}^2 + \xi^{-2} + i\omega_n/|\vec{q}|^{z-2}}. \tag{6.11}$$

After this brief general introduction to classical and quantum phase transitions, in the following sections, the corresponding magnetic phase diagrams of the Hubbard model on a simple cubic lattice computed in the dynamical vertex approximation will be analyzed. As the DΓA approach includes spatial correlations on top of DMFT, which provides already a non-perturbative description of all local quantum fluctuations, it is particularly suited to study both the classical and quantum critical regions of strongly correlated models.

6.2 Classical criticality: the half-filled Hubbard model

Before discussing the (more general) case of the (hole-)doped Hubbard model on a three dimensional (cubic) lattice in the following section, is it instructive to first consider the half-filled case, where electronic correlations are expected to have the biggest impact on the Hubbard model physics.

Fig. 6.4 exhibits this phase diagram as a function of temperature T and interaction strength U for several many-body techniques [171]. Starting with the analysis of the DMFT data, the momentum-dependent spin susceptibility $\chi_{\mathsf{s}}(\omega,\vec{q})$ is calculated via a Bethe-Salpeter equation [15]

$$\chi_{\mathsf{s}}(\omega,\vec{q}) = \frac{1}{\beta^2}\sum_{\nu\nu'}\left[\chi_0^{\nu\nu'}(\omega,\vec{q}) - \Gamma_{\mathsf{s}}^{\nu\nu'}(\omega)\right]^{-1}_{\nu\nu'} \tag{6.12}$$

using the irreducible vertex in the spin channel $\Gamma_{\mathsf{s}}^{\nu\nu'}(\omega) \equiv \Gamma_{\mathsf{s}}^{\nu\nu'\omega}$, which, in turn, is extracted from a (self-consistently determined) AIM of the DMFT solution (see Sec. 2.2). $\chi_0^{\nu\nu'}(\omega,\vec{q})$ is the

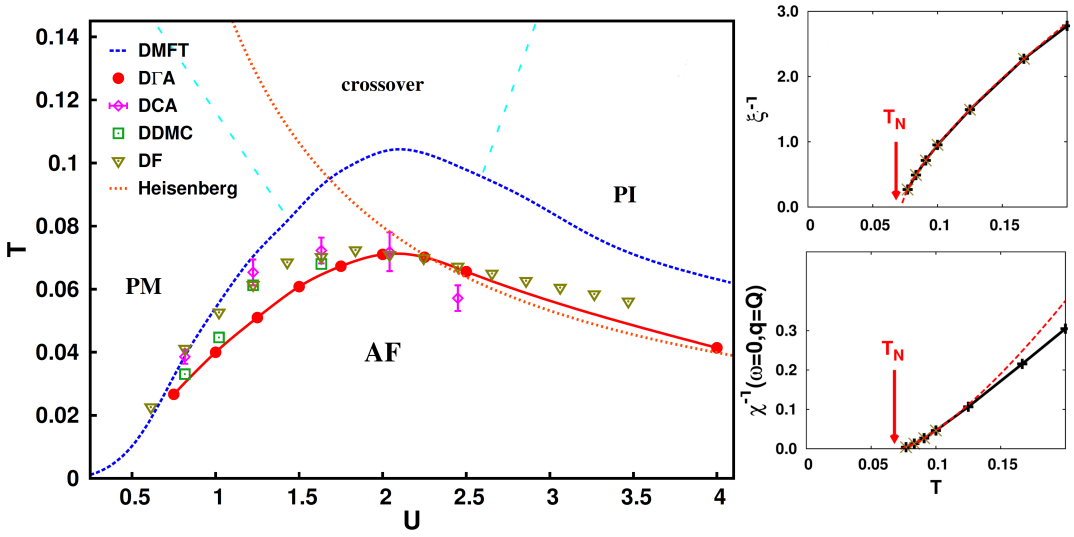

Figure 6.4: (taken from [68]) Phase diagram of Néel temperatures revealed by several many-body techniques for the 3D Hubbard model at half filling (see corresponding Refs. in [68]). Also the comparison to the transition temperature of the 3D Heisenberg model is shown (main panel). The critical exponents have been extracted from the spin susceptibility (γ) and correlation length (ν) at $U = 2.0$ and yield 3D Heisenberg critical exponents (right panel).

momentum-dependent DMFT particle-hole bubble

$$\chi_0^{\nu'}(\omega, \vec{q}) = -\beta \sum_{\vec{k}\vec{k}'} G_{\text{DMFT}}(\nu, \vec{k}) G_{\text{DMFT}}(\nu + \omega, \vec{k} + \vec{q}) \delta_{\vec{k}\vec{k}'} \delta_{\nu\nu'}. \tag{6.13}$$

Please note that the inversion in Eq. (6.12) is done over the fermionic frequency pair (ν, ν').

The dashed blue line in Fig. 6.4 marks the points (T_N^{DMFT}, U) where the static spin susceptibility $\chi_{\text{s}}(\omega = 0, \vec{q} = \vec{Q})$ diverges at a certain ordering vector $\vec{Q}$, when lowering the temperature starting from the unordered paramagnetic phase. This indicates (see also the discussion in the previous section), a second order phase transition in the spin channel. The ordering pattern is determined by the momentum $\vec{Q}$. For the half-filled system the vector is always $\vec{Q} = (\pi, \pi, \pi)$. In this respect, it is noteworthy that:

1. The transition temperature in DMFT T_N^{DMFT} increases with U in the weak-coupling regime and displays a maximum at $U \approx 2.0$.

2. In the strong-coupling regime, where a mapping of the three-dimensional Hubbard model onto the Heisenberg model can be performed, the shape of the evolution of T_N in the Hubbard model should become similar to the one of an Heisenberg model with $J = \frac{4t^2}{U}$ (orange dashed line in Fig. 6.4). However, as DMFT is a mean-field theory in space, which neglects spatial correlations, the transition temperature is significantly overestimated, approaching the one

expected for the corresponding Ising model.

3. The dynamical exponents are $\gamma = 1$ for the spin susceptibility and $\nu = 0.5$ for the spin correlation length in DMFT (not shown), consistent with its nature of a bosonic mean-field theory.

Comparing this result to a similar analysis in DΓA[4] (red circles in Fig. 6.4), due to the **inclusion of spatial correlations**, the transition temperature gets significantly reduced $T_N^{\mathrm{D}\Gamma\mathrm{A}} < T_N^{\mathrm{DMFT}}$. These values of the transition temperature agree well with accurate DCA [239], QMC [240] and determinental diagrammatic Monte Carlo (DDMC) [191] data. With respect to the dual fermion approach [241] and DCA [239], the DΓA yields slightly smaller Néel temperatures in the weak-intermediate coupling regime. At the same time, the DΓA seems to approach the exact strong coupling (Heisenberg) result more accurately than the other techniques.

Also, the critical exponents can be extracted in DΓA for the correlation length and susceptibility: $\nu \approx 0.72$ and $\gamma \approx 1.37$, respectively [171]. This agrees well with the ones obtained by other methods for the **3D Heisenberg universality class** (see previous section) [171, 241]. Specifically, subsequent dual fermion analyses are fully consistent with this result [241].

The analysis at half-filling reveals a continuous classical finite-temperature antiferromagnetic phase transitions with a transition temperature $T_N(U) > 0$. However, as it is presented in the following section, by doping the system the Néel temperature can be quenched down to $T_N \to 0$, triggering the appearance of a quantum critical point.

6.3 From classical to quantum criticality: doping the Hubbard model

In the previous section, by means of the DMFT and DΓA, it was shown, that the three-dimensional half-filled Hubbard model on a cubic lattice exhibits a second order magnetic phase transition from a paramagnetic to an antiferromagnetically ordered phase. For this system, the Néel temperature is maximal at $U \approx 2$ and the critical exponents for spin susceptibility and correlation length agree with the 3D Heisenberg ones. In this section, the restriction to the half-filled case $n = 1$ is lifted and the system is **doped with holes**. The interaction is fixed to $U = 2$, i.e. to the value where the highest Néel temperature is is found in the half-filled system.

The transition temperatures as a function of doping are shown in Fig. 6.2, with a dashed green line

[4] To obtain the results of this section for the magnetic phase diagram, the ladder-DΓA with λ-correction only in the spin-channel (see Sec. 2.3.2.2) was used. The data shown for DΓA are always extracted from the λ-corrected DΓA susceptibility (Eq. (2.61)).

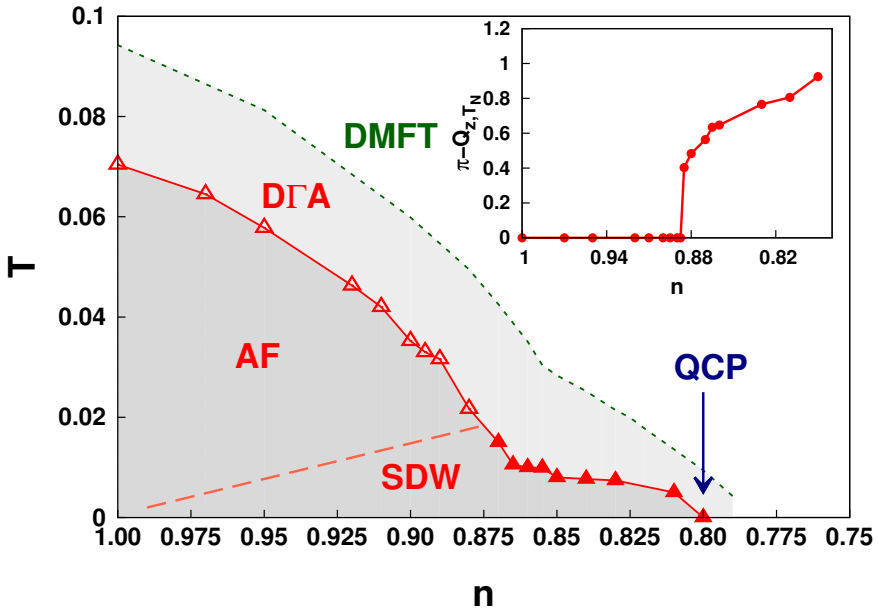

Figure 6.5: (taken from [220]) Phase diagram of the $3d$ Hubbard model at $U = 2$, showing the leading magnetic instability as a function of the density n in both DMFT and DΓA. Inset: Evolution of the magnetic ordering vector along the magnetic instability line of DΓA, showing a transition from an commensurate AF ordering with $Q_z = \pi$ (open triangles in the main panel) to incommensurate SDW ordering with $Q_z < \pi$ ordering (full triangles in the main panel). The dashed line of the main panel indicates the presumptive crossover between AF and SDW in the ordered phase.

representing the DMFT calculation and a solid red one for the DΓA[5]. Similarly to the half-filled case, the DΓA significantly reduces the ordering temperature. However, only for small doping $n \gtrsim 0.88$ the emerging ordering remains **commensurate** with the lattice, specifically purely antiferromagnetic [$\vec{Q} = (\pi, \pi, \pi)$, open triangles]. At higher doping, the ordering vector of the phase transition changes from the one of a commensurate antiferromagnetic order to the one of an **incommensurate spin-density wave** (SDW) (filled triangles) as a function of doping, i.e. to $\vec{Q} = (\pi, \pi, \pi - \delta)$ where $\delta > 0$ depends on the doping level. The grade of incommensurability can be expressed by $\pi - Q_z$, which is shown for the DΓA Néel temperatures in the inset of Fig. 6.2. Eventually, at high enough doping $n \geq n_c$, the finite-temperature ordering is fully suppressed and a **quantum critical point (QCP)** appears at $(T = 0, n = n_c)$.

In order to analyze the critical properties of the doped Hubbard model on a cubic lattice, Fig.

[5]Again, the ladder-DΓA in the spin channel was used for determining the transition line. However, in contrast to the previous section, both particle-hole channels (i.e. charge as well as spin) have been used to determine the λ-correction (see discussion of the λ-corrections in Sec. 2.3.2.2, Sec. 2.4 and Ref. [68]). This change is motivated by the possibility that the suppression of charge fluctuations is expected to become less effective when doping the system out of half-filling.

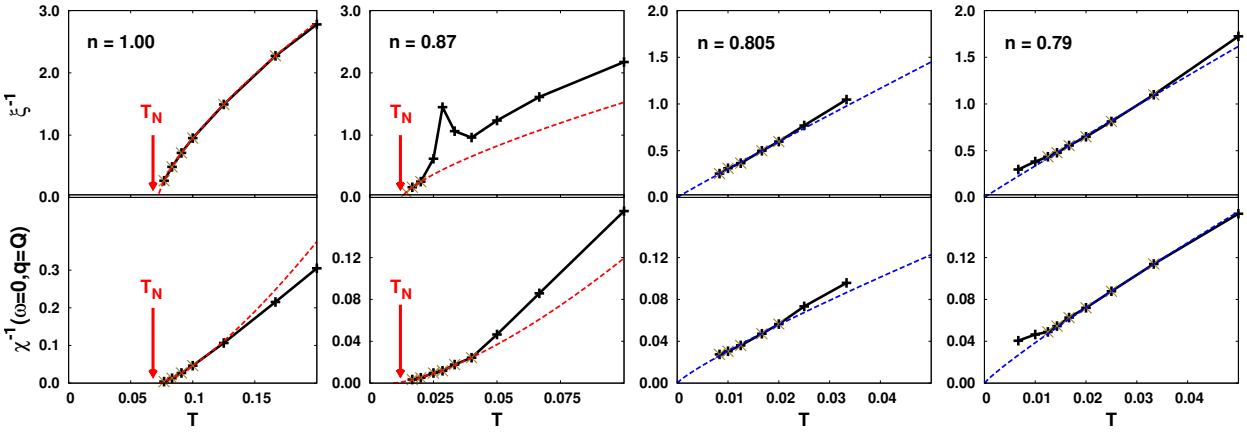

Figure 6.6: (taken from [220]) DΓA results for the inverse correlation length (ξ^{-1}, upper panels) and maximal spin susceptibility (χ^{-1}, lower panels) as a function of temperature for four different densities. The fits of the corresponding critical behavior, from which ν and γ have been extracted, are reported as dashed lines.

6.6 shows the obtained DΓA results of the temperature dependence of the (inverse) spin correlation length $\xi^{-1}(T)$ (upper panels) and spin susceptibility $\chi_s^{-1}(\omega = 0, \vec{q} = \vec{Q})$ (lower panels) at its maximum at wave vector $\vec{Q}$, respectively. Four exemplary doping levels $n = 1/0.87/0.805/0.79$ have been selected. The leftmost column recapitulates the half-filled case of the previous section. Here, the Néel temperature is $T_N(n = 1) \approx 0.072$ and the numerically extracted critical exponents are $\nu \approx 0.72$ and $\gamma \approx 1.37$, which, as expected, agree well with the ones of the 3D Heisenberg model.

The situation remains qualitatively similar for small dopings: the transition temperature is reduced, but the critical exponents persist (within the numerical uncertainties) to be the 3D Heisenberg ones, with $\nu \approx 0.72$ and $\gamma \approx 1.36$ (second column of Fig. 6.6). However, at a first glance, the temperature dependence of the correlation length appears to be dramatically altered, because, starting from the high temperature regime and cooling the system, after an initial increase of the correlation length $\xi(T)$, it starts to decrease again, before, eventually, diverging at the phase transition temperature. Yet, this fact just reflects the **inapplicability of the standard definition of the correction length** as the (inverse) width of the peak around the maximum of the susceptibility (see Eq. (6.3)). In fact, when reducing the temperature, additionally to the peak at $\vec{q} = (\pi, \pi, \pi)$ at high temperatures (antiferromagnetic), a second (incommensurate) peak at $\vec{q} = (\pi, \pi, \pi - \delta)$ appears and starts to separate from the first one. Effectively, this causes the peak to broaden and, eventually, the correlation length apparently to decrease. Fig. 6.7 illustrates this fact for a temperature cut at fixed $n = 0.87$.

Approaching the **critical doping** $n_c \approx 0.805$, where $T_N(n \to n_c) \to 0$, and, hence entering the

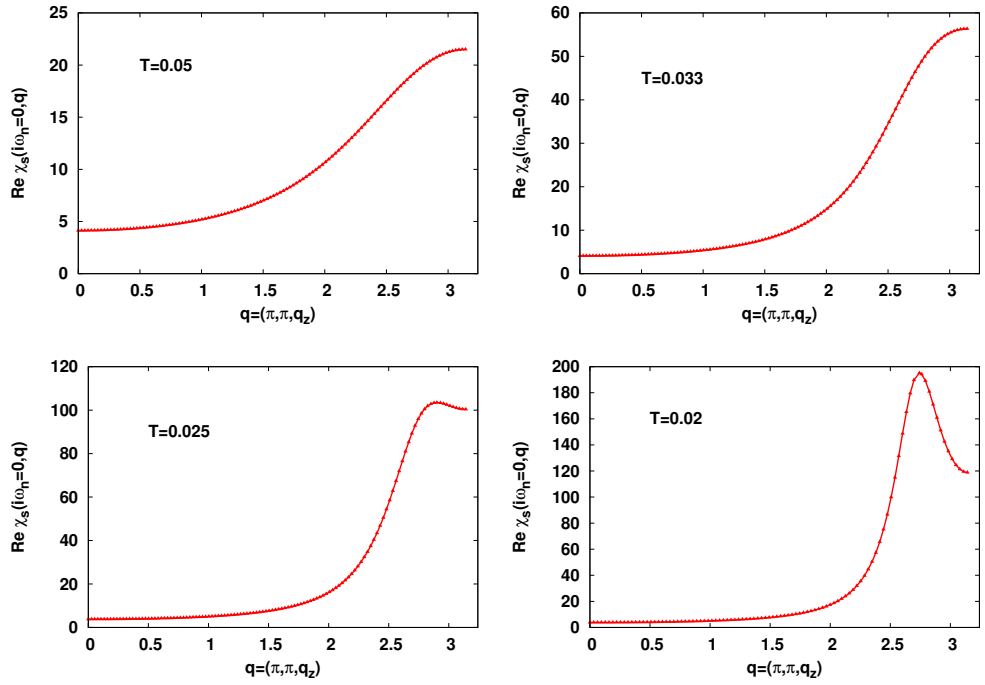

Figure 6.7: Momentum cut $\vec{q} = (\pi, \pi, q_z)$ of the (real parts of the) spin susceptibilities $\chi_{\mathrm{S}}(\omega = 0, \vec{q})$ for the doping level $n = 0.87$ and the temperatures (from top left) $T = 0.05/0.033/0.025/0.02$.

quantum critical regime illustrated in Fig. 6.2, the influence of the QCP becomes evident (see third column in Fig. 6.6), i.e. the critical exponents are altered. However, due to the influence of the Kohn lines of the Fermi surface, they are **not equivalent to the ones of standard Hertz-Millis-Moriya theory** $\nu^{\mathrm{HMM}} = 0.75$ and $\gamma^{\mathrm{HMM}} = 1.5$ (see Sec. 6.1): the numerical data extracted from the DΓA-data ($\nu \approx 0.98$ and $\gamma \approx 0.86$) provide clear evidence, that the quantum criticality in the 3D Hubbard model is indeed **controlled by the Kohn anomalies** of the underlying Fermi surface.[6] In spite of the numerical uncertainty for the exact determination of γ, the DΓA data show (i) a large value of ν close to the RPA prediction for the Kohn-anomaly controlled exponent and (ii) evidently that the **scaling relation** $\gamma = 2\nu$ (which is satisfied in case of the standard HMM theory as well as approximately for the 3D Heisenberg model) is **strongly violated** (actually, even reversed) in the presence of Kohn anomalies.

Eventually, by further increasing the doping (fourth column in Fig. 6.6), one can observe a finite correlation length and susceptibility at low temperatures, which signals the abandoning of the quantum critical region and, therefore, the inapplicability of the scaling relations Eqs. 6.5 and 6.4 at these temperatures.

[6] Please note that the determination of the critical exponents of the susceptibility γ is numerically challenging, while the critical exponent of the correlation length seems to be more robust numerically (see also Sec. 2.4).

At the end of this chapter about quantum critical magnetism in the three dimensional Hubbard model on a simple cubic lattice, several conclusions can be drawn from the first application of DΓA to this (largely unexplored) problem:

- The DΓA, due to the inclusion of spatial correlations, significantly reduces the ordering temperatures with respect to DMFT.
- For the classical, finite-temperature magnetic phase transitions, one obtains 3D Heisenberg critical exponents for the temperature dependences of spin susceptibility and correlation length.
- The, at a first sight, peculiar temperature-dependence of the magnetic correlation length can be ascribed to the competition between AF and (incommensurate) SDW fluctuations at finite doping. The classical critical exponents, however, are still compatible with the 3D Heisenberg universality class.
- The influence of the Fermi surface properties of the simple cubic lattice (**Kohn anomalies**) becomes evident, when the ordering temperature is quenched to zero by a non-thermal control parameter, i.e. when entering the quantum critical funnel-shaped region around the QCP. This results in **non-standard** Hertz-Millis-Moriya **quantum critical exponents**. Specifically, (i) the scaling relation between the critical exponents of magnetic susceptibility and correlation length is strongly violated, (ii) the values of critical exponents are strongly modified with respect to the ones expected by HMM theory and (iii) a dynamical critical exponent z cannot be identified unambiguously any longer.

As the above results of a predominant influence of the Kohn anomalies have been found for a relatively large value of the electronic interaction, the conclusions drawn above could be extremely relevant for identifying the origin of the often controversial interpretations of the quantum phase transitions in correlated oxides and heavy fermions. Moreover, these studies pave the way for future investigations of the interplay between Kohn anomalies and quantum critical fluctuations below the upper critical dimension.

7 Conclusions and outlook

"Once we accept our limits, we go beyond them."

- Albert Einstein (German theoretical physicist, *1879 - †1955)

The main goal of this thesis was to achieve a substantial progress in describing phase transitions of strongly correlated model systems in their classical and quantum occurrences. The difficulties of a complete theoretical treatment of this subject arise from two facts: (i) the large mutual interactions of the particles in these systems, and (ii) that at the vicinity of second-order phase transitions, long-range spatial fluctuations must be taken into account. The first argument implies that common perturbation theory, mean-field theories and density functional theory are often not applicable in these systems, so that non-perturbative many-body techniques such as - at least - the DMFT have to be applied. From the second point one can expect, however, that even DMFT is not enough in the proximity of second-order phase transitions in finite dimensions, because it neglects spatial correlations. Hence, the focus of this thesis was a cutting-edge diagrammatic extension of DMFT, the DΓA, and its application it to the most fundamental model for electronic correlations, the Hubbard model, in the vicinity of its phase transitions.

To set the stage, starting from an every-day example, **Chapter 1** gave a short introduction to phase transitions in general and the basic classification into classical (temperature-triggered) and quantum phase transitions (occurring at zero temperature as a function of a non-thermal control parameter). In order to illustrate this introduction, examples were given in terms of the famous and rich phase diagrams of the high-temperature cuprates.

Chapter 2 introduced the concepts and methods used throughout the thesis. After stating the full condensed matter many-body Hamiltonian, it was simplified to the most fundamental model of electronic correlations, the Hubbard model. Also, the even more basic Anderson impurity model was introduced. Afterwards, the DMFT was sketched, the self-consistency cycle described and its

diagrammatic content specified in terms of a purely local self-energy, highlighting how purely local correlations are taken into account in this theory. Next, several ways of extending the DMFT in order to include non-local correlations were specified. After an introduction to the building blocks of all cutting-edge diagrammatic extensions of DMFT (among which the DΓA was used throughout this thesis), the two-particle (vertex) quantities and their calculation within the DMFT framework, two variants of the DΓA, the parquet and the ladder formulation, were characterized. In the ladder case, a method of mimicking the full self-consistency, the Moriyaesque λ-corrections was discussed in detail. Eventually, at the end of Chapter 2, the state-of-the-art implementation of the ladder-DΓA was summarized.

Starting with a two-particle level analysis of the DMFT-solution to the Hubbard model, non-perturbative precursor features of phase transitions were characterized in **Chapter 3**. Specifically the divergence of the two-particle vertex irreducible in the charge channel Γ_c was interpreted as a precursor of the Mott-Hubbard transition in the DMFT phase diagram of the paramagnetic single-band Hubbard model at half-filling. At higher interactions, also the irreducible particle-particle up-down vertex $\Gamma_{\mathrm{pp}}^{\uparrow\downarrow}$ diverges. Both divergences are located "before" the Mott-Hubbard transition, i.e. well in the metallic region of the phase diagram. Approaching the Mott-Hubbard transition, infinitely many divergence lines could be identified, which were described in the atomic limit by analytic calculations. These divergences have direct implications on analytic diagrammatic techniques. For instance, the physical interpretation of the self-energy through its parquet decomposition gets dramatically more complicated after crossing the lines of the divergences. However, these divergence lines are not connected to a thermodynamic phase transition, as the finiteness of the full vertex F shows. For the parquet decomposition, such interpretational difficulties can be circumvented by the formulation of the decomposition through the full vertex F in different representations and partial summations of the Dyson-Schwinger equation of motion, a novel approach coined "fluctuation diagnostics".

In **Chapter 4** the influence of the dimensionality of systems on their one-particle spectra was analyzed. As the role of spatial fluctuations gets more pronounced as the dimensionality of the systems is decreased, in order to get accurate solutions in finite dimensions, one needed to go beyond DMFT, taking non-local fluctuations into account. In three dimensions, it could be shown that local and non-local correlations are not substantially interwoven, in the sense that the self-energy is separable (at least in an energy-window around the Fermi surface) into a local but frequency-dependent and a static but momentum-dependent part. In two dimensions, a collapse of the self-energy onto a single curve was observed when reparametrizing it via the non-interacting electron dispersion. This collapse could be observed to a very high degree for the half-filled, isotropic system also in the vicinity of the Fermi surface, if no pseudogap was present. For the anisotropic and/or doped cases, the imaginary part of the self-energy was reproduced quite accurately, however, the accuracy of the reparametrization of its real part strongly depended on the degree of

anisotropy/doping. Reducing the dimensionality of the system, eventually, to one dimension and to finite systems (Hubbard nano-rings), one arrived at an interesting (and quite stringent) test-bed for benchmarking the DMFT and the variants of DΓA, since there (numerically) exact solutions are possible. The Green functions, self-energies and vertices were analyzed and compared. Interestingly, the parquet-based (but not yet fully self-consistent) implementation of the DΓA gave a quantitative improvement over the DMFT description. However, for systems that exhibit a gap in the exact solution, non-local corrections stemming from the (local) fully irreducible vertex from DMFT were not strong enough to open this gap in the approximation. The description was improved by the ladder-version of the DΓA including λ-correction, which in some sense mimics the self-consistency which is lacking in the (one-shot) parquet approach.

The central topic of **Chapter 5** was the fate of the Mott-Hubbard metal-insulator transition in two spatial dimensions. After a recapitulation of the phenomenon of the transition itself and the results of DMFT for the half-filled, paramagnetic system, the influence of spatial correlations was analyzed by including progressively more extended spatial fluctuations. Short-ranged spatial correlations reduced the size of the transition's coexistence region and changed its slope. The inclusion of spatial correlations on every length scale by DΓA, eventually revealed that the Mott-Hubbard transition vanishes in favor of a crossover: At every finite interaction, for low enough temperature, one always observes an insulating behavior. The reason for this striking result could be traced to the spin-fluctuations in the paramagnetic phase, which are induced by the underlying antiferromagnetic transition at zero temperature, consistent with the Mermin-Wagner theorem. At weak coupling this ordering is triggered by Fermi-surface properties, which is why the fluctuations have been classified as Slater-paramagnons.

Finally, in **Chapter 6**, the magnetic phase diagram and the quantum critical point of the (hole-doped) three-dimensional Hubbard model was analyzed. Upon doping, the ordering temperature decreases and the magnetic phase transition changes from antiferromagnetic to incommensurate at high doping. However, the critical exponents for magnetic susceptibility (γ) and correlation length (ν) remained 3D Heisenberg ones until no classical, finite-temperature could be observed anymore. There, in the quantum critical region, however, a significant violation of the predictions of the standard theory for quantum critical phenomena, the Hertz-Millis-Moriya theory, was observed for both critical exponents. This includes a violation of the scaling relations $\gamma = 2\nu$ and the lack of a univocal definition of the dynamical exponent z. This anomalous behavior could be again traced back to Fermi-surface properties, specifically lines connected by a wave-vector $\vec{Q}$ and exhibiting opposite Fermi velocities (Kohn lines), whose effects are no longer hidden by thermal fluctuations and become manifest at the QCP.

All the progress made by applying cutting-edge many-body methods to the Hubbard model in

this thesis are inspiring several future investigations:

1. **Further studies and interpretation of precursors of Mott transitions**
   The physical interpretation and understanding of the divergent irreducible vertex functions, which are regarded as a precursor of the Mott-Hubbard transition, is far from being complete. Recent progress was achieved by analyzing the (simpler) binary mixture and Falicov-Kimball models in addition to DMFT calculations for the Hubbard model [242]. There it was found, that a certain single energy scale can be defined, up to which the self-energy cannot be obtained unambiguously by perturbative techniques. If and how such a scenario can be realized also in the (more complicated) case of the Hubbard model and Anderson impurity model, is an open subject of current investigation.

2. **Quantum criticality for heavy fermion systems**
   To a certain degree, the three-dimensional Hubbard model was chosen for the first basic description of strong coupling quantum criticality by the DΓA. Despite the importance of the determination of the magnetic phase diagram of this model including quantum critical points, even more interesting for the comparison to experiment would be the analysis of models for heavy-fermion systems. One of the most prominent models in this respect is the periodic Anderson model, as it represents the minimal model for the description of f-electron systems and it is of great importance to also analyze this model in DΓA with respect to its quantum criticality.

3. **Magnetic and superconducting phase transitions in lower dimensions**
   As already discussed in the introduction, many interesting phenomena can occur in systems of low spatial dimensionality. For instance, the famous high-temperature cuprates exhibit a plethora of different kinds of phase transitions. In this context, the DΓA vertex could be exploited as an input quantity for a Eliashberg type of approach to the determination of the superconducting region in the phase diagram of the (doped and frustrated) two-dimensional Hubbard model, similar to FLEX+DMFT [243]. Also, it was recently found in these systems, that the electron's scattering rate is proportional to T^2 not only in the metallic regime [244], but also in the pseudogap region of the cuprates phase diagram. Whether this phenomenon can be described by a theory based purely on spin-fluctuations like the ladder-version of the DΓA, which does not couple spin-fluctuations into the particle-particle (Cooperon) channel, future investigations have to clarify.

4. **Separability of spatial and temporal correlations going towards two dimensions**
   The remarkable property, that the self-energy is separable in a purely frequency-dependent and a purely momentum-independent part, has been shown only for systems in three dimensions. One could also think of a systematic analysis of the dimensional crossover by progressively going towards even lower (two) dimensions by introducing a rescaled hopping

amplitude into the non-interacting electron dispersion and reducing it to approach the case of two dimensions. In fact, in two dimensions, spatial and temporal correlations should be more interwoven and such a separation should (in general) not be possible anymore, which raises the question of the location of its point of breakdown going progressively from bulk (three dimensions) to layered systems (two dimensions).

5. **Non-local interactions**
   In the models addressed in this thesis, the Coulomb interaction was acting only between electrons on the same lattice site (purely local). However, the nature of the Coulomb interaction is intrinsically long-ranged, as its potential is given by

$$V(\vec{r}) = \frac{e^2}{|\vec{r}|}.$$

   Often, the "real" Coulomb interaction gets significantly screened, so that the purely local approximation is justified. However, in some cases, this can become a very bad approximation, e.g. for describing charge-ordered phases or adatoms on semiconductor surfaces [245,246]. For the description of such phenomena, one has to consider (at least) the extended Hubbard model. At the level of DMFT one can do so by means of the so-called extended DMFT (EDMFT) [247], which was very successful in the description of, e.g., satellite features of plasmonic excitations [248]. In this context, also the fluctuation diagnostics method can shed light on types of fluctuations are dominating in different regimes of these systems. However, for a full inclusion of spatial correlations, DMFT/EDMFT are not applicable and more powerful extensions are needed (e.g. dual boson [249] or the ab-initio DΓA [250], see below).

6. **Ab-initio DΓA**
   A natural extension of DΓA, namely the application to realistic systems as an ab-initio technique, was already proposed [250]. The basic idea is, to replace the lowest order contribution to the fully irreducible vertex Λ (which is assumed to be purely local in DΓA, i.e. the Hubbard-U) by the full Coulomb interaction V_{ij}. With this assumption for the input vertex, the (ladder-)DΓA equations are solved. By this procedure, all DMFT as well as all GW diagrams are included and non-local correlations beyond these two approaches are taken into account. The solution of the corresponding equations could provide one of the most complete treatments with a quantum many-body theory, useful for the understanding of several, still hot-debated topics in condensed matter physics.

A

Common checks for ED-DMFT calculations

As already discussed in Sec. 2.2.2.2, for the solution of the Anderson impurity model (Eq. (2.7)), specifically embedded in a DMFT self-consistency cycle, several algorithms can be applied. One of them, the exact diagonalization (ED), consists in discretizing the bath of non-interacting electrons, in which the single (interacting) impurity is incorporated. This has the advantage (with respect to QMC-based techniques) that statistical errors are avoided, however, the discretization of the bath can lead to systematic errors, especially in situations, where one is limited to a low number of bath sites n_s, e.g. when calculating two-particle functions (see Sec. 2.3.1). In this Appendix, some checks are summarized, which can be utilized to judge, whether an ED calculation can be referred to as "physically reliable" in the sense that the ED solution represents a possible solution to the AIM. These checks are listed in the following in the order of ease of applicability.

1. **Convergence parameter**

   The DMFT self-consistency depicted in Fig. 2.3 is reached, if a convergence parameter falls below a certain threshold. The definition of this parameter can be based on several quantities, e.g. the (integrated) values of self-energy or Green function or the difference of the Anderson parameters of consecutive DMFT cycles themselves. An empirical value of this convergence parameter, which has been used in all published calculations of this thesis, for which a solution can be called "converged" is $\texttt{conv.param.} < 10^{-13}$ (the differences of the Anderson parameters has been used to quantify the threshold in these cases).

2. **Anderson parameters**

   A glimpse on the Anderson parameters themselves is a further quick check. First, the couplings of the baths should be (numerically) finite. Otherwise one effectively performs a calculation with less bath sites than expected. Second, the bath energies should be mutually different as well as fall in the order of magnitude of physical energy scales of the system. Fur-

thermore, the hybridizations fulfill (at least approximately) the following sum rule (see [251]):

$$\sum_{l=2}^{n_s} V_l^2 = \frac{1}{(2\pi)^d} \int d^d k \epsilon_{\vec{k}} = \sum_n z_n t_n^2 \tag{A.1}$$

($l = 1$ is the impurity site itself), with hoppings t_n to the z_n n-th nearest neighbors. For the special case of the Bethe lattice, this sum-rule reads

$$\sum_{l=2}^{n_s} V_l^2 = t^2.$$

This sum-rule can also be used as an initialization starting point for the first DMFT cycle.

3. **Self-consistency in Green function**

   If the convergence parameter is not directly related to the Green function (see check 1.), one can test the self-consistency condition

   $$G(\nu) = \int d^d k \frac{1}{i\nu_n - \epsilon_{\vec{k}} + \mu - \Sigma_{\text{DMFT}}(\nu)}$$

   itself, by inserting the DMFT self-energy into the equation above. Empirically, for the program used in this thesis, this condition may be violated for the real part of the Green function in cases of finite frustration of the lattice (i.e. t', t'', etc.). Usually, these deviations are small with respect to the imaginary part of the Green function. This issue, however, is left to further investigations.

4. **Asymptotics of the self-energy**

   As already discussed in Sec. 2.3.2.2, the imaginary part of the physical self-energy on the Matsubara axis exhibits the following asymptotic behavior

   $$\text{Im } \Sigma(\nu) \overset{\nu\to\infty}{\to} -U^2 \frac{n}{2}\left(1 - \frac{n}{2}\right)\frac{1}{\nu_n} \tag{A.2}$$

   while the real part

   $$\text{Re } \Sigma(\nu) \overset{\nu\to\infty}{\to} \frac{Un}{2}. \tag{A.3}$$

   Please note, that for the imaginary part, it is most convenient to actually plot Im $\Sigma(\nu)\nu_n \overset{\nu\to\infty}{\to} -U^2\frac{n}{2}\left(1-\frac{n}{2}\right)$ for performing this check.

5. **Stability of the solution**

One may perform the DMFT self-consistency with a different initial set of Anderson parameters in order to check the stability of the solution. Please note, that small deviations from the previous results can occur nevertheless, and that, in the vicinity of a first order phase transition, also completely different (but physical) solutions, can be obtained due to the coexistence region occurring there. However, starting from the non-interacting solution, in this case, one should always end up on the metallic side of the solution.

6. **Increasing the number of bath sites n_s**

   A test for the influence of the bath-discretization is the increase of the number of bath site n_s as well as checking how much the solution changes with respect to the one with less bath sites. The usual number of bath sites (including the impurity site) in the calculations performed in this thesis was $n_s = 5$ for two-particle quantities and $n_s = 6/7$ for checking one-particle quantities.

7. **Comparison to other methods**

   Of course, the solution can be compared to the ones obtained by other impurity solvers, preferably from those which do not suffer from a bath discretization error, e.g. CT-QMC (see Sec. 2.2.2.3). In this thesis, for such checks, the `w2dynamics` code [252] was used.

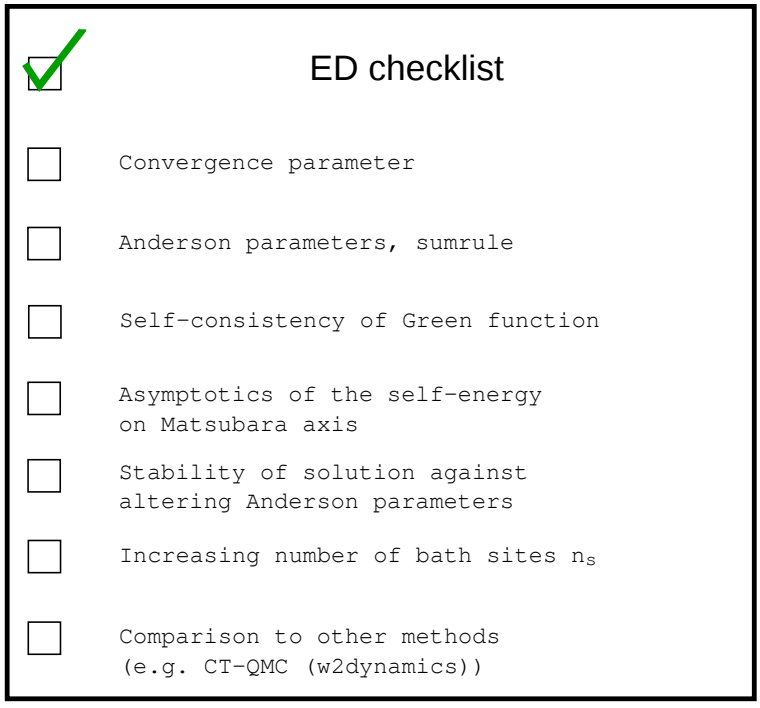

B

Common checks for ladder-DΓA calculations

Similarly to the checks presented in the previous appendix for ED-DMFT calculations, here, checks for the current implementation of the ladder-DΓA as outlined in Sec. 2.4 are enumerated. They may be helpful to the potential user of this program to either detect mistakes in the usage or check the convergence of the obtained results. Of course, as the DΓA procedure requires (converged and valid) DMFT input data. If ED is used to this end, one should hence also test the degree of fulfillment of the ED-checklist in the previous appendix.

1. **Asymptotics of the local irreducible vertices**

   Before starting the actual DΓA calculation, a check of its input quantities is advised. The ladder-DΓA with the spin-channel as dominant fluctuation channel requires the local irreducible vertex in charge as well as spin channel $\Gamma_{\mathrm{c/s}}^{\nu\nu'\omega}$, whose asymptotics for high Matsubara frequency indices are well-known (see, e.g., [64]):

   $$\beta^2\Gamma_{\mathrm{c}}^{\nu'=\pi/\beta,\omega=0}(\nu) \quad \xrightarrow{\nu\to\infty} \quad +U \tag{B.1}$$
   $$\beta^2\Gamma_{\mathrm{s}}^{\nu'=\pi/\beta,\omega=0}(\nu) \quad \xrightarrow{\nu\to\infty} \quad -U, \tag{B.2}$$

   where U is the local interaction of the corresponding (in DMFT self-consistently determined) Anderson impurity model and $\beta = 1/T$ is the inverse temperature. Please note that in the notation of the codes used to produce the results of this work, one has to multiply the vertex by additional factor of β^2 in order to get the right asymptotics.

2. **Local Dyson-Schwinger equation of motion vs. DMFT**

   As described in detail in Sec. 2.4, mainly as a check, in the first part of the program, the DMFT self-energy is calculated in two ways: (i) via the Dyson-equation (2.12) from one-particle quantities (interacting and non-interacting local Green functions) and (ii) via the (lo-

cal) Dyson-Schwinger equation of motion (2.70) from two-particle vertex quantities and the local Green function. Of course, if the vertex was known for all (infinite number of) Matsubara frequencies, as the Dyson-Schwinger equation is an exact relation between the vertex and the self-energy, both quantities would be exactly the same. However, if just a finite number of Matsubara frequencies is known, still the low-frequency behavior of (i) should also be reproduced by (ii) for both the imaginary and the real part the self-energy. The results of both calculations are written to `klist/SELF_LOC_parallel`, where the format of the file is

$$\nu \quad \mathrm{Re}\Sigma_{\mathrm{DMFT}}(\nu) \quad \mathrm{Im}\Sigma_{\mathrm{DMFT}}(\nu) \quad \mathrm{Re}\Sigma_{\mathrm{loc}}^{\mathrm{ladder}}(\nu) \quad \mathrm{Im}\Sigma_{\mathrm{loc}}^{\mathrm{ladder}}(\nu)$$

and can be easily compared by optical inspection.

3. **Convergence in number of frequencies N_ω**

   The results of the ladder-DΓA should be converged in the number of (bosonic and fermionic) frequencies N_ω of the local vertices used as input quantities. The influence of a change in N_ω can be checked in various quantities, e.g., (i) the self-energy calculated via the local Dyson-Schwinger equation of motion (see previous point), (ii) the momentum-dependent DMFT susceptibility $\chi_{\mathrm{r},\vec{q}}^{\lambda_\mathrm{r}=0,\nu\nu'\omega}$ given in the `chisp_omega` and `chich_omega` directories (see Sec. 2.4), (iii) the values of the λ-corrections and (iv) the asymptotics of the DΓA self-energy (see below). Please note that, due to computational limitations, in some cases a full convergence in N_ω cannot be reached and extrapolations $N_\omega \to \infty$ of the quantities of interest have to be performed.

4. **Convergence of the grid of internal momenta N_k**

   The calculation of the momentum-dependent DMFT susceptibility $\chi_{\mathrm{r},\vec{q}}^{\lambda_\mathrm{r}=0,\nu\nu'\omega}$ (and its derived quantities) crucially depends on the number of internal momentum points used, i.e. N_k, as well as on the integration method (see Sec. 2.4). One can check the convergence by inspecting the change in $\chi_{\mathrm{r},\vec{q}}^{\lambda_\mathrm{r}=0,\nu\nu'\omega}$ with N_k.

5. **Convergence of the grid of external momenta N_q**

   The influence of the number of external momentum points used, i.e. N_q, is crucial to (i) the values of the λ-corrections and (ii) the DΓA self-energy and its convergence can be checked in these quantities.

6. **Asymptotics of DΓA vs. DMFT self-energies**

   As already explained in Sec. 2.3.2.2, the λ-corrections introduced there ensure the asymp-

totics of the DΓA self-energy to be

$$\Sigma(k) = \frac{Un}{2} + \frac{1}{i\nu}U^2\frac{n}{2}\left(1-\frac{n}{2}\right) + \mathcal{O}\left(\frac{1}{(i\nu)^2}\right), \tag{B.3}$$

which agrees with the DMFT result. Hence, the (imaginary part of the) ladder-DΓA self-energy (multiplied by the Matsubara frequency leading to constant asymptotics), can be plotted as a function of the Matsubara frequency on top of the DMFT one (which exhibits the correct $\frac{1}{i\nu}$ asymptotics), in order to check the accuracy of the λ-corrections.

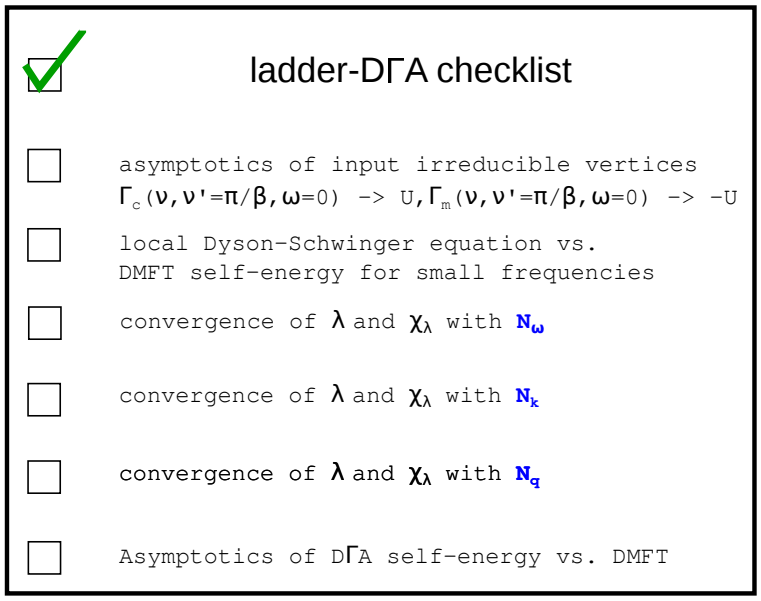

Curriculum vitae

PERSONAL INFORMATION

Thomas Schäfer

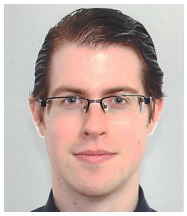

A-1090 Vienna (Austria)

tschaefer@gmx.at

http://tschaefer.bplaced.net

Sex Male | Date of birth 05/04/1987 | Nationality Austrian

EDUCATION AND TRAINING

01/02/2013–28/09/2016

PhD studies (completed with distinction)

ISCED 8

TU Wien
13, Karlsplatz, 1040 Vienna (Austria)

Doctor rerum naturalium under the supervision of Prof. Karsten Held and Prof. Alessandro Toschi

Admission to "**Promotio sub auspiciis Praesidentis rei publicae**" (highest achievable honor for university and school studies, promotion by the federal president of Austria), every final grade in high school and university studies was the highest possible ("sehr gut")

Thesis "Classical and quantum phase transitions in strongly correlated electron systems" graded with the highest possible degree ("sehr gut") by Prof. Karsten Held (TU Wien) and Prof. Walter Metzner (Max-Planck Institute Stuttgart)

funded by FWF (Austrian Science Fund) Doctoral School "Building Solids for Function", http://solids4fun.tuwien.ac.at

01/10/2010–16/12/2012

Master studies (Master of Science awarded with distinction)

ISCED 7

TU Wien, Technical Physics

Thesis: "Electronic correlations at the Two-Particle Level" awarded with the Award for an outstanding and excellent thesis of the City of Vienna (2013)

Diploma student funded by the FWF project “Quantum criticality in strongly correlated magnets (QMC)" (I 610-N16) under the supervision of Prof. Alessandro Toschi and Dr. Georg Rohringer

01/10/2007–30/09/2010

Bachelor studies (Bachelor of Science awarded with distinction)

ISCED 6

TU Wien, Technical Physics

Thesis "Numerical Simulation of μSR for specific Kondo-systems"

01/09/2001–30/06/2006

School leaving examinations and general qualification for university entrance (awarded with distinction)

ISCED 5

HTBLuVA St. Pölten (Higher Technical College for Electronic Data Processing and Business Administration)
3 Waldstraße, 3100 St. Pölten (Austria)

01/09/1997–30/06/2001

Grammar School

ISCED 2

Piaristengymnasium Krems
2, Piaristengasse, 3500 Krems/Donau (Austria)

01/09/1993–30/06/1997

Elementary School

ISCED 1

Josef Rucker Volksschule
12, Auböckallee, 3550 Langenlois (Austria)

WORK EXPERIENCE

01/10/2016–Present

Postdoctoral Researcher

TU Wien

FWF project "Collective phenomena in oxide films and hetero-structures" (F4115-N28), project leader Prof. Alessandro Toschi

01/02/2013–30/09/2016

Project Assistant (PhD position)

TU Wien

FWF doctoral school "Building Solids for Function" (W1243)
FWF project "Quantum criticality in strongly correlated magnets" (I610-N16), project leader Prof. Alessandro Toschi

01/01/2013–30/06/2016

Freelancer

Systemic-Agile-Project (s-a-p), Kottingbrunn (Austria)

webpage creation and administration, setup of content management system

01/09/2011–30/11/2012

Student Research Assistant

TU Wien

FWF-funded master thesis

13/06/2011–05/08/2011

CERN Summer Student (CMS collaboration)

European Organization for Nuclear Research (CERN)
23 Genève, 1211 Genève (Switzerland)

project thesis: "Statistical tests of CMS L1T Occupancy Plots for DQM"

01/10/2009–31/01/2013

University Tutor

TU Wien

Fundamental Principles of Physics I-III, Analysis for Physicists I, Quantum theory I, Statistical Physics I, Electrodynamics I, Quantum theory II

01/07/2008–31/07/2008

Internship (User Helpdesk)

Henkel CEE
29, Erdbergstraße, 1030 Vienna (Austria)

01/10/2006–30/06/2007

Civil Service (Legal Office)

Justizanstalt Stein
4, Steiner Landstraße, 3500 Krems/Stein (Austria)

01/07/2005–31/07/2005

Internship (Infrastructure and Ressource Management)

IBM Austria
95, Obere Donaustraße, 1020 Vienna (Austria)

02/06/2003–27/07/2003

Internship (Department of Accounting)

WIFI Niederösterreich
97 Mariazellerstraße, 3100 St. Pölten (Austria)

PERSONAL SKILLS

Mother tongue(s): German

Other language(s)

UNDERSTANDING		SPEAKING		WRITING
Listening	Reading	Spoken interaction	Spoken production	
English C1	C1	C1	C1	C1
Cambridge Certificate in Business English (BEC) B2				

Levels: A1 and A2: Basic user - B1 and B2: Independent user - C1 and C2: Proficient user
Common European Framework of Reference for Languages

Organisational / managerial skills

Organizer of the "Condensed Matter Theory Journal Club", Institute of Solids State Physics (2016)

Organizer assistant of ICAME (International Conference on the Applications of the Mössbauer Effect), Vienna University of Technology 2009

Class representative 2001 – 2006

School Department representative EDVO 2004/2005

Project manager "Siemens Storage Management System“ (school project)

Digital competence

Programming Languages: C, C++, FORTRAN, Java, COBOL, SQL, Python

ECDL (European Computer Driving License)

SCJP (Sun Certified Java Programmer)

CCNA (Cisco Certified Network Associate)

Other skills

Scuba Diving License

Competitive Ballroom Dancing

Delegate to the European Youth Parliament, Berlin November 2004

International summer academy for gifted pupils, Semmering 2004

Course “Applied Mathematics - Cryptography“, Seitenstetten 2006

Driving licence: B

ADDITIONAL INFORMATION

Research Interests

Strongly correlated electron systems

- Physics of the Hubbard model
- Mott-Hubbard metal-insulator transition
- low-dimensional systems

Quantum criticality

- quantum and classical critical phenomena
- quantum magnetism
- electronic Kohn anomalies

High-temperature superconductivity

- pseudogap physics
- unconventional pairing mechanisms

Quantum many-body techniques

- dynamical mean field theory (DMFT)
- cluster (DCA) and diagrammatic (DΓA) extensions of DMFT
- many-particle Green functions and Luttinger-Ward formalism in the non-perturbative regime
- fluctuation diagnostics and parquet decomposition

Peer-reviewed Journal Publications

1. Parquet decomposition calculations of the electronic self-energy
O. Gunnarsson, T. Schäfer, J. P. F. LeBlanc, J. Merino, G. Sangiovanni, G. Rohringer, and A. Toschi
Phys. Rev. B **93**, 245102 (2016) featured as Editor's Suggestion
http://dx.doi.org/10.1103/PhysRevB.93.245102

2. Momentum structure of the self-energy and its parametrization for the two-dimensional Hubbard model
P. Pudleiner, T. Schäfer, D. Rost, G. Li, K. Held, and N. Blümer
Phys. Rev. B **93**, 195134 (2016), http://dx.doi.org/10.1103/PhysRevB.93.195134

3. Fluctuation Diagnostics of the Electron Self-Energy: Origin of the Pseudogap Physics
O. Gunnarsson, T. Schäfer, J. LeBlanc, E. Gull, J. Merino, G. Sangiovanni, G. Rohringer, and A. Toschi
Phys. Rev. Lett. **114**, 236402 (2015), http://dx.doi.org/10.1103/PhysRevLett.114.236402

4. Separability of dynamical and nonlocal correlations in three dimensions
T. Schäfer, A. Toschi, and Jan M. Tomczak
Phys. Rev. B **91**, 121107(R) (2015), http://dx.doi.org/10.1103/PhysRevB.91.121107

5. Fate of the false Mott-Hubbard transition in two dimensions
T. Schäfer, F. Geles, D. Rost, G. Rohringer, E. Arrigoni, K. Held, N. Blümer, M. Aichhorn, and A. Toschi
Phys. Rev. B. **91,** 125109 (2015), http://dx.doi.org/10.1103/PhysRevB.91.125109

6. Dynamical vertex approximation in its parquet implementation: Application to Hubbard nanorings
A. Valli, T. Schäfer, P. Thunström, G. Rohringer, S. Andergassen, G. Sangiovanni, K. Held, and A. Toschi
Phys. Rev. B **91**, 115115 (2015), http://dx.doi.org/10.1103/PhysRevB.91.115115

7. Divergent Precursors of the Mott-Hubbard Transition at the Two-Particle Level
T. Schäfer, G. Rohringer, O. Gunnarsson, S. Ciuchi, G. Sangiovanni, and A. Toschi
Phys. Rev. Lett. **110,** 246405 (2013), http://dx.doi.org/10.1103/PhysRevLett.110.246405

Conference Proceedings

8. Fluctuation Diagnostics of Electronic Spectra
O. Gunnarsson, T. Schäfer, J. LeBlanc, E. Gull, J. Merino, G. Sangiovanni, G. Rohringer, and A. Toschi
Proceedings of the Vienna Young Scientists Symposium, 9.-10.06.2016
ISBN 978-3-9504017-2-1

9. Dynamical vertex approximation for the two-dimensional Hubbard model
T. Schäfer, A. Toschi, and K. Held
J. Magn. Magn. Mater. **400**, 107–111 (2015), http://dx.doi.org/10.1016/j.jmmm.2015.07.103

10. Development of the digital storage Fuon
H. Ostad-Ahmad-Ghorabi, T. Schäfer, A. Spielauer, G. Aschinger, and D. Collado-Ruiz
Proceedings of the 19th International Conference on Engineering Design (ICED13), Design for Harmonies, Vol.2: Design Theory and Research Methodology, Seoul, Korea, 19-22.08.2013
ISBN 978-1-904670-45-2

Preprints

11. Non-perturbative landscape of the Mott-Hubbard transition: Multiple divergence lines around the critical endpoint
T. Schäfer, S. Ciuchi, M. Wallerberger, P. Thunström, O. Gunnarsson, G. Sangiovanni, G. Rohringer, and A. Toschi
arXiv preprint: http://arxiv.org/abs/1606.03393

12. Quantum criticality with a twist - interplay of correlations and Kohn anomalies in three dimensions
T. Schäfer, A. A. Katanin, K. Held, and A. Toschi
arXiv preprint: http://arxiv.org/abs/1605.06355

Reference Contacts

- Prof. Alessandro Toschi (TU Wien, supervisor Master thesis, co-supervisor PhD thesis)
- Prof. Karsten Held (TU Wien, supervisor PhD thesis)
- Prof. Walter Metzner (MPI Stuttgart, referee and examiner PhD thesis)
- Prof. Giorgio Sangiovanni (University of Würzburg, research partner)
- Dr. Olle Gunnarsson (MPI Stuttgart, research partner)

Teaching

Lecturer substitute for "Advanced Theory of Superconductivity and Magnetism" (2016)

Organizer of the "Condensed Matter Theory Journal Club", Institute of Solids State Physics (2016)

Organizer and teaching assistant for the lectures "Quantum Theory I" (2013), "Quantum Theory II" (2014) and "Quantum Field Theory for Many-Body Systems" (2015)

Scientific Supervision

Marie-Therese Philipp: "Influcence of electronic correlations on the temperature behavior of scattering rates for cuprates"
Co-supervision together with Prof. Alessandro Toschi
Master Thesis, Inst. of Solid State Physics, TU Wien, 2016

Benjamin Klebel: "Space-time separability of the electronic self-energy: the crossover from three to two dimensions"
Co-supervision together with Prof. Alessandro Toschi
Project work, Inst. of Solid State Physics, TU Wien, 2016

Clemens Watzenböck: "Multidimensional density of states for many-electron calculations"
Co-supervision together with Prof. Alessandro Toschi
Bachelor Thesis, Inst. of Solid State Physics, TU Wien, March - July 2015

Honors and awards

Admission to "Promotio sub auspiciis Praesidentis rei publicae" (highest achievable honor for university and school studies, promotion by the federal president of Austria) 2016/2017

Award for an outstanding and excellent diploma thesis of the City of Vienna 2013

Awardee of the “Siegfried Ludwig Stiftung" scholarship 2010, 2011 and 2013

Awardee of the "Windhag" student scholarship 2007, 2008, 2009, 2011 and 2012 by the government of Lower Austria

Awardee of the student scholarships of the Faculty for Physics of the TU Wien, for excellent achievement (2008 and 2009)

Awardee of the Stiftungsstipendium of the TU Wien (2010 and 2012)

Social Award HTBLuVA St. Pölten 2005

“Best of the Year“-Award of HTBLuVA St. Pölten 2004, 2005, 2006

Golden Ring of Honour of HTBLuVA St. Pölten 2006

Invited Talks

"Irreducible Vertex Divergences: Non-Perturbative Landscape of the Mott-Hubbard transition"
14 June 2016
Workshop on multiple solutions in condensed matter theories, Paris, France

"The Mott-Hubbard transition in (in)finite dimensions - divergent precursors and a sad fate"
26 November 2015
Invited Seminar Talk in the seminar "Quantum many-body phenomena in the solid state, University of Würzburg", Germany

Talks

"The physics underlying electronic spectra: from parquet decomposition to fluctuation diagnostics"
23 October 2016
ViCoM workshop, Vienna, Austria

"Magnetic transitions and quantum criticality in the three-dimensional Hubbard model"
16 March 2016
APS March Meeting, Baltimore (MD), USA

"Fluctuation diagnostics of the electron self-energy – origin of the pseudogap physics"
14-18 September 2015
The New Generation in Strongly Correlated Electron Systems 2015, Trogir, Croatia

"Phase transitions and criticality of the Hubbard model in two and three dimensions"
1-4 September 2015
Annual meeting of the Austrian Physical Society, Vienna, Austria

"What is the fate of the Mott metal-insulator transition in two dimensions?"
16-20 March 2015
DPG Spring Meeting, Berlin, Germany

"The Mott-Hubbard transition in (in)finite dimensions: precursors and a sad fate"
11-12 February 2015
FOR 1346: Young Scientists' meeting, Würzburg, Germany

"Fate of the Mott metal-insulator transition in the two-dimensional Hubbard Model"
1-2 July 2014
Workshop of the DFG Research Group FOR 723 Functional Renormalization Group for Correlated Fermion Systems, Vienna, Austria

"Understanding Electronic Scattering beyond Fermi-liquid Theory: from Pseudogap Phases to the MIT"
16-20 June 2014
The New Generation in Strongly Correlated Electron Systems 2014, Nice, France

"Divergent precursors of the Mott metal-insulator transition in DMFT and beyond"
22 April 2014
ViCoM Young Researchers Meeting 2014, Vienna, Austria

"Divergent precursors of the Mott metal-insulator transition in dynamical mean field theory and beyond"
3 April 2014
DPG Spring Meeting, Dresden, Germany

"Quantum criticality in the 3D Hubbard model"
14 January 2014
Solids4Fun seminar, Vienna, Austria

"Beware of ... Dragons: Divergent Precursors of the Mott-Hubbard Transition"
17 December 2013
Vienna Theory Lunch Seminar, Vienna, Austria

"Divergent Precursors of the Mott Transition"
3 September 2013
ERC Ab-Initio Dynamical Vertex Approximation Kickoff-Meeting, Baumschlagerberg, Austria

"Divergent Precursors of the Mott-Hubbard Transition at the Two-Particle Level"
12 July 2013
Solids4Fun Summer School, Hernstein, Austria

"Local Electronic Correlations at the Two-Particle Level"
28 June 2013
Solids4Fun seminar, Vienna, Austria

"Electronic correlation at the two-particle level"
26 March 2012
DPG Spring Meeting, Berlin, Germany

Posters

"Fluctuation diagnostics of the electronic self-energy - origin of the pseudogap physics"
24-25 February 2016
FOR 1346: Young Scientists' meeting, Würzburg, Germany

"Quantum phase transitions and criticality in strongly correlated electron systems"
25 September 2015
Hearing for the prolongation of the Graduate School Solids4Fun, Vienna, Austria

"Fate of the Mott metal-insulator transition in the two-dimensional Hubbard Model"
18-23 August 2014
QCM14 - Quantum Critical Matter - From Atoms To Bulk, Obergurgl, Austria

"Fate of the Mott metal-insulator transition in the two-dimensional Hubbard Model"
14-18 July 2014
Solids4Fun Summer School, Hernstein, Austria

"Divergent Precursors of the Mott-Hubbard transition in DMFT and Beyond"
27 February 2014
ViCoM Conference "From Electrons to Phase Transitions", Vienna, Austria

"Divergent Precursors of the Mott-Hubbard Transition at the Two-Particle Level"
1 July 2013
The New Generation in Strongly Correlated Electron Systems, Sestri Levante, Italy

"Electronic Correlations at the Two-Particle Level"
27 June 2012
The New Generation in Strongly Correlated Electron Systems, Portoroz, Slovenia

Other International and Scientific Activities

Referee for Europhysics Letters (EPL)

Young Scientist Attendee of the 65th Interdisciplinary Lindau Nobel Laureate Meeting (after multi-level international selection process), June/July 2015

Visit of Max-Planck Institute Stuttgart and scientific collaboration with O. Gunnarsson (FWF project I 610-N16), February 2012

Attendee of the official CERN summer student programme, Genève 2011

International summer academy for gifted pupils, Semmering 2004

Delegate to the European Youth Parliament, Berlin 2004

Memberships

Member of the American Physical Society (APS)

Member of the Austrian and World DanceSport Federation (WDSF)

Bibliography

[1] P. Coleman, *Introduction to Many-Body Physics*, Cambridge University Press (Cambridge, 2015).

[2] University of Massachusetts, Amherst, course material "Thermodynamics", http://courses.umass.edu/plecprep/thermo/4c5020.html.

[3] G. R. Stewart, Rev. Mod. Phys. **56**, 755 (1984);
S. Kondo, D. C. Johnston, C. A. Swenson, F. Borsa, A. V. Mahajan, L. L. Miller, T. Gu, A. I. Goldman, M. B. Maple, D. A. Gajewski, E. J. Freeman, N. R. Dilley, R. P. Dickey, J. Merrin, K. Kojima, G. M. Luke, Y. J. Uemura, O. Chmaissem, and J. D. Jorgensen, Phys. Rev. Lett. **78**, 3729 (1997);
A. Krimmel, A. Loidl, M. Klemm, S. Horn, and H. Schober, Phys. Rev. Lett. **82**, 2919 (1999);
K.Andres, J.E.Graebner, and H. R. Ott, Phys. Rev. Lett. **35**, 1779 (1975);
F. Steglich, J. Aarts, C. D. Bredl, W. Lieke, D. Meschede, W. Franz, and H. Schäfer, Phys. Rev. Lett. **43**, 1892 (1979);
O. Trovarelli, C. Geibel, S. Mederle, C. Langhammer, F. M. Grosche, P. Gegenwart, M. Lang, G. Sparn, and F. Steglich, Phys. Rev. Lett. **85**, 626 (2000).

[4] Q. Si, R. Yu, and E. Abrahams, Nature Reviews Materials **1**, 16017 (2016).

[5] see, e.g., M. Imada *et al.*, Rev. Mod. Phys. **70**, 1039 (1998) and references therein.

[6] see, e.g., P. A. Lee, N. Nagaosa, and X.-G. Wen, Rev. Mod. Phys. **78**, 17 (2006) and references therein.

[7] T. Wu, H. Mayaffre, S. Krämer, M. Horvatić, C. Berthier, W. N. Hardy, R. Liang, D. A. Bonn, and M.-H. Julien, Nature **477**, 191-194 (2011);
J. Zaanen and O. Gunnarsson, Phys. Rev. B **40**, 7391(R) (1989);

K. Machida, Physica C **158**, 192 (1989);
M. Kato, K. Machida, H. Nakanishi and M. Fujita, J. Phys. Soc. Jpn. **59**, 1047 (1990).

[8] S. Sachdev, *Quantum Phase Transitions*, second edition, Cambridge University Press (2011).

[9] H. v. Löhneysen, A. Rosch, M. Vojta, and P. Wölfle, Rev. Mod. Phys. **79**, 1015 (2007).

[10] A. Kopp and S. Chakravarty, Nature Physics, **1**, 53 (2005);
S. Sachdev and B. Keimer, *Quantum Criticality*, Physics Today **64**, 29 (2011).

[11] J. J. Binney, N. J. Dowrick, A. J. Fisher, and M. E. J. Newman, *The theory of critical phenomena - An introdcution to the renormalization group*, Oxford Science Publications, Oxford University Press (New York, 2002).

[12] J. A. Hertz, Phys. Rev. B **14**, 1165 (1976).

[13] A. J. Millis, Phys. Rev. B **48**, 7183 (1993).

[14] T. Moriya and A. Kawabata, Journ. Phys. Soc. Jpn **34**, 639 (1973); **35** 669 (1973).

[15] A. Georges, G. Kotliar, W. Krauth, and M. Rozenberg, Rev. Mod. Phys. **68**, 13 (1996).

[16] W. Metzner, and D. Vollhardt, Phys. Rev. Lett. **62**, 324 (1989).

[17] A. Georges, and G. Kotliar, Phys. Rev. B **45**, 6479 (1992).

[18] K. Held, Adv. in Phys. **56**, 6, 829-926 (2007).

[19] D. Vollhardt, *Dynamical mean-field theory for correlated electrons*, Einstein lecture, Ann. Phys. (Berlin) **524**, No. 1, 119 (2012).

[20] A. Toschi, A. A. Katanin, and K. Held, Phys. Rev. B **75**, 045118 (2007),
A. A. Katanin, A. Toschi, and K. Held, Phys. Rev. B **80**, 075104 (2009).

[21] J. Hubbard, Proc. Roy. Soc. London A **276**, 238 (1963); M. C. Gutzwiller, Phys. Rev. Lett. **10**, 159 (1963); J. Kanamori, Progr. Theor. Phy. **30**, 275 (1963).

[22] T. Schäfer, *Electronic correlations at the two-particle level*, Master thesis, TU Wien, Vienna (2013).

[23] A. Altland and B. Simons, *Condensed Matter Field Theory*, Cambridge University Press (2006).

[24] A. Toschi, *Mastering the electronic correlations: a challenge for the contemporary physics*, Tenure Track Talk, Vienna (2012).

[25] P. W. Anderson, Phys. Rev. **124**, 41 (1961);
P. W. Anderson, in *Moment formation in solids*, edited by W. J. L. Buyers (Plenum Press, New York, 1984), p. 313.

[26] A. C. Hewson, *The Kondo problem to heavy fermions*, Cambridge University Press (1993).

[27] T. Schäfer, G. Rohringer, and A. Toschi, *Electronic correlation at the two-particle level*, poster presentation at the DPG Spring Meeting 2012.

[28] P. W. Anderson, Phys. Rev. **124**, 41-53 (1961).

[29] R. Bulla, T. A. Costi, and T. Pruschke, Rev. Mod. Phys. **80**, 2, 395-450 (2008).

[30] E. Müller-Hartmann, Zeitschrift für Physik B Condensed Matter, 76, 2, 211-217 (1989).

[31] J. E. Hirsch, and R. M. Fye, Phys. Rev. Lett. **56**, 2521-2524 (1986),
R. M. Fye, and J. E. Hirsch, Phys. Rev. B **38**, 433-441 (1988).

[32] M. Jarrell, T. Maier, C. Huscroft, and S. Moukouri, Phys. Rev. B **64**, 1915130 (2001).

[33] N. Blümer, *Mott-Hubbard Metal-Insulator Transition and Optical Conductivity in High Dimensions*, PhD Thesis, Augsburg (2002).

[34] M. Suzuki, Progress of Theoretical Physics **56**, 5, 1454-1469 (1976).

[35] E. Gull, A. J. Millis, A. I. Lichtenstein, A. N. Rubtsov, M. Troyer, and P. Werner, Rev. Mod. Phys. **83**, 349-404 (2011).

[36] N. Parragh, A. Toschi, K. Held, and G. Sangiovanni, Phys. Rev. B **86**, 155158 (2012).

[37] M. Wallerberger, *w2dynamics: Continuous time quantum Monte Carlo calculations of one- and two-particle propagators*, PhD thesis, Vienna (2016).

[38] P. Gunacker, *Diagrammatic Quantum Monte Carlo with Worm Sampling*, MSc thesis, Vienna (2014).

[39] T. Maier, M. Jarrell, T. Pruschke, and M. H. Hettler, Rev. Mod. Phys. **77**, 1027-1080 (2005).

[40] M. Jarrell and A. Macridin, *Dynamical Mean Field and Dynamical Cluster Approximation*, http://www.phys.lsu.edu/∼jarrell/Green/ (07/04/2016).

[41] E. Gull, M. Ferrero, O. Parcollet, A. Georges, and A. J. Millis, Phys. Rev. B **82**, 155101 (2010).

[42] A. A. Katanin, J. Phys. A: Math. Theor. 46, 045002 (2013).

[43] A. N. Rubtsov, M. I. Katsnelson, and A. I. Lichtenstein, Phys. Rev. B **77**, 033101 (2008), A. N. Rubtsov, M. I. Katsnelson, A. I. Lichtenstein, and A. Georges, Phys. Rev. B **79**, 045133 (2009).

[44] H. Park, *The study of two-particle response functions in strongly correlated electron systems within the dynamical mean field theory*, PhD thesis, Rutgers (2011).

[45] G. Rohringer, A. Toschi, H. Hafermann, K. Held, V. I. Anisimov, and A. A. Katanin, Phys. Rev. B **88**, 115112 (2013).

[46] C. Taranto, S. Andergassen, J. Bauer, K. Held, A. A. Katanin, W. Metzner, G. Rohringer, and A. Toschi, Phys. Rev. Lett. **112**, 196402 (2014).

[47] T. Ayral and O. Parcollet, Phys. Rev. B **92**, 115109 (2015); T. Ayral and O. Parcollet, Phys. Rev. B **93**, 235124 (2016).

[48] T. Ayral and O. Parcollet, arXiv:1605.09048 (2016).

[49] A. A. Abrikosov, L. P. Gorkov, F. A. Davis, Methods of Quantum Field Theory in Statistical Physics (Dover, New York, 1963).

[50] N. E. Bickers, *Self-Consistent many-body theory for condensed matter systems*, Chap. 6 in *Theoretical Methods for Strongly Correlated Electrons* (Springer, Berlin, 2003), D. Sénéchal et al. (Editors).

[51] G. Rohringer, A. Valli, and A. Toschi, Phys. Rev. B **86**, 125114 (2012).

[52] D. B. McWhan, A. Menth, J. P. Remeika, W. F. Brinkman, and T. M. Rice, Phys. Rev. B **7**, 1920 (1973).

[53] V. Janiš, J. Phys.: Condens. Matter 10, 2915 (1998); Phys. Rev. B **60**, 11345 (1999).

[54] L. D. Landau, A. A. Abrikosov, and I. M. Khalatnikov, Doklady Akad. Nauk S.S.S.R. **95**, 497 (1954).

[55] C. de Dominicis and P. C. Martin, J. Math. Phys. **5**, 31 (1964).

[56] G. Rohringer, *New routes towards a theoretical treatment of nonlocal electronic correlations*, PhD thesis, Vienna (2014).

[57] G. D. Mahan, *Many-particle physics*, Kluwer-Academic, New York (2000).

[58] N. E. Bickers, D. J. Scalapino, and S. R. White, Phys. Rev. Lett. **62**, 961 (1989), J. J. Deisz, D. W. Hess, and J. W. Serene, Phys. Rev. Lett. **76**, 1312 (1996), J. Altmann, W. Brenig, and A. P. Kampf, Eur. Phys. J. B **18**, 429 (2000).

[59] G. Li, N. Wentzell, P. Pudleiner, P. Thunström, K. Held, Phys. Rev. B **93**, 165103 (2016).

[60] A. Valli, T. Schäfer, P. Thunström, G. Rohringer, S. Andergassen, G. Sangiovanni, K. Held, and A. Toschi, Phys. Rev. B **91**, 115115 (2015).

[61] S. X. Yang, H. Fotso, J. Liu, T. A. Maier, K. Tomko, E. F. DÁzevedo, R. T. Scalettar, T. Pruschke, and M. Jarrell, Phys. Rev. E **80**, 046706 (2009).

[62] K. Held, A. Katanin, and A. Toschi, Progress of Theoretical Physics **176**, 117 (2008).

[63] K. Held, C. Taranto, G. Rohringer, and A. Toschi, *Hedin Equations, GW, GW+DMFT and All That*, lecture notes of the Autumn School 2011 Hands-on LDA+DMFT, Forschungszentrum Jülich GmbH (2011).

[64] N. E. Bickers, *Theoretical methods for Strongly Correlated Electrons*, Ch. 6, 237-296, Springer (New York, Berlin, Heidelberg) (2004).

[65] L. P. Kadanoff and G. Baym, *Quantum Statistical Mechanics: Green's Function Methods in Equilibrium and Non-Equilibrium Problems*, W.A. Benjamin (New York) (1962).

[66] T. Moriya, *Spin Fluctuations in Itinerant Electron Magnetism*, Springer Series in Solid-State Sciences, Vol. 56 (1985).

[67] L. S. Ornstein and F. Zernicke, Proc. Acad. Sci. Amsterdam **17**, 793 (1914).

[68] G. Rohringer and A. Toschi, preprint arXiv:1604.08748 (2016).

[69] N. F. Mott, Rev. Mod. Phys. **40**, 677 (1968); *Metal-Insulator Transitions*, Taylor & Francis London (1990),
F. Gebhard, *The Mott Metal-Insulator Transition*, Springer Berlin (1997).

[70] G. Kotliar *et al.*, Rev. Mod. Phys. **78**, 865 (2006).

[71] P. Hansmann, A. Toschi, G. Sangiovanni, T. Sasha-Dasgupta, S. Lupi, M. Marsi, and K. Held, Physica Status Solidi B **250**, 7 (2013).

[72] K. Byczuk, *et al.*, Nat. Phys. **3**, 168 (2007); A. Toschi *et al.*, Phys. Rev. Lett. **102**, 076402 (2009).

[73] A. Toschi, R. Arita, P. Hansmann, G. Sangiovanni, and K. Held, Phys. Rev. B **86**, 064411 (2012).

[74] M. Eckstein, M. Kollar, and P. Werner, Phys. Rev. Lett. **103**, 056403 (2009),
M. Schirò and M. Fabrizio, Phys. Rev. B **83**, 165105 (2010).

[75] C. Taranto *et al.*, Phys. Rev. B **85**, 085124 (2012),
A. Toschi, M. Capone, and C. Castellani, Phys. Rev. B **72**, 235118 (2005).

[76] R. Bulla, Phys. Rev. Lett. **83** 136 (1999).

[77] C. Raas and G. Uhrig, Phys. Rev. B, **79**, 115136 (2009).

[78] S. Ciuchi, G. Sangiovanni, and M. Capone, Phys. Rev. B, **73**, 245114 (2006).

[79] H. Terletska, *et al.*, Phys. Rev. Lett. **107**, 026401 (2011).

[80] Jan Kuneŝ, Phys. Rev. B **83**, 085102 (2011).

[81] G. Baym and L. P. Kadanoff, Phys. Rev. **124**, 287 (1961).

[82] J. Bauer and Alex C. Hewson, Phys. Rev. B **81**, 235113 (2010).

[83] Nan Lin, *et. al*, Phys. Rev. Lett. **109**, 106401 (2012).

[84] H. Hafermann *et. al*, Europhys. Lett. **85**, 27007 (2009).

[85] R. Zitzler, PhD Thesis (Augsburg, 2004),
R. Bulla, Phys. Rev. Lett. **83** 136 (1999).

[86] M. Karski, C. Raas, and G. Uhrig, Phys. Rev. B, **77**, 075116 (2008).

[87] J. K. Freericks and V. Zlatić, Rev. Mod. Phys. **75**, 1333 (2003).

[88] V. Janiš and V. Pokorný, Phys. Rev. B **90**, 045143 (2014).

[89] S. Pairault, D. Sénéchal, and A.-M.S. Tremblay, Eur. Phys. J. B **16**, 85105 (2000).
Th. Maier, Phys. Rev. Lett. **97**, 056402 (2006).

[90] O. Gunnarsson, T. Schäfer, J. P. F. LeBlanc, E. Gull, J. Merino, G. Sangiovanni, G. Rohringer, and A. Toschi, Phys. Rev. Lett. **114**, 236402 (2015).

[91] N. F. Berk and J. R. Schrieffer, Phys. Rev. Lett. **17**, 433 (1966).

[92] D. J. Scalapino, Rev. Mod. Phys. **84**, 1383 (2012).

[93] B. Kyung, S. S. Kancharla, D. Senechal, A.-M.S. Tremblay, M. Civelli, and G. Kotliar, Phys. Rev. B **73**, 165114 (2006). A. Macridin, M. Jarrell, T. Maier, P.R.C. Kent, and E. D'Azevedo, Phys. Rev. Lett. **97**, 036401 (2006).

[94] N. Bulut, D. J. Scalapino, and S. R. White, Phys. Rev. B **47**, 2742 (1993).

[95] K. Haule, A. Rosch, J. Kroha, and P. Wölfle, Phys. Rev. Lett. **89**, 236402 (2002).

[96] T. Schäfer, G. Rohringer, O. Gunnarsson, S. Ciuchi, G. Sangiovanni, and A. Toschi, Phys. Rev. Lett. **110**, 246405 (2013).

[97] V. Janiš and V. Pokorny, Phys. Rev. B **90**, 045143 (2014).

[98] S.-X. Yang, H. Fotso, H. Hafermann, K.-M. Tam, J. Moreno, T. Pruschke and M. Jarrell, arXiv:1104.3854v1 (unpublished appendix).

[99] E. Kozik, M. Ferrero, and A. Georges, Phys. Rev. Lett. **114**, 156402 (2015).

[100] A. Stan, P. Romaniello, S. Rigamonti, L Reining and J.A. Berger New J. of Physics **17** 093045 (2015).

[101] R. Rossi and F. Werner, J. Phys. A **48**, 485202 (2015).

[102] T. Ribic, G. Rohringer, and K. Held, Phys. Rev. B **93**, 195105 (2016).

[103] E. Dagotto, Rev. Mod. Phys. **66**, 763 (1994).

[104] D. J. Scalapino, J. Superconductivity Novel Magnetism, **19**, 195 (2006).

[105] See, e.g., A. Toschi, M. Capone and C. Castellani, Phys. Rev. B **72**, 235118 (2005), D. Nicoletti, O. Limaj, P. Calvani, G. Rohringer, A. Toschi, G. Sangiovanni, M. Capone, K. Held, S. Ono, Yoichi Ando, and S. Lupi Phys. Rev. Lett. **105**, 077002 (2010).

[106] S. Hummel, *Asymptotic behavior of two-particle vertex functions in dynamical mean-field theory*, Master thesis, TU Wien (2014).

[107] A. Damascelli, Z. Hussain, and Zhi-Xun Shen, Rev. Mod. Phys. **75**, 473 (2003).

[108] G. Binnig and H. Rohrer, Rev. Mod. Phys. **59**, 615 (1987).

[109] O. Fischer, M. Kugler, I. Maggio-Aprile, C. Berthod, and Christoph Renner, Rev. Mod. Phys. **79**, 353 (2007).

[110] T. Timusk and B. W. Statt, Rep. Prog. Phys. **62**, 61 (1999).

[111] M. Uchida *et al.*, Phys. Rev. Lett. **106**, 027001 (2011).

[112] D. J. Scalapino, Rev. Mod. Phys. **84**, 1383 (2012).

[113] C. Huscroft, M. Jarrell, Th. Maier, S. Moukouri, and A.N. Tahvildarzadeh, Phys. Rev. Lett. **86**, 139 (2001).

[114] D. Sénéchal and A.M.S. Tremblay, Phys. Rev. Lett. **92**, 126401 (2004).

[115] A. Macridin, M. Jarrell, T. Maier, P.R.C. Kent, and E. D'Azevedo, Phys. Rev. Lett. **97**, 036401 (2006).

[116] V.J. Emery and S.A. Kivelson, Nature **374**, 434 (1995).

[117] Z. A. Xu, N. P. Ong, Y. Wang T. Kakeshita, and S. Uchida, Nature **406**, 486 (2000).

[118] Y. Wang, L. Li, M. J. Naughton, G. D. Gu, S. Uchida, and N. P. Ong, Phys. Rev. Lett. **95**, 247002 (2005).

[119] Y. Kosaka, T. Hanaguri, M. Azuma, M. Takano, J. C. Davis, and H. Takagi, Nature Physics **8**, 534 (2012).

[120] M. Norman, Nature Physics, **10** 357 (2014).

[121] T. D. Stanescu and P. Phillips, Phys. Rev. Lett. **91** 017002 (2003).

[122] M. Imada, S. Sakai, Y. Yamaji, and Y. Motome, J. Phys.: Conf. Ser. **449** 012005 (2013).

[123] E. H. da Silva Neto, P. Aynajian, A. Frano, R. Comin, E. Schierle, E. Weschke, A. Gyenis, J. Wen, J. Schneeloch, Z. Xu, S. Ono, G. Gu, M. Le Tacon, and A. Yazdani, Science **343**, 393 (2014).

[124] K.-Y. Yang, T. M. Rice, and R. C. Zhang, Phys. Rev. B **73**, 174501 (2006).

[125] T. M. Rice, K.-Y. Yang, and F. C. Zhang, Rep. Prog. Phys. **75**, 016502 (2012).

[126] R. Comin, *et al.*, Science, **343**, 390 (2013).

[127] S. I. Mirzaei, D. Strickera, J. N. Hancocka, C. Berthoda, A. Georges, Erik van Heumen, M. K. Chan, X. Zhao, Y. Li, M. Greven, N. Barisiĉ, and D. van der Marel, PNAS **110**, 5774 (2012).

[128] R. J. Birgeneau, C. Stock, J. M. Tranquada, and K. Yamada, J. Phys. Soc. Jpn. **75**, 111003 (2006).

[129] D. N. Basov and T. Timusk, Rev. Mod. Phys. **77**, 721 (2006).

[130] F. Cilento, S. Dal Conte, G. Coslovich, S. Peli, N. Nembrini, S. Mor, F. Banfi, G. Ferrini, H. Eisaki, M. K. Chan, C. J. Dorow, M. J. Veit, M. Greven, D. van der Marel, R. Comin, A. Damascelli, L. Rettig, U. Bovensiepen, M. Capone, C. Giannetti, and F. Parmigiani, Nat. Commun. **5**, 4353 (2014).

[131] J. Sonier, J. Brewer, and R. Kiefl, Rev. Mod. Phys. **72**, 769 (2000).

[132] F. O. Schumann, J. Kirschner, and J. Berakdar, Phys. Rev. Lett. **95**, 117601 (2005), F. O. Schumann, C. Winkler, and J. Kirschner, Phys. Rev. Lett. **98**, 257604 (2007).

[133] I. S. Brandt, Z. Wei, F. O. Schumann, and J. Kirschner, Phys. Rev. Lett **113**, 107601 (2014).

[134] F. O. Schumann, L. Behnke, C.-H. Li, J. Kirschner, Journal of Physics: Cond. Mat. **25**, (9), 094002 (2013).

[135] W. Metzner, M. Salmhofer, C. Honerkamp, V. Meden, and K. Schönhammer, Rev. Mod. Phys. **84**, 299 (2012).

[136] R. Blankenbecler, D. J. Scalapino, and R. L. Sugar, Phys. Rev. D **24**, 2278 (1981).

[137] N. E. Bickers, D. J. Scalapino, and S. R. White, Phys. Rev. Lett. **62**, 961 (1989).

[138] V. Janiŝ, Phys. Rev. B **60**, 11345 (1999).

[139] S.-X. Yang, H. Fotso, H. Hafermann, K.-M. Tam, J. Moreno, T. Pruschke, and M. Jarrell, Phys. Rev. B **84**, 155106 (2011).

[140] K.M. Tam, H. Fotso, S.X. H. Yang, and T.W. Lee, J. Moreno, J. Ramanujam, and M. Jarrell, Phys. Rev. E, **87**, 013311 (2013).

[141] R. Micnas, J. Ranninger, and S. Robaszkiewicz, Rev. Mod. Phys. **62**, 113 (1990).

[142] Sà de Melo, M. Randeria, and J. R. Engelbrecht, Phys. Rev. Lett. **71**, 3202 (1993).

[143] R. Haussmann, Z. Phys. B **91**, 291 (1993).

[144] F. Pistolesi and G. C. Strinati, Phys. Rev. B **53**, 15168 (1996).

[145] B. Kyung, S. Allen, and A.-M. S. Tremblay, ibid. **64**, 075116 (2001).

[146] A. Moreo and D. J. Scalapino, Phys. Rev. Lett. **66**, 946 (1991).

[147] B. Kyung, S. Allen, and A.-M. S. Tremblay, Phys. Rev. B **64**, 075116 (2001).

[148] T. Paiva, R. R. dos Santos, R. T. Scalettar, and P. J. H. Denteneer, Phys. Rev. B **69**, 184501 (2004).

[149] M. Keller, W. Metzner, and U. Schollwöck, Phys. Rev. Lett. **86**, 4612 (2001).

[150] A. Toschi, P. Barone, M. Capone, and C. Castellani, New J. Phys. **7**, 7 (2005).

[151] A. Toschi, M. Capone, and C. Castellani, Phys. Rev. B **72**, 235118 (2005).

[152] A. Garg, H. R. Krishnamurthy, and M. Randeria, Phys. Rev. B **72**, 024517 (2005).

[153] E. Gull, O. Parcollet, P. Werner, and A.J. Millis, Phys. Rev. B **82**, 155101 (2010).

[154] J. Merino and O. Gunnarsson, Phys. Rev. B **89**, 245130 (2014); see also: arXiv:1310.4597.

[155] D. Rohe and W. Metzner, Phys. Rev. B **71**, 115116 (2005).

[156] E. Gull, O. Parcollet, P. Werner, and A.J. Millis, Phys. Rev. B **80**, 245102 (2009).

[157] E. Gull and A. J. Millis, Phys. Rev. B **86**, 2411106(R) (2012).

[158] J. Merino and O. Gunnarsson, J. Phys.: Cond. Matter. **25**, 052201 (2013).

[159] Y.M. Vilk and A.M.S.Tremblay, J. Phys. I **7**, 1309 (1997).

[160] E. Z. Kuchinskii, I. A. Nekrasov, and M. V. Sadovskii, Sov. Phys. JETP Lett. **82**, 98 (2005).

[161] A. Avella, Adv. Cond. Matt. Phys. **2014**, 515698 (2014).

[162] C. Karrasch, R. Hedden, R. Peters, Th. Pruschke, K. Schönhammer, and V. Meden, J. Phys.: Condensed Matter **20**, 345205 (2008).

[163] E. Kozik, E. Burovski, V. W. Scarola, and M. Troyer, Phys. Rev. B **87**, 205102 (2013).

[164] J. M. Tomczak, M. van Schilfgaarde, and G. Kotliar, Phys. Rev. Lett. **109**, 237010 (2012).

[165] J. M. Tomczak, M. Casula, T. Miyake, F. Aryasetiawan, and S. Biermann, Europhys. Lett. **100**, 67001 (2012).

[166] L. Hedin and S. Lundqvist, Solid State Physics **23**, 1 (1969).

[167] L. Hedin, Phys. Rev. **139**, A796 (1965).

[168] F. Aryasetiawan, O. Gunnarsson, Rep. Prog. Phys. **61**, 237 (1998).

[169] M. Liu, L. W. Harriger, H. Luo, M. Wang, R. A. Ewings, T. Guidi, H. Park, K. Haule, G. Kotliar, S. M. Hayden, and P. Dai, Nat. Phys. **8**, 376-381 (2012).

[170] T. Ayral, P. Werner, and S. Biermann, Phys. Rev. Lett. **109**, 225401 (2012).

[171] G. Rohringer, A. Toschi, A. A. Katanin, and K. Held, Phys. Rev. Lett. **107**, 256402 (2011).

[172] T. Ayral, S. Biermann, and P. Werner, Phys. Rev. B **87**, 125149 (2013).

[173] Y. Zhang and S. Das-Sarma, Phys. Rev. B **70**, 035104 (2004).

[174] E. Müller-Hartmann, Zeitschrift für Physik B Condensed Matter **76**, 211 (1989).

[175] X. Deng, J. Mravlje, R. Žitko, M. Ferrero, G. Kotliar, and A. Georges, Phys, Rev. Lett. bf 110, 086401 (2013).

[176] S. Biermann, F. Aryasetiawan, and A. Georges, Phys. Rev. Lett. **90**, 086402 (2003).

[177] A. van Roekeghem, T. Ayral, J. M. Tomczak, M. Casula, N. Xu, H. Ding, M. Ferrero, O. Parcollet, H. Jiang, and S. Biermann, Phys. Rev. Lett. **113**, 266403 (2014).

[178] A. Toschi, G. Rohringer, A. A. Katanin, K. Held, Annalen der Physik **523**, 698 (2011).

[179] P. Ghaemi, T. Senthil, and P. Coleman, Phys. Rev. B **77**, 245108 (2008).

[180] D. Tanasković, G. Kotliar, and V. Dobrosavljević, Phys. Rev. B **84**, 115105 (2011).

[181] H. Ikeda and K. Miyake, Journal of the Physical Society of Japan **65**, 1769 (1996).

[182] Q. Si and F. Steglich, Science **329**, 1161 (2010).

[183] S. Paschen and J. Larrea, Journal of the Physical Society of Japan **83**, 061004 (2014).

[184] H. Weber and M. Vojta, Phys. Rev. B **77**, 125118 (2008).

[185] J. Won-Rim and J. Hoon-Han, Journal of the Physical Society of Japan **82**, 104704 (2013).

[186] M. Civelli, M. Capone, S. S. Kancharla, O. Parcollet, and G. Kotliar, Phys. Rev. Lett. **95**, 106402 (2005).

[187] T. Schäfer, F. Geles, D. Rost, G. Rohringer, E. Arrigoni, K. Held, N. Blümer, M. Aichhorn, and A. Toschi, Phys. Rev. B **12**, 125109 (2015).

[188] P. Pudleiner, T. Schäfer, D. Rost, G. Li, K. Held, and N. Blümer, Phys. Rev. B **93**, 195134 (2016).

[189] D. Rost, E. V. Goreli, F. Assaad, and N. Blümer, Phys. Rev. B **86**, 155109 (2012).

[190] T. Schäfer, A. Toschi, and K. Held, J. Magn. Magn. Mater. **400**, 107-111 (2015).

[191] S. Fuchs, E. Gull, L. Pollet, E. Burovski, E. Kozik, T. Pruschke, and M. Troyer, Phys. Rev. Lett. **106**, 030401 (2011); E. Gull, P. Staar, S. Fuchs, P. Nukala, M. S. Summers, T. Pruschke, T. C. Schulthess, and T. Maier, Phys. Rev. B **83**, 075122 (2011).

[192] M. Potthoff and W. Nolting, Phys. Rev. B **59**, 2549 (1999).

[193] S. Florens, Phys. Rev. Lett. **99**, 046402 (2007).

[194] M. Snoek, I. Titvinidze, C. Töke, K. Byczuk, and W. Hofstetter, New J. Phys. **10**, 093008 (2008).

[195] A. Valli, G. Sangiovanni, O. Gunnarsson, A. Toschi, and K. Held, Phys. Rev. Lett. **104**, 246402 (2010).

[196] I. Titvinidze, A. Schwabe, N. Rother, and M. Potthoff, Phys. Rev. B **86**, 075141 (2012).

[197] A. Valli, G. Sangiovanni, A. Toschi, and K. Held, Phys. Rev. B **86**, 115418 (2012).

[198] D. Rotter, A. Valli, G. Sangiovanni, and K. Held, Eur. Phys. J. B **86**, 68 (2013).

[199] D. Jacob, K. Haule, and G. Kotliar, Phys. Rev. B **82**, 195115 (2010).

[200] H. Das, G. Sangiovanni, A. Valli, K. Held, and T. Saha-Dasgupta, Phys. Rev. Lett. **107**, 197202 (2011).

[201] M. Karolak, D. Jacob, and A. I. Lichtenstein Phys. Rev. Lett. **107**, 146604 (2011).

[202] V. Turkowski, A. Kabir, N. Nayyar, and T. S. Rahman, J. Chem. Phys. **136**, 114108 (2012).

[203] C. Slezak, M. Jarrell, Th. Maier, and J. Deisz, J. Phys.: Condens. Matt. **21**, 435604 (2009).

[204] T. Schäfer, G. Rohringer, O. Gunnarsson, S. Ciuchi, G. Sangiovanni, and A. Toschi, Phys. Rev. Lett. **110**, 246405 (2013).

[205] H. Hafermann, Phys. Rev. B **89**, 235128 (2014).

[206] T. A. Maier, M. S. Jarrell, and D. J. Scalapino, Phys. Rev. Lett. 96, 047005 (2006).

[207] M. Sentef, J. Kuneš, P. Werner, and A. P. Kampf, Phys. Rev. B **80**, 155116 (2009).

[208] L. F. Mattheiss, J. Phys.: Condens. Matter **6**, 64776484 (1994).

[209] P. Phillips, *Advanced Solid State Physics*, 2nd edition, Cambridge University Press (2012).

[210] J. Hubbard, Proc. R. Soc. Lond. A **281**, 401 (1964).

[211] W. F. Brinkman and T. M. Rice, Phys. Rev. B **2**, 4302 (1970).

[212] G. Sordi, P. Sémon, K. Haule, and A.-M. S. Tremblay, Nature Scientific Reports **2**, 547 (2012).

[213] G. Sordi, P. Sémon, K. Haule, and A.-M. S. Tremblay, Phys. Rev. B **87**, 041101(R) (2013).

[214] H. Park, K. Haule, and G. Kotliar, Phys. Rev. Lett. **101**, 186403 (2008).

[215] N. D. Mermin and H. Wagner, Phys. Rev. Lett. **17**, 1133-1136 (1966).

[216] C. Taranto, G. Sangiovanni, K. Held, M. Capone, A. Georges, and A. Toschi, Phys. Rev. B **85**, 085124 (2012).

[217] E. C. Stoner, Proc. Royal Soc. A **165** (922): 372 (1938).

[218] S. Moukouri and M. Jarrell, Phys. Rev. Lett. **87**, 167010 (2001).

[219] T. Baier, E. Bick, and C. Wetterich, Phys. Rev. B **70**, 125111 (2004).

[220] T. Schäfer, A. A. Katanin, K. Held, and A. Toschi, preprint arXiv:1605.06355 (2016).

[221] M. F. Collins, *Magnetic Critical Scattering*, Oxford University Press (New York, 1989).

[222] C. Holm and W. Janke, Phys. Rev. B **48**, 936 (1993).

[223] P. Gegenwart, Q. Si, and F. Steglich, Nature Physics **4**, 186-197 (2008).

[224] Q. Si and S. Paschen, Phys. Status Solidi B **250**, 425-438 (2013).

[225] I. E. Dzyaloshinskii and P. S. Kondratenko, Sov. Phys. JETP **43**, 1036 (1976).

[226] R. Jaramillo, Y. Feng, J. Wang, and T. F. Rosenbaumc, PNAS **107**, 13631 (2010).

[227] R. Jaramillo, Y. Feng, J. C. Lang, Z. Islam, G. Srajer, H. M. Ronnow, P. B. Littlewood, and T. F. Rosenbaum, Phys. Rev. B **77**, 184418 (2008).

[228] A. Yeh, Yeong-Ah Soh, J. Brooke, G. Aeppli, T. F. Rosenbaum, and S. M. Hayden, Nature, **419**, 459 (2002); M. Lee, A. Husmann, T. F. Rosenbaum, and G. Aeppli, Phys. Rev. Lett. **92**, 187201 (2004).

[229] D. A. Sokolov, M. C. Aronson, L. Wu, Y. Zhu, C. Nelson, J. F. Mansfield, K. Sun, R. Erwin, J. W. Lynn, M. Lumsden, and S. E. Nagler, Phys. Rev. B **90**, 035139 (2014).

[230] A. Schröder, G. Aeppli, R. Coldea, M. Adams, O. Stockert, H. v. Löhneysen, E. Bucher, R. Ramazashvili, and P. Coleman, Nature **407**, 351-355 (2000).

[231] J. Custers, P. Gegenwart, H. Wilhelm, K. Neumaier, Y. Tokiwa, O. Trovarelli, C. Geibel, F. Steglich, C. P'epin, and P. Coleman, Nature **424**, 524-527 (2003).

[232] S. Paschen, T. Lühmann, S. Wirth, P. Gegenwart, O. Trovarelli, C. Geibel, F. Steglich, P. Coleman, and Q. Si, Nature **432**, 881 (2004).

[233] Q. Si, S. Rabello, K. Ingersent, and J. Lleweilun Smith, Nature **413**, 804 (2001).

[234] P. Coleman and A. J. Schofield, Nature **433**, 226 (2005).

[235] T. Schäfer, A. A. Katanin, K. Held, and A. Toschi, Supplemental Material to [220] (2016).

[236] T. Holder and W. Metzner, Phys. Rev. B **90**, 161106 (2014).

[237] B. L. Altshuler, L. B. Ioffe, and A. J. Millis, Phys. Rev. B **52**, 5563 (1995).

[238] T. Holder and W. Metzner, Phys. Rev. B **85**, 165130 (2012).

[239] P. R. C. Kent, M. Jarrell, T. A. Maier, and T. Pruschke, Phys. Rev. B **72**, 060411(R) (2005).

[240] R. Staudt, M. Dzierzawa, and A. Maramatsu, Eur. Phys. J. B **17**, 411 (2000).

[241] D. Hirschmeier, H. Hafermann, E. Gull, A. I. Lichtenstein, and A. E. Antipov, Phys. Rev. B **92**, 144409 (2015).

[242] T. Schäfer, S. Ciuchi, M. Wallerberger, P. Thunström, O. Gunnarsson, G. Sangiovanni, G. Rohringer, and A. Toschi, arXiv:1606.03393 (2016).

[243] M. Kitatani, N. Tsuji, and H. Aoki, Phys. Rev. B **92**, 085104 (2015).

[244] N. Barišić, M. K. Chan, M. J. Veit, C. J. Dorow, Y. Ge, Y. Tang, W. Tabis, G. Yu, X. Zhao, and M. Greven, arXiv:1507.07885 (2015).

[245] E. Tosatti and P. W. Anderson, Jap. J. Appl. Phys. Suppl. **2**, 381 (1974).

[246] P. Hansmann, T. Ayral, L. Vaugier, P. Werner, and S. Biermann, Phys. Rev. Lett. **110**, 166401 (2013).

[247] A. M. Sengupta and A. Georges, Phys. Rev. B **52**, 10295 (1995);
R. Chitra and G. Kotliar, Phys. Rev. Lett. **84**, 3678 (2000);
R. Chitra and G. Kotliar, Phys. Rev. B **63**, 115110 (2001);
Q. Si and J. L. Smith, Phys. Rev. Lett. **77**, 3391 (1996).

[248] H. Martensson and P. O. Nilsson, Phys. Rev. B **30**, 3047 (1984).

[249] A. N. Rubtsov, M. I. Katsnelson, A. I. Lichtenstein, Annals of Physics **327**, 5, 1320-1335 (2012).

[250] A. Toschi, G. Rohringer, A. Katanin, and K. Held, Annalen der Physik **523**, 698 (2011).

[251] E. Koch, G. Sangiovanni, and O. Gunnarsson, Phys. Rev. B **78**, 115102 (2008).

[252] `w2dynamics` - Würzburg/Wien strong coupling impurity solver, N. Parragh, M. Wallerberger, A. Hausoel, P. Gunacker, and G. Sangiovanni
available under http://www.ifp.tuwien.ac.at/forschung/arbeitsgruppen/cms/software-download/w2dynamics/ or https://git.physik.uni-wuerzburg.de/users/sign_in.